

**CATHODOLUMINESCENCE AND CHARACTERISATION OF
DEFECT STRUCTURES IN QUARTZ WITH APPLICATIONS
TO THE STUDY OF GRANITIC ROCKS**

Dissertation
zur Erlangung des Doktorgrades
der Mathematisch-Naturwissenschaftlichen Fakultäten
der Georg-August-Universität zu Göttingen

vorgelegt von
Axel Müller
aus Dresden

Göttingen, Juni 2000

D7

Referent: Prof. Dr. H.-J. Behr

Korreferent: Prof. Dr. K. Weber

Tag der mündlichen Prüfung: 21.06.2000

Summary

The presented study contributes in solving the causes of cathodoluminescence (CL) of quartz. For this purpose a variety of quartzes from different geological environments has been systematically studied. The results have been applied to a number of granitic systems for the understanding of the textural evolution, intrusion mechanism, and the phasing of magmatic events of felsic igneous melts.

The spectral response of the CL of quartz in the range of visible light is characterised by emission bands between 1.7 – 2.2 eV (red) and 2.4 – 3.1 eV (blue) resulting in blue, violet, and red-brown colours. The emission bands with characteristic (relative) intensities, positions, and half-widths have been mathematically captured. The intensity of CL normally changes during electron radiation, whereby the blue emission decreases and the red emission increases, indicating that the luminescence centres are unstable. The decay and generation of luminescence centres during electron radiation have been quantified by recording time-resolved spectra and by using the kinetic law. The concentration of unstable luminescence centres is highest for quartz formed at low temperatures. In order to study the stability of luminescence centres at different temperatures a number of heating experiments have been carried out. Four emission bands (1.73, 1.85, 1.96, and 2.96 eV) are more intense after heating, whereas a band at 2.48 eV disappears. Studies of samples with different polishing qualities show that the CL intensity is reduced for rough surfaces, but the time-dependent ratios of the emission bands remain unchanged. Besides radiation the CL intensity is influenced by the temperature (quenching) during the measurement. Also this correlation has been described here with the kinetic law.

A part of the study deals with the correlation between the CL properties and trace element contents (mainly Al, Ti, Li). Analytical conditions for EPMA, LA ICP-MS, SIMS were carefully chosen in order to achieve the highest possible sensitivity of these microanalytical methods applied to quartz analysis. Trace element line profiles explained the growth and alteration zones visible in CL. The average Fe concentration increases with the quartz formation temperature. Therefore, the Fe content can be used to distinguish magmatic and hydrothermal quartz. Substitutional incorporation of Fe^{3+} in the quartz lattice causes CL emission at 1.73 eV. The increase of the 1.85 and 1.96 eV CL emissions during electron radiation is explained by the abundance of hydroxyl defects in the quartz lattice. Upon

electron radiation H^+ diffuses away and forms non-bridging oxygen hole centres, resulting in higher CL intensity. This increase is steeper for hydrothermal and granitic (“wet”) quartzes and is flatter for rhyolitic (“dry”) quartz. The 2.15 eV CL emission (yellow) is characteristic for some granitic quartzes with high Mn (3 – 6 ppm). The 2.48 eV CL emission (turquoise) is typical for hydrothermal quartz, which shows a high Li-associated 3474 cm^{-1} IR absorption band. The 2.58 eV, 2.68 eV emissions occurring in spectra of all investigated quartzes may be caused by intrinsic defects such as oxygen vacancies. Hydrothermal quartz may contain high Al concentrations up to up to 5000 ppm; magmatic quartz shows Al concentrations up to 200 ppm. The hydrothermal quartz is characterised by a blue “flash” at initial electron radiation caused by the 2.79 eV CL emission. It is assumed that this CL emission is related to the positively charged interstitial cations H^+ , Na^+ , Li^+ and K^+ which compensate substitutional Al^{3+} . However, the concentrations of these trace elements do not simply correlate with the CL intensity. Besides the unstable blue CL, we found also a more stable CL emission at a slightly different wavelength (2.96 eV) in quartz phenocrysts in rhyolite and granite. This luminescence could be related with Ti (up to 130 ppm) and is responsible for the contrasting of growth zoning.

Based on the CL properties and trace elements, magmatic quartz has been subdivided into (1) euhedral quartz phenocrysts showing stable, dominantly blue CL and growth zoning related to Ti distribution and (2) anhedral matrix quartz with unstable red-brown CL and homogeneous trace element distribution. The red-brown CL is related to the concentration of OH^- and molecular H_2O in the crystal lattice. Rhyolitic and granitic quartz phenocrysts show similar growth textures and trace element signatures indicating a similar low to mid-crustal crystallisation environment. The phenocrysts are characterised by a fine-scale oscillatory zoning (2 - 20 μm width), within super-ordinate stepped zoning (50 - 1000 μm width), resorption surfaces, diffusion-induced wavy surfaces, and growth impediments. Except for the oscillatory zoning, formed by self-organising growth, all growth textures formed by external physico-chemical changes (temperature, pressure and magma composition) which result in abrupt changes of the Ti concentration in the quartz crystals. The Ti content in the quartz phenocrysts increases with increasing growth rate. Whereas the properties of the quartz phenocryst point at low to mid-crustal origin, the matrix quartz must have been formed during the conditions of magma emplacement.

Hydrothermal quartz shows similar growth patterns as magmatic quartz, but stepped zoning is dominant here. This indicates quartz crystallisation in a disturbed (open) system. A

characteristic feature of hydrothermal quartz is the so-called sector zoning caused by different impurity concentrations dependant of the growth direction. The zoning patterns in hydrothermal quartz are explained by the distribution of Al-defects. The Al uptake is mainly controlled by the pH of the aqueous solution; high pH (=5) results in high Al concentrations in the quartz lattice. Additionally, the charge compensating ions H^+ , Li^+ , Na^+ , and K^+ stimulates the Al^{3+} uptake.

Besides primary growth textures both magmatic and hydrothermal quartz mostly show a large variety of secondary structures, which formed during retrograde processes. These processes include (1) micro cataclasis, (2) healing, (3) diffusion, and (4) α -radiation. Based on the CL measurements, we proposed a classification in (a) secondary structures with reduced defects and (b) secondary structures with induced defects. Secondary structures with reduced defects are basically the result of healing, dissolution-precipitation and diffusion, typically occur in micro shear zones, along grain boundaries, and as halos around fluid inclusions. Decrepitometry studies of fluid inclusions with halos of secondary non-luminescent quartz showed they hold anomalous high fluid pressure on heating. The formation of secondary quartz around fluid inclusions indicates the healing of defect structures and are possibly initiated by the local increase of stress in part due to pressure gradients between fluid inclusion and host quartz. Structures with higher defect concentrations are the result of natural α -radiation and trace element diffusion and comprise bright CL halos around radioactive mineral inclusions, diffusion rims along grain boundaries, and radiation-induced non-luminescent spots. The radiation-induced spots are interpreted as aggregations of aqua complexes with a gel-like structure, i.e. regions with a high local concentration of H_2O and substitutional Al compensated by hydroxyl groups. Non-luminescent spots and secondary quartz around fluid inclusions are frequent in granitic matrix quartz and less common or lacking in phenocrysts.

Cathodoluminescence has been applied to granitic systems from 2 magmatic provinces: the Krušné Hory/Erzgebirge (Czech Republic/Germany) and the Eastern Lachlan Fold Belt (Australia). In this way, the reconstruction of petrogenetic processes during granitic melt generation, ascent and emplacement and related fractionation, could be achieved. The quartz phenocrysts occurring in the F-Li-enriched granites of the Krušné Hory/Erzgebirge show distinct contrasted growth zoning, being more common for phenocrysts in rhyolites. Similarities in grain size, grain shape and growth texture found for phenocrysts in different

granite varieties of a intrusion complex proof a common history during the earliest stage of crystallisation. The CL properties of different quartz generations in granite reflect the change of the water content of the melt. During the early crystallisation stage the magma contained <2.5wt% H₂O and produced euhedral phenocrysts with stable CL and growth zoning. During magma evolution the water content of the melt increases until about 5wt% H₂O. At the latter stage anhedral matrix quartz was formed. The quartz phenocrysts from different complexes of F-Li-enriched granites may show different trace element contents (Ti/Al ratios). However, the magmatic rock textures, quartz generations, growth patterns observed in CL are very similar for all rocks. These similarities suggest that the magmatic quartz textures in the granite and the phenocryst growth patterns found in Krušné Hory/Erzgebirge province are typical for F-Li-enriched melts which are related to Sn-W-mineralisations.

Snowball-textured quartz phenoblasts occur common in highly evolved F-Li-enriched granites and represent a late-magmatic solidification texture. Contrary to the rhyolitic quartz phenocrysts these snowball quartzes show red CL. A trigonal habit of the zoning in the phenoblasts indicates crystallisation temperatures <600°C (at <1 kbar). The irregular zoning is explained due to periodic degassing during melt cooling in the granite roof. We found that snowball quartz is a textural indicator for fluid-saturated, F-Li-enriched melts of alkali feldspar granites with sub-volcanic (shallow) emplacement. Furthermore, it serves as an indirect indicator for Sn-W-mineralisation.

The application of CL to greenschist facial deformed quartz of granites from the Eastern Lachlan Fold Belt, Australia showed that magmatic undeformed and deformed quartz can be easily distinguished based on CL properties. Deformed quartz exhibits structures of newly formed (secondary) quartz with weak red-brown CL whereas undeformed quartz shows blue to violet CL. The secondary quartz is depleted in trace elements. In deformed magmatic quartz the unstable 1.85 and 1.96 eV CL emissions related to water-bearing defects remain constant during electron radiation, indicating that the interstitial molecular water has been removed from the quartz lattice during deformation and subsequently was incorporated into muscovite micro flakes.

Acknowledgements

First of all I like to thank all my co-workers from the Earth Science Institutes in Göttingen for their contribution to having a pleasant time throughout the last three years.

I would like to express my sincere thanks to Prof. Dr. H.-J. Behr and Dr. A.M. van den Kerkhof for setting up the project, their continuous, motivating support, and the numerous discussions we had during the course of study. They reviewed the whole manuscript critically and improved the quality of the thesis significantly. I also like to thank Prof. Dr. Weber for taking on the function of co-adviser.

I am extremely happy about the effective and smooth collaboration with Dr. R. Seltmann and Dr. R. Trzebski. I appreciate many fruitful scientific discussions with them.

I greatly appreciate the help of Dr. A. Kronz, Dr. K. Simon, T. Scherer, and Dr. M. Wiedenbeck with their tremendous technical knowledge they were instrumental for the progress of the present work.

Special thanks go to Dr. J. Götze, Dr. N. Stenina, Dr. K. Breiter, Dr. U. Hein, Dr. M. René, Dr. A. Vollbrecht, Dr. S. Siegesmund for invaluable advice, discussions which largely contributed to the success of this study.

Dr. P. Lennox is thanked for his introduction to the Australian geology and for the organisation of the field work in Australia.

For the correction of the English I wish to thank B. Peters-Kewitz, Dr. F. Wall, Dr. C.J. Stanley, Dr. C.T. Williams, Dr. R. Armstrong, and C. Gross.

Funding for the project was provided by the Collaborative Research Centre SFB 468 “Wechselwirkungen an geologischen Grenzflächen”.

Above all, I thank my parents for their extraordinary support, both morally and financially. During all my university education they have been a constant source of encouragement.

Contents

Summary	3
Acknowledgement	7
Contents	8
1 Introduction	11
1.1 The application of cathodoluminescence to the study of quartz.....	11
1.2 Aims of the study.....	15
<i>Part I – CL properties and defect structures in quartz</i>	15
<i>Part II – CL applied to the study of granitic rocks</i>	17
1.3 Sample material.....	20
<i>Damara Orogen</i>	20
<i>Krušne Hory/Erzgebirge</i>	21
<i>Oberpfalz/NW Saxony/Harz/Odenwald</i>	23
<i>Eastern Lachlan Fold Belt</i>	24
PART I	
Cathodoluminescence properties and defect structures in quartz	
2 Fundamentals of cathodoluminescence	27
2.1 Point defects in quartz.....	30
2.2 The state of water in quartz.....	32
3 Cathodoluminescence equipment	35
3.1 Sample preparation.....	35
3.2 Optical CL.....	36
<i>Cathodoluminescence microscope HC3-LM</i>	36
<i>The TRIAX 320 spectrograph</i>	36
3.3 Scanning electron microscope (SEM) CL.....	41
3.4 Mathematical treatment of CL spectra	43
4 Microanalysis of trace elements and defect centre characterisation in quartz	45
4.1 Electron probe microanalysis (EPMA).....	46
4.2 Laser ablation inductively coupled plasma mass spectrometry (LA- ICPMS).....	51
4.3 Secondary ion mass spectroscopy (SIMS)	54
4.4 Fourier-transform infrared (FTIR) spectroscopy.....	57
4.5 Electron paramagnetic resonance (EPR)	58
5 Analytical results	59
5.1 Characterisation of the cathodoluminescence of quartz.....	59
5.2 Instability of luminescence centres during electron bombardment	66
<i>The effect of temperature</i>	68
<i>CL of thermally treated quartz</i>	73
<i>The effect of sample preparation on the CL of quartz</i>	73
<i>Quantification of CL intensity change during electron radiation</i>	75

5.3	Comparison of CL spectral and trace element analysis	77
	<i>LA-ICPMS, EPMS, and SIMS analysis</i>	77
	<i>FT-IR spectroscopy</i>	78
	<i>Paramagnetic defect centres</i>	87
	<i>Overview of CL emission lines of quartz</i>	89
6	Genetic significance of CL structures and trace element distribution	95
6.1	Impurity uptake during quartz crystallisation in silicate melts.....	95
6.2	Impurity uptake during quartz crystallisation in aqueous solution.....	102
6.3	Secondary CL structures and processes resulting in modification of defect centres.....	107
	<i>Secondary CL structures with reduced defect centres</i>	107
	<i>Secondary CL structures with induced defect centres</i>	112
 PART II Cathodoluminescence of quartz applied to the study of granitic rocks 		
7	Application of Cathodoluminescence to Magmatic Quartz in a Tin Granite – case study from the Schellerhau Granite Complex, Eastern Erzgebirge, Germany (co-authors: Seltmann R. and Behr H.-J.).....	114
7.1	Abstract.....	114
7.2	Introduction	114
7.3	Analytical methods	118
7.4	Geology and geochemistry of the SGC	119
	<i>Geological setting</i>	119
	<i>Phasing</i>	121
	<i>Geochemistry</i>	123
7.5	Textural studies.....	125
	<i>The quartz texture of the SG1</i>	125
	<i>The quartz texture of the SG2</i>	129
	<i>The quartz texture of the SG3</i>	129
7.6	CL-properties of the quartz in the SGC	130
	<i>CL-colours</i>	130
	<i>Primary growth textures</i>	131
	<i>Secondary CL structures</i>	137
7.7	Relationships between CL and trace element distribution in quartz of the SGC	138
7.8	A multistage quartz crystallisation model of the SGC	142
	<i>Early phenocryst crystallisation</i>	142
	<i>Melt separation, intrusion, and main crystallisation of SG1, SG2 and SG3</i>	145
7.9	Summary.....	147
8	The genetic significance of snowball quartz in highly fractionated tin granites of the Krušné Hory/Erzgebirge (co-author: and Seltmann R.).....	149
8.1	Abstract.....	149
8.2	Introduction.....	149
8.3	Petrography and texture.....	151

8.4	CL and growth zoning	151
8.5	Trace elements	153
8.6	Conclusions.....	153
9	Cathodoluminescence (CL) of magmatic quartz: applications to topaz granites from the Hub Stock (Slavkovský Les Mts., Czech Republic)	
	(co-author: René M. and Behr H.-J.)	156
9.1	Abstract.....	156
9.2	Introduction.....	156
9.3	Geological setting	158
9.4	Petrography.....	160
9.5	Methodology.....	160
9.6	Quartz CL colours and growth patterns	162
9.7	Quartz CL spectroscopy and trace element distribution.....	162
9.8	Discussion.....	167
10	Magma crystallisation, emplacement and deformation of S- and I-type granites in the Eastern Lachlan Fold Belt (SE Australia) indicated by quartz texture, cathodoluminescence, and Al-in-hornblende barometry	
	(co-authors: Lennox P., and Trzebski R.).....	171
10.1	Summary.....	171
10.2	Introduction.....	172
10.3	Geological Setting.....	172
10.4	Methods	174
10.5	Geochemistry.....	176
10.6	Quartz texture and foliation development	177
	<i>Carcoar Granodiorite</i>	177
	<i>Barry Granodiorite</i>	179
	<i>Sunset Hills Granite</i>	179
10.7	Cathodoluminescence of quartz.....	182
	<i>Primary magmatic CL textures</i>	182
	<i>Secondary CL structures</i>	182
	<i>CL patterns and properties linked to trace elements in the quartz</i>	183
10.8	Al-in-hornblende geobarometry on the Carcoar and Barry granodiorites.	188
10.9	Conclusions.....	189
	<i>Quartz CL</i>	189
	<i>Magmatic quartz textures</i>	190
	<i>Geochemistry and Al-in-hornblende geobarometry</i>	191
	<i>Deformation fabrics</i>	191
10.10	Geological implications	192
	References	195
	Appendix A	207
	Appendix B	214
	Appendix C	215
	Appendix D	222
	Appendix E	228

1 Introduction

1.1 The application of cathodoluminescence to the study of quartz

The electron-excited luminescence, or cathodoluminescence (CL), is an efficient technique for the visualisation of intra-granular growth textures and alteration structures in quartz. A distinction is made between growth textures such as zonation, resorption, incrustation, cementation, etc., and secondary, late-formed structures such as alteration halos along grain boundaries, healed microcracks formed by brittle deformation and healing structures around fluid inclusions (Behr and Frenzel-Beyme, 1988; Behr, 1989). In the following the term “primary CL textures” is used for intra-granular growth patterns developed during crystal growth which is in agreement with the general application of the term “growth textures” for crystal arrangements and zoning patterns in igneous rocks (e.g. Bard, 1986; Shore and Fowler, 1996; Watt et al., 1997). The term “secondary CL structures” is used for the wide variety of structures formed during alteration, healing, and retrograde processes.

These structures which become visible using CL are principally based on the distribution of trace elements and defects in the crystal lattice. The CL depends on the kind of chemical bond, lattice defects (vacancies), and impurity elements which can act as activators, sensitizers, and quenchers. Changes in the quantity and quality of defects in a mineral revealed by CL and complementary microanalytical methods reflect physico-chemical changes of melts and fluids (nature, concentration and oxidation state of trace elements, temperature and pH of solutions etc.) during crystal growth, deformation or alteration, or post-crystallisation dose rates of natural α - and γ -irradiation. However, the relationship between the CL emission and the defect structures of quartz are complex, most still not completely understood. Therefore, CL microscopy has been underused for the reconstruction of geological processes so far. The presented study contributes in solving the causes of the CL of quartz and uses CL for the interpretation of rock-forming processes.

The CL of minerals was studied more than a hundred years ago by Crookes (1879), who observed that “substances known to be phosphorescent shine with great splendour when subjected to the negative discharge in high vacuum”. The first report about cathodoluminescence of quartz was given by Goldstein (1907). The possibilities afforded by the microscopic examination of minerals under electron bombardment was not explored until the 1960’s when the luminescence was studied since introduction of the electron microprobe.

Smith and Stenstrom (1965) and Long and Agrell (1965) independently made luminescence microphotographs by illuminating the surface of thin sections with a electron beam (~1 mm diameter). The results clearly showed the correlation between luminescence colour and brightness and the concentration of trace elements in quartz and zoned calcite. Sippel (1965) and Smith and Stenstrom (1965) used CL for the distinction of detrital quartz grains of igneous or metamorphic origin and cement quartz. During the last 30 years, the application of quartz CL in geosciences has grown in both extent and diversity. Major contributions pointing out the use of CL as a petrologic tool have been published by Smith and Stenstrom (1965), Remond (1977), Zinkernagel (1978), Hagni (1984, 1987), Walker (1985), Marshall (1988), Remond et al. (1992), and Pagel et al. (2000).

Applications of CL in geosciences with special emphasis to quartz and quartz-bearing rocks are summarised as follows:

1. CL facilitates the rapid characterisation of modal mineralogy and the identification of economic or pathfinder minerals. It is possible to distinguish mineral constituents by colour contrast, even in fine-grained rocks like sandstone or quartzite (e.g. Magnus and Götze, 1998).
2. CL is well suitable to distinguish between different mineral generations of quartz and carbonate. It enables the distinction of detrital quartz and cement quartz in siliciclastic rock (e.g. Sippel, 1968) or of different quartz generations in igneous rocks (D'Lemos et al., 1997; Müller et al., 2000). CL imaging clearly yields superior quantification of quartz cement volumes in siliciclastic rocks (e.g. Evans et al., 1988). It has been suggested that CL colours and structures visible in CL in detrital quartz grains may be used as provenance indicators in study of siliciclastic rocks (Matter and Ramseyer, 1985; Owen, 1991; Kennedy and Arıkan, 1990; Milliken, 1994).
3. CL is a sensitive method for revealing growth zonation, twinning patterns, grain shapes and secondary overgrowths which are not distinguishable in transmitted or polarised light (e.g. D'Lemos et al., 1997; Watt et al., 1997). Zoning patterns result from the combination of progressive growth, boundary layer effects and episodes of crystal-melt/fluid disequilibria caused by fluctuations in temperature and melt/fluid composition during crystallisation. The intragranular growth textures yield important information about the nature and evolution of the crystal-forming melt/fluid.
4. The distribution of luminescence colours reveals alteration patterns in crystals, like grain boundary alteration. The knowledge of the alteration pattern is important, for instance, for the interpretation of oxygen isotope distribution in quartz crystals (Valley and Graham,

1996). In ore exploration CL studies of alteration structures facilitates the delineation of the alteration zones affected by mineralising fluids and therewith of the size of ore bodies (Hagni, 1984; 1987).

5. Alteration and deformation (secondary) structures like healed micro-fractures and recrystallised phases can be easily detected in quartz by CL. These structures are indicators for the paleopermeability and paleoporosity of crustal rocks, which are of particular interest for oil exploration (e.g. Behr and Frenzel-Beyme, 1988; Laubach, 1997). Boiron et al. (1992) and Winslow et al. (1994) demonstrated that CL can be used to distinguish between different inclusion generations. Furthermore, CL investigations of secondary structures contribute in solving the problem of fluid loss and re-equilibration of fluid inclusions in quartz (e.g. Audétat and Günther, 1999).
6. CL spectroscopy provides information about the impurity and defect centre quality of a crystal. For example, in carbonate REE can be measured by CL analysis of carbonate at levels down to 0.1 ppm (Habermann et al., 2000). In some cases, CL spectrometry allows the semi-quantitative analysis of trace elements (Townsend and Rowlands, 2000). Defect identification of silicates by CL are also of interest for material sciences e.g., semiconductor industry, silicate technique, optical industry, and for the protection of historical monuments i.e. the study of weathering of building materials like marble and limestone.

Despite considerable benefits of the phenomenological investigation of CL colours in quartz, the causes of CL have not been resolved. This is partly due to the complex CL spectrum, about 12 emission bands were detected in quartz (Kalceff and Phillips, 1995 and references therein), and partly to the fact that the incorporation of trace elements and natural irradiation causes a great number structural defects which strongly influence the quartz CL (e.g. Richter and Zinkernagel, 1975; Zinkernagel, 1978; Sprunt, 1981; Ramseyer et al., 1988; Owen, 1988; Ramseyer and Mullis, 1990; Perny et al., 1992; Kalceff and Phillips, 1995). The determination of trace element distribution is impeded by the general low trace element content of quartz which is in the range of the detection limits of micro analytical techniques. Furthermore, the structure of the defects in the quartz lattice is partly unknown.

Trace elements in quartz which substitute for Si^{4+} are Al^{3+} , Fe^{3+} , Ti^{4+} , Ge^{4+} , P^{5+} , 4H^+ and Ga^{3+} ordered of average frequency (e.g. Bambauer, 1961; Lehmann, 1975; Lehmann and Bambauer, 1973; Nuttall and Weil, 1980; Maschmeyer and Lehmann, 1983a and 1983b; Weil, 1984). Cations such as H^+ , Li^+ , Na^+ , K^+ , Fe^{2+} , Cu^+ , and Ag^+ function as compensators of the electric charge at interstitial positions. It has been striven to obtain quantitative analysis of

trace elements in quartz at the ppm level and with high spatial resolution. Variations in trace element concentrations proved to be useful as petrogenetic indicators. Earlier studies showed a large variation in the chemistry of quartz crystals from different environments (e.g. Suttner and Leininger, 1972; Schrön et al., 1988; Blankenburg et al., 1994 and references therein, Müller et al., 2000). Several authors have tried to relate specific trace elements and the related defect structures in quartz to the formation environment and to a genetic interpretation. Examples are given by Dennen et al. (1970), Siebers (1986), Ramseyer and Mullis (1990), Gerler (1990), and Perny et al. (1992) for hydrothermal quartz, and Suttner and Leininger (1972), Schrön et al. (1988), and Watt et al. (1997) for magmatic quartz. Dennen et al. (1970) proposed a geothermometer based on the incorporation of Al in hydrothermal quartz as a function of formation temperature. Using the electron paramagnetic resonance (EPR) technique, Agel and Petrov (1990) confirmed that the concentration of $[\text{AlO}_4]^{0-}$ centres in quartz increases with increasing crystallisation temperature. The concentration of paramagnetic Ti and Al-related defect centres created by natural irradiation can be used for rock dating (e.g. Grün et al., 2000). Schrön et al. (1988) grouped pegmatitic, granitic, and rhyolitic quartz according to their Ge – Ti – Al contents.

A number of trace elements have been found to activate CL in quartz: Ti (Sprunt, 1981; Kerkhof et al., 1996), Fe (Pott and McNicol, 1971; Sprunt, 1981; Gorobets et al., 1989), Al (Grant and White, 1978; Perny et al., 1992), H and Li (Matter and Ramseyer, 1985; Perny et al., 1992), Mn (Richter and Zinkernagel, 1975; Dudley, 1976), OH⁻ and H₂O (Behr, 1989; Kalceff and Phillips, 1995), Ge (Luff and Townsend, 1990), and Ga (Dudley, 1976). There are only a few studies about the CL of quartz in comparison with trace element studies which have been done to visualise intra-granular growth patterns, to distinguish different quartz generations and to explain crystallisation processes e.g. Sprunt (1981), Ramseyer and Mullis (1990), Perny et al. (1992), Demars et al. (1996), Bruhn et al. (1996), and Watt et al. (1997). The heterogeneous distribution of the trace elements (growth zoning) reflects the physico-chemical variations of the fluid or the melt during crystal growth (e.g. Ramseyer and Mullis, 1990; Watt et al., 1997). Structural and/or chemical variations within crystals, which may relate to crystal growth zones, can be identified by spatial variations in wavelength and intensity of CL (e.g. Waychunas, 1988; Marshall, 1988). CL-contrasted growth zoning are observed e.g., by Ramseyer et al. (1988), Ramseyer and Mullis (1990) and Perny et al. (1992) in hydrothermal quartz and e.g., by Schneider (1993) and Watt et al. (1997) in rhyolitic quartz phenocrysts. Retrograde processes (alteration) may change CL properties resulting in the creation of secondary CL structures may be caused by the redistribution of defects. Most

secondary structures represent migration pathways of fluids which migrate along grain boundaries, microcracks, or channelways by pore overpressure or tectonic strain (Behr and Frenzel-Beyme, 1988; Behr, 1989). In spite of the fact that quartz is one of the common rock-forming minerals, yet the relation between its CL properties, trace element distribution, and petrogenesis is far from be solved.

1.2 Aims of the study

The aim of this study is to better explain the causes for the CL properties of quartz and to find the petrological significance of structures visible in CL. The study is subdivided in 2 parts. In the first part (chapters 2-6) defect structures of quartz are characterised and quantified by CL microscopy, spectroscopy and complementary micro-analytical studies. In the second part (chapters 7-10) CL-studies are applied of the results from the first part to mineralised granitic systems on the hand of examples from the magmatic provinces Krušné Hory/Erzgebirge (Czech Republic/Germany) and the Eastern Lachlan Fold Belt (Australia).

Part I - CL properties and defect structures in quartz

The first part of the study deals with the CL of quartz and its correlation with defect structures. The defect structures in quartz are characterised and their formation during crystallisation and re-distribution during retrograde processes are discussed. Quartz samples from Upper Carboniferous granite intrusions in Germany and related rhyolitic dykes, flows and domes of the Permian continental crust and hydrothermal quartzes of the Upper Proterozoic Damara Orogen of Namibia were taken for the studies of the CL of quartz . The main characteristics of the samples are summarised in table 1.1.

Defect structures in quartz are unstable under electron radiation bombardment resulting in changes of the CL. Looking at the problem of the mathematical capturing of CL parameters like beam energy, radiation time, and sample temperature have been considered. Time-resolved CL spectra with high resolution of the emitted wavelength were recorded to detect the intensity, position and half-width of the emission bands and their changes during electron radiation. In order to establish the parameters which may effect the CL of quartz the spectra were recorded using different beam currents, sample surface roughness, and also by the study of heat-treated samples. Temperature measurements were carried out to determine

temperature changes of the sample during electron radiation. For the quantification of the CL emission spectra were resolved by best fitting with Gaussian curves.

A larger part of the study comprises the correlation between CL properties of quartz and trace element distribution. Electron probe micro analysis (EPMA), laser ablation - inductively coupled plasma mass spectrometry (LA ICP-MS), and secondary ion mass spectrometry (SIMS) were used for the determination of trace elements. Since the determination of trace elements in quartz is not a routine analysis, the sensitivities of the different microanalytical methods were investigated. Furthermore, the defect centres were characterised by using electron paramagnetic resonance spectroscopy (EPR). Fourier transform infra-red (FTIR) spectroscopy facilitates the qualitative characterisation of crystallographic bound water. Water occurs in quartz as different modifications: as hydroxyl groups related to different defect structures (e.g. with Al), as molecular water in micropores and in fluid inclusions. During electron radiation and heating crystallographic bound water may change to molecular water which concentrates in micro pores. These processes are not completely understood and a main topic of this study.

After studying CL properties CL structures and processes responsible for trace element distribution and defect structure formation were discussed. At first quartz growth textures were classified. The rhyolites as well as a number of the granites contain euhedral quartz phenocrysts showing a CL-contrasted complex growth pattern. The euhedral phenocrysts in granite are recognisable only by using CL because they are overgrown and embedded in homogeneous anhedral quartz. The euhedral quartz phenocrysts in granite showing CL-contrasted growth textures have been described in a few cases (Frentzel-Beyme, 1989; Seltmann, 1994; D'Lemos et al., 1997; Müller and Behr, 1997). The questions arise if these phenocrysts have the same origin and formed at similar conditions like phenocrysts in rhyolite. This is important for the understanding Upper Carboniferous magma formation during the Variscan orogeny. The development of growth zoning during magmatic crystallisation is explained by a number of models (e.g. Sibley et al., 1976; Anderson, 1984; Fowler, 1990) that have been derived from the zoning pattern of plagioclase. We apply these models to the crystallisation of magmatic quartz having a similar growth pattern as plagioclase. The classification of growth zoning helps in distinguishing between zoning caused by self-organised growth and zoning caused by physico-chemical changes of external factors such as temperature, pressure and magma composition (Bottinga et al., 1966; Allègre et al., 1981; Shore and Fowler, 1996). The zoning caused by external factors is of interest for the reconstruction of the crystallisation history of felsic melts (magma storage, ascent, mixing,

emplacement, and cooling rate). In a further step the zoning of magmatic quartz was compared with zoning observed in hydrothermal quartz. The differences between impurity uptake in quartz crystals in a melt and in aqueous solutions were discussed.

In CL quartz shows secondary structures which formed during retrograde processes. Typical secondary structures of quartz are healed veinlets and domains along micro shear zones, grain and subgrain boundaries, diffusion rims at grain boundaries, patchy halos of secondary quartz around fluid inclusions, radiation-induced non-luminescent spots, and halos around radioactive inclusions. Mostly, secondary quartz shows a weak luminescence and is therefore mostly easily distinguishable from the host crystal. The formation of secondary quartz may be stimulated by fluid activity. The CL properties of the secondary quartz in comparison with the host quartz indicate a redistribution of defect structures.

The study focuses on two types of secondary structures occurring in magmatic quartz: halos of secondary quartz around fluid inclusions and non-luminescent spots with gel-like defect structure. A wide variety of patchy halos around fluid inclusions have been observed by CL since about one decade (Frentzel-Beyme, 1989; Behr, 1989; Kerkhof and Müller, 1999). The CL-contrasted halos around fluid inclusions are assumed to be related to explosion and implosion-decrepitation at changing PT conditions and to healing processes resulting in volumetric and compositional changes of fluid inclusions. A better understanding of the physical and chemical conditions leading to formation of halos of secondary quartz around fluid inclusions is essential for a proper interpretation of fluid inclusion data. Non-luminescent spots (1-5 μm) observed by SEM-CL become visible first in CL after a radiation time of some minutes. The spots may be associated with larger defect clusters containing structural water in the form of H^+ , OH^- , and H_2O .

Part II - CL applied to the study of granitic rocks

In the second part of the study (chapters 7-10) CL is applied to the study of quartz in granitic rocks and comprises four papers. Two papers (chapter 7 and 8) have been published by Müller, Seltmann, and Behr (2000) in "Mineralum Deposita" (vol. 35: pp. 169-189) and by Müller and Seltmann (1999) in "Mineral Deposits: Processes to Processing" edited by Stanley et al. (pp. 409-412). The other two papers (chapter 9 and 10) have been submitted by Müller, René, and Behr to "Terra Nova" and by Müller, Trzebski, and Lennox to "Mineralogy and Petrology".

Samples were collected from two magmatic provinces, the Krušné Hory/Erzgebirge (Czech Republic/Germany) and the Eastern Lachlan Fold Belt (Australia). The sample material used

for the studies is described in § 7.4, 8.3, 9.3, and 10.3. Principally, in the four papers the results of quartz CL and trace element analysis are utilised to reconstruct interactions at the crystal-melt interface during crystal growth and the state and changes in chemistry and physics of the melt (mixing, differentiation, pulsation, degassing). Complimentary analysis of the magmatic textures (grain size distribution, grain shape, grain relationship) with special emphasis to fabrics influenced by late-magmatic volatiles will provide information about cooling rate of the melt, emplacement conditions, role of volatile. The studies links CL studies with micro-analytical studies and provide principally a new level in the knowledge about petrogenetic and metallogenetic processes in magmatic systems.

On the basis of field work, geochemical and textural investigations, and CL a model of the quartz crystallisation history of the Schellerhau granite melt is presented in *chapter 7* (Müller et al., 2000a). The late-Variscan Schellerhau granite complex (Eastern Erzgebirge, Germany) is characterised by the intrusion sequence of porphyritic (SG1) to weakly porphyritic monzogranites (SG2) and mostly seriate albite granite containing snowball-textured quartz (SG3) (e.g. Seltmann, 1994; Schilka and Baumann, 1996). The intrusions are related to Sn-W-mineralisations. The source of magma and its physico-chemical evolution during ascent and fractionation is of particular interest for the formation of Sn-W-deposits. In the first step different quartz generations were distinguished based on CL studies and the grain size distribution. The SG1 and SG2 contain euhedral phenocrysts overgrown by an anhedral quartz phase (matrix quartz). The phenocrysts show distinct contrasted growth zoning, being normally more common for rhyolitic phenocrysts (Schneider, 1993). On the base of microthermometric studies of silicate melt inclusions, Thomas (1992) calculated the crystallisation depth of granitic quartz phenocrysts of the Erzgebirge granites (e.g. Eibenstock and Schellerhau granites) of up to 21 km. Beside the Schellerhau granites a number of the other investigated granites (samples 6, 7, 8) show such quartz phenocrysts which are overgrown by a younger euhedral quartz generation (matrix quartz). The study of CL properties, growth zoning, and trace element distribution of the different quartz generations in Schellerhau granites answered the following questions: 1) Are granitic phenocrysts comparable with phenocrysts occurring in rhyolites and which crystallisation environment they represent? 2) Which crystallisation conditions cause the differences in CL and trace element distribution of quartz phenocrysts and anhedral matrix quartz? 3) Do the quartz CL and trace element distribution of different quartz generations reflect different crystallisation environments? 4) How does the volatile content of the melt effect the quartz CL and defect

structure distribution? And 4) How can the analysis of growth zoning contribute to reconstruct the melt crystallisation history?

The fluid saturation textures of the SG3 Schellerhau granite are discussed in *chapter 8* (Müller and Seltmann, 1999). This chapter contributes to solving the problem of the formation of snowball-textured alkali feldspar granites and their significance for genesis of Sn-W-deposits. Snowball-textured quartz occurring in highly evolved alkali feldspar granites worldwide are ellipsoidal phenoblasts up to 1 cm in size. They are characterised by zonal arrangement of entrapped matrix minerals (albite, K-feldspar, mica) alternating with inclusion free zones. Since long the origin and interpretation of snowball-texture are controversially discussed and lacked application of CL based arguments. It is considered to be either metasomatic (e.g. Beus et al., 1962; Sonyushkin et al., 1991), or magmatic origin (Kovlenko, 1977; Pollard, 1989; Yin et al., 1995; Renno, 1997; Poutiainen and Scherbakova, 1998). Snowball-textured quartz occurs also in the roof of late Variscan tin-bearing alkali feldspar granite stocks of the Krušné Hory/Erzgebirge. For textural, CL and trace element studies on snowball quartz were chosen the third intrusion stage SG3 of the Schellerhau Granite Complex (Eastern Erzgebirge/Germany) and the Podlesi dyke granite (Western Krušné Hory/Czech Republic). The problem of magmatic or metasomatic origin is discussed on the base of the analysis of the growth zoning visible by CL and the trace element distribution.

Chapter 9 discusses the significance of Ti distribution in quartz phenocrysts for the interpretation of growth patterns on the example of the topaz-bearing granites of Hub Stock, Slavkovsky Les Mountains, Czech Republic (Müller and René, 2000). The Hub Stock hosts the Sn-W deposit Krásno on the SE margin of the Krušné Hory/Erzgebirge Batholith. The trace element signature and growth patterns of quartz phenocryst of the different granite intrusions are compared. The study is focused on high-resolution CL spectroscopy of the quartz CL. Finally, similarities between quartz crystallisation history derivable from the quartz CL and trace element distribution of the Schellerhau and Hub stock tin granites are discussed.

In *chapter 10* the significance of quartz CL for reconstruction of magma crystallisation, emplacement and deformation of S- and I-type granites in the Eastern Lachlan Fold Belt is discussed (Müller et al., 2000b). The samples were collected from Carcoar, Barry and Sunset Hills granites. In contrary to the investigated granites of Krušné Hory/Erzgebirge the three

Australian granites are less fractionated and can be subdivided into the metaluminous I-type Carcoar and Barry granodiorites and the peraluminous S-type Sunset Hills Granite. They were intruded in the Late Ordovician-Early Silurian into Ordovician graywacke and volcanoclastic rocks and were subsequently repeatedly deformed. In this paper quartz CL has been applied to qualify and quantify the conditions of emplacement and deformation of the Carcoar and Barry granodiorites and the Sunset Hills Granite with special emphasis on the macro- and microtextures, trace element distribution of quartz, Al-in-hornblende barometry, and whole rock geochemistry. Structural analysis of granites with a polyphase deformation history often faces the difficulty in discriminating between generations of magmatic and deformation fabrics. The application of quartz CL enables easily the distinction between magmatic and deformation fabrics. Furthermore, the study demonstrates how the quartz CL properties and quartz textures reflect the temperature and pressure conditions during magmatic crystallisation and subsequent greenschist facies deformation. High-resolution spectroscopy is used to show differences in CL of deformed and undeformed magmatic quartz. The causes of this differences which may be associated with crystallographic bound water in the quartz lattice are discussed.

1.3 Sample material

As study objects we have chosen samples for which an extensive state of knowledge based on mapping, chemical and petrographical data already exists but some petrogenetic questions are unsolved. The quartz samples and quartz-bearing rocks were taken from 4 regions (table 2.1).

Damara Orogen

The *first sample group* is represented by hydrothermal quartzes from the southern margin of the Upper Proterozoic Damara Orogen of Namibia. Previous fluid inclusion studies on this quartzes were done by Behr and Horn (1982), Behr et al. (1983), Schmidt-Mumm et al. (1986), and Behr and Schmidt-Mumm (1987) who contributed to the understanding of the formation and activity of tectonic brines during the Proterozoic Damara Orogen (Namibia).

The name “megaquartz” (sample 1) came from mega quartz crystals, which are outstanding, up to 60 m high monoliths in the Hakos Mountains. The quartz bodies are intergrown with dolomite and are emplaced tectonically during an early deformation event of the Damara Orogen. This event was characterised by thrusting of nappes over a fluvial-lacustrine and

evaporitic metaplaya sequence (Behr and Schmidt-Mumm, 1987). The fluids forming this quartz-dolomite body are related to dehydration and leaching of evaporitic hydrate minerals of the metaplaya sequence and had salinities of up to 69 wt% total salt content revealed from fluid inclusion studies sequence (Behr and Schmidt-Mumm, 1987). The formation temperature, as determined in fluid inclusion studies, ranged from 150 to 250°C. The clear fissile quartz (sample 2) representing a special variety of the megaquartz shows perfect cleavage parallel to the positive rhombohedral faces {1011}. The oil-bearing quartz (sample 3) is a pebble found in the gravel plain around the Geelkop Dome and contains fluid inclusions of higher hydrocarbons.

Krušné Hory/Erzgebirge

The *second group* of samples were taken from the magmatic province Krušné Hory/Erzgebirge (Czech Republic/Germany) forming. The study of the granitic rocks with special emphasis on quartz CL and textural analyses contributed to IGCP-373 project “Correlation, anatomy and magmatic-hydrothermal evolution of ore-bearing felsic igneous systems in Eurasia” (Seltmann et al., 2000). The project covers all aspects of the formation of silicic igneous systems (plutonic to volcanic) and their magmatic evolution. Our contribution is important for the understanding of textural evolution, physico-chemical balancing and intrusion mechanism, temporal scale and phasing of magmatic events of Li-F-enriched melts. The samples 4, 5, 6 represent felsic volcanics and subvolcanics of the Altenberg-Teplice caldera (ATC) of the Eastern Erzgebirge/Germany. Neoproterozoic gneisses of the metamorphic basement and volcano-sedimentary rocks form the host rocks of the 500 km² large ATC. Late-collisional extensional tectonics and collapse of the Variscan orogen controlled during the Upper Carboniferous the block and graben tectonics in the area, caldera formation with pre-dominantly ignimbritic rhyolites (Schönfeld and Teplice rhyolite) and porphyritic microgranites (Altenberg microgranite), and finally the post-tectonic multiple intrusion of tin granites of the Schellerhau Granite Complex (SGC) into a subvolcanic level. The volcanogenic fill of the ATC is divided into four volcanic phases two of which have been sampled: The *Schönfeld Rhyolite* (sample 4) as the oldest phase and the effusive-subvolcanic Teplice Rhyolite (phase 2; TPR2), the youngest phase. The grey-greenish Schönfeld Rhyolite contains only a few quartz phenocrysts (<3 vol.%) showing an amoebic and skeletal shape. The *Teplice Rhyolite* (sample 5), volcanic fill of the ATC is the largest outcropping Carboniferous volcanic suite of the Bohemian Massif (Hoth et al., 1995). TPR2 displays hiatalporphyric texture with euhedral quartz (2-3 mm), anhedral alkalifeldspar and few biotite

phenocrysts, sometimes also plagioclas. The caldera collapse was later followed also by a multiple intrusion of highly differentiated *Schellerhau granites* hosting Sn-W-mineralisations (Breiter et al., 1991). The subvolcanic Schellerhau Granite Complex (SGC) belongs to the highly evolved younger intrusion complex (YIC) of the Erzgebirge batholith (e.g. Tischendorf and Förster, 1990). The SGC is characterised by the intrusion sequence of porphyritic (SG1) to weakly porphyritic monzogranites (SG2) and mostly seriate albite granite (SG3). The SG1, SG2 and SG3 chemically represent the suite of P-poor, Li-F-enriched A-type series leucogranites. They are weakly peraluminous ($A/CNK \leq 1.2$), enriched in HREE, Y, Th, Hf, Zr, Sc, Nb, Ta, U and display from SG1 towards SG3 elevated abundances especially of Rb, Li, F, and Sn. There is only a moderate chemical contrast between SG1 and SG2. The SG3 is more highly evolved as to be seen also from fluid saturation textures. NW- and NE-striking faults with vertical dislocations of several hundred metres form the SGC as horst and as a result some deeper pluton parts are uncovered by erosion within the ATC. The granite variety SG2 (sample 6) was selected for investigations in part I (see also § 7.4 and 7.5). The SG2 exhibits a weak hiatalporphyritic texture. Euhedral quartz phenocrysts with an average size of 2.6 mm are overgrown by an anhedral quartz phase with an average grain size of 0.7 mm.

The *Eibenstock granites* (sample 7) are related to the younger intrusive complex (YIC) of the Krušné Hory/Erzgebirge Batholith in Western Erzgebirge (Lange et al., 1972; Fiala, 1968). The batholith extends over an area of about 6000 km², belongs to the largest Variscan granite bodies of the Variscan Orogen. The sample 7 represents the first intrusion phase of the Eibenstock granites and is characterised by a coarse grained, perthitic texture with porphyritic kalifeldspars (3 cm). The porphyritic two mica *Aue Granite* (sample 8) which forms small satellite intrusions located northwestern of the Eibenstock Granite Massif belongs to the older intrusion complex (OIC) of the Krušné Hory/Erzgebirge Batholith.

In chapter 9 the study is focused on the topaz-bearing granites of the Hub Stock hosting the Sn-W deposit Krásno, Slavkovský Les Mountains, Czech Republic (Jarchovský et al., 1994; René, 1998). The Hub stock is situated at the SE margin of the Krušné Hory/Erzgebirge Batholith. The porphyritic topaz-albite granite (sample Ju-10) comprises fine-grained equigranular groundmass containing a phenocryst population dominated by quartz (2-5mm), platy zinnwaldite, and sparse K-feldspar (0.5-2 cm). Topaz-albite microgranites (sample Ju-20) found in the upper part of the Hub stock form the matrix to the intrusion breccias. The hydrothermal *vein quartz* (sample 9) originates from a post-Variscan mylonite zone situated in Hub stock granites.

Oberpfalz/NW Saxony/Harz/Odenwald

The *third group* is represented by Permo-Carboniferous granites and rhyolites from different localities of the Variscan Orogen of Germany (Oberpfalz, NW Saxony, Harz, Odenwald). This group includes rocks which were investigated with CL by Schneider (1993). In our study the trace element analysis of these samples facilitates a better understanding of the phenomena described by Schneider (1993). Furthermore, these samples were chosen to compare the quartz properties of the magmatic rocks of the Krušné Hory/Erzgebirge with other magmatic provinces of the Variscan Orogen.

The *Wachtelberg Rhyolite* (sample 10) intruded metamorphic units of the Variscan Frankenberg – Hainichener Zwischengebirge at the Northern edge of the Erzgebirge. The Frankenberg – Hainichener Zwischengebirge is part of the SW-NE striking Central Saxonian Lineament. The intrusion marks the intersection of Central Saxonian Lineament with the Flöha Lineament.

The *Beucha Rhyolite* (sample 11) belongs to youngest subvolcanics of the Permo-Carboniferous Volcanic Complex of Northwest Saxony. The rhyolite is characterised by the inhomogeneous occurrence of xenolithes and pyroxenes indicating assimilation of lower and mid-crustal rocks. Mineral framework indicates a strong whole rock alteration: discordant calcite veins, apatite in opaque biotites, sericitised and kaolinised orthoclas and plagioclas, and pyroxenes dulled by iron oxides.

The medium-grained two-mica *Flossenbürg Granite* (sample 12) intruded Moldanubian paragneisses of the Northern Oberpfalz/Germany. The anhedral quartz fills irregular cavities between the subhedral to euhedral feldspar and mica. Sample 21 is a clear, pegmatoid quartz lens (*leucosome quartz*) of migmatitic, Variscan HT-LP-paragneisses of the Northern Oberpfalz. During the Variscan peak metamorphism the Proterozoic educts were overprinted at temperatures around 600°C and pressures between 2.5 and 4 kbar. The sample locality, the quarry Böhmischbruck, is about 15 km southern of the Flossenbürg Granite.

The subvolcanic *Ramberg Granite* (sample 14) is beside the Brocken Granite the most northern exposed Variscan granite in Germany situated in the Rhenoharzian zone of the Harz Mountains. The sample represents the medium-grained variety of the locality Rosstrappe. The medium-grained variety occurs in the western and eastern part of the massif, whereas a porphyritic type forms the central part of the pluton.

The *Weinheim Rhyolite* (sample 15) is situated in the Southern part of the Odenwald Mountains/Germany, which forms part of the Mid-German Crystalline Rise (MGCR) within the Saxothuringian zone of the Variscan Orogen. The magma formation of the near-surface

intruded rhyolite is explained by lower crustal anatexis and assimilation of upper crystal rocks. Secondary processes lead to the pneumatolytic hydrothermal alteration of the rhyolite (Flick, 1986; Arikas, 1964).

Eastern Lachlan Fold Belt

Granite samples collected from the Eastern Lachlan Fold Belt/Australia form the *fourth group*. The study of these samples contributes to the DFG project “Morphogenesis and tectonic setting of magma emplacement in the Eastern Lachlan Fold Belt, Australia” in cooperation with the University of New South Wales, Sydney, Australia (Trzebski et al., 1999). The northern part of the eastern Lachlan Fold Belt evolved in an island-arc setting during the lower Palaeozoic (Powell, 1984; Coney, 1992; Collins and Vernon, 1992; Gray et al., 1997). The Carcoar, Barry and Sunset Hills granites intruded the multiply deformed Ordovician metasedimentary and volcanoclastic rocks during the Silurian.

The I-type Carcoar Granodiorite is a fine- to medium-grained, enclave-containing, hornblende-biotite granodiorite to tonalite. The I-type Barry Granodiorite is a meridionally elongated body (5 x 12 km), consisting mainly of hornblende and biotite granodiorite of tonalitic composition with minor microtonalite enclaves (Lennox et al., 1998). The Sunset Hills Granite shows an S-type aluminium saturation index (Wyborn and Henderson, 1996) and contains 40-50% quartz, 30-40% plagioclase, 10-20% biotite and less than 10% muscovite (Lennox et al., 1998). All three granites show a pervasive tectonic caused by the multiple deformation during the Early Devonian Bowring, late Middle Devonian Tabberabberan and Early Carboniferous Kanimblan events (Lennox et al., 1998; Trzebski et al., 1999).

Table 1.1 Reference list of the sample material with origin and characteristics.

Damara Orogen						
No.	Sample name	Lokality	Formation process	Age	Formation temperature	Specific features
1	megaquartz	Hakos Mts./ Namibia	hydro- thermal	Upper Proterozoic	150-250°C	Megacrystals up to 60 m
2	fissile quartz	Hakos Mts./ Namibia	hydro- thermal	Upper Proterozoic	150-250°C	perfect cleavage parallel to the positive rhombohedral faces {1011}
3	oil-bearing quartz	Geelkop Dome/ Namibia	hydro- thermal	Upper Proterozoic	150-250°C	oil-bearing inclusion

Krušne Hory/Erzgebirge						
No.	Sample name	Lokality	Formation process	Age	Formation temperature	Specific features
4	Schoenfeld Rhyolite	Eastern Erzgebirge/ Germany	magmatic	310±5 Ma	>850°C	phenocrysts
5	Teplice Rhyolite (TPR2)	Eastern Erzgebirge/ Germany	magmatic	308±2 Ma (Lobin 1983)	>850°C	phenocrysts
SH22	SG1 Schellerhau Granite	Eastern Erzgebirge/ Germany	magmatic	300±5 Ma	>650°C	phenocrysts overgrown by matrix quartz
6; SH16, SH32	SG2 Schellerhau Granite	Eastern Erzgebirge/ Germany	magmatic	300±5 Ma	>650°C	phenocrysts overgrown by matrix quartz
SH18	SG3 Schellerhau Granite	Eastern Erzgebirge/ Germany	magmatic	300±5 Ma	>500°C	Snowball-textured quartz
	Podlesi dyke granite	Krušne Hory / Germany	magmatic	300±10 Ma	>500°C	Snowball-textured quartz
7	Eibenstock Granite	Western Erzgebirge/ Germany	magmatic	300±10 Ma	695±6 °C ^l (Solidus- temp.; Thomas 1994a)	phenocrysts over-grown by matrix quartz
8	Aue Granite	Western Erzgebirge/ Germany	magmatic	325±5 Ma (Förster and Tischendor f 1994)	>650°C	phenocrysts over-grown by matrix quartz
Ju 10	Krásno Granite	Hub Stock, Slavkovský Les Mts./Czech Republic	magmatic	Upper Carbo- niferous	>650°C	phenocrysts overgrown by matrix quartz

Krušné Hory/Erzgebirge

No.	Sample name	Lokality	Formation process	Age	Formation temperature	Specific features
Ju14	Krásno Micro-granite	Hub Stock, Slavkovský Les Mts./Czech Republic	magmatic	Upper Carboniferous	>650°C	phenocrysts overgrown by matrix quartz
9	vein quartz	Hub Stock, Slavkovský Les Mts./Czech Republic	hydro-thermal	<300 Ma	<500°C	Berg crystals (3 mm)

Oberpfalz/NW Saxony/Harz/Odenwald

No.	Sample name	Lokality	Formation process	Age	Formation temperature	Specific features
10	Wachtelberg Rhyolite	Frankenberg Mts./Germany	magmatic	Rotliegendes	>850°C	phenocrysts
11	Beucha Rhyolite	NW Saxonia/Germany	magmatic	Rotliegendes	>850°C	phenocrysts
12	Flossenbuerg Granite	Oberpfalz/Germany	magmatic	312±3 Ma (Rb/Sr WR; Siebel et al. 1997)	>650°C	euهدral matrix quartz
13	leucosome quartz	Oberpfalz/Germany	pegmatitic	~320 Ma (Peak metamorphose)	~600°C	clear crystals
14	Ramberg Granite	Harz/Germany	magmatic	290 - 295 Ma (Rb/Sr WR; Schust et al. 1991)	>650°C	phenocrysts over-grown by matrix quartz
15	Weinheim Rhyolite	Odenwald/Germany	magmatic	Rotliegendes	>850°C	phenocyst

Eastern Lachlan Fold Belt

No.	Sample name	Lokality	Formation process	Age	Formation temperature	Specific features
AU4-AU7	Barry Granodiorite	Eastern Lachlan Fold Belt/Australia	magmatic	Early Silurian	752±37°C	phenocrysts overgrown by matrix quartz
AU9-AU16	Sunset Hills Granite	Eastern Lachlan Fold Belt/Australia	magmatic	Early Silurian	>700°C	phenocrysts overgrown by matrix quartz
AU28-AU55	Carcoar Granodiorite	Eastern Lachlan Fold Belt/Australia	magmatic	Early Silurian	766±36°C	euهدral matrix quartz

2 Fundamentals of cathodoluminescence

The term cathodoluminescence (CL) designates the luminescence induced by electron bombardment. The interaction of the electron beam with the sample gives rise to a number of effects: the emission of secondary electrons (SE), back-scattering of electrons (BSE), electron absorption (“sample current”), characteristic X-ray, and CL emission (Fig. 2.1). Most energy of the beam is converted into heat. The penetration depth of electrons and accordingly, the excitation depth depends on the energy of the electrons (10-20 keV) and is in the range of 2-8 μm (e.g. Marshall, 1988).

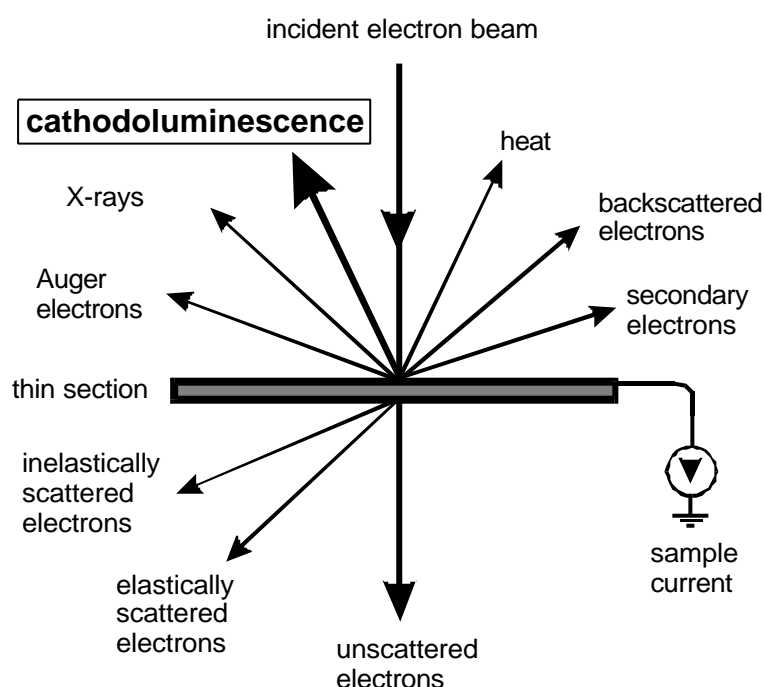


Fig. 2.1 Schematic representation of processes resulting from electron bombardment (modified after Potts et al., 1995). Note that the emissions come from different depths, e.g. CL and X-rays are emitted from deeper section levels than secondary electrons.

Luminescence can be divided into two: intrinsic CL which is characteristic of the host lattice and extrinsic CL which results from impurities. Larger defects such as dislocations and clusters may also effect the CL.

Intrinsic luminescence is enhanced by non-stoichiometry (vacancies), structural imperfections (poor ordering, radiation damage, shock damage), and impurities (non-activators), which distort the crystal lattice. Some trace elements like Ti may provoke both intrinsic and extrinsic CL. However, the role of Ti in enhancing intrinsic CL is a matter of discussion. Ti-rich feldspar and quartz show blue CL, but the effective state of Ti charge and lattice position is

not answered (Marshall, 1988). Both the use of the term “activator” and the term “intrinsic” have been used to characterise the CL of minerals containing Ti.

The impurities, responsible for the *extrinsic luminescence*, are called activators. Elements are referred to as sensitizers when their presence is necessary to create a luminescence centre with an activator. The latter is transferred into an excited state which results in a sensitized luminescence (e.g. Waychunas, 1988; Remond et al., 1992). The luminescence properties are mostly the result of luminescence-activating ions such as transition metals, rare-earth elements or actinides. Changes of the crystal field properties i.e., field strength, site symmetry, and coordination number, cause differences in the magnitude of the energy levels of the activator elements and also the splitting of closely spaced levels. Therefore the CL spectrum is not a characteristic property of the activator but a property of the mineral. The CL intensity generally increases with the concentration of the activator to a maximum and then decreases. This decrease is referred to as concentration quenching (self-quenching). It can be explained by the transfer of a part of the excitation energy to other activator ions which is more effective than luminescence emission. Some ions (quenchers) such as Fe^{3+} , Fe^{2+} , Co^{2+} , and Ni^{3+} show broad and intense charge transfer bands in the absorption spectrum and cause quenching of the luminescence of activators with interfering emission bands. The quenching by ions with intense charge transfer bands especially influences the visible and near UV spectral ranges, whereas luminescence emissions in the IR are more or less unaffected. Apparently, the quenchers cause new closely-spaced energy levels so that the electron can easily return to the ground state with the emission of low-energy photons (IR) or by losing heat energy (Marshall, 1988).

Quenching due to lattice defects may occur if the crystal structure is damaged by mechanical processes, radiation, growth defects or impurities. These lattice defects create new energy levels between the conduction and the valence bands resulting in absorption of the excitation energy, non-luminescent energy transfer or low frequency emission.

Another process which may be responsible for lowering the luminescence intensity is thermal quenching. Principally, heating of a sample results in the release of electrons and accordingly in the excitation of thermoluminescence. During irradiation of a sample with high-energy particles (e.g., electrons, ions) a part of the energy can be transformed into heat which influences the energy transfer and non-luminescent transitions. As a consequence, the luminescence intensity decreases during electron bombardment and then stabilises.

Cathodoluminescence is considered to form in 3 steps: (1) the absorption of excitation energy and stimulation of the atoms into an excited state, (2) transformation and transfer of the excitation energy, and (3) emission of light and relaxation to a non-excited state (Marfunin, 1995). The first two steps mainly depend on the mode of excitation, whereas the third step depends on the character of specific luminescence centres.

In crystals, complex interaction between atoms leads to the broadening of the energy levels into bands. In insulators like quartz, a broad gap, called the forbidden gap, exists between the valence band and the conduction band. A precondition for cathodoluminescence is the existence of activators (impurity ions, lattice defects), which cause and occupy discrete energy levels in this forbidden zone. Luminescence centres can be differentiated by their energy position within the forbidden gap and divided into into electron traps near the conduction band (donor level) and recombination sites in the vicinity of the valence band (acceptor level) (e.g. Marfunin, 1979).

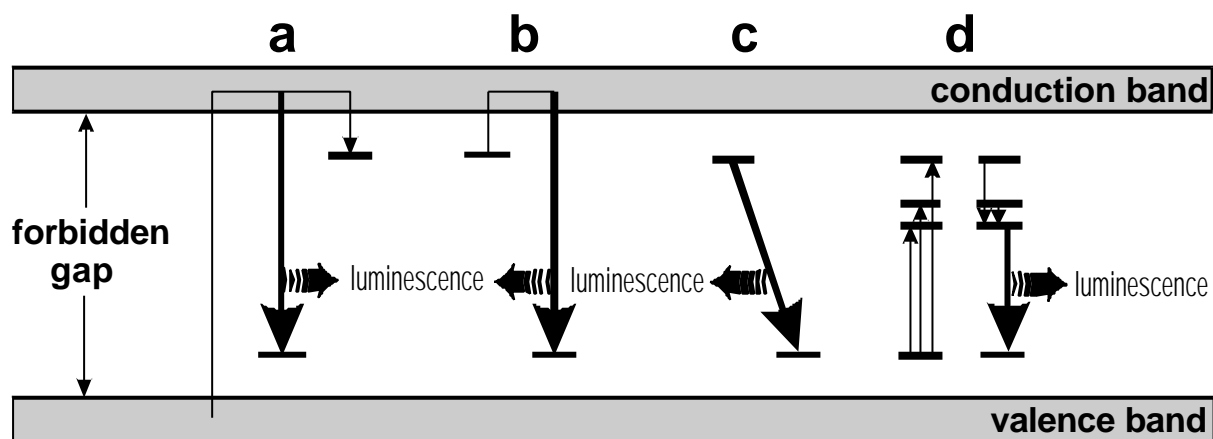


Fig. 2.2 Processes of charge transfer and luminescence production in crystals after Krbetschek et al. (1997).

CL involves electron radiation induced excitation of an electron from the ground state to an excited state. The following de-excitation leads to a state of lower energy within the forbidden gap. Excitation results in the trapping of an electron or in the recombination with a luminescent or a non-luminescent centre (Fig. 2.2a). In the case of a luminescent transition, a photon is emitted. If the atom or ion is placed in a crystal lattice, non-luminescent transitions are possible due to absorption or emission of lattice vibrations. A trapped electron can be excited again, transits into the conduction band and may recombine with an activator element level under emission of a photon (Fig. 2.2b). In the case of a small energy difference between electron trap and activator level, a direct luminescent transition of the electron to the

recombination centre is possible (Fig. 2.2c). In figure 2.2d the excitation of several energy levels and the subsequent relaxation and luminescence emission of a single activator is shown.

2.1 Point defects in quartz

Quartz lattice defects can be grouped into three types according to their structure and size: 1) point defects (most important for luminescence studies), 2) dislocations, 3) inclusions and clusters of foreign minerals and volatiles. During crystallisation the impurity and lattice defects are generally incorporated as charge compensated, diamagnetic defect centres. Natural radioactivity as well as the electron radiation during experiments causes the transformation of diamagnetic precursor centres into paramagnetic centres. The irradiation changes the defects by trapping an electron or creating a hole at the site of a precursor defect. Additionally,

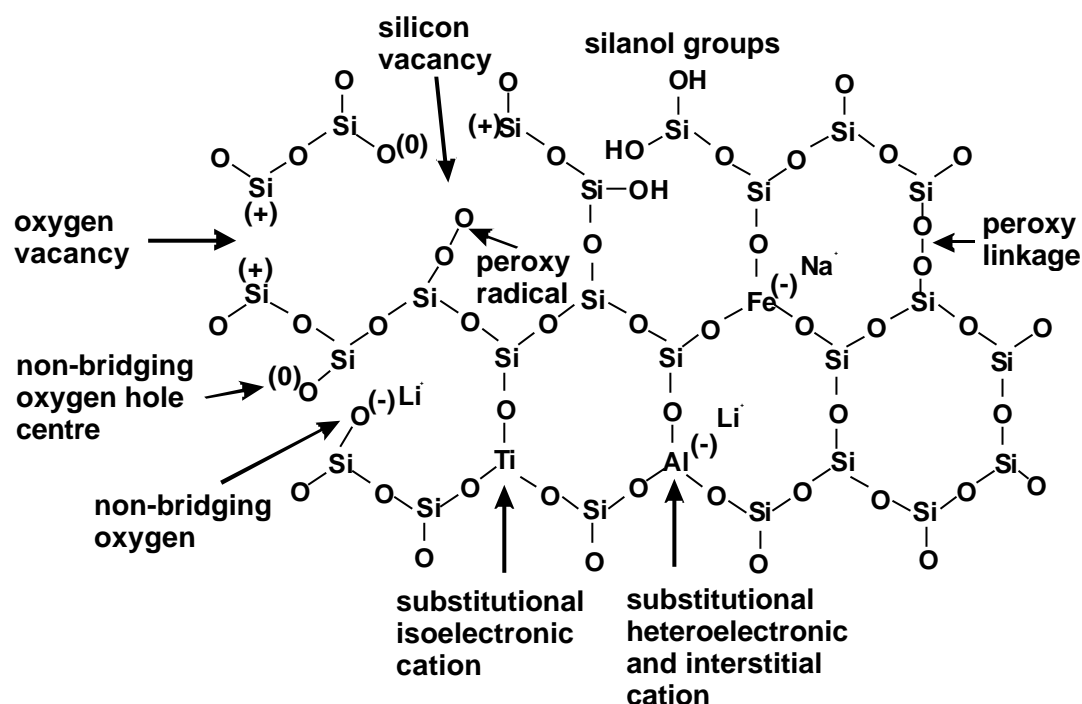


Fig. 2.3 Synopsis of the most common lattice defects in quartz modified after Götze (2000).

atomic displacements from the normal bonding (defect-free) sites may form by radiolysis processes (Kalceff and Phillips, 1995).

EPR studies have identified about 20 different *paramagnetic defect centres* in quartz which can be divided into 2 main types: 1) vacancy centres, which are subdivided into electron

centres (oxygen vacancies) and hole centres (silicon vacancies) and 2) impurity centres which are subdivided into electron centres ($M^{4+} + e^-$) and hole centres (M^{3+} , M^{2+} ions, as well as atomic hydrogen). (e.g. Marfunin, 1979; Kostov and Bershov, 1987; Agel, 1992; table 2.1). The type 2 has different varieties, depending on the kind of ion-charge compensator in structural channels, such as H^+ , Li^+ , Na^+ , as well as on the position of the compensator.

The *paramagnetic vacancy centres* are represented by the frequent E' centre ($\equiv Si\cdot$), the peroxy radical ($\equiv Si-O-O\cdot$), and the nonbridging oxygen hole centre (NBOHC) ($\equiv Si-O\cdot$) (e.g. Weeks, 1956; Weil, 1984; Marfunin, 1979; Griscom, 1985; Kalceff and Phillips, 1995; Fig. 2.3). The non-paramagnetic oxygen vacancy (Si-Si) and the trapped electron centre ($\equiv Si\cdot$) are possible precursors for an E' centre and the peroxy linkages (Si-O-O-Si) for a peroxy radical and/or the NBOHC. The paramagnetic O^- and O^{3-}_2 centres represent different types of NBOHC in tetrahedra with silicon vacancy (e.g. Bershov et al., 1978; Serebrennikov et al., 1982).

Table 2.1 Common paramagnetic centres of quartz after Plötze (1995).

		Impurity centres		Vacancies	
		Si ⁴⁺ substitution	Interstitial	Oxygen vacancies	Silicon vacancies
<i>Metastable</i>	Electron centres (+e ⁻)	[TiO ₄] ⁻ [TiO ₄ /M ⁺] ⁰ [GeO ₄] [GeO ₄ /M ⁺] ⁰	M ⁺ = H ⁺ , Li ⁺ M ⁺ = H ⁺ , Li ⁺	E' centres: [SiO ₃] ³⁻	
	Electron centres (-e ⁻)	[AlO ₄] ⁰ [FeO ₄] ⁰			O ⁻ centres: O ⁻ , O ₂ ³⁻ , O ₂ ³⁻ M ⁺
<i>Stable</i> (paramagnetic without charge receive)		[FeO ₄ /M ⁺] ⁰ ?[FeO ₄] (precursor for [FeO ₄] ⁰	M ⁺ = Na ⁺ , Li ⁺ , Fe ³⁺		

Impurity ions enter either interstitial or substitutional positions in the quartz lattice depending on ion radius and charge. The number of ions which can substitute for the silicon atom in the quartz lattice is limited because of the small ionic radius of Si⁴⁺ compared to its 4-valency. Typical substitutes are Al³⁺, Ti⁴⁺, Fe³⁺, Ge⁴⁺, P⁵⁺, and Ga³⁺ (Xⁿ⁺; order of average frequency) (e.g. Bambauer, 1961; Lehmann, 1975; Lehmann and Bambauer, 1973; Maschmeyer and Lehmann, 1983b; Weil, 1984). Nuttall and Weil (1980) and McLaren et al. (1983) reported a

hydrogenic trapped hole-center with four hydrogen atoms on a silicon position. Large open channels (smallest O-O diameter 3.55 Å) thread through the quartz structure parallel to the c-axis and offer locations for interstitial cations such as H⁺, Na⁺, K⁺, Li⁺, Fe²⁺, Cu⁺, Co²⁺, Ag⁺ ... (Mⁿ⁺; order of average frequency). They act as charge compensators for the substitutional X³⁺ and X⁵⁺ ions. The possible incorporation of other cations in interstitial position (e.g. Ni²⁺, Al³⁺, Fe³⁺, Co³⁺, Cr³⁺, Ti⁴⁺) is a matter of discussion (Lehmann and Bambauer, 1973a, b; Weil, 1984).

The paramagnetic impurity centres which are built by tetravalent ions (mostly Ti⁴⁺ and Ge⁴⁺) cause the formation of the diamagnetic [XO₄]⁰ centres. These centres act as a precursor for the paramagnetic [XO₄][•], which develops during ionisation irradiation (table 2.1). At room temperature these centres bind diffusing M⁺ cations such as H⁺, Li⁺, Na⁺ forming a paramagnetic [XO₄/M⁺]⁰ centre (Wright et al., 1963; Rinneberg and Weil, 1972; Mackey, 1963; Rakov et al., 1985; Agel, 1992; Weil, 1993). The trivalent ions build up diamagnetic [YO₄/M⁺]⁰ centres associated with an adjacent charge compensating cation M⁺ (H⁺, Li⁺, Na⁺). The paramagnetic defects are metastable and decay depending on the temperature. The closure temperature varies e.g. 55-82°C for the [TiO₄/M⁺]⁰ centre and 49-64°C for the [AlO₄]⁰ centre (Grün et al., 2000).

2.2 The state of water in quartz

Apart from Al, bonded water in the quartz lattice in the form of H⁺, OH⁻ and H₂O is the most important impurity. Brunner et al. (1961) proposed that water can be incorporated into the quartz lattice according to the reaction: -Si-O-Si- + H₂O = -Si-OH + HO-Si-. This is a preferred stress-induced mechanism and referred to as “hydrolytic weakening” (e.g. Griggs and Blacic, 1965; Griggs, 1967; Fig. 2.4a). Calculations of total energy indicate that this reaction which uses an energy of ~0.1 eV is spontaneous for a Si-O bond stretched beyond 4% of its normal bond length (Heggie, 1992). Another possible configuration is described by Nuttall and Weil (1980) and McLaren et al. (1983), who assumed that hydrogen is

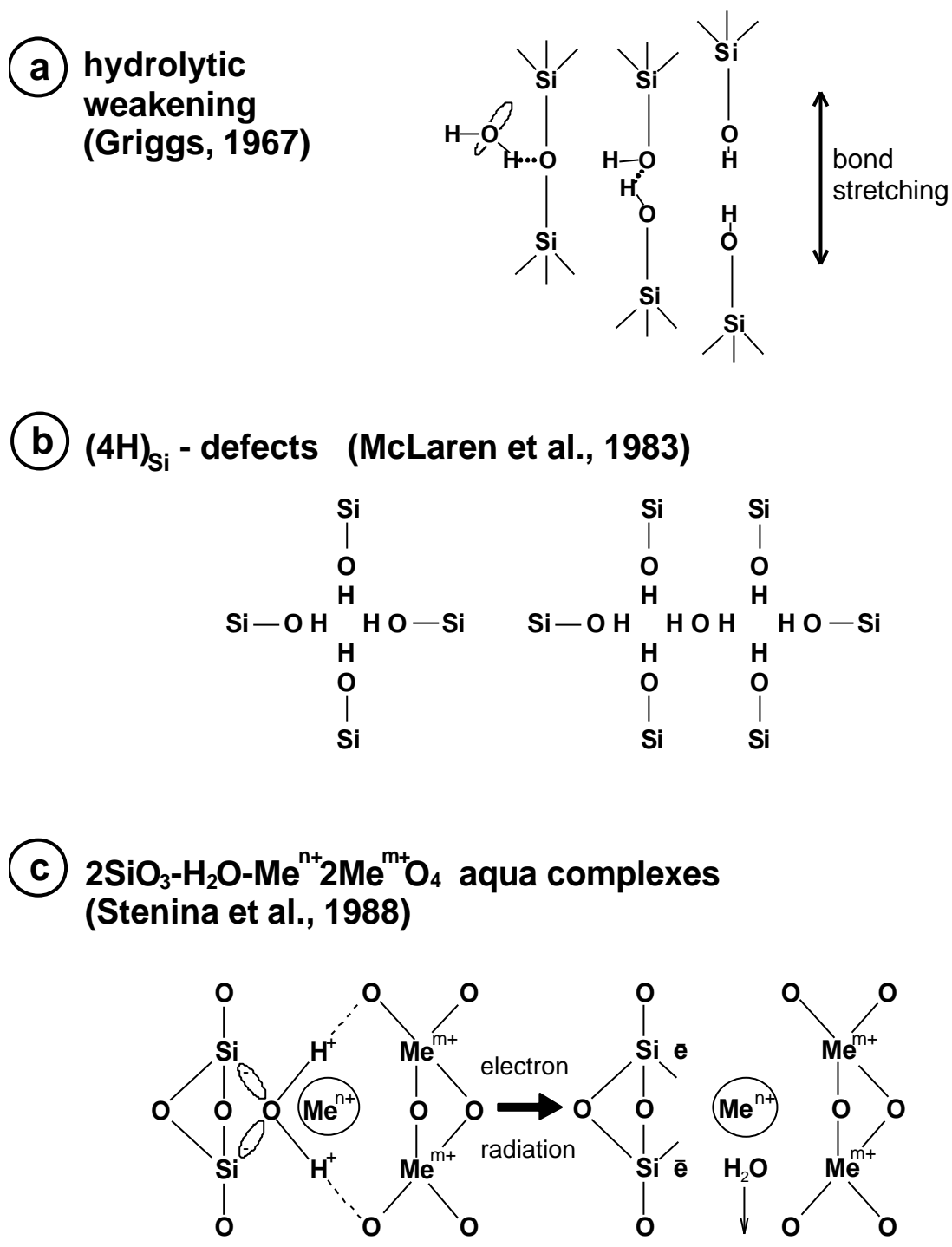


Fig. 2.4 Models of the structural state of water in the quartz lattice. a – hydrolytic weakening according to Griggs (1967); b - $(4H)_{Si}$ defects according to McLaren et al. (1983) where $4H^+$ substitutes for Si^{4+} ; c- model of aqua complexes after Stenina et al. (1988). The incorporated water molecule forms weak donor-acceptor and hydrogen bonds with the surrounding matrix. This bonds break during electron radiation.

incorporated in the quartz structure by means of $(4H)_{Si}$ defects where $4H^+$ substitutes for Si^{4+} (Fig. 2.4b). The infrared absorption spectra of natural quartz crystals typically exhibit sharp absorption peaks between 3000 and 3700cm^{-1} which are associated with hydrogen and hydroxyl acting as a charge compensator of Al^{3+}/M^{n+} (e.g. Brunner et al., 1961; Kats, 1962; Bambauer et al., 1963). Kronenberg et al. (1986) showed that the solubility of water in the quartz lattice depends on the Al content. Maschmeyer and Lehmann (1983a) proposed a model where two OH groups are neighbouring substitutional X^{3+} and interstitial M^{n+} . Based on transmission electron microscopy (TEM), X-ray microanalysis and EPR Stenina et al. (1988, 1995) showed that the trace substitutional X^{3+} and related compensating M^{n+} create parts of aqua complexes and clusters in the form of $2SiO_3-H_2O-M^{n+}2X^{m+}O_4$, where X^{m+} is mostly Al^{3+} and Fe^{3+} and M^{n+} mostly Li^+ and Na^+ (Fig. 2.4c). The tetrahedrally charged water molecule is built between two defective positively charged SiO_3^+ tetrahedra and the two defective negatively charged $[X^{m+}O_4]$ tetrahedra. M^{n+} cations enter interstitial position as charged compensators. This scheme of heteroisomorphic substitution $M^{n+}X^{m+}$ for Si^{4+} is typical for quartz. The incorporated water molecule forms weak donor-acceptor and hydrogen bonds with the surrounding matrix. This tetrahedrally-charged water can be revealed in the IR-spectrum as molecular water and hydroxyl. Under electron beam irradiation the aqua complexes become visible by TEM in form of several microns small, non-crystalline (gel like) micro-areas with diffuse boundaries.

3 Cathodoluminescence equipment

3.1 Sample preparation

In this CL study thin sections with a thickness of 250 μm were used so as to provide demountable thin sections on which to carry out LA-ICPMS, FTIR spectroscopy, EPMA, and CL on the same area of the quartz samples. The laser of the ICPMS ablated craters 100 – 150 μm in depth and for the FTIR spectroscopy demounted thin sections polished on both sides are necessary.

The first stage of sample preparation consists of cutting the section, which was mounted on a glass slide with epoxy resin. Subsequent polishing was carried out with progressively finer grades of abrasive (carborundum). The final stage involves polishing with diamond paste with a grade of 0.3 μm . The samples were thoroughly cleaned. The polished surface was mounted on a standard glass slide (48x24x2.8 mm) with Akemi Mamorkitt 1000. The other glass slide was removed and the procedure of polishing was repeated until a section thickness of 250 μm was reached. For sample temperature measurements during CL and FTIR spectroscopy the section was removed from the glass slide with Xylol. In addition, a number of thin sections were chemically polished with a OP-S suspension of different granularities (1 μm and 3 μm) in order to test the effect of the surface quality on the CL properties.

Quartz being a non-conductor, requires a conductive coating to prevent charging under electron bombardment. The preferred coating for CL studies is carbon. It is also the best choice for X-ray analysis, because has a minimal effect on the X-ray spectrum. However, it is not ideal for SEM imaging, owing to its low secondary electron field. The coating was done at standard conditions to a thickness of about 15nm to avoid variations in CL-intensity.

3.2 Optical CL

Cathodoluminescence microscope HC3-LM

The commercially produced hot-cathodoluminescence microscope (HC1-LM) after Neuser et al. (1995) is provided with a high-vacuum chamber ($<10^{-5}$ mbar) and uses an acceleration voltage of 14keV (Fig. 3.1). The HC1-LM is a development of the prototype constructed at the IGDL Göttingen 1987 (Neuser, 1988) according to the model of Zinkernagel (1978). The electron gun operates as a “hot cathode”, i.e. the electrons are emitted from a heated filament. In a “cold cathode” CL microscope the electron beam is generated during discharge between the cathode and anode in an ionised gas. The hot-cathode technique provides a considerably greater beam stability and CL intensity than the cold cathode instruments and thus is suitable for investigation of the weakly luminescent quartz. The electron gun directs a focused beam upwards onto an inverted thin section; the CL is viewed through the sample from above. The electron beam with a diameter of ca. 4.8 mm irradiates the thin section surface with a current density of ca. 10 mA/mm². The basis of the HC3-LM is a polarisation microscope model OLYMPUS BX30M with some modifications, for instance, the vacuum sample chamber is mounted in place of the sample stand. The polarisation objectives have a magnification/numerical aperture of 5x/0.15, 10x/0.30, 20x/0.40. The high vacuum of the sample chamber is attained by a Diffstak oil diffusion pump combined with an Edwards rotary vane pump.

The TRIAX 320 Spectrograph

CL spectra were recorded with a triple-grating spectrograph TRIAX 320 provided with a liquid N₂-cooled Charge Coupled Device (CCD) camera (Fig. 3.2). The system is well suited to applications with very low signals such as the CL of quartz. The spectrograph is attached to the CL microscope ocular with a quartz fibre guide of 1.5 m length (transmission range 200-900 nm). The quartz fibre guide is coupled via a fibre optic interface to the entrance slit of the TRIAX 320. The system is controlled by an external PC using the software programs HWINIT for hardware initialisation and SpectraMax for Windows for data processing.

The triple-grating spectrograph is equipped with one ruled grating (100 lines/mm) and two blazed holographic gratings (1200 and 1800 lines/mm) which are mounted on a rotating triple grating turret. The higher spectral resolution obtained with the 1200 and 1800 lines/mm gratings results in small ranges of the recorded spectra, namely 70 nm and 40 nm, respectively (Table 3.1).

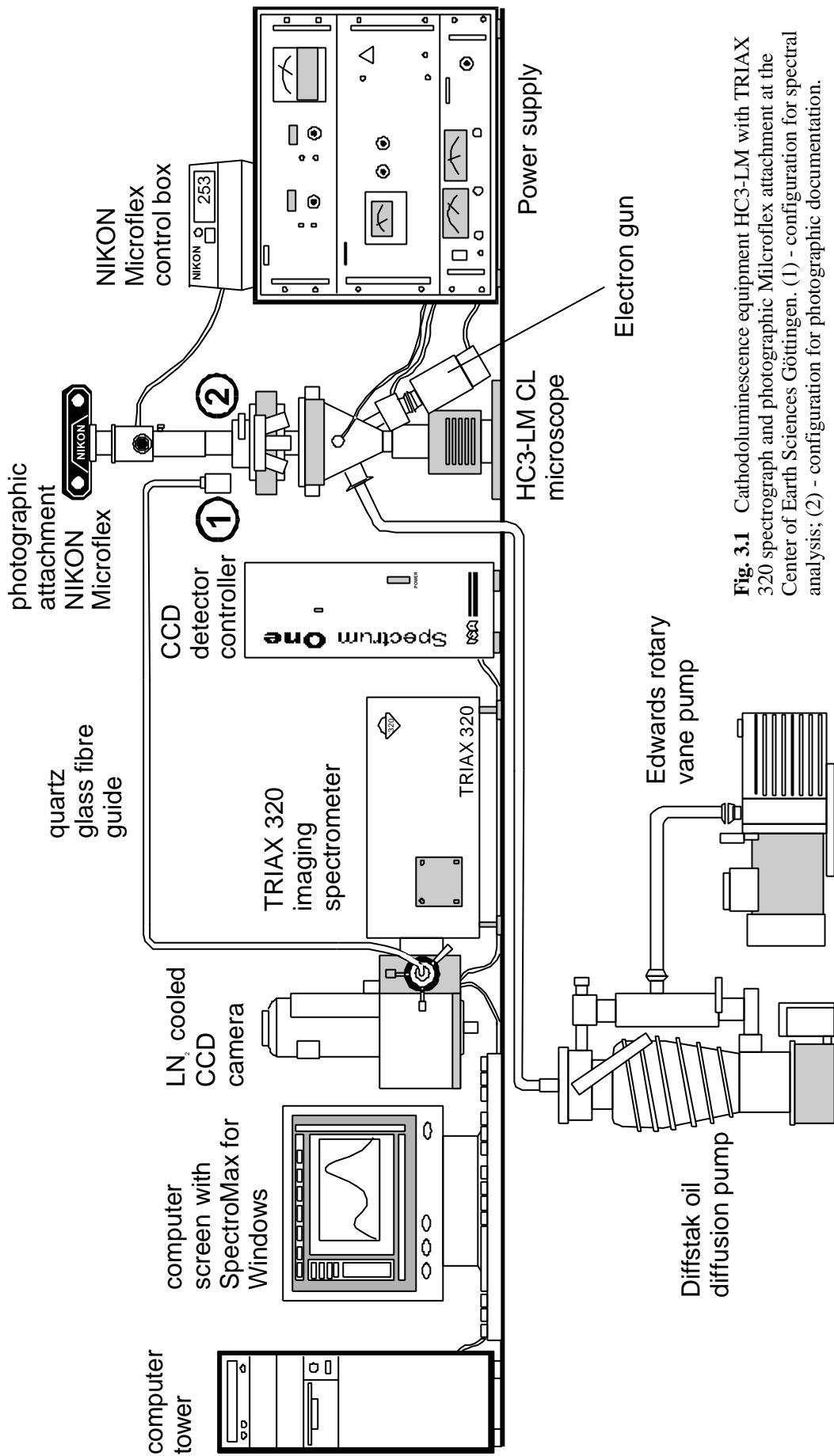


Fig. 3.1 Cathodoluminescence equipment HC3-LM with TRIAX 320 spectrograph and photographic Microflex attachment at the Center of Earth Sciences Göttingen. (1) - configuration for spectral analysis; (2) - configuration for photographic documentation.

Table 3.1 Specification of the used optical gratings.

Grating	100 lines/mm	1200 lines/mm	1800 lines/mm
Working range	250 – 900 nm	190 – 1200 nm	250 – 900 nm
Scanning range per recording	1000 nm	70 nm	40 nm
Spectral resolution	0.5 nm	0.06 nm	0.02 nm
Wavelength position accuracy	1 nm	0.3 nm	0.1 nm

The back-illuminated CCD camera with UV-AR-coating has a spectral response between 200 and 1050 nm (Fig. 3.3). The CCD detector array is built up of an area of silicon photodiodes divided into a 2-dimensional matrix of pixels. Each pixel integrates a charge arising from the photoelectric effect caused by the incident light. The charges of adjacent pixels are kept separated by a grid of electrodes that confine the charges by electrostatic force. The pixel charge is controlled and read out by the detector interface unit (DIU). The signal from the CCD is processed, amplified and converted to digital datapoints by electronics in the DIU and transferred to the host PC.

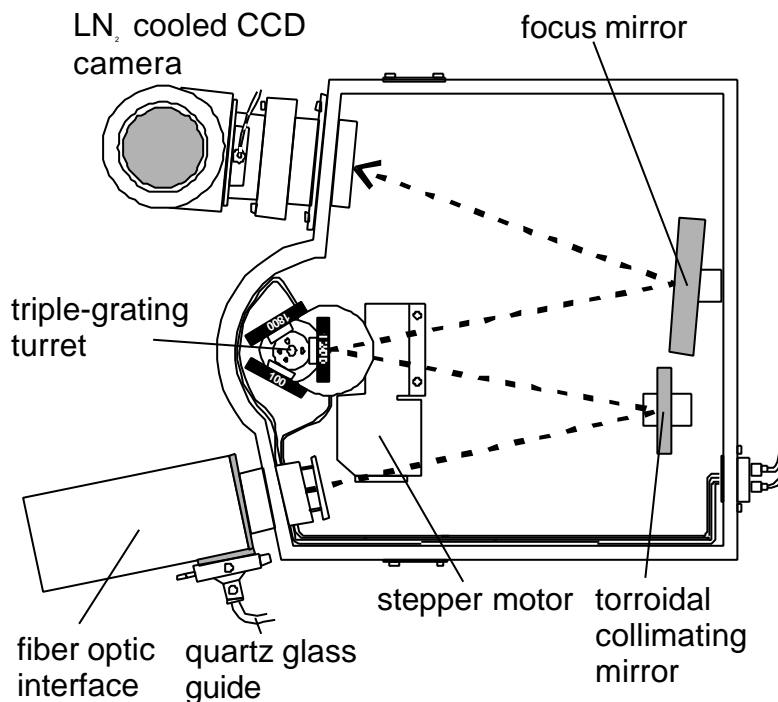


Fig. 3.2 Top view of the Spectrum One TRIAX 320 spectro-graph.

The CCD array head is cooled by liquid nitrogen which works with a temperature below – 140°C. The cooling is necessary to lowering the dark current and to obtain a better signal/noise ratio at low photon emission rates.

A mercury lamp was attached to the entrance slit of the spectrometer in order to calibrate the wavelength. A difference between the position of the measured peak and the known mercury peak at 546.1 nm was corrected by setting the wavelength difference into the lines “MultiAUtoCaloffset 0 =” (1200 lines/mm grating), “MultiAUtoCaloffset 1 =” (1800 lines/mm grating), and “MultiAUtoCaloffset 2 =” (100 lines/mm grating) of the file MONO1.ini.

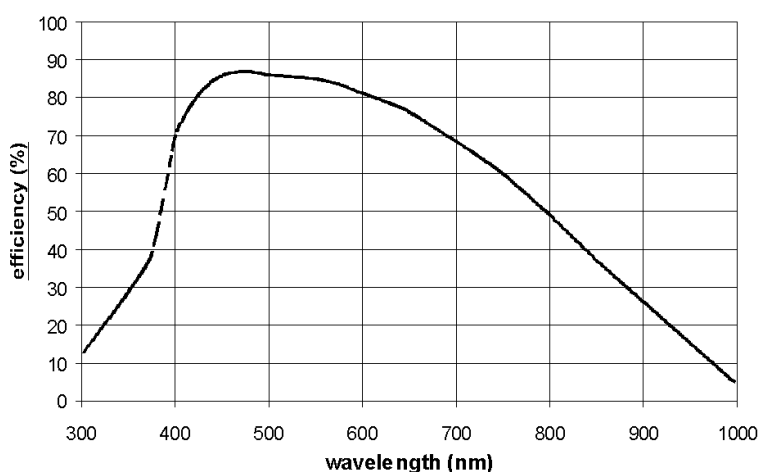


Fig. 3.3 Spectral sensitivity of the TRIAX 320 CCD-camera

The CL spectra were recorded for the same instrumental setting: a filament current of 0.18 nA using the objective 20x/0.40. The analysed area was 800 μm in diameter. The 100 lines/mm grating was used to fully detect the emitted spectra of visible light between 400 and 900 nm (3.1 - 1.4 eV). The 1200 lines/mm grating provided high-resolution spectra of 70 nm width sectors. The high wavelength resolution obtained by using the 1800 lines/mm grating was not suitable as the half-width of the quartz CL bands varies between 20 and 100 nm.

The time-resolved spectra were recorded within 40 s (100 lines/mm grating) and of 60 s (1200 lines/mm grating) using the maximum entrance slit width of 2 mm and an acquisition time of 20 and 30 s, respectively. The system needed twice the acquisition time to accumulate the low emission intensity and to measure the background. The intensities are integrated over the duration of exposure. The first spectrum was recorded immediately after the initialisation of the electron bombardment because of drastic CL change of quartz during the first seconds of radiation (Fig. 3.4). Subsequent spectra were recorded in steps of one minute or several minutes.

The change of the CL intensity of the 1.96 and 2.79 eV emissions during electron radiation was measured with the f/3.4 Grating Monochromator at a speed of 10 mm/min using the CL

a) 100 lines/mm grating

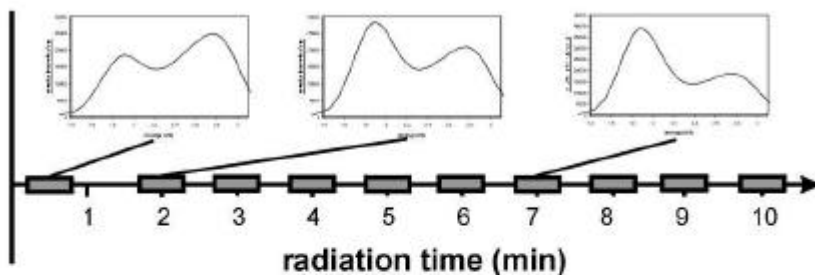
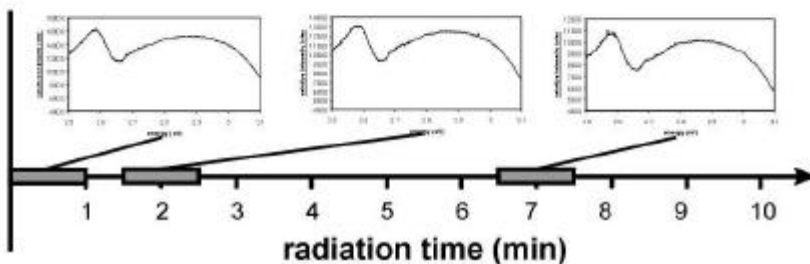


Fig. 3.4 Used time steps for time-resolved spectrum recording with the 100 lines/mm (a) and 1200 lines/mm grating (b). The grey squares represent the duration which is necessary for spectrum acquisition.

b) 1200 lines/mm grating



microscope after Zinkernagel (1978) at the University Göttingen (10 keV, 0.2 nA). In contrary to the TRIAX 320 the monochromator allows the record of the CL intensity change from time zero of electron radiation. The CL intensity drastically changes during the first seconds of electron radiation and its recording is of interest for solving the causes of CL.

The photographic documentation was carried out by a NIKON Microflex UFX-II system equipped with a NIKON FX-35A reflex camera (Fig. 3.1). Colour slides of the luminescent images were taken with high-sensitive films KODAK Ektachrome 400 HC (400 ASA) and KODAK Ektachrome 1600 (1600 ASA). High-sensitive films were chosen because of the low CL intensities. The exposure times were of 100 – 250 s for the 400 HC and of 10 – 30 s for the 1600 using the 10x/0.30 objective.

3.3 The scanning electron microscope (SEM) CL

The scanning electron microscope (SEM) is along with the light microscope the most important imaging instrument. The scanning electron microprobe utilises a scanned electron beam with a small spot size normally around 2 μm in diameter. By scanning the electron beam, synchronized with the X, Y deflection of a display oscilloscope, and modulating the display oscilloscope intensity with the photomultiplier output, a magnified map of the CL of the specimen is obtained. Total photomultiplier output intensities were used for the intensity function.

The SEM-CL offers advantages over the conventional (optical) CL microscopy for CL studies (Grant, 1978; Tovey and Krinsley, 1980). The main advantage is the larger spatial resolution of $\leq 1\mu\text{m}^2$. Other advantages are the higher magnification, the capability of combining CL and SEM investigations like back scattered electron (BSE) imaging and microanalytical analysis on the same area. The possibility of increasing the power density over small sample areas is useful for samples with low CL intensity like quartz. A disadvantage is the monochromatic (grey scale) image.

Two scanning electron microscopes equipped with different CL detectors, the Cambridge Instruments 250-MK3 with a S20-Extended photomultiplier and the JEOL JXA 8900 with a CLD40 R712 photomultiplier, were used for the study of internal growth patterns and secondary CL structures within individual quartz crystals. The voltage and sample current for both SEM was 15 keV and 5-15 nA. A quartz glass lens in front of the S20-Extended detector collects the emitted light of the sample; the photomultiplier of the JEOL system works without additional lenses and mirrors. Images were collected from the JEOL system using slow beam scan rates of 20 s at processing resolution of 1024x860 pixels and 256 grey levels. The documentation of the CL images at the 250-MK3 were carried out with a photcamera with Agfapan APX 25 films and by using slow beam scan rates of 250 sec.

The detectable wavelength for both photomultipliers ranges from 380 to 850 nm. The lower limit of detection is 380 nm, which is determined by the absorption of the lead glass plate in front of the photomultipliers. The maximum wavelength responses are at 600 nm for the CLD40 R712 and at 420 nm for the S20-Extended photomultiplier. The spectral sensitivity of both photomultipliers are shown in the figure 3.5.

Remarkable differences between the images produced by the photomultipliers have been found (Fig. 3.6). The S20 Extended photomultiplier is more sensitive for blue emissions and was therefore used for imaging of samples with dominant blue luminescence, whereas the

CLD40 R712 photomultiplier was preferred to contrast reddish luminescent secondary textures. Dark contrasted areas of quartz SEM-CL images always correspond to red to reddish

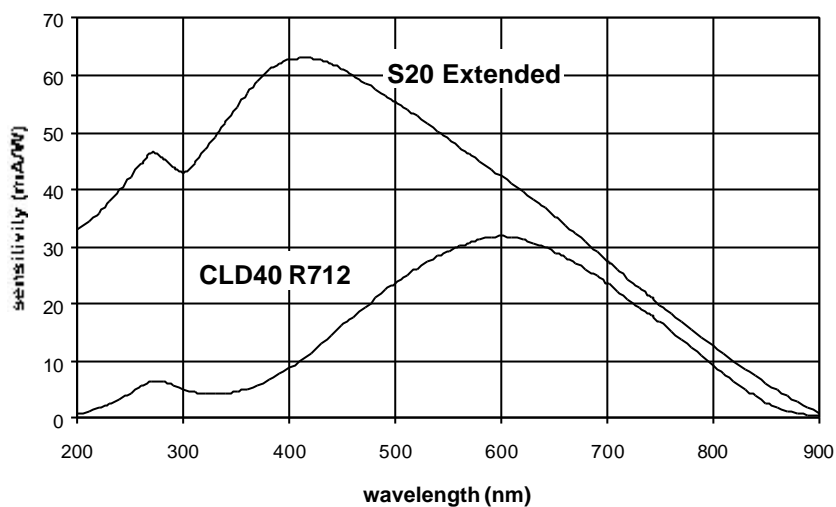


Fig. 3.5 The spectral sensitivity characteristics of the Cambridge Instruments S20 Extended and the JEOL CLD40 R712 photomultipliers.

brown CL-colours and bright areas correspond to blue to violet colours. The luminescence colours were checked by optical CL prior to or after SEM-CL investigations.

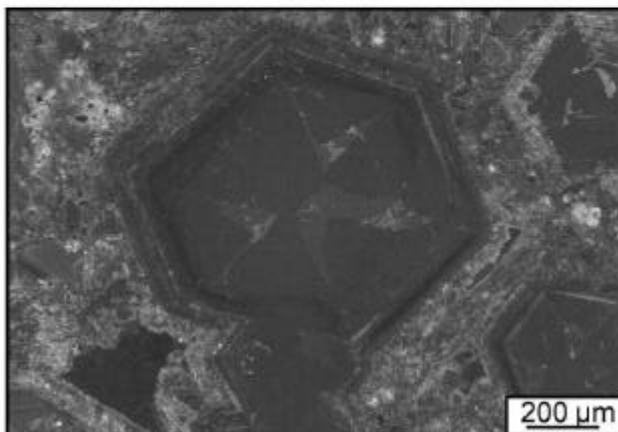
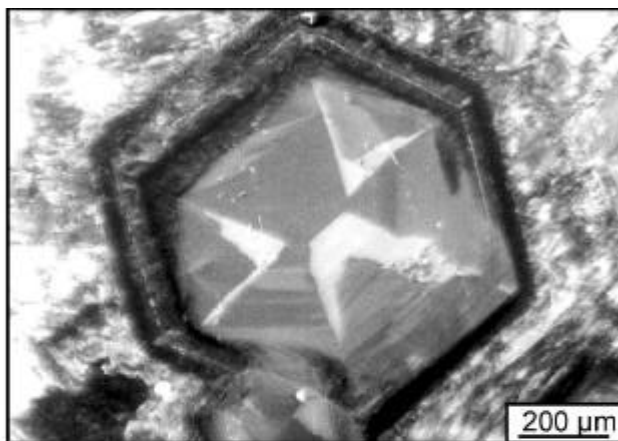


Fig. 3.6 Unprocessed SEM-CL images of a vein quartz (sample 9) using different photomultipliers. a - Cambridge Instruments S20 Extended photomultiplier; b - JEOL CLD40 R712 photomultiplier.

Image processing was carried out using the software Optimas 6.0 for Windows. Starting with an unprocessed CL image a typical sequence of processing steps was: (1) producing a grey level histogram (2) selection of the grey level range responsible for contrasting of structures within the quartz crystal (3) extension of the chosen grey level range to 256 grey levels (4) treatment of the image with several filters for sharpening and smoothing (5) determination of grey-scale profiles e.g. along trace element traverses of zoned quartz crystals, as shown in figure.

3.4 Mathematical treatment of CL-spectra

Spectral data acquisition was carried out by using the software SpectraMax for Windows. The emitted light was recorded in nanometer (nm). The emission bands are not immediately obvious from visual inspection of the experimental data due to the close proximity of broad emission bands which results in complex peak overlapping. The asymmetry of the broad peaks and the shift in the different quartz samples suggests the presence of several bands. The processing steps for spectra analysis were the following:

- 1) For processing of the spectra the data were exported as ASCII data into the EXCEL program.
- 2) The spectra were corrected for the sensitivity of the spectrometer (Fig. 3.3). For that the measured intensities were multiplied by the factor of efficiency.
- 3) Spectral emission bands normally have a Gaussian shape if plotted in energy space (Kalceff and Phillips, 1995). Therefore, the data in nanometer (nm) were converted into electron volts (eV) according: $E = 1239.8/\lambda$, where E is the energy (eV), and λ the wavelength (nm).

The shape of the intensity distribution of an emission band plotted versus the light energy is described by the Gaussian function. The emission intensity $I(E)$ at the energy E (eV) of an emission band centred at λ is described by the following equation:

$$I(E) = I_f \frac{1}{s \sqrt{2\pi}} e^{-\frac{(E-a)^2}{2s^2}} \quad (3.3)$$

where I_f = intensity factor; E = energy (eV); a = position of the maximum of the Gaussian curve and centre of symmetry; s = distance from a to the turning point of the Gaussian curve (Fig. 3.7).

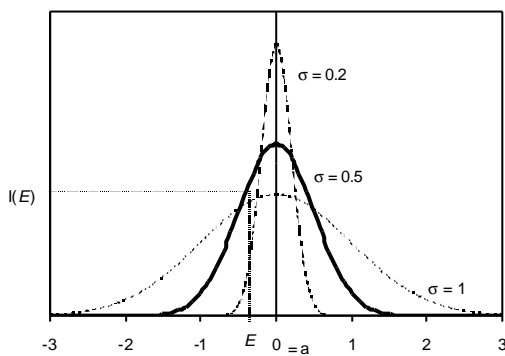


Fig. 3.7 Gaussian curves for $a = 0$, $I_f = \text{const.}$, and different s (0.2, 0.5, and 1).

The position (a), width (s), and size (I_f) of the Gaussian curves were calculated and adjusted in such a way that the sum of the individual components equals the recorded spectrum. The band positions (a) were determined by manual setting of the peak configurations using the high-resolution spectra recorded with the 1200 lines/mm grating. The intensity factor I_f corresponds to the area under the Gaussian curve (the integral of Gaussian distribution from -8 to +8 is 1). I_f was used to determine ratio and percentage of the individual emission bands of the total spectra between 1.4 and 3.1 eV recorded with the 100 lines/mm grating.

4 Microanalysis of trace elements and defect centre characterisation in quartz

Amongst the suite of microanalytical techniques commonly used for trace element determination, *secondary ion mass spectrometry (SIMS)*, *electron probe micro analysis (EPMA)*, and *laser ablation inductively coupled plasma mass spectrometer (LA ICP-MS)* can provide element analysis data with a high sensitivity and a high spatial resolution, which allows the determination of element zoning of crystals. Therefore, the three methods were chosen for the determination of the trace element distribution in quartz. The *electron paramagnetic resonance (EPR)* and the *Fourier-transform infrared (FTIR) spectroscopy* are powerful techniques available for the characterisation of defects centres in quartz. Clearly, no single instrument gives a complete characterisation of a mineral, but if the five techniques are employed in a complementary fashion, the chances for success are better.

The *LA ICP-MS* has the potential to determine most elements of the periodic system at the part-per-million level in solids with a spatial resolution down to 20 μm . The instrument allows fast and accurate analysis of most important trace elements in quartz (Li, Al, Ti, Cr, Mn, Fe, and Ge). A laser beam with larger diameter and higher energy ablates more material and results in lower detection limits. On the other hand the trace element distribution of zoned quartz crystals requires highest spatial resolution. Therefore a compromise between detection limit and spatial resolution has to be found. For a mean ablation crater size of about 20 μm the detection limit for LA ICP-MS are comparable with those of EPMA.

The *EPMA* is based on X-ray emission of a solid bombarded with a focused electron beam. Characteristic X-rays are analysed according to their wavelength, the peak intensity counted relative to a standard. The main advantages of the EPMA are the high spatial resolution of $\sim 4 \mu\text{m}$ and the capability of combining microanalytical analysis with CL and BSE imaging.

Trace and ultra-light elements (e.g. Li) which can not be measured by EPMA can be measured by the ion microprobe. The *SIMS* instrument uses a focused primary ion beam to perform in situ microanalysis of minerals in samples prepared as gold coated polished thin sections. A very small percentage of the sample material sputtered from the polished surface of the sample is ionised, and these ions are accelerated into a mass spectrometer where they are separated according to their mass. Nearly all elements from H to U can be detected and many can be analysed quantitatively down to part-per-million levels, or lower. $^{16}\text{O}^-$ beam currents

are required for trace element analysis and beam diameters of 30 μm allow the determination of the chemical zoning of minerals.

The *EPR* is a powerful spectroscopic technique available for the detection and identification of paramagnetic defects. Paramagnetic defects arising from impurities (Al, Ti, Fe, Ge, H, P, Cu, Ag) and oxygen and silicon vacancies are induced by natural or artificial irradiation of the quartz lattice. EPR describes the interaction between an electronic spin submitted to the influence of crystal field and an external magnetic field. The technique based upon the resonance absorption of induced magnetic microwaves caused by the magnetic moment of unpaired electrons resulting from paramagnetic defects. The determination of centres were made using powders.

The *FTIR spectroscopy* of quartz allows the qualification of structural bounded water in form of H_2O molecules, hydroxyl, hydrogen-compensated aluminium and lithium defects. Records of spectra of single points and along profiles through quartz crystals were used to determine variations of kind and quantity of water associated defects.

4.1 Electron probe microanalysis (EPMA)

Trace elements in quartz were determined by wavelength-dispersive Electron Probe Micro Analysis (EPMA) on the JEOL JXA 8900 operating at an accelerating potential of 15 keV, at a beam current of 120 nA on the Faraday cup, and with a beam diameter of 7 μm . Analyses were performed for Al, Ti, K, and Fe. Raw intensities converted into concentrations, making appropriate matrix corrections after the phi-rho-z method by Armstrong (1991). Measurements were carried out as single point analysis, or as line scans, yielding distribution profiles. CL imaging was performed prior and after EPMA analysis. In this way the measurement points in relation to the CL textures can be exactly located.

Quartz contains trace elements of at such low concentrations that a quantification by EPMA poses a major difficulty. Therefore, particular attention had to be paid to a number of parameters: 1) long counting time, 2) high beam current, 3) precise background measurement, 4) high polishing quality of the sample surface, and 4) carbon coating with constant thickness. The most decisive and often underestimated is the effect of the sample surface quality on the sensitivity of the measurement (Fig. 4.1). The increase of the Al background between measurement 39 and 48 during sample change is caused by sample surface contamination,

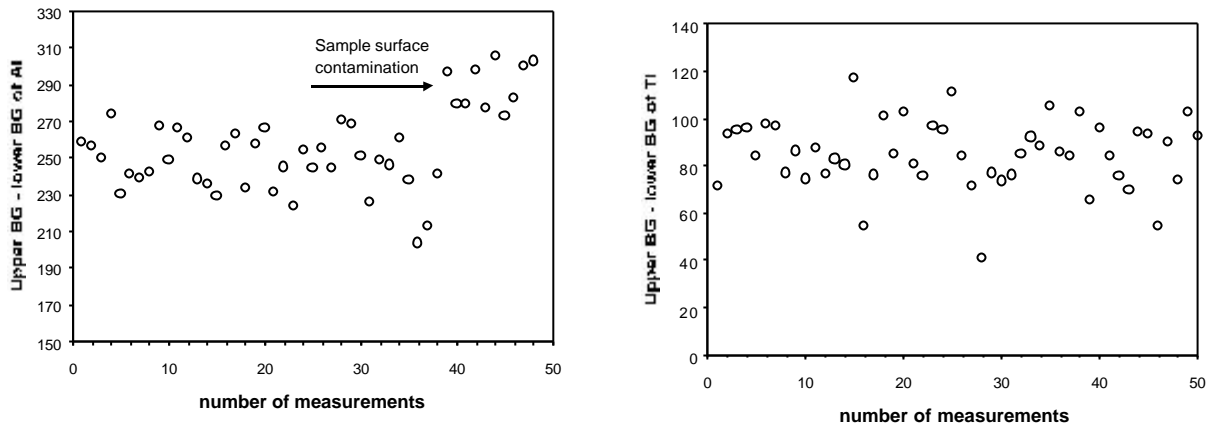


Fig. 4.1 Variation of brutto intensities of the Al and Ti background measurements (upper minus lower background) of three trace element profiles.

whereas the Ti background remains constant. This effect results in a decrease of the detection limit for Al from 27 ppm to 50 ppm. Finally, for high precision and sensitivity, the high beam current of 120 nA, the beam diameter of 7 μm , and the counting rate of 10 min per shot means 180 s per element were chosen.

The determination of element concentrations in analytical chemistry is based on repetitive measurements and on the application of statistical methods (e.g. Miller and Miller, 1988; Miller, 1991). In EPMA, concentrations are calculated from the difference between the accumulated peak counts and the background (BG) at the position of the X-ray line maximum. For extremely low concentrations only qualitative analysis is possible. The concentration at the detection limit, C_{DL} , as the lowest concentration of an analysed element that can be distinguished with reasonable confidence from zero concentration of the analysed element in a sample (blank). Ziebold (1967) suggested different definitions of the C_{DL} , and also Miller (1991) emphasises that a single, “correct”, definition of the limit of detection, cannot be given and should be specified.

We used two definitions of the detection limit. The intensity (in counts) of the detection limit (I_{IDL}) is given in equation (4.1) (e.g. Merlet and Bodinier, 1990):

$$I_{1DL} = 3 \sigma_{BG} \quad (4.1)$$

where σ_{BG} = standard deviation of the background.

To reach a probability of 95% that a peak is present, the peak counts must exceed three times the standard deviation of the background, whereby the number of background measurements n must be ≥ 5 . I_{1DL} was calculated for each trace element profile on the base of 12 background measurements.

A second method for determining of the intensity of the detection limit (I_{2DL}) is based on the level of significance applied to Student's t-distribution and the standard deviation obtained from background measurements (Plesch, 1982):

$$I_{2DL} = t_z (P;f) s_{BG} \quad (4.2)$$

where s_{BG} = standard deviation of the mean of the background; $t_z (P;f)$ = level of significance of the Student's t-distribution for binomial limitation determined by the confidence level P and the degrees of freedom f = number of background measurements $n - 2$.

For each trace element profile both I_{1DL} and I_{2DL} were determined. For the latter a confidence level of 95% and 12 background measurements were used which result in the binomial level of significance $t_z (P;f)$ of 2.228 (Table 4.1). The application of the equation (4.2) in this case results in a lowering of I_{DL} .

For the determination of the detection limit C_{DL} the determination of the regression coefficients a and b are necessary, which represent the gradients of the regression line intensity vs. concentration of an element:

$$C_{DL} = a + b I_{DL} \quad (4.3)$$

where a and b = the regression coefficients of the regression line intensity vs. concentration.

The regression coefficients a and b were determined by equation (4.4) and (4.5):

$$a = \frac{\sum C \sum I^2 - \sum C I \sum I}{n \sum I^2 - (\sum I)^2} \quad (4.4)$$

$$b = \frac{n \sum C I - \sum I \sum C}{n \sum I^2 - (\sum I)^2} \quad (4.5)$$

where I = intensity; C = concentration of measurements; n = number of measurements.

The regression lines of intensity vs. concentration for the elements Al, Ti, K, and Fe are illustrated in figure 4.2. The regression coefficients a and b were calculated from 273 measurements for each element. The coefficient a represents the concentration for zero counts and should be theoretically zero. But small systematic errors of the equipment result in a shift of the regression line ($a \neq 0$) for Al at about 19 ppm. Consequently, the Al content calculated by the EPMA software is generally 19 ppm to high. For the other elements a is about zero. The concentrations of the detection limit for Al, Ti, K and Fe calculated after the equations (4.2) and (4.3) are shown in figure 4.3 and listed in table 4.2.

Table 4.1 Level of significance of the Student's t-distribution for binomial limitation (Plesch, 1982).

f	$t_z(P;f)$	
	P = 95%	P = 99%
1	12.710	63.660
2	4.303	9.925
3	3.182	5.841
4	2.776	4.604
5	2.571	4.032
6	2.447	3.707
7	2.365	3.499
8	2.306	3.355
9	2.262	3.250
10	2.228	3.169
12	2.179	3.055
15	2.131	2.947
20	2.086	2.845
30	2.042	2.750
50	2.009	2.678
8	1.960	2.576

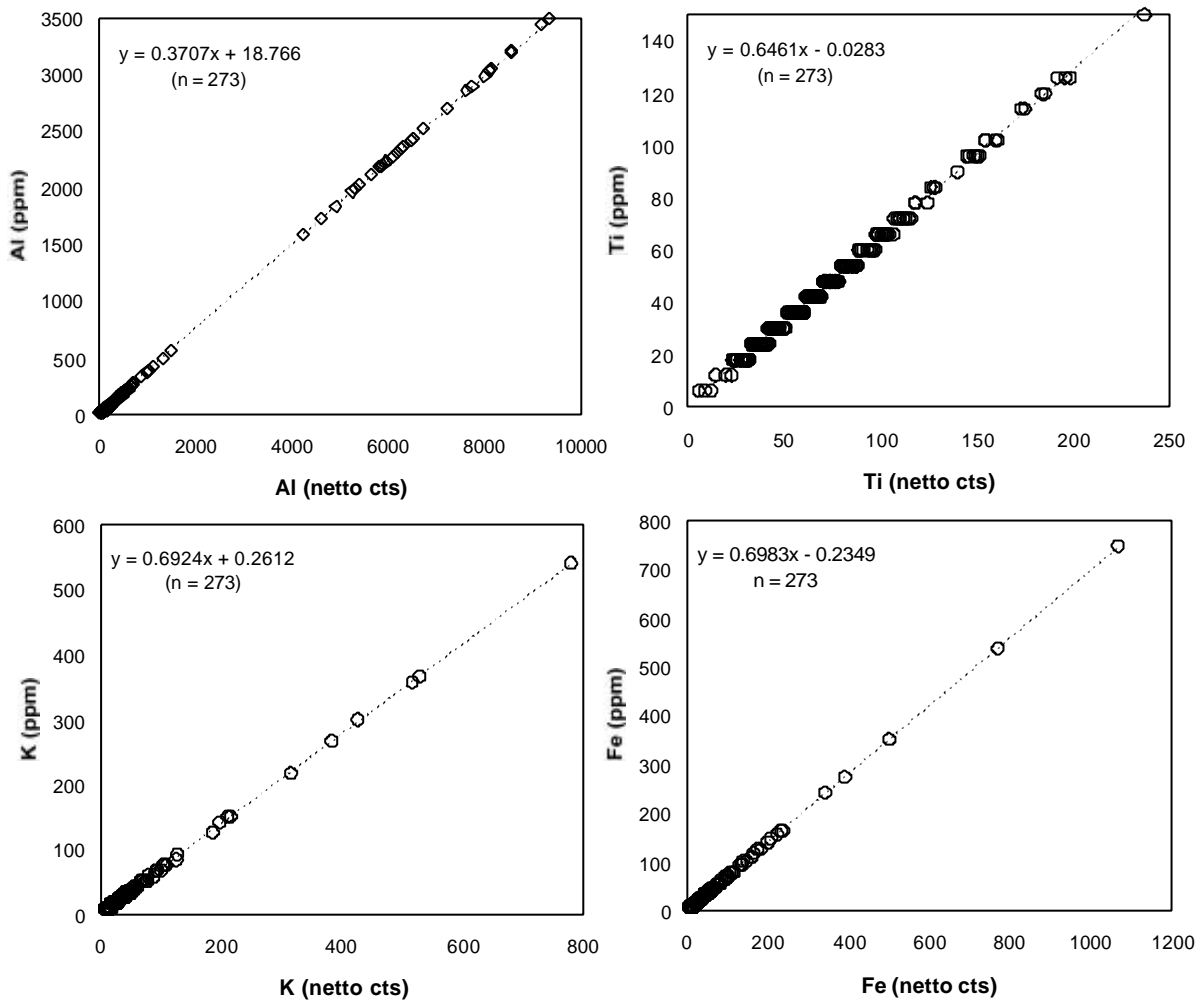


Fig. 4.2 Calculated regression coefficients a and b of regression lines of netto counts vs. element concentration. Under ideal conditions a should be zero, but systematic errors of the equipment cause a shifting of the regression line for Al at about 19 ppm.

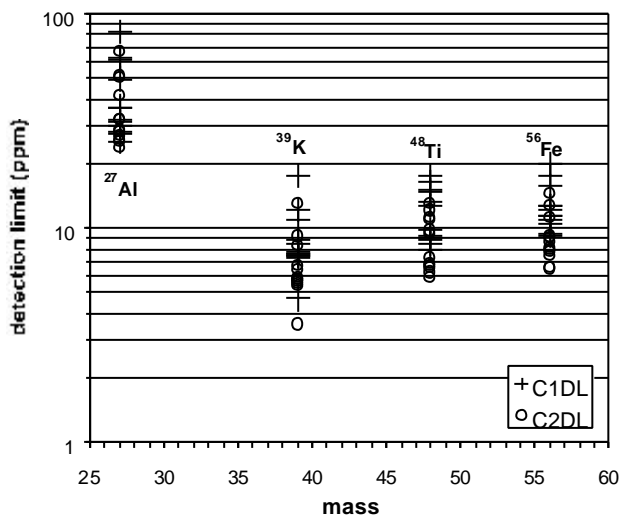


Fig. 4.3 Detection limits of trace elements in quartz for EPMA. The detection limit C1DL bases on the calculated intensity I_{DL} after equation (4.1) and C2DL on the intensity I_{2DL} after equation (4.2). In the case of the EPMA the C2DL is ca. 25% lower than C1DL caused by the level of significance which is lower than three standard deviations.

Table 4.2 Detection limits C_{DL} (ppm) of EPMA calculated after the equations (4.2) and (4.3) with a confidence level of 95%.

Profile number	n	f	Al	Ti	K	Fe
1	12	10	41.8	10.9	9.1	9.1
2	12	10	27.9	11.2	5.5	11.2
3	12	10	51.3	7.3	13.0	14.5
4	12	10	66.4	13.0	5.7	7.4
5	12	10	32.2	6.8	5.6	8.0
6	12	10	32.1	12.1	5.7	12.7
7	12	10	28.6	9.5	5.4	7.7
8	12	10	27.2	6.5	6.4	6.4
9	12	10	26.0	5.9	5.8	8.6
10	12	10	23.6	6.2	6.7	8.1
11	12	10	50.2	9.7	3.6	6.6
12	12	10	25.2	6.7	8.3	9.1

4.2 Laser ablation - inductively coupled plasma mass spectrometry (LA ICP-MS)

The trace element composition of quartz grains has been determined using a Laser Ablation micro-sampler coupled to an Inductively Coupled Plasma Mass Spectrometer (LA ICP-MS) model FISIONS PQ2+ with “S-option”. A Nd:YAG UV-laser (266 nm) model FISIONS UV Microprobe with a laser pulse repetition rate of 5 Hz was focused onto the surface of a polished sample. Using a laser beam energy of 2.25 mJ, the middle aperture, and an acquisition time of 40 s, the laser ablated craters 30 to 50 μm in diameter and between 100 to 150 μm deep. The ablated sample volume per shot amounted up to 300 000 μm^3 of which approximately 80% reached the mass spectrometer and was analysed. The determination of the optimal laser configurations was carried out by several test measurements and varying counting rates, to reach very low detection limits, to avoid sample outbreak during ablation, and to get craters as small as possible for better spatial resolution of the trace element distribution (Fig. 4.4). A laser beam with larger diameter and higher energy ablates more material and results in lower detection limits which are inversely proportional to 3rd root of the ablation volume (Potts et al., 1995). Nevertheless, the risk that micro-inclusions within this volume were also analysed cannot be avoided.

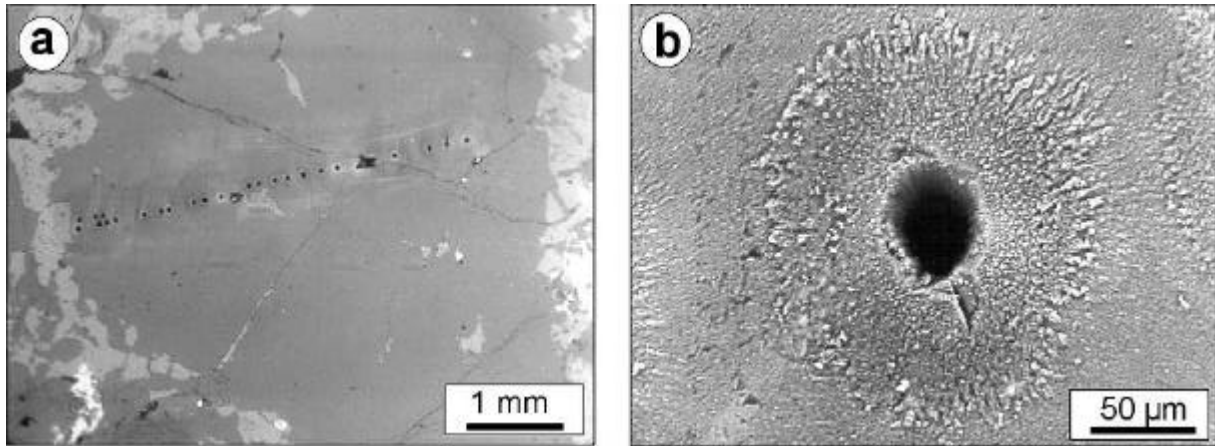


Fig. 4.4 BSE images of Nd-YAG laser ablation craters in quartz. a – Craters of a measurement profile through a quartz phenocryst of the Schellerhau Granite (sample 6). b – A close view shows that the craters are surrounded by wall of molten quartz glass.

The ablated material was swept by high purity Ar gas (flow rate 0.8-1.3 l/min) into an inductively coupled plasma. Isotopic masses were analysed by an quadrupole mass filter. Time resolved measurements showed that the plasma needed about 3 s before reaching the mass spectrometer; during the following 5 s high count rates were detected. This may be caused by sample outbreak and sample surface contamination. After 8 s a stable count rate was reached, therefore, the counts of the first 8 s of the measurement were neglected.

Analyses were performed for the isotopes of ^7Li , ^{23}Na , ^{27}Al , ^{29}Si , ^{30}Si , ^{44}Ca , ^{49}Ti , ^{53}Cr , ^{55}Mn , ^{57}Fe , and ^{72}Ge . The choice of the isotope of the element to be analysed depends on two criteria: (1) interferences with masses of other isotopes should be avoided, and (2) the ratio between intensity (peak) maximum of the isotope mass and the background should as high as possible. Figure 4.6 shows the detection limits for the different isotopes. Note the detection limit may highly vary for different isotopes of one element. For example, ^7Li isotope has a higher peak maximum/background ratio than ^6Li resulting in a lower detection limit.

The data were calibrated against the NBS610 glass standard (external standard) and the internal standard of the Si value (4.67×10^5 ppm = stoichiometric concentration of Si in quartz). The element abundance of LA ICP-MS measurements were calculated by the equation (4.6):

$$c_{\text{sample}}^{\text{elem}} = \frac{\text{cps}_{\text{sample}}^{\text{elem}} * c_{\text{sample}}^{\text{Si}29} * \text{cps}_{\text{NSB}}^{\text{Si}29}}{\text{cps}_{\text{sample}}^{\text{Si}29} * c_{\text{NSB}}^{\text{Si}29} * \text{cps}_{\text{NSB}}^{\text{elem}}} * c_{\text{NSB}}^{\text{elem}} \quad (4.6)$$

where $c_{\text{sample}}^{\text{elem}}$ = the concentration of the element of interest in the sample; $\text{cps}_{\text{sample}}^{\text{elem}}$ = count rate of mass of element of interest in the sample; $c_{\text{sample}}^{\text{Si}29}$ = assumed concentration of the ^{29}Si isotope in the sample (21980 ppm); $\text{cps}_{\text{NSB}}^{\text{Si}29}$ = count rate of mass of the ^{29}Si isotope in the standard; $\text{cps}_{\text{sample}}^{\text{Si}29}$ = count rate of the ^{29}Si isotope in the sample; $c_{\text{NSB}}^{\text{Si}29}$ = concentration of the ^{29}Si isotope in the standard (15305 ppm); $\text{cps}_{\text{NSB}}^{\text{elem}}$ = count rate of mass of element of interest in the standard; $c_{\text{NSB}}^{\text{elem}}$ = concentration of the element of interest in the standard.

The detection limit is influenced by the acquisition time, the volume of ablated sample material, the flow rate of the Ar gas, and the isotope of the element. Furthermore, the sensitivity of the ICP-MS may change during the course of one measurement day. This drift found by standard and background measurements in regular time intervals was not a linear function of time (Fig. 4.5). Therefore, the measurements were done in the sequence: five background measurements – one standard measurements – ten sample analysis measurements.

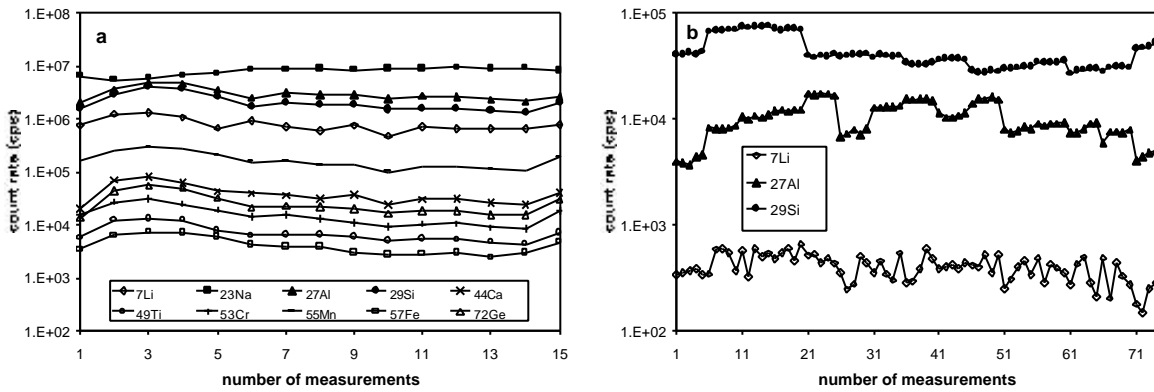


Fig. 4.5 Fluctuation of standard (a) and background (b) count rates of LA ICP-MS measurements during one measure day.

The mean and the standard deviation (σ_{BG}) were calculated for each sequence of background measurements. These values were then used to calculate the intensity of the detection limits (I_{DL}) in accordance with the equations (4.1) and (4.2). The regression coefficient b was determined from a single point calibration, assuming a linear calibration line which passes through the origin of the intensity vs. concentration plot (Table 4.3). It follows from equation (4.7):

$$C_{DL} = C_{STD} I_{DL}/I_{STD} \quad (4.7)$$

where I_{STD} = intensity of the standard measurement; C_{STD} = given concentration of the element in the standard.

The high sensitivity of the ICP-MS for most trace elements in quartz leads to very low detection limits shown in figure 4.6 and listed in table 4.3. Ca and Na cannot be measured because the high detection limit. For Na it is mainly caused by molecular interferences with $^{12}C^{32}O_2$ which is present in small amounts in the sample chamber. The determination of Na is a general problem of micro beam analysis because its high volatility and frequency leads to a omnipresent Na contamination.

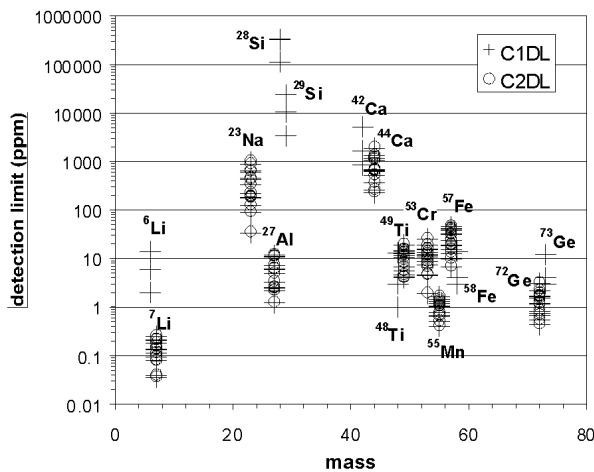


Fig. 4.6 Detection limits of trace elements in quartz for LA ICP-MS. The detection limit C1DL bases on the calculated intensity I_{IDL} after equation (4.1) and C2DL on the intensity I_{EDL} after equation (4.2). In the case of the EPMA the C2DL is ca. 25% lower than C1DL caused by the level of significance which is lower than three standard deviations.

4.3 Secondary ion mass spectrometry (SIMS)

The SIMS analyses were performed on a Cameca IMS-6f magnetic sector ion microprobe at the GeoForschungsZentrum Potsdam by M. Wiedenbeck. The mass filtered beam had a impact energy of 12.5 keV, a 40 nA primary current and was focused to a spot size of 25 μm . The gold-coated polished samples were embedded in rings of one inch in diameter with a vacuum compatible medium. During analysis, the material was gradually removed from the sample surface by the incident primary $^{16}O^-$ beam in a process termed “sputtering”. After selecting a position to analyse, a 50x50 μm area was pre-sputtered with the rastered primary beam for 240 s to remove the gold coating and any surface contamination. Within any one set

Table 4.3 Detection limits C_{DL} (ppm) of LA ICP-MS calculated after the equations (4.2) and (4.7) with a confidence level of 95%.

Number of Sequence	n	f	Li	Na	Al	Ca	Ti	Cr	Mn	Fe	Ge
1	6	4	0.04	446	6.3	1383	13.8	16.3	0.66	32.9	0.46
2	6	4	0.12	189	2.3	239	4.4	2.0	0.42	24.9	1.59
3	6	4	0.10	95	2.7	382	4.2	7.8	0.72	7.2	0.57
4	6	4	0.10	132	1.3	273	4.8	4.8	0.80	13.6	0.87
5	6	4	0.08	190	2.5	1292	8.5	7.0	1.20	38.3	1.65
6	6	4	0.14	475	7.6	542	12.2	9.0	0.53	20.2	1.27
7	6	4	0.16	200	2.3	706	16.0	10.4	1.29	23.6	2.00
8	6	4	0.26	194	2.6	684	5.8	14.1	1.72	15.9	1.77
9	6	4	0.04	236	6.5	716	11.1	26.8	1.28	10.4	1.73
10	6	4	0.19	36	11.3	661	14.9	19.8	1.28	48.0	0.78
11	6	4	0.14	686	5.1	1133	15.6	11.3	1.12	34.4	1.22
12	6	4	0.14	352	3.5	712	20.2	13.0	1.52	44.0	1.78
13	6	4	0.22	647	12.4	1219	13.5	16.6	1.08	42.8	3.26
14	6	4	0.22	922	11.7	2017	7.0	12.2	1.38	40.6	2.27
15	6	4	0.08	1061	7.6	546	13.5	5.0	0.71	19.7	0.71
16	6	4	0.14	391	5.7	833	11.0	11.7	1.05	27.8	1.46
17	6	4	0.06	301	3.6	468	4.8	6.2	0.37	12.8	0.72

of analyses, the energy distribution stayed constant (± 1 eV). The total counting time of one analysis was 1240 s, composed of 20 cycles of 10 s for each isotope, except for Si with 2 s. Li, Na, Al, Si, K, Ti, and Fe were measured on masses 6, 23, 27, 30, 39, 48, and 54, respectively. These masses were selected either because they represent an abundant isotope of the element in question or because interferences by molecular complexes would be at a

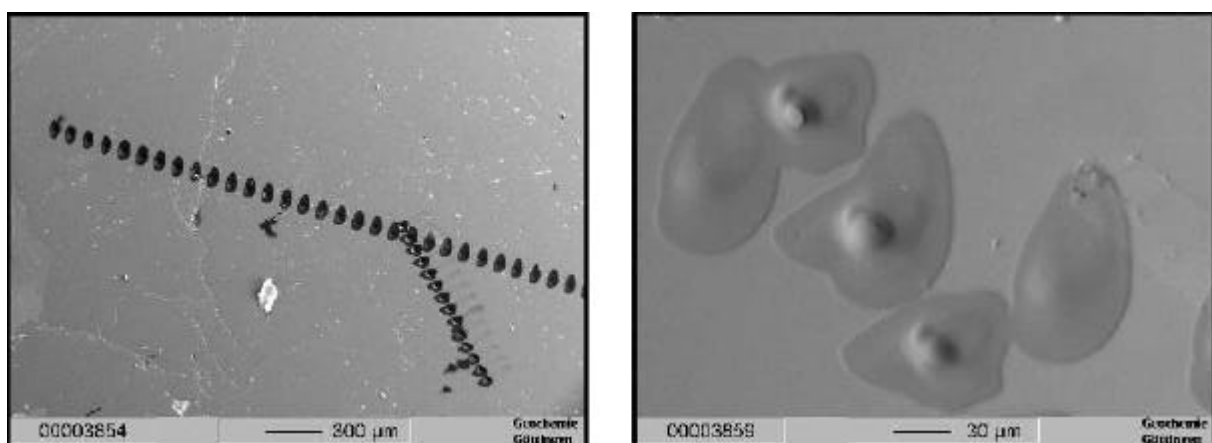


Fig. 4.7 BSE images of microcraters in quartz produced by primary $^{16}\text{O}^+$ beam. a – Measurement profile through a quartz phenocryst of the Aue Granite (sample 8). b – Closer view of microcraters.

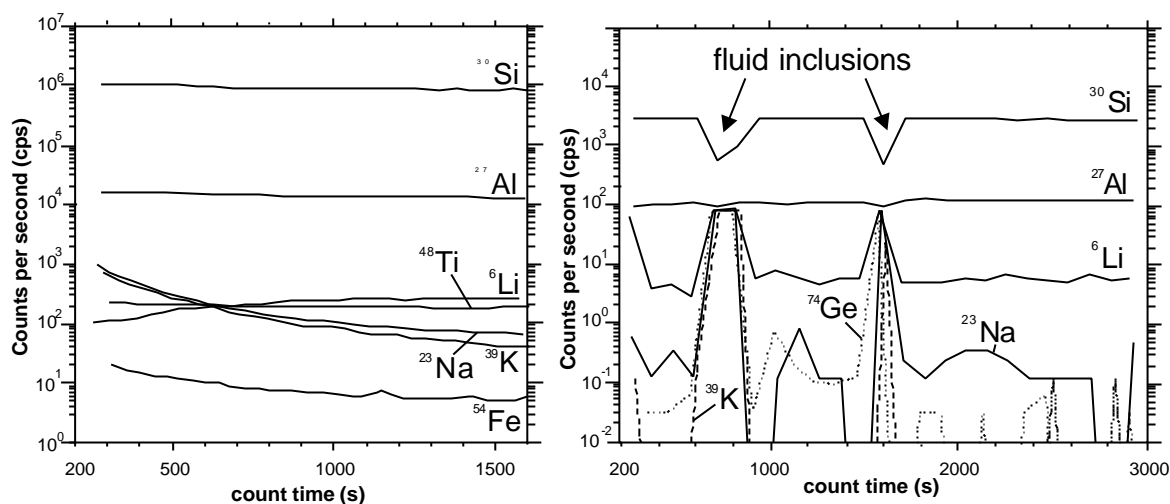


Fig. 4.8 Plots of secondary ion intensity as a function of sputter time. a – Analysis of sample 8 (Aue Granite) where a slight initial increase in ^6Li and a decrease in ^{23}Na , ^{39}K , and ^{54}Fe intensity with time have been observed. This intensity change is a general phenomena of the measurements. b – Analysis of recrystallised quartz along a fluid inclusion trail in sample 1 (megaquartz). Extreme changes of $X/^{30}\text{Si}$ ratios reflect analysed fluid or mineral inclusions.

minimum. The beam produces a microcrater 25 μm in diameter and a depth ranging 5-20 μm which allows subsequent verification of the spot location (Fig. 4.7). CL observations were performed prior and after SIMS analysis. Measurements were carried out as single point analysis and point traverses, yielding distribution profiles. The plot of secondary ion intensity as a function of sputter time facilitated the quality control of the analysis. Figure 4.8b shows a time resolved analysis in recrystallised quartz of a fluid inclusion trail in sample 1 (megaquartz). Extreme changes of $X/^{30}\text{Si}$ ratios reflect analysis of a fluid or mineral inclusion. A slight initial increase in ^6Li and a decrease in ^{23}Na , ^{39}K , and ^{54}Fe intensity with time have been observed in most measurements (Fig 4.8a; Aue Granite 8). Li^+ , K^+ , Na^+ , and Fe^{2+} are beside H^+ frequent and relative mobile interstitials in the quartz lattice. The cause of this often observed phenomena during SIMS analysis is controversial, and may be a consequence of electromigration due to sample charging and heating and/or sample surface contamination (e.g. Hughes et al., 1972; Wilson et al., 1989; Hervig and Peacock, 1989; Perny et al., 1992). In our case, the previous treatment of the sample with an electron beam during CL investigations may also result in a change of the element distribution at the sample surface. The electron radiation during CL investigations causes radiation-induced bond breaking resulting in impurity diffusion of interstitial ions which is additionally triggered by the sample charging and heating (e.g. Remond et al., 1979). The diffusion direction of a given impurity

from the bulk to the surface or vice versa is controlled by the surface potential distribution. Nevertheless, the observed change in the line intensity with exposure time of alkalis and Li is an often observed phenomena during SIMS measurements (e.g. Shimizu et al., 1978). The electromigration near the surface will give low results for the Na, K, and Fe and high results for Li. After ca. 500 s the count rates are nearly stabilised. Therefore, counts from the first 8 analytical cycles (496 s) were neglected. Because no standard was available the relative intensities were given in $X/^{30}\text{Si}$ ratios.

4.4 Fourier-transform infrared (FTIR) spectroscopy

Transmission FTIR spectra of quartz were obtained using the Perkin Elmer 1760-X FTIR spectrometer by S. Vaupel at the University Göttingen. The spectrometer can operate with an internal ray path and a triglycine-sulphate-detector or an external microscope with a separate mercury-cadmium-telluride-detector. The change between the two configurations is effected by a swivelling mirror. The external microscope is supplemented with a vacuum sample chamber (Dewar K-770-T) which is required for liquid N_2 -cooling of the sample and ray path (-190 - -194°C) to avoid interference with atmospheric H_2O and CO_2 . The cooling resulted in a maximal signal/noise ratio of the detected spectra.

FTIR spectroscopy is the only method for the determination of the distribution and specification of structural water in quartz crystals. The quartz wafer is penetrated by an electromagnetic UV beam (wavelength = $2\text{-}25\ \mu\text{m}$). The radiation excites the vibration of the atoms which lead to the absorption of distinct wavelengths depending on the kind of atoms and their bonds.

The analysis were carried out on doubly polished wafers $250\ \mu\text{m}$ in thickness. Prior to the measurement the wafers were cleaned with acetone and dried for 10 h at 110°C . The spectra were acquired in a range of wave numbers between 5000 to $2000\ \text{cm}^{-1}$ with 200 scans in the transmission modus. The resolution of the measurements was $4\ \text{cm}^{-1}$. The spot size of the beam on the sample was $40\ \mu\text{m}$ in diameter which allows the recording of several spectra along a traverse within one grain. Background were taken after each spectra. The spectrum processing was carried out on a PC for baseline correction, sample thickness correction and converting of the transmission spectrum to the absorption spectrum.

4.5 Electron paramagnetic resonance (EPR)

The paramagnetic defect centres of the quartz samples were investigated by EPR at frequencies of the X-band (9.5 GHz) at 20, 70, and 295 K using a Varian E-line spectrometer at the Department of Mineralogy, University of Marburg. The measurements were carried out by T. Scherer. The influence of technical parameters such as modulation amplitude, microwave power, temperature, scan time, etc. on the spectra were checked for the optimal settings for recording the spectra. These settings (modulation field $H_M = 1$ G, temperature $T = 295$ K, microwave power $p = 0.2$ mW for E' and $H_M = 1$ G, $p = 7$ mW, $T = 70$ K for $[AlO_4]^0$ centres) were kept constant throughout all the measurements to allow correct comparison between the signal intensities of the different spectra.

The samples were crushed and quartz crystals were separated from the parent rock material by hand-picking under binocular microscope. Isolated quartz was sieved to obtain the 63-125 μm fraction, followed by a HF acid treatment at room temperature to remove feldspar (not necessary for the hydrothermal quartz). Finally the fraction was treated with distilled water and then air dried.

The specific peak positions of the paramagnetic centres were drawn from simulated spectra and from literature data. The centres were calculated in relative intensities. For the calculation of the relative intensity of the paramagnetic defect centres the following equation was used:

$$I_{\text{rel}} = \frac{I_s * 10000}{G_s * m_s} \quad 4.8$$

where I_s = measured intensity of the EPR signal, G_s = intensification factor used during spectrum recording, and m_s = mass of the sample.

5 Analytical results

5.1 Characterisation of the cathodoluminescence of quartz

The quartz CL spectra in the range of 1.4 to 3.1 eV generally consist of two broad emission peaks at 1.7 – 2.2 eV (red emission) and 2.4 – 3.1 eV (blue emission; Fig. 5.1). The CL colour, mostly shades of blue, violet, and red-brown is dependent on the ratio of the two main emission peaks (Table 5.1). The peak ratio changes with the exposure time of electron radiation, whereby the blue emission generally decreases and the red emission increases (Fig. 5.2). The maximum of the two peaks shifts for different quartz types indicating that the peaks are built up of different emission bands of different stability. Nine emission bands have been detected in all the spectra by fitting the spectra with Gaussian curves. Three emission bands can be distinguished in the red emission range (1.73, 1.84, and 1.96 eV) and five bands in the blue emission range (2.47, 2.58, 2.68, 2.79, and 2.96 eV) (Fig. 5.3). Additionally, a broad band has been observed in the yellow range of the spectrum at 2.15 eV. Depending on the quartz sample the emission bands show different intensities, half-width, and different stability during irradiation. The parameters of CL emission bands obtained from best-fit listed in Appendix A. Most CL band positions are consistent with the values reported in the literature (e.g. Remond et al., 1992; Gorton et al., 1996; Kalceff et al., 2000 and references therein; Table 5.2). Characteristics of the spectra can be summarised as follows (Fig. 5.1, 5.2, 5.3):

1. Nine emission bands are developed in the CL spectra of all samples.
2. The intensity of the blue emissions decreases whereas the intensity of red emission generally increases during electron radiation. A frequently observed bright blue “flash” at initial electron radiation is caused by the unstable blue emission at ~2.79 eV.
3. Dominant emission bands of *rhyolitic quartz* (samples 4, 10, 11, 15) are the 1.96, 2.58, 2.68, 2.79, and 2.96 eV band. The spectra are very similar although they originate from different volcanic provinces. An exception is the quartz of the Teplice Rhyolite showing a dominant 1.73 eV emission. The blue and red luminescent growth zones in quartz phenocrysts are caused by the variation of the blue CL emission whereas the red CL remains essentially constant (sample 10, 11, 15).
4. The 1.73 and 2.15 eV bands are characteristic for the *granitic quartz* and some rhyolites (sample 5). The 2.15 eV emission is dominant in the quartz of the Aue and Eibenstock granites from the Western Erzgebirge.

5. *Hydrothermal quartz* (sample 1, and 3) exhibit a distinctive 2.47 eV band and sample 9 a dominant 2.79 eV band. The bands are characterised by a fast intensity decrease during electron exposure. The 2.47 eV emission causes a turquoise CL at initial electron radiation (sample 1 and 3).
6. The 2.68 and 2.58 eV emission bands are developed with about constant peak area ratios in all samples: 1 : 0.34±0.08. Similar observations were made for the 1.96 and 1.84 eV red emission bands which show ratios of 1 : 0.51±0.17. The 2.58 eV and 2.68 eV emission are not immediately obvious from visual inspection of the other 100 mm-grating spectra due to the close proximity of more intense emissions, but the bands are detectable in spectra recorded with the 1200 line/mm grating (Fig. 5.3).

Table 5.1 CL colours and structures revealed by CL.

No.	Sample name	Initial CL colour	Duration of initial colour (s)	Final CL colour	Primary CL structures	Secondary CL structures*
1	megaquartz	intense turquoise	60	orange-brown	-	3, 5
2	fissile quartz	bright blue	30	red-brown	-	-
3	oil-bearing quartz	intense turquoise	60	red-brown	-	-
4	Schoenfeld Rhyolite	bright blue	120	blue-violet	zoned phenocrysts	3, 4
5	Teplice Rhyolite (TPR2)	bright blue ¹⁾ weak blue ²⁾	30 ¹⁾ 10 ²⁾	violet-blue ¹⁾ dark red ¹⁾	zoned phenocrysts	2, 3, 4, 5
6	Schellerhau Granite	bright blue ¹⁾ weak blue ²⁾ bright blue ³⁾	30 ¹⁾ 5 ²⁾ 20 ³⁾	violet-blue ¹⁾ red-brown ²⁾ red-brown ³⁾	zoned phenocrysts	1, 2, 3, 5
7	Eibenstock Granite	bright blue ¹⁾ bright blue ³⁾	30 ¹⁾ 20 ³⁾	violet-red-brown ¹⁾ red-brown ³⁾	zoned phenocrysts	1, 2, 3, 5
8	Aue Granite	bright blue	20	orange-brown	zoned phenocrysts	1, 2, 3, 5
9	vein quartz	intense blue	300	dark blue	-	-
10	Wachtelberg Rhyolite	bright blue ¹⁾ weak blue ²⁾	30 ¹⁾ 10 ²⁾	violet ¹⁾ red-brown ²⁾	zoned phenocrysts	3, 4
11	Beucha Rhyolite	bright blue ¹⁾ bright blue ²⁾	120 ¹⁾ 10 ²⁾	blue-violet ¹⁾ red-brown ²⁾	zoned phenocrysts	2, 3, 4, 5
12	Flossenbuerg Granite	bright blue	60	red-brown	-	1, 2, 3, 5
13	leucosome quartz	bright blue	20	red-brown	-	-
14	Ramberg Granite	bright blue	30	red-brown	zoned phenocrysts	1, 2, 3, 5
15	Weinheim Rhyolite	bright blue ¹⁾ bright blue ²⁾	120 ¹⁾ 10 ²⁾	violet-blue ¹⁾ red-brown ²⁾	zoned phenocrysts	3, 4

* Secondary CL textures (see chapter 7.3): 1 – micropores; 2 – patchy halos of secondary quartz around fluid inclusions; 3 – veinlets of recrystallised quartz; 4 – diffusion rims along grain boundaries; 5 – bright halos caused by radioactive inclusions and fluids;

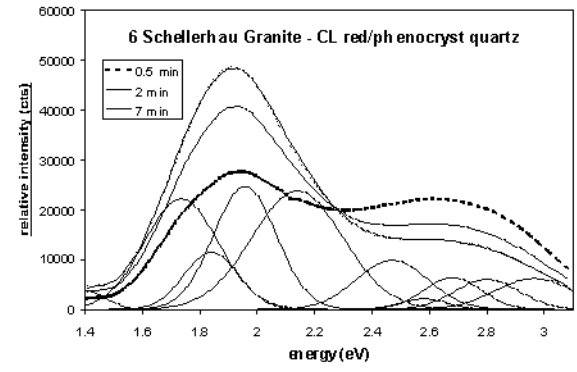
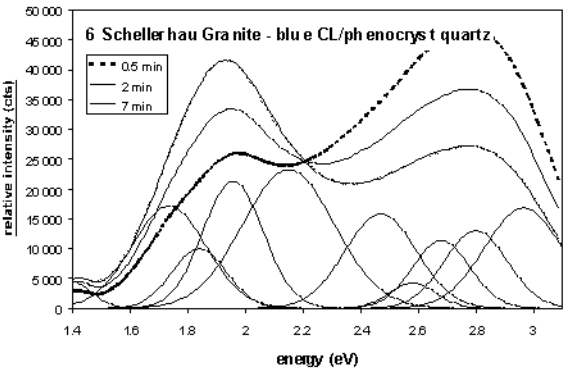
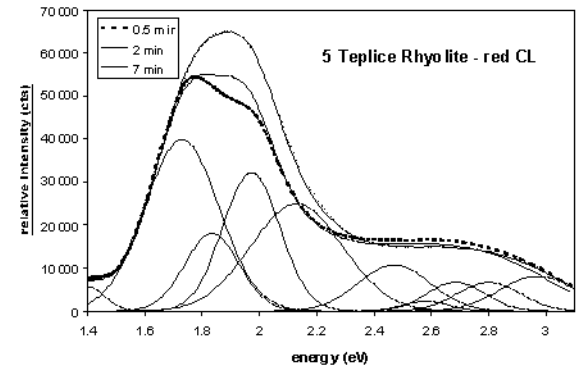
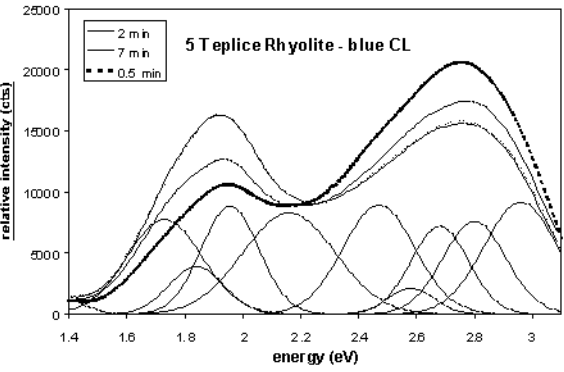
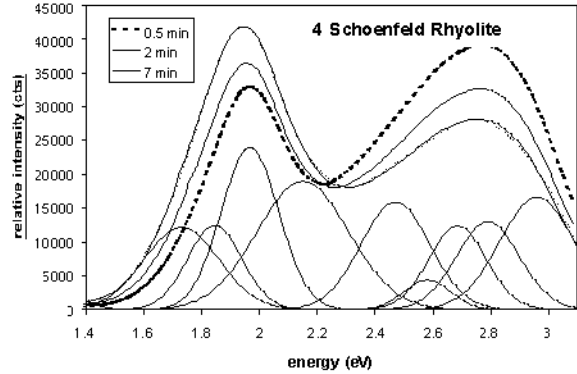
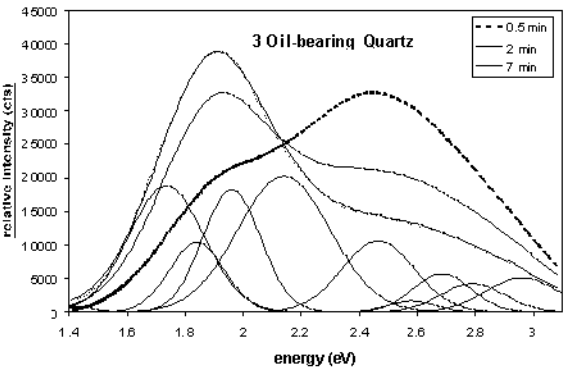
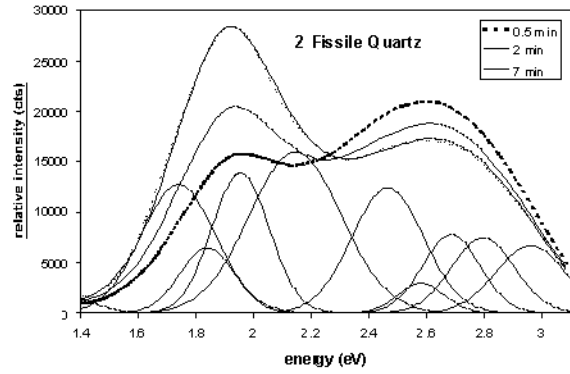
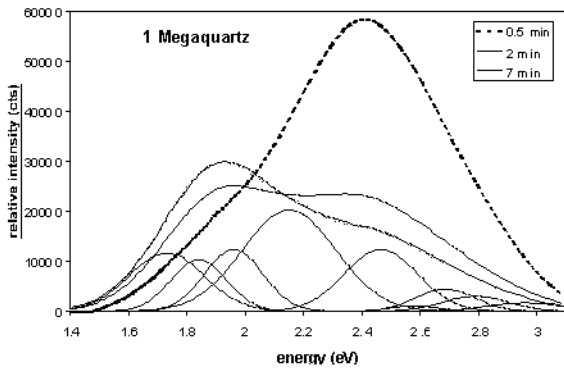
¹⁾ Blue luminescent growth zones in magmatic phenocryst

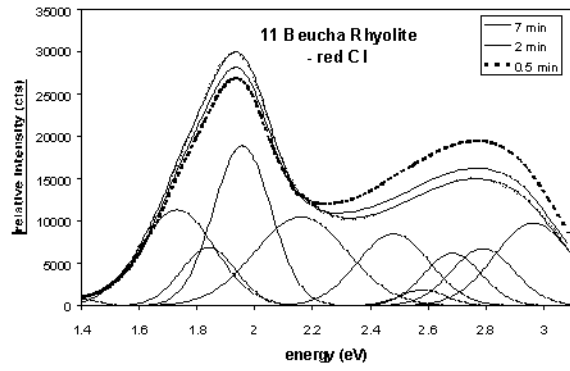
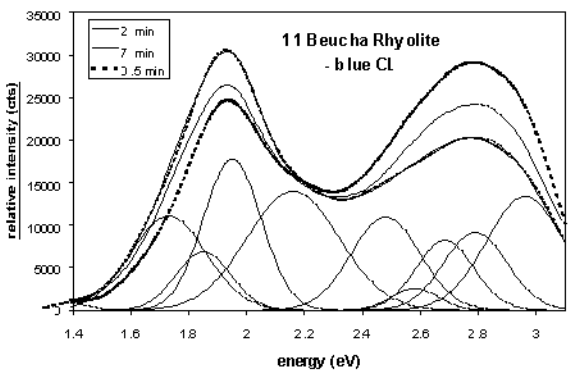
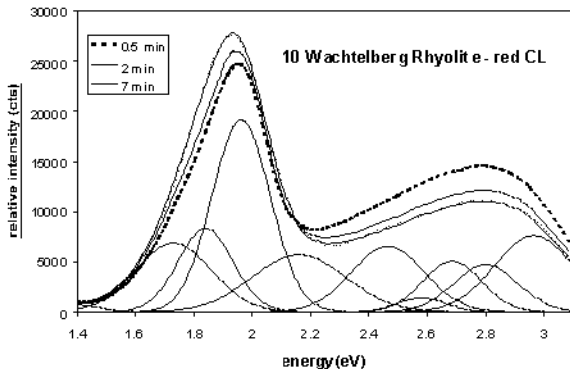
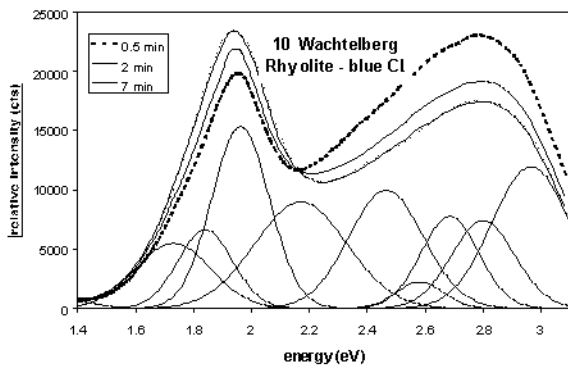
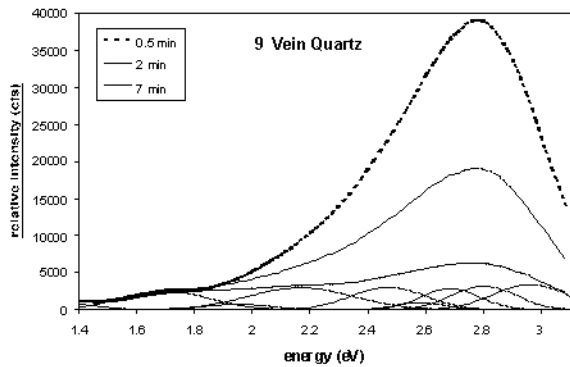
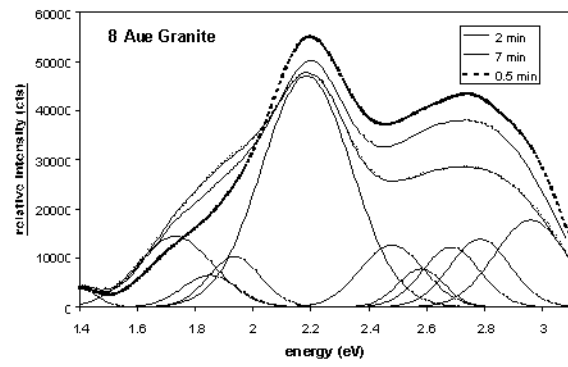
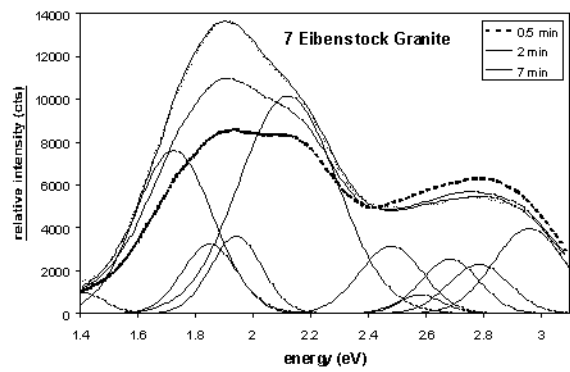
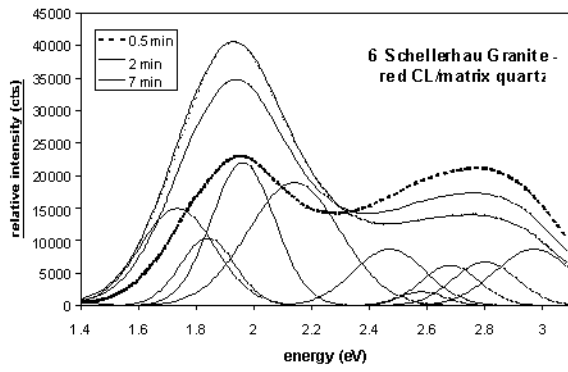
²⁾ Red luminescent growth zones in magmatic phenocryst

³⁾ Magmatic matrix quartz

Table 5.2 Comparison of frequently reported CL emissions of SiO₂ and proposed associations and identification (a-SiO₂ = amorphous SiO₂).

Wave-length (nm)	Energy (eV)	Peak position (eV)	Specimen	Association/identification	References
775	1.60				
763	1.625				
751	1.65				
740	1.675				
729	1.70				
719	1.725				
708	1.75				
698	1.775				
689	1.800				
679	1.825				
670	1.850				
661	1.875				
653	1.900				
644	1.925				
636	1.950				
628	1.975				
620	2.000				
612	2.025				
605	2.050				
598	2.075				
590	2.100				
584	2.125				
577	2.150				
570	2.175				
564	2.200				
557	2.225				
551	2.250				
545	2.275				
539	2.300				
533	2.325				
528	2.350				
522	2.375				
517	2.400				
511	2.425				
506	2.450				
501	2.475				
496	2.500				
491	2.525				
485	2.550				
481	2.575				
477	2.600				
472	2.625				
468	2.650				
464	2.675				
459	2.700				
455	2.725				
451	2.750				
447	2.775				
443	2.800				
439	2.825				
435	2.850				
431	2.875				
428	2.900				
424	2.925				
420	2.950				
417	2.975				
413	3.000				
410	3.025				
407	3.050				
403	3.075				
400	3.100				
397	3.125				
393	3.150				
390	3.175				
387	3.200				
384	3.225				
381	3.250				
379	3.275				
376	3.300				
373	3.325				
370	3.350				
		1.65 – 1.8	Opal α-SiO ₂ , sandstone	Associated with Fe ³⁺ impurity	Pott and McNicol (1971), Sprunt (1981), Kalceff et al. (1997), Bruhn et al. (1996)
		~1.9	a- and α-SiO ₂	NBOHC (Si-O precursor)	Remond et al. (1992), Kalceff and Phillips (1995), Zinkernagel (1978), Friebele et al. (1985)
		1.93	SiO ₂	Na impurity	Luff and Townsend (1990)
		1.95	Hydrated a and α-SiO ₂	Oxygen vacancy	Remond et al. (1992); Khanlary et al. (1993); Yang et al. (1994)
		1.95	Hydrated a and α-SiO ₂	NBOHC (-OH precursor)	Kalceff and Phillips (1995), Koyama (1980), Nishikawa et al. (1992)
		2.1-2.4	a-SiO ₂ , irradiated α-SiO ₂	STE	Luff and Townsend (1990)
		2.17	Ge doped α-SiO ₂	STE associated with Ge	Kalceff et al. (1995), Itoh et al. (1990)
		2.25-2.8	Natural α-SiO ₂	Associated with interstitial cations	Luff and Townsend (1990)
		2.4	Synthetic amethyst	Fe impurity	Ramseyer and Mullis (1990)
		2.5	α-SiO ₂	Impurity	Ruppert (1987)
		2.55	Smoky α-SiO ₂	(Al ³⁺) ⁰ hole center	Itoh et al. (1988), Kalceff and Phillips (1995)
		2.6-2.8	α-SiO ₂ , Opal, rose quartz	STE	Nassau and Prescott (1975)
		2.74	a-SiO ₂	(Ti ³⁺ , Ti ³⁺ , interstitial Ti ³⁺ , TiO ₂ micro inclusions)	Remond et al. (1992), Kalceff and Phillips (1995)
		2.75	O implanted a-SiO ₂	Oxygen deficient centre	Griscom (1991), Kalceff et al. (1997)
		2.75	O implanted a-SiO ₂	Oxygen related centre	Hagni (1987)
		~2.9	Natural α-SiO ₂	Substitutional Al and cation	Ramseyer and Mullis (1990)
		~2.95	α-SiO ₂	Intrinsic defect	Alonso et al. (1983), Kalceff and Phillips (1995), Gorton et al. (1996)
		2.99	C implanted a-SiO ₂	C impurity	Koyama (1980)
		3.0	a-SiO ₂	STE's associated with Ge, Al, H	Khanlary et al. (1993), Yang et al. (1994)
		3.1-3.3	a and α-SiO ₂ , sandstone, opal	Al ³⁺ -M ⁺ (where M ⁺ = H ⁺ , Li ⁺ , Na ⁺ , or K ⁺)	Ramseyer and Mullis (1990), Remond et al. (1992), Khanlary et al. (1993), Kalceff and Phillips (1995), Gorton et al. (1996)
				Impurity incorporation during growth	Skuja and Trukhin (1989), Luff and Townsend (1990)
		~3.7	α-SiO ₂ in sandstone	Associated with Al and Li impurities	Demars et al. (1996)
		4.3	α-SiO ₂	Na impurity	Sprunt (1981)





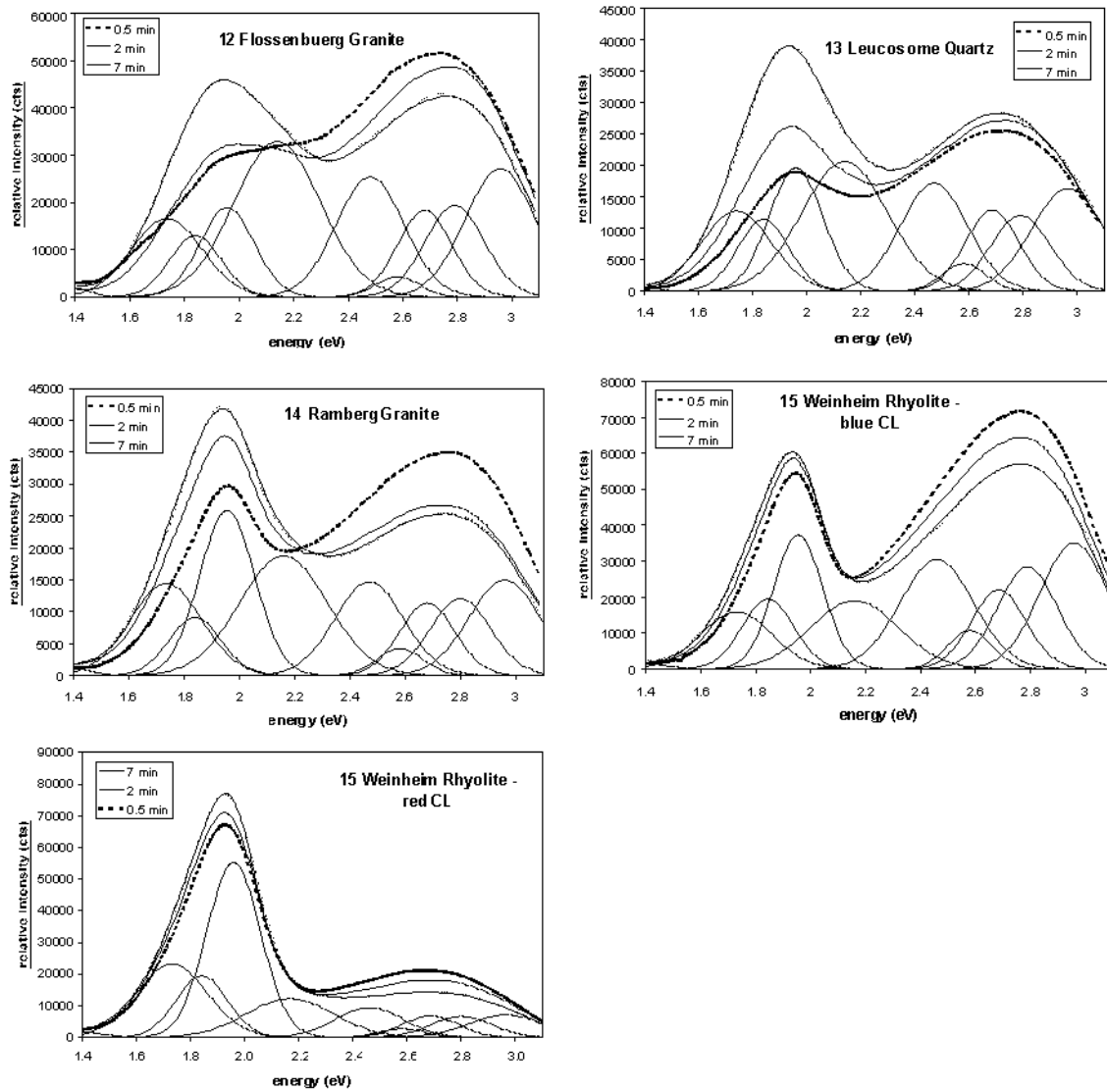


Fig. 5.1 Quartz CL spectra recorded with the 100 lines/mm grating after 0.5, 2, and 7 min electron radiation. The 7-min-spectrum is fitted in Gaussian curves so that the sum of the Gaussian curves corresponds the recorded spectra.

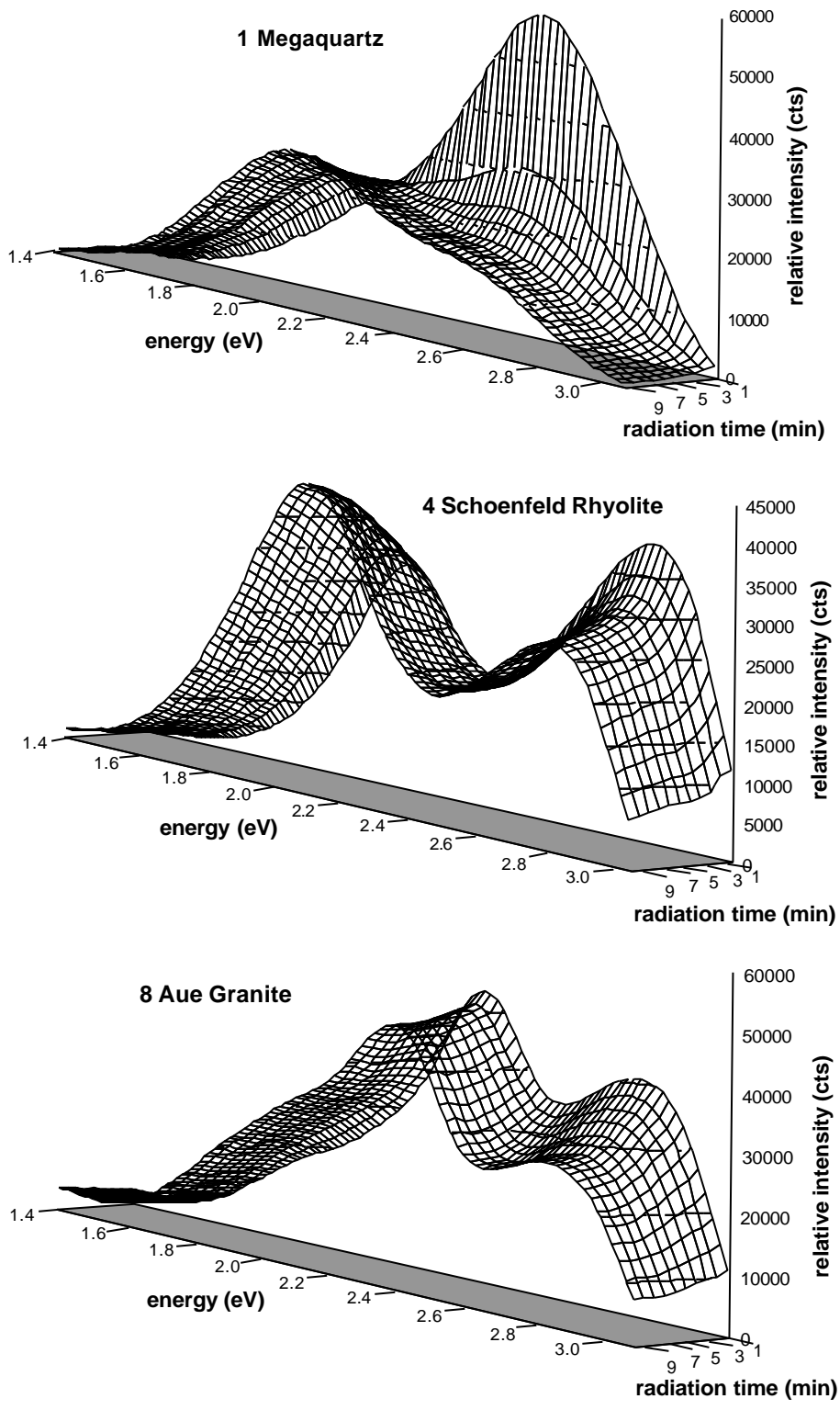


Fig. 5.2 CL intensity change during 10 min electron radiation of the samples 1, 4, and 8. Note the high instability of the blue emission of sample 1 and the dominance of the relative constant intensity of the yellow 2.15 eV band of sample 8.

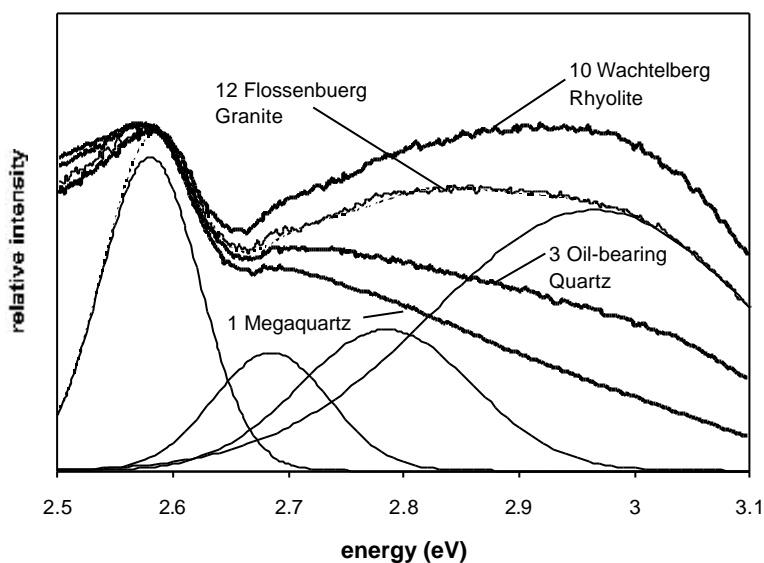


Fig. 5.3 Blue CL emission range of several quartzes recorded 1200 lines/mm grating after 7 min electron radiation. The spectrum of the sample 12 is fitted in Gaussian curves.

5.2 Instability of CL during electron bombardment

The blue emission (2.6 – 3.1 eV) is characterised by high intensity at initial electron bombardment visible as a blue “flash”. The initial intensity of this blue emission, mostly centred at ~2.8 eV may drop by 1/2 to 1/3 after a few seconds. The intensity is stabilised after 30 to 100 s of electron bombardment (Fig. 5.4). The steady state of CL-changes during electron radiation points at a saturation effect. The saturation status is reached faster with higher electron radiation dose. Figure 5.5 shows CL spectra of sample 12 after 2 minutes electron beam exposure using different beam currents. Note that the intensity of blue emission remains constant after 2-minutes spectra at beam currents =0.18 mA indicating a saturation status. In the case of the megaquartz (sample 1) and oil-bearing quartz (sample 3) the initial blue emission is centred at ~2.5 eV which causes turquoise CL at initial electron radiation.

In contrast to the blue emission, the red emission (1.75 – 2.2 eV) generally shows an intensity minimum at initial electron bombardment followed by a steep parabolic increase during first minute of electron radiation followed by a slight increase until saturation is reached. The intensity increase of red CL together with the decrease of the blue CL causes a change from initial blue/violet to red/red-brown CL. However, the decrease of blue and the increase of red emission behave independently: in the case of the deformed magmatic quartz from the Eastern Lachlan Fold Belt (see § 10.7) the red emission remains constant whereas the blue one decreases.

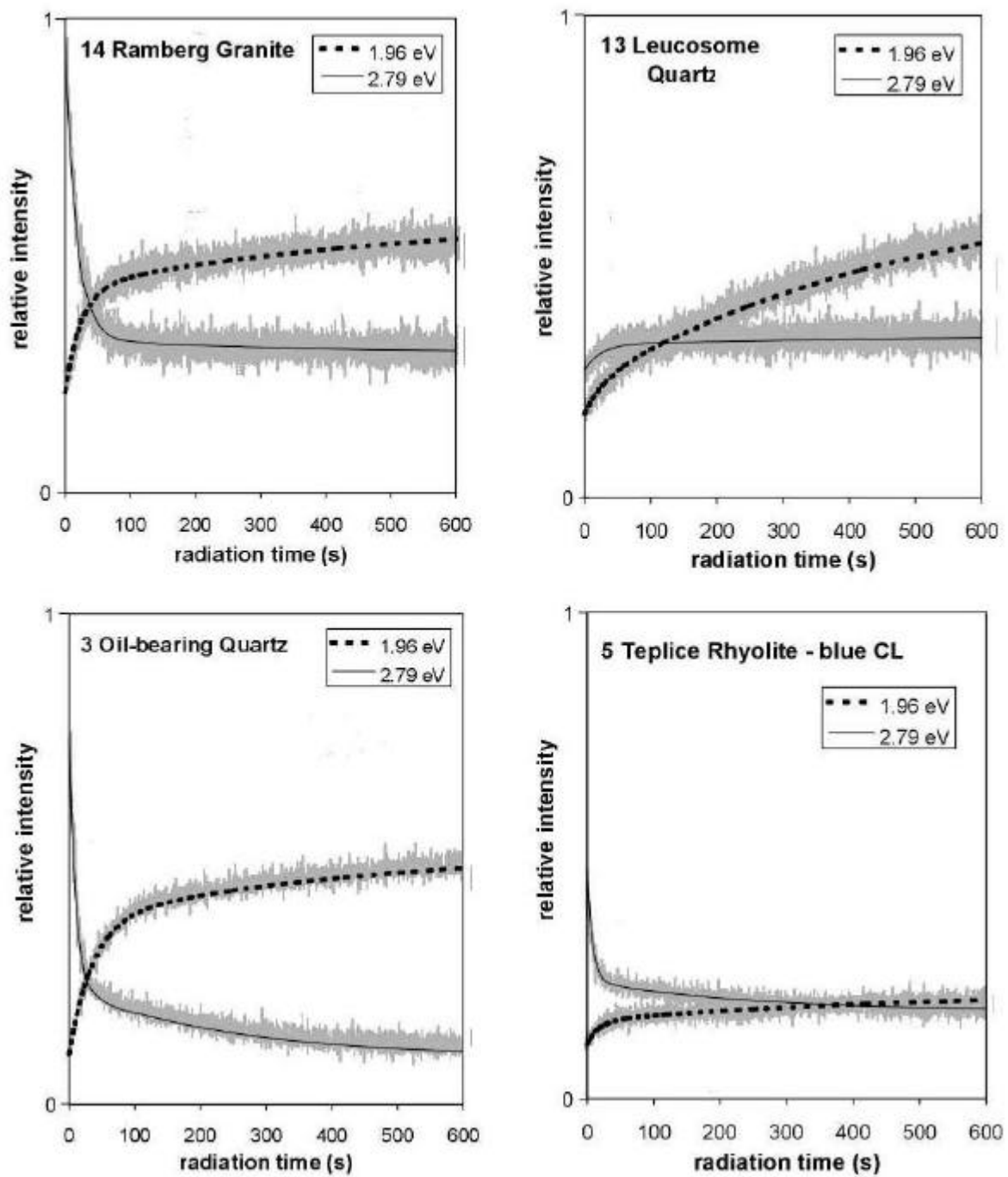


Fig. 5.4 Intensity change of the 1.96 and 2.79 eV emission of some characteristic samples during the radiation time of 10 min recorded with the $f/3.4$ Grating Monochromator using the CL microscope after Zinkernagel (1978) at the University Göttingen (10 keV, 0.25 mA). The experimental curves are grey and the fitted curves are black lines.

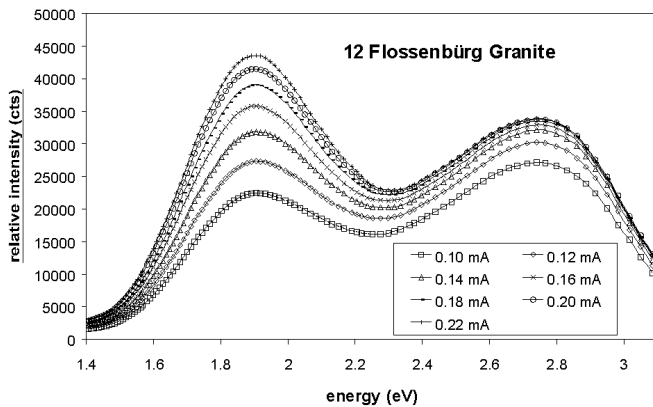


Fig. 5.5 CL spectra of sample 12 after 2 min electron beam exposure using different beam currents.

The effect of temperature

Most of the energy of the electron beam is converted into heat in the sample near the surface (e.g. Remond et al., 1992). After Reimer (1985) the portion of the converted beam energy into heat amounts between $f = 40\text{-}80\%$ ($f =$ degree of effectiveness); Castaing (1951) assumed an average portion of $f = 70\%$ which transforms into heat. The energy $Q = f * U * I * t$ which effects the samples measured here reaches $Q = 2.016 \text{ J}$ using a beam voltage $U = 1.4 \cdot 10^4 \text{ V}$, current $I = 1.8 \cdot 10^{-4} \text{ A}$ and $f = 0.8$.

The heat production at the irradiated spot was calculated by several authors and several types of equipment (Castaing, 1951; Friskney and Haworth, 1967; Dudek, 1970; Reimer, 1985). These calculations, which give an idea about the maximum temperature of the sample, assume, that firstly, the electron beam radius r_b corresponds to the interaction depth of the electron beam r_e in the sample. Secondly, the radius of the sample r_s should be so large that the external surface of the sample remains at ambient temperature ($\Delta T = 0$) meaning that $r_s \gg r_b$. Both conditions are not fulfilled for the used CL microscope: the electron beam radius r_b (2.4 mm) is ca. 500 times larger than the penetration depth of the electrons ($r_e \sim 5 \mu\text{m}$) and the beam radius is so large that the temperature at the external sample surfaces rises considerably. As a consequence the thin section turns hot after some minutes of electron radiation.

The heat developed in a cylindrical interaction volume is controlled by the thermal conductivity of the sample (e.g. $\lambda_{\text{quartz}} = 1.38 \text{ W m}^{-1} \text{ K}^{-1}$ or $\lambda_{\text{granite/rhyolite}} = 2.1 - 2.9 \text{ W m}^{-1} \text{ K}^{-1}$), of the carbon coating ($\lambda_{\text{graphite}} = 169 \text{ W m}^{-1} \text{ K}^{-1}$), of the glass slide of the thin section ($\lambda_{\text{window glass}} = 0.7 \text{ W m}^{-1} \text{ K}^{-1}$), and of the sample holder ($\lambda_{\text{brass}} = 111 \text{ W m}^{-1} \text{ K}^{-1}$). The heat flow problem is very complex due to the different thermal conductivities and thermal transition coefficients, and the heterogeneous heat transmission. Therefore, temperature measurements

were carried out to know the thermal changes of the sample during electron radiation. The temperatures were measured with a sensor on the reverse of demounted thin sections about 250 μm away from the incident beam and by using different beam currents (Fig. 5.6a, b, c). The measurements were corrected by the maximal temperature difference ΔT between the target of the incident electron beam and the sensor:

$$\Delta T = f * U * I * l / \lambda_{\text{sample}} \pi r_b^2 \quad 5.1$$

where l = distance between temperature measure point and incident beam on the thin section surface, λ_{sample} = thermal conductivity of the sample, and πr_b^2 = area of the incident beam.

The temperature difference ΔT amounts 19.7 K by taking the electron beam voltage is $U = 1.4 \cdot 10^4$ V, the current $I = 1.8 \cdot 10^{-4}$ A, $f = 0.8$, the distance $2.44 \cdot 10^4$ m, the beam radius $r_b = 2.4 \cdot 10^3$ m, and $\lambda_{\text{quartz}} = 1.38 \text{ W m}^{-1} \text{ K}^{-1}$.

Figures 5.6a, f, and k show the temperature increase in the target of the electron beam for the samples 1, 4 and 8 during 600 seconds. The temperature increase is an exponential function of the radiation time and shows a linear correlation with the beam current (Fig. 5.7). The plots 5.6b, g, and l show the CL intensity change of the single emission bands during the first electron exposure and the plots 5.6d, i, and n during the second electron exposure of the same sample area after 24 h. The emission band areas and their change were determined from time-resolved spectra recorded with the 100 lines/mm grating of the TRIAX 320. Note, that the spectrum recording with the TRIAX 320 does not allow the determination of the fast intensity change during the first 30 s of electron beam exposure. The intensity change during the second electron exposure is much lower than the change during the first electron exposure indicating that 1) the CL is mainly caused by the electron radiation, 2) the temperature has a low influence of the CL, 3) the electron exposure causes a permanent modification of luminescence centres, and 4) the creation and destruction of luminescence centres take place mainly during the first three minutes of electron radiation. In the plots showing CL intensity change versus temperature (5.6c, e, h, j, m, and o) a clear mathematical correlation does not exist demonstrating a low dependence of CL on the temperature.

However, thermoluminescence bands may have identical positions as the CL bands. Characteristic thermoluminescence bands are the 2.95-2.85 eV, 2.21-2.14 eV and 2.00-1.98 eV bands (e.g. Jani et al., 1983; Yang et al., 1994; Zhang et al., 1994; Rink et al., 1993).

Especially the latter is a frequent and intensive thermoluminescence band of natural quartz (e.g. Rink et al., 1993). The intensity maximum of the 2.21-2.14 eV and 2.00-1.98 eV bands is in the temperature range of the CL measurements. Therefore, the temperature should have a secondary influence on the CL intensity and its change.

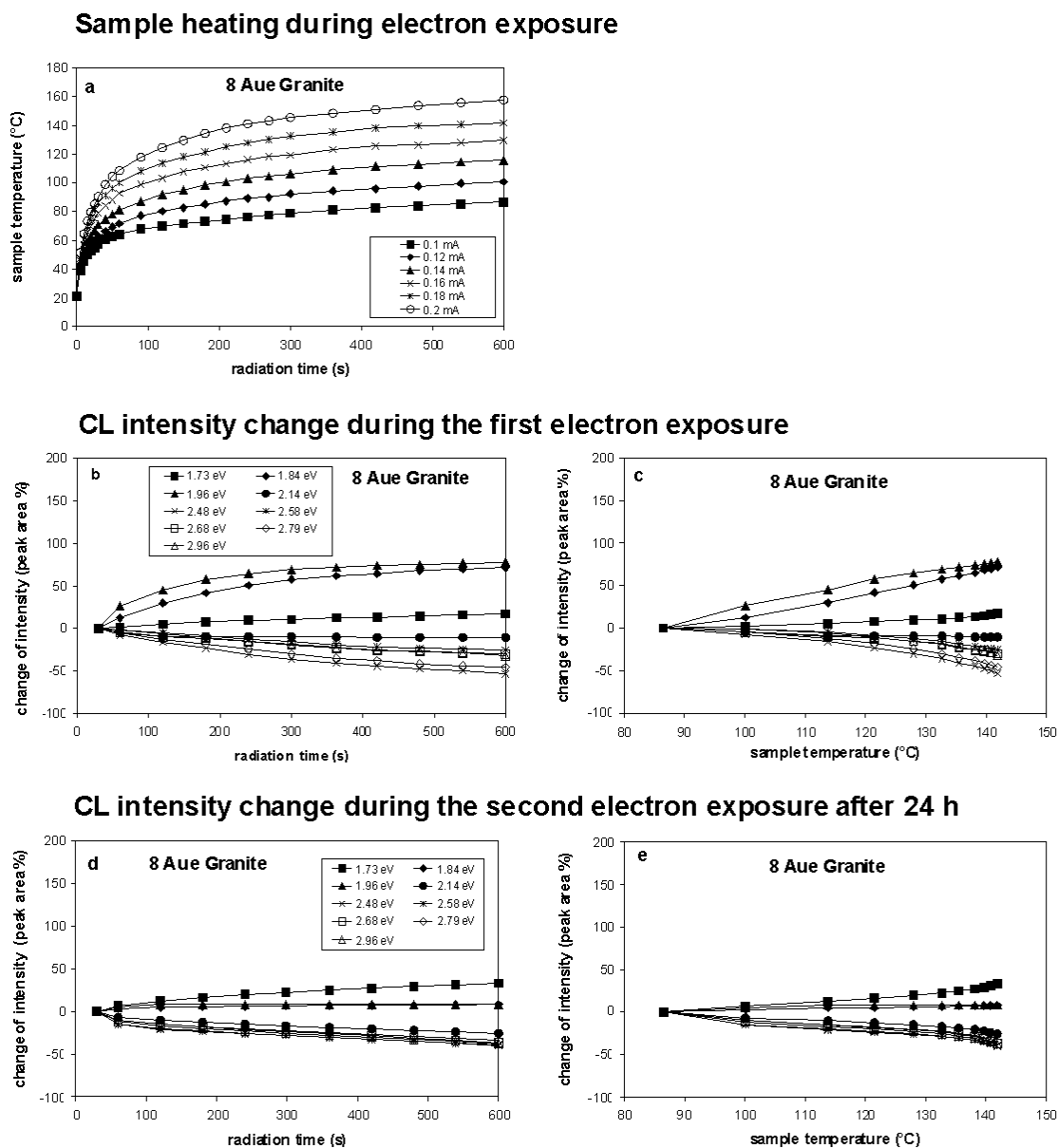
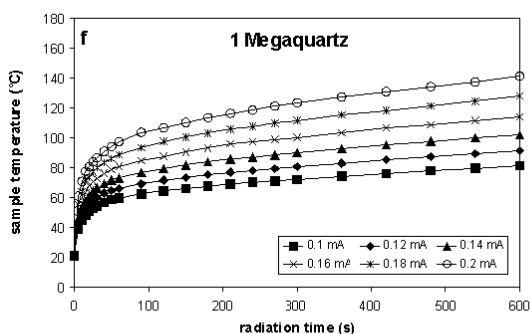
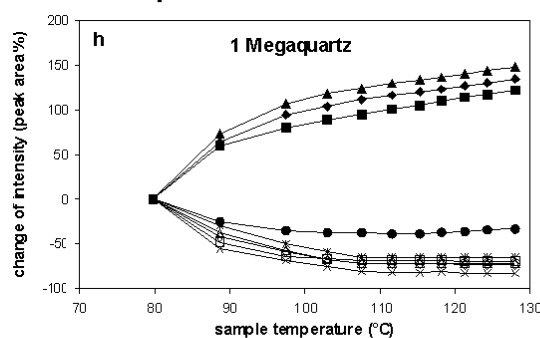
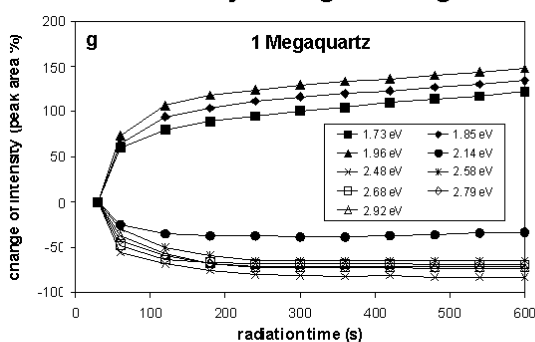


Fig. 5.6a-e Plots of radiation time versus sample temperature and CL intensity change of the sample 8. a - Change of the sample temperature in the target of the electron beam using different beam currents; b – Change of CL band intensities given in percentage emission band area during the first electron exposure of 10 min using the beam current of 0.18 mA; c – Plot of emission band area change versus sample temperature rise; d - Change of CL band intensities given in percentage emission band area during the second electron exposure after 24 h using the beam current of 0.18 mA; e – Plot of emission band area change versus sample temperature rise.

Sample heating during electron exposure



CL intensity change during the first electron exposure



CL intensity change during the second electron exposure after 24 h

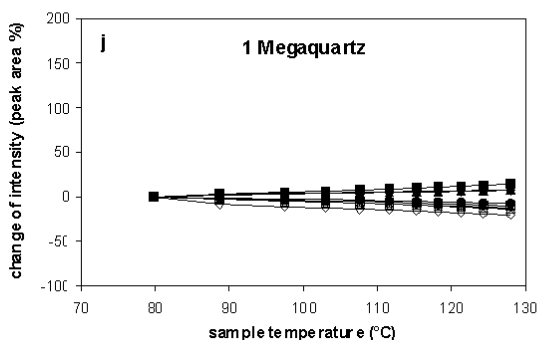
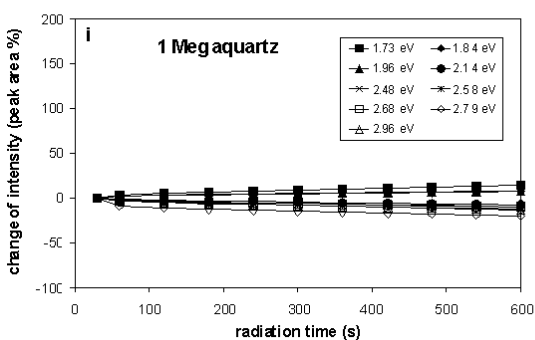


Fig. 5.6f-j Plots of radiation time versus sample temperature and CL intensity change of the sample 1. f - Change of the sample temperature in the target of the electron beam using different beam currents; g – Change of CL band intensities given in percentage emission band area during the first electron exposure of 10 min using the beam current of 0.18 mA; h – Plot of emission band area change versus sample temperature rise; i - Change of CL band intensities given in percentage emission band area during the second electron exposure after 24 h using the beam current of 0.18 mA; j – Plot of emission band area change versus sample temperature rise.

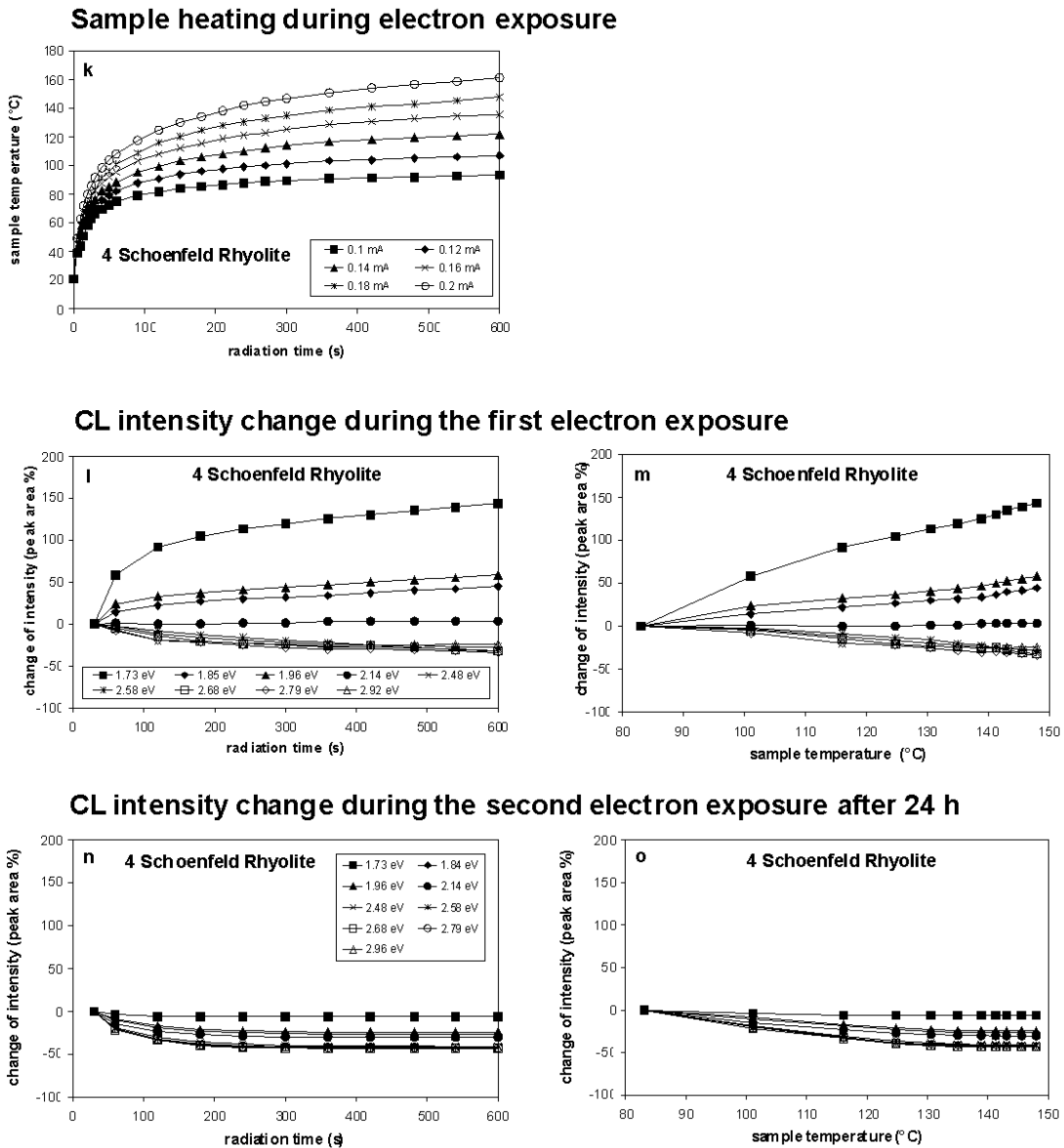


Fig. 5.6k-o Plots of radiation time versus sample temperature and CL intensity change of the sample 4. k - Change of the sample temperature in the target of the electron beam using different beam currents; l – Change of CL band intensities given in percentage emission band area during the first electron exposure of 10 min using the beam current of 0.18 mA; m – Plot of emission band area change versus sample temperature rise; n - Change of CL band intensities given in percentage emission band area during the second electron exposure after 24 h using the beam current of 0.18 mA; o – Plot of emission band area change versus sample temperature rise.

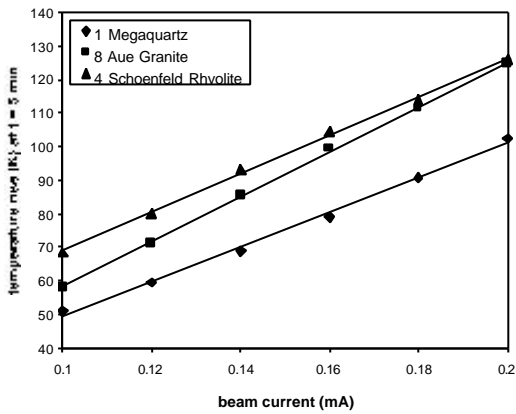


Fig. 5.7 Linear correlation of sample temperature increase in the target of the electron beam versus electron beam current.

CL of thermally treated quartz

The samples 1, 14, and 15 were thermally treated at 300°C and at 600°C for 24 hours. The spectra of the thermally treated quartzes show the following changes in the emission properties (Fig. 5.8, 5.9):

- 1) The treatment generally results in a significant increase of the 1.73 eV band after 300°C heating from room temperature and a slight increase of both the 1.85 and 1.96 eV bands.
- 2) The initial peak observed at 2.48 eV is destroyed at > 600°C.
- 3) All three samples show a more or less intensive shift of the blue peak to higher energy after 600°C heat-treatment, caused by the intensification of the 2.96 eV (sample 1, 14, 15) and of the 2.79 eV bands (sample 14).

The intensification of the 2.96 eV band in all three samples may indicate that this peak is characteristic for quartz formed at high temperature, whereas the 2.48 eV band is typical for hydrothermal quartz.

The effect of sample preparation on the CL of quartz

The method of specimen preparation (polishing) may affect the concentration of defects participating in radiative and non-radiative processes in the surface regions (Ruppert, 1987). The influence of specimen preparation and surface roughness on the CL signal of SiO₂ has been mentioned in Sprunt (1981) and Ruppert (1987). In order to study the effect of sample preparation spectra were recorded for (a) unpolished thin sections using different granularities of carborundum (1 μm and 3 μm) and (b) thin sections polished chemically (OP-S suspension) and compared with (c) the normally used polishing with diamond paste (0.3 μm). As a result we found systematic lower CL intensities for rougher surfaces. However, the peak area ratios of the emission bands and the stability of the CL-activator centres remained unchanged.

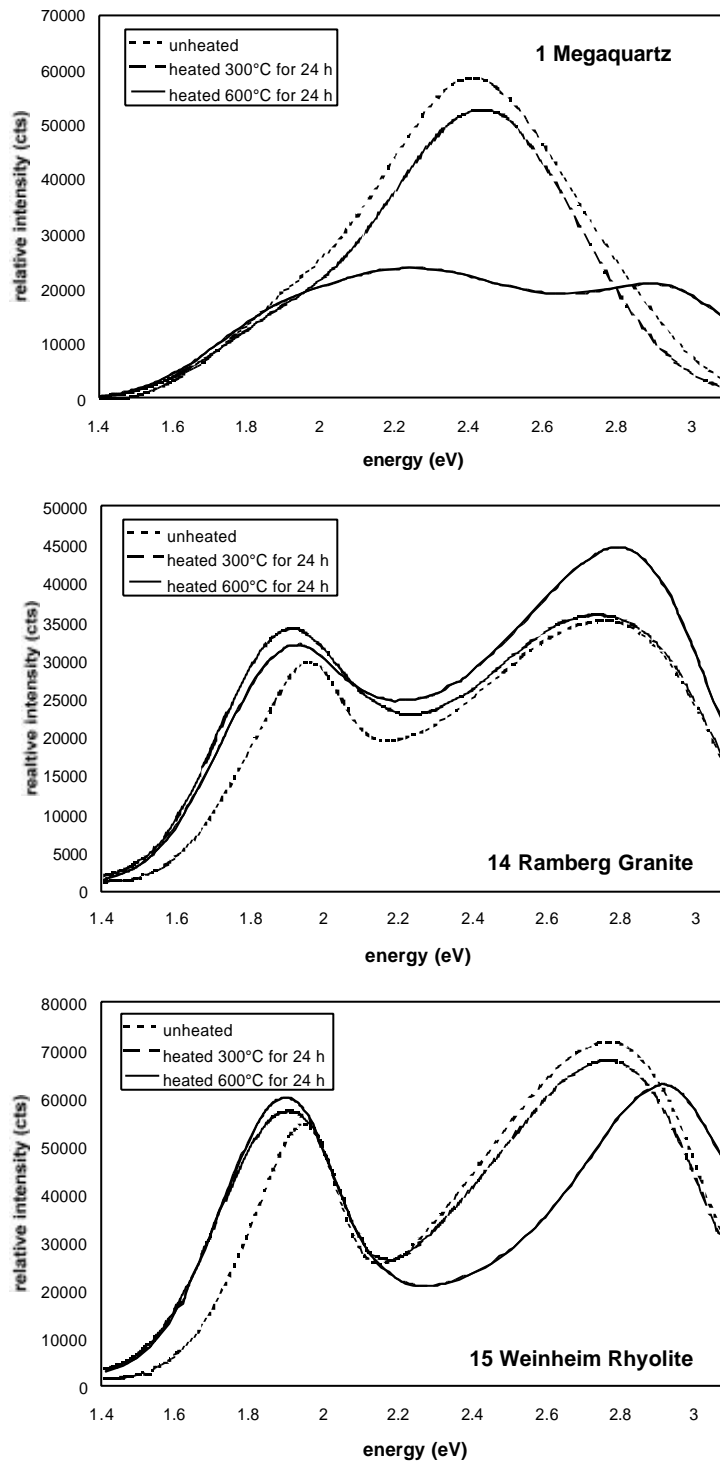


Fig. 5.8 Initial CL spectra (after 30 s electron radiation) of unheated, and at 300 and 600°C for 24 h treated quartzes.

Quantification of CL intensity change during electron radiation

The kinetic of physicochemical reactions in natural systems can be generally described by the kinetic law $c = c_0 \exp(-kt)$, where c = concentration of the component at time t , c_0 = concentration of the component at time $t = 0$, and k = velocity (equilibrium) constant. The equation is the base for the determination of velocity constants (e.g. diffusion coefficients, thermal conductivity). The equation was applied to quantify the decay of the blue intensity and the simultaneously increase of the red emission intensity during electron radiation. The

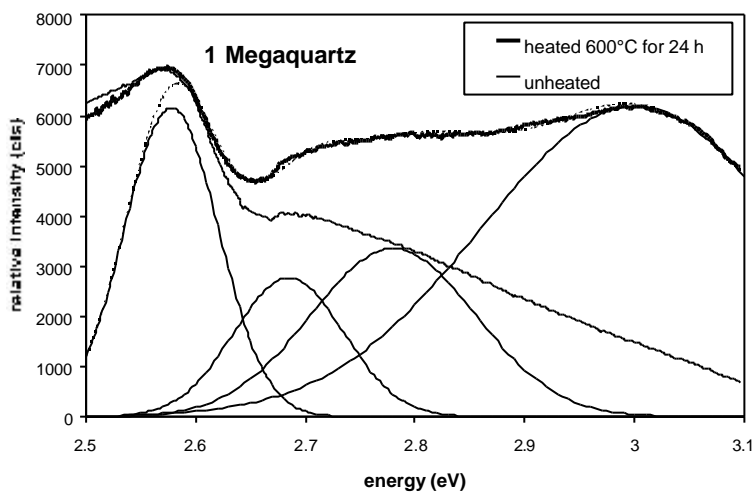


Fig. 5.9 CL spectra of the blue emission range of unheated and heated quartz of the megaquartz. The spectrum of the heated quartz were fitted with Gaussian curves.

latter may be described by the reverse equation of the kinetic law. Application of the equation resulted in an approximate quantification of the intensity change as a function of time. A complicating factor is the composite character of the blue emission intensities, which subdivides into a fast decaying component and a slowly decaying component. Picouet (1999) suggested an equation being the sum of two kinetic law equations:

$$I_b = I_{bs} + I_{b1} * \exp(-t/k_{b1}) + I_{b2} * \exp(-t/k_{b2}) \quad 5.2$$

where I_b = intensity of blue CL at the radiation time t ; I_{bs} = intensity of stable blue CL; I_{b1} = intensity of the slow decreasing CL component at $t = 0$; k_{b1} = velocity constant of the slow decreasing CL component; I_{b2} = intensity of the fast decreasing CL component at $t = 0$; k_{b2} = velocity constant of the fast decreasing CL component; t = radiation time.

This equation fits very well with the measured time-dependent intensity change (Fig. 5.4). The increase of red emission between 1.75 to 2.2 eV may be described by the following equation which is the reverse function of equation 5.2:

$$I_r = I_{rs} - I_{r1} * \exp(-t/k_{r1}) - I_{r2} * \exp(-t/k_{r2}) \quad 5.3$$

where I_r = intensity of red CL at the radiation time t ; I_{rs} = intensity of red CL for $t \rightarrow \infty$; I_{r1} = intensity of the slow increasing CL component for $t \rightarrow \infty$; k_{r1} = velocity constant of the slow increasing CL component; I_{r2} = intensity of the fast increasing CL component for $t \rightarrow \infty$; k_{r2} = velocity constant of the fast increasing CL component; t = radiation time.

The red CL emission is composed of a fast increasing component during the first minute of electron radiation and a slowly increasing component. Figure 5.4 shows the intensity change of the 1.96 and 2.79 eV emissions during 10 min electron beam exposure. The curves were fitted using the equations 5.3 and 5.2, respectively. The samples 9 and 13 show a reverse time-dependent behaviour of the CL signal.

The fitted parameters of the radiation-time-dependent intensities at 1.96 and 2.79 eV are given in Appendix B. The velocity constants k_{r1} , k_{r2} , k_{b1} , and k_{b2} are similar for all samples: namely 502 ± 16 , 24 ± 11 , 252 ± 9 , and 14 ± 5 , respectively. The lower the velocity constant the faster the decay and formation of CL activator centres. That implies that the decay of the centres causing blue CL is about 2 times faster than the formation of the activator centres causing red CL.

The emission intensities I represent the concentration of luminescence centres in the interaction volume of the electron beam. The parameters I_{rs} , I_{r1} , I_{r2} , I_{bs} , I_{b1} , and I_{b2} are intensity portions of the respective emission, whereby I_{r1} , I_{r2} , I_{b1} , and I_{b2} are intensity portions which compose the changeable CL. These parameters are proportional to the concentration of luminescence centres. The rhyolitic quartz has a low I_{r2} and I_{b2} indicating a more stable CL (Fig. 5.10). The granitic and hydrothermal quartz exhibit a wide scattering of intensity parameters which corresponds to unstable and highly variable CL. Particularly the high I_{r1} and I_{r2} of granitic quartz demonstrates the high instability of the red CL. Generally, we conclude that the higher the quartz formation temperature and pressure the lower is the concentration of unstable luminescence centres.

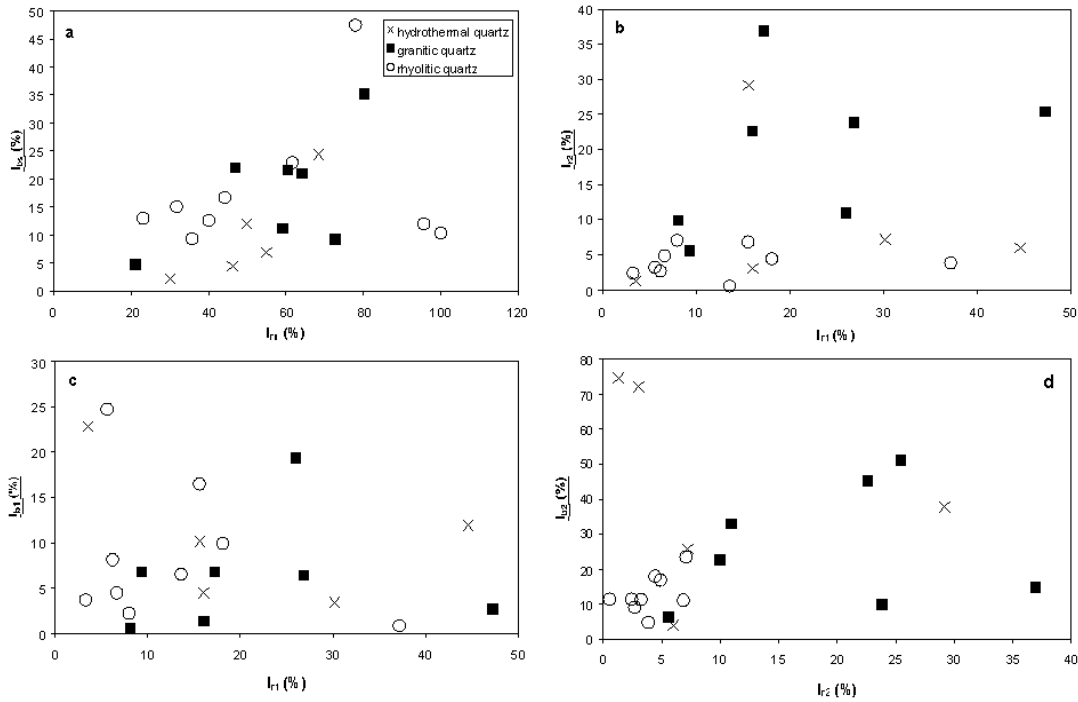


Fig. 5.10 Plots of fitted parameters I_{rs} , I_{r1} , I_{r2} , I_{bs} , I_{b1} , and I_{b2} of the equation 5.2 describing the decrease of 2.79 eV (blue) CL emission and of the equation 5.3 describing the increase of 1.96 eV (red) CL emission during electron exposure. a – Plot of the stable blue CL intensity I_{bs} versus the intensity of red CL I_{rs} for radiation time $t \geq 8$ showing that samples with high intensity of blue CL exhibit also a high intensity of red CL; b – Plot of the fast increasing red CL component I_2 versus the slow increasing red CL component I_1 . There is no correlation between the two components; c – Plot of the slow changing CL components of the blue CL I_{b1} and red CL I_{r1} ; d – Plot of the fast changing CL components of the blue CL I_{b2} and red CL I_{r2} . Note, that rhyolitic quartz has a low no fast changing CL.

5.3 Comparison of CL spectral and trace element analysis

EPMA, LA-ICPMS, and SIMS analysis

In order to measure trace element distributions complementary to the CL colours and spectra, quartz has been analysed by LA-ICPMS and EPMA. SIMS analysis were carried out on a selection of samples (megaquartz; Aue Granite; and Weinheim Rhyolite). The analysis were performed by EPMA for Al, Ti, Fe, Mn, by LA-ICPMS for Al, Ti, Li, Ge, Fe, and by SIMS for Li, Na, K, Al, Ti, and Fe. Trace element profiles traversing different growth and alteration zones were measured (Fig. 5.11a, b, c; see also chapter 7, 8, 9, 10).

Quartz formed at high temperatures ($\approx 600^\circ\text{C}$) such as rhyolitic quartz shows an average high Ti concentration up to 130 ppm (Fig. 5.11, 5.12a, 5.13). The growth zones are mainly characterised by variations in Ti. The Ti concentration correlates exponentially with the

intensity of the 2.96 eV emission (Fig. 5.14). The content of Ti in hydrothermal quartz is always below 40 ppm. Magmatic quartzes show a maximal Al content of 200 ppm, whereas hydrothermal quartz may contain much more Al e.g. up to 5000 ppm in vein quartz. The vein quartz shows unstable CL at 2.79 eV of very high intensity, suggesting that this luminescence is associated with Al defect structures. Large variations in Al between adjacent growth zones of hydrothermal quartz have been found. Furthermore, Al concentration differs for the rhombohedral faces z to r of the zoned hydrothermal α -quartz (Fig. 5.11b). The sum of Li, Na, K, and Fe shows a good correlation with Al (Fig. 5.13). This confirms the general assumption that Li, Na, K, and Fe act as interstitial charge compensators for substitutional Al (e.g., Dennen, 1965; Smith and Steele, 1984).

Hydrothermal quartz exhibits elevated Ge concentrations, between 3-16 ppm (Fig. 5.12.). The LA-ICPMS analysis shows a strong enrichment in Mn, Fe, Ge, and Cr. The enrichment of all these element may caused by micro inclusions situated in the measured sample volume.

The quartz of the Erzgebirge Batholite (Eibenstock and Aue Granite) exhibits high Fe and Mn. The CL spectra of these samples show a characteristic stable 2.15 eV band which is possibly associated with Mn.

The average Fe concentration increases with the quartz formation temperature. Therefore, the Fe content of quartz is a good criteria to distinguish quartz of different genesis. Pott and McNicol (1971) and Kempe et al. (1999) found that high Fe^{3+} causes the 1.73 eV CL emission. However, in our samples we found no correlation between the Fe concentration and the 1.73 eV band intensity. The lack of correlation may be explained by the fact that Fe occurs as divalent and trivalent ions. It was frequently observed that Fe increases towards the grain boundary indicating a high diffusion rate of Fe in the quartz lattice (Fig. 5.11a, see also § 10.7). The preferred diffusing ion is likely to be the Fe^{2+} due to its smaller ion radius. Weak or non-luminescent secondary quartz in healed microcracks, or formed around fluid inclusions is typically depleted in all trace elements (Fig. 5.11c).

FT-IR spectroscopy

Spectra of quartz containing structural water in the form of H^+ , OH^- , and H_2O show characteristic absorption bands between $3000\text{-}3700\text{ cm}^{-1}$. The absorption bands are caused by stretching vibrations of H-related chemical bonds excited by electromagnetic UV radiation. Generally two classes of absorption occur in the IR spectra: sharp absorption bands (low half width) at 3305 , 3365 , 3425 , and 3470 cm^{-1} and broad absorption bands (high half-width) at 3440 cm^{-1} , 3220 cm^{-1} and 3110 cm^{-1} (Brunner, 1961; Kats, 1962; Aines and Rossman, 1984).

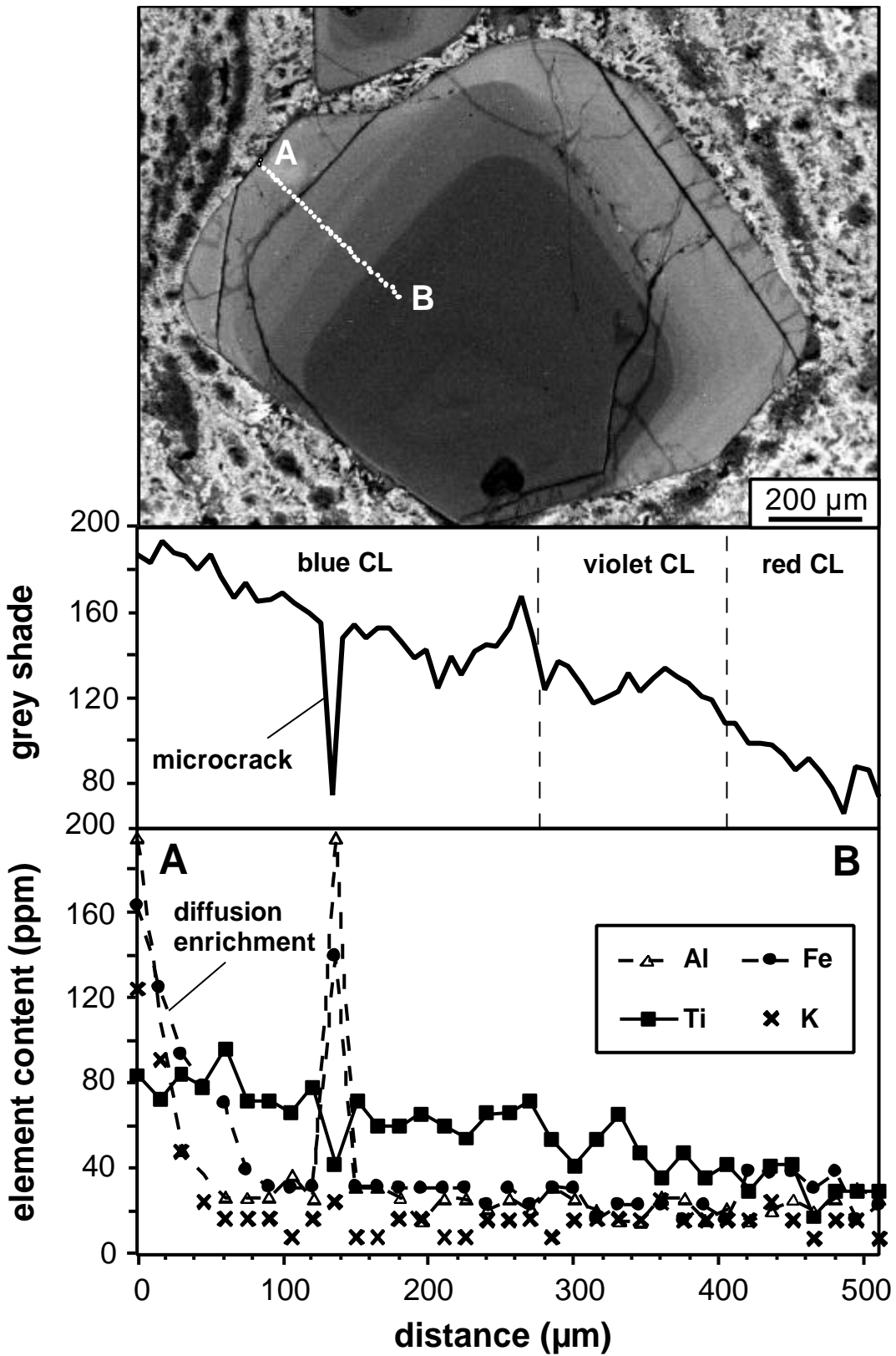


Fig. 5.11a Trace element profile of a quartz phenocryst of the Wachtelberg Rhyolite (sample 12) determined by EPMA and compared with relative CL intensity (grey shade).

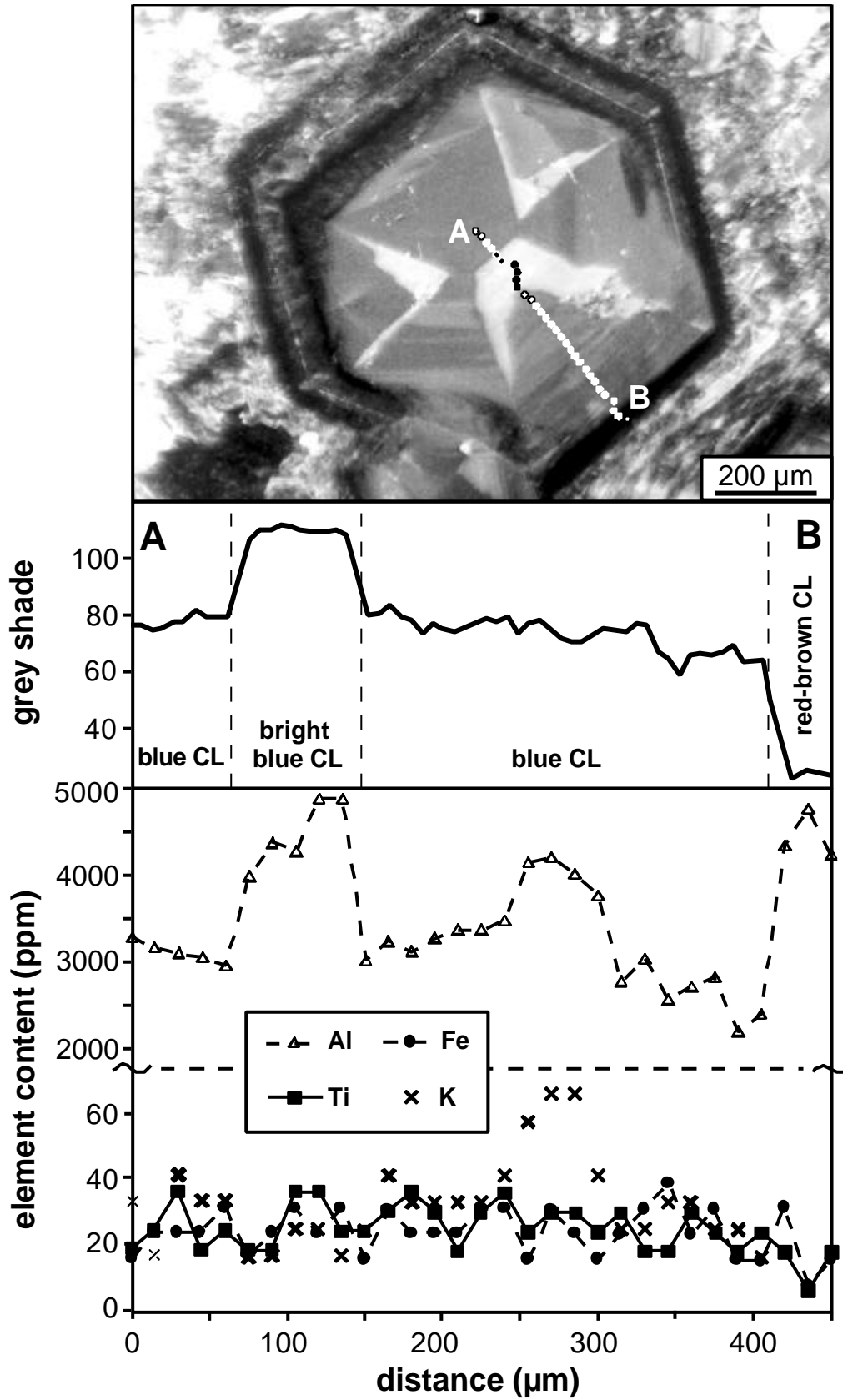


Fig. 5.11b Trace element profile of a Berg crystal (vein quartz; sample 9) determined by EPMA compared with relative CL intensity (grey shade).

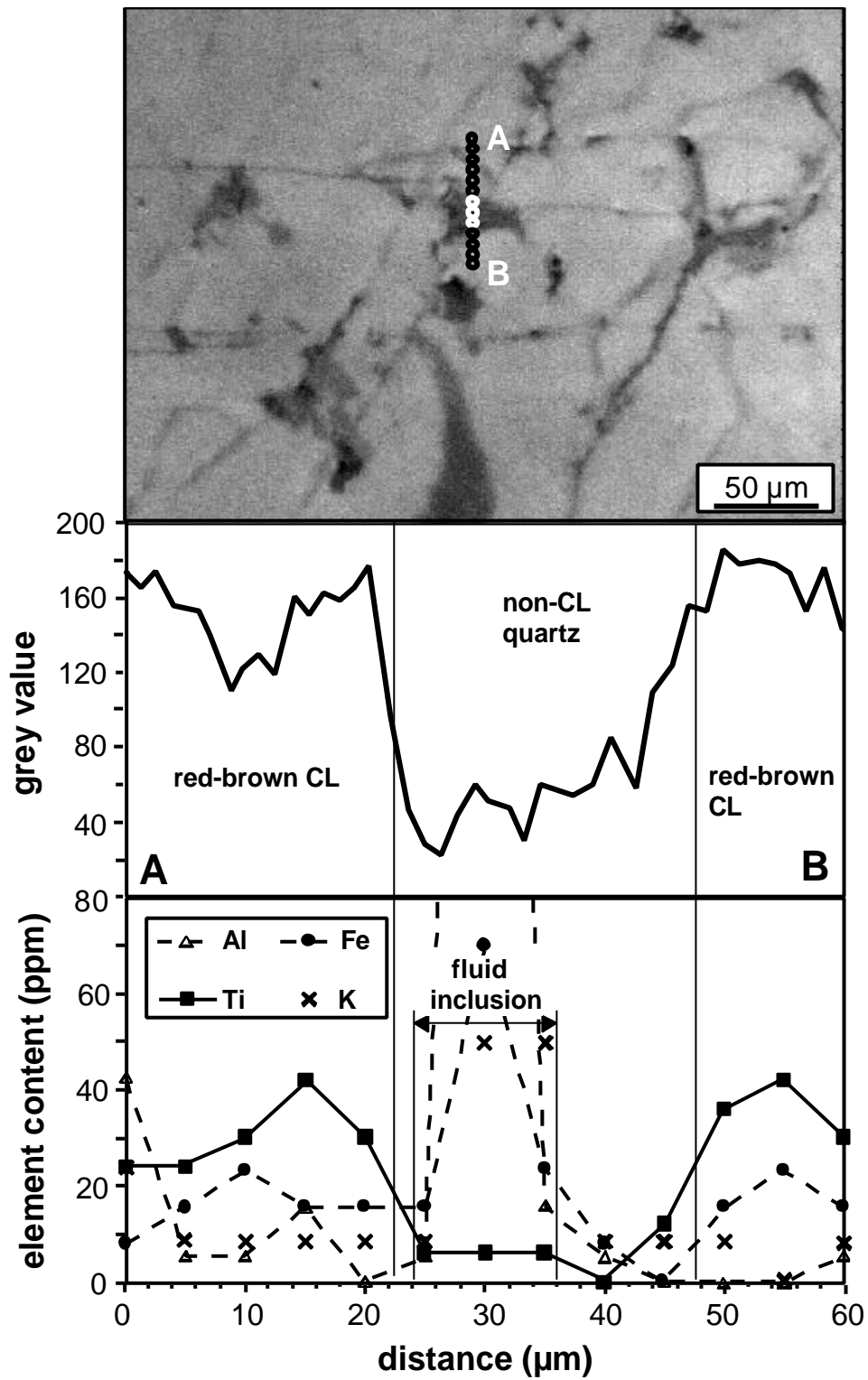


Fig. 5.11c Trace element profile of a quartz crystal of the Flossenbürg Granite (sample 12) determined by EPMA compared with relative CL intensity (grey shade). The microprofile cuts a weak luminescent secondary quartz (dark grey) around a fluid inclusion. The secondary quartz is depleted in trace elements.

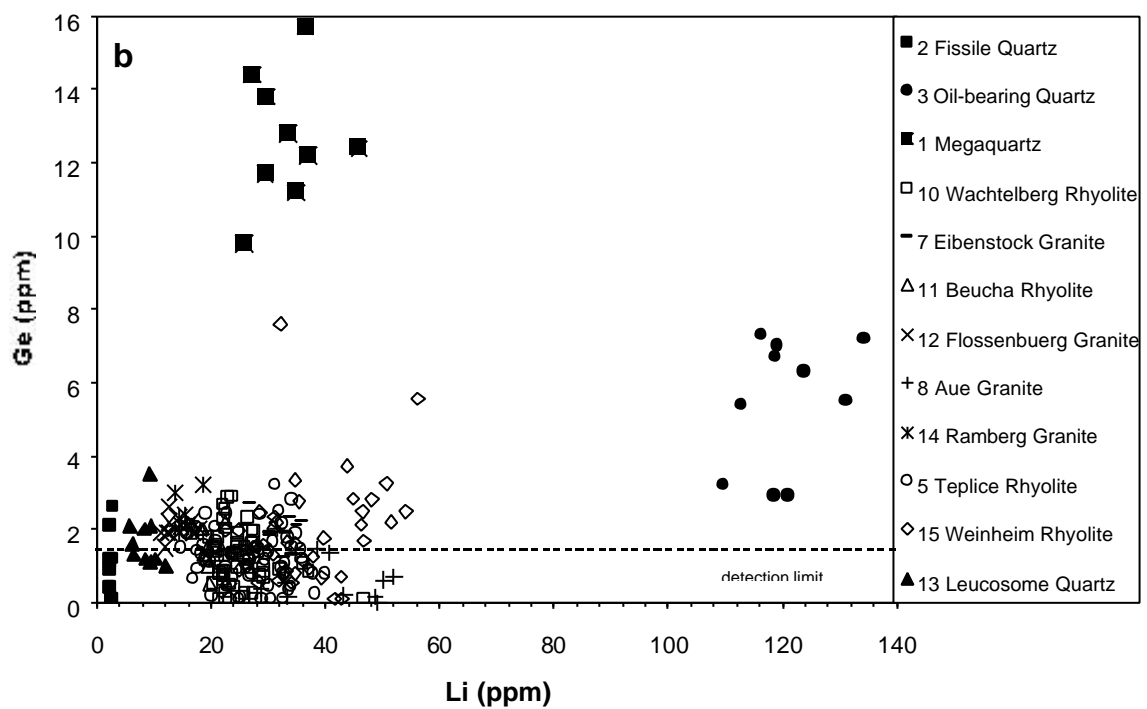
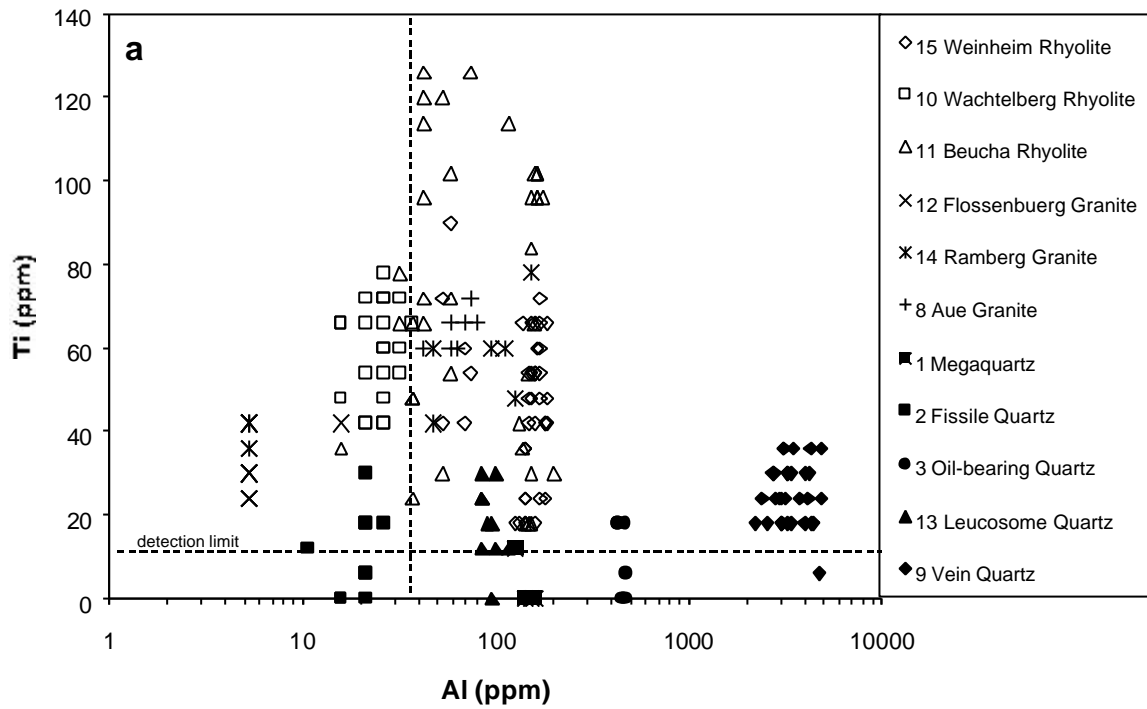


Fig. 5.12a, b Plots of trace element concentration of quartz. a – Al vs Ti determined by EPMA. b – Li vs. Ge determined by LA-ICPMS.

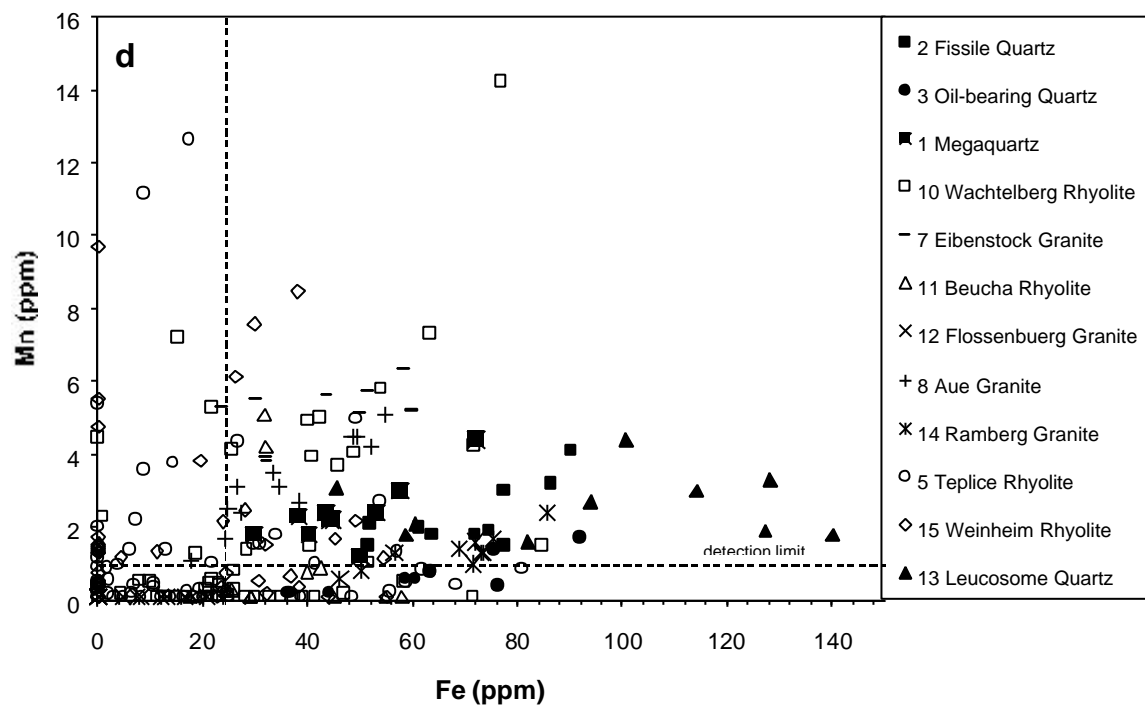
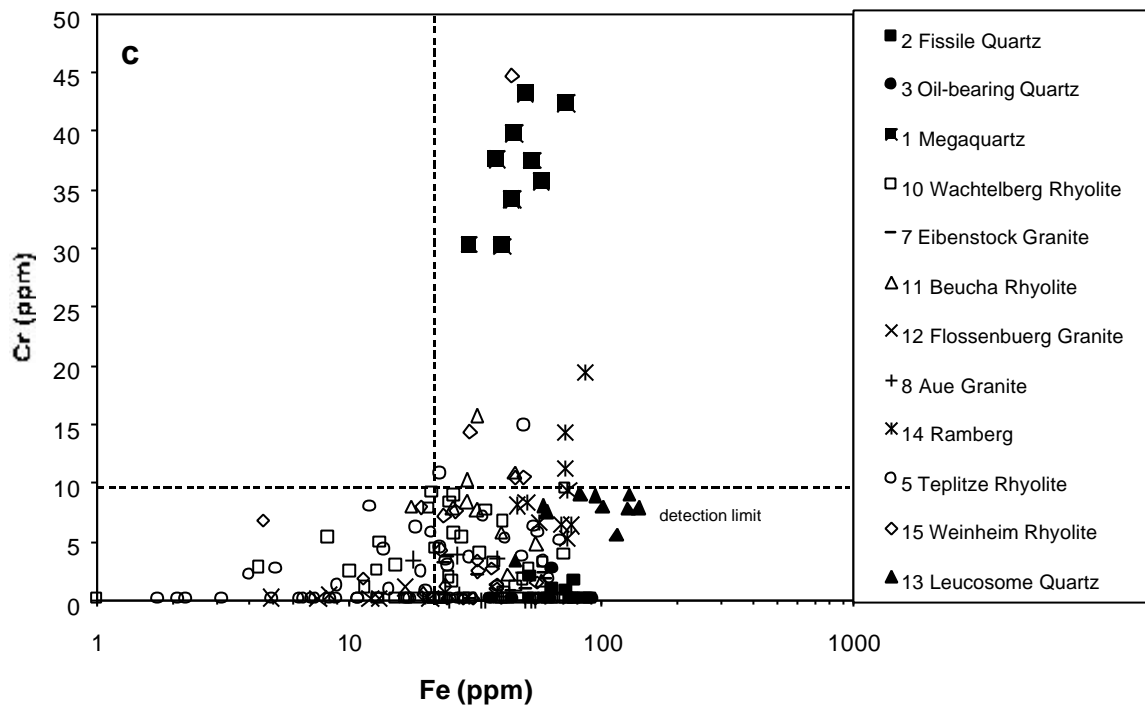


Fig. 5.12c, d Plots of trace element concentration of quartz. c – Fe vs. Cr determined by LA-ICPMS. d – Fe vs. Mn determined by LA-ICPMS.

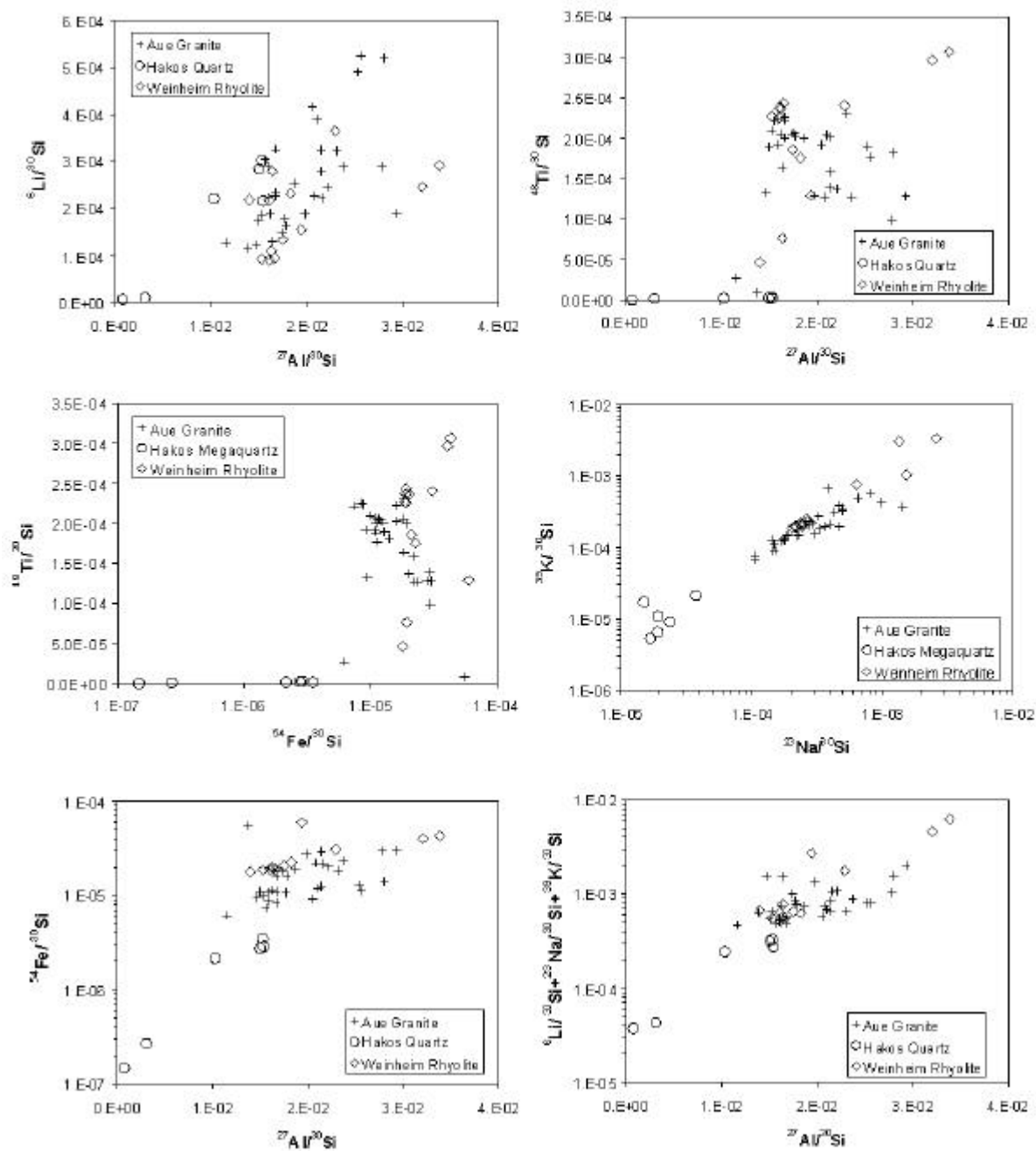


Fig. 5.13 Variation diagrams of relative concentrations ($X/^{30}\text{Si}$, where $X = ^6\text{Li}, ^{23}\text{Na}, ^{27}\text{Al}, ^{39}\text{K}, ^{54}\text{Fe}, ^{48}\text{Ti}$) of trace elements determined by SIMS.

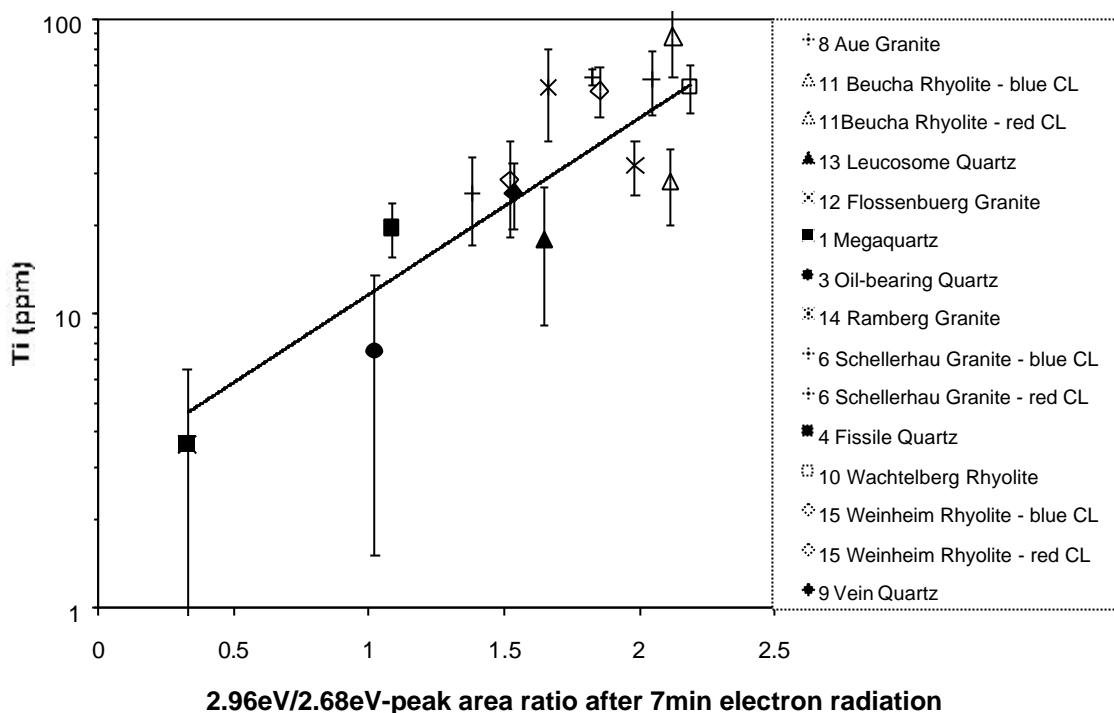


Fig. 5.14 Correlation of average Ti concentration with the peak area of the 2.96 eV emission.

A band with low half-width indicates a well definite bond, which is not effected by other bond vibrations. Sharp bands are developed if H-related bonds are isolated and have a sufficient large distance to similar bonds. The sharp peaks at 3365 and 3305 cm^{-1} , attributed to proton-compensated aluminium defects, are the most significant peaks in the hydroxyl band. The Al-H-defects ($[\text{AlO}_4/\text{H}^+]^0$ centres) are very stable up to temperatures of 1000°C (Kats, 1962; Schneider, 1993). The peak at 3474 cm^{-1} was assigned by Kats (1962) to proton-compensated aluminium defect perturbed by Li^+ (marked as “Li-H” in Fig. 5.15). This absorption band was absent after >450°C quartz heating (Schneider, 1993).

Molecular water exists in the quartz lattice as micropores and fluid inclusions as well as structural bound water. The vibrations of the water molecules affect one another which results in broader absorbed wavelength ranges. At room temperature the broad absorption bands at 3440 cm^{-1} are caused by the asymmetrical stretching vibrations and the 3220 cm^{-1} and 3110 cm^{-1} bands by the symmetrical stretching vibrations of molecular water (Aines and Rossman, 1984). To distinguish fluid water from crystallographic bounded water, spectra are obtained at cryogenic temperatures between -190 and -194°C. The change of the state from the water to ice during sample cooling results in the quenching of the asymmetrical vibrations (3440 cm^{-1}) in the crystal lattice and the rise of the symmetric vibrations (3220 cm^{-1} and 3110 cm^{-1}).

Structural bounded OH-groups can not change into solid H₂O (ice). The change into the solid state of water presupposed, that the water molecules are able to built hydrogen bonds which can be problematic if the number of water molecules is small (Aines and Rossman, 1984).

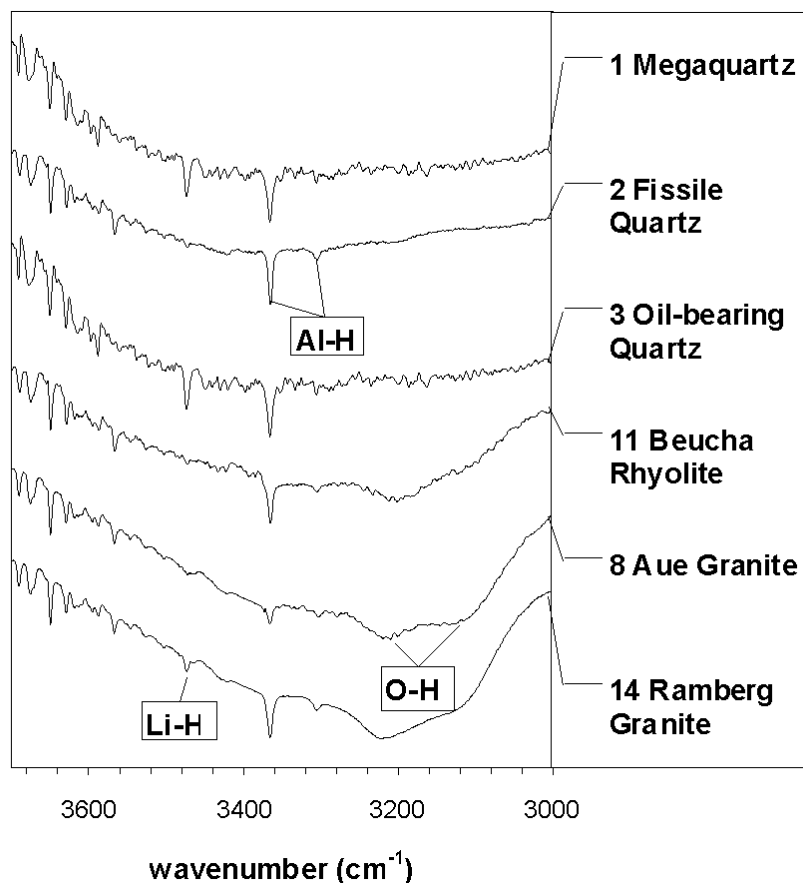


Fig. 5.15 Representative IR-absorption spectra of different quartz types measured at ~190°C.

The IR absorption spectra of one sample recorded along profiles are very homogeneous. There is no variation of Al-H- and Li-H-defect concentrations found in different growth zones of the rhyolitic phenocrysts (sample 11). The lack of correlation between spectroscopic data and growth zoning in the quartz phenocrysts shows that neither proton-compensated Al nor Li-defect concentrations control the luminescence contrast of this growth zones. Similar observations were made by Liebetrau (1991) and Schneider (1993) in rhyolitic quartz phenocrysts.

The associated 3365 and 3305 cm⁻¹ absorption bands are found in all spectra and are indicative for proton-compensated Al defects (Fig. 5.15). The bands are most intense in

hydrothermal quartz (samples 1, 2, 3). However, the relative absorption intensities (integrated peak areas) do not correlate with the Al concentrations.

Hydrothermal quartz (Fig. 5.12a) shows a high intensity of the Li-associated 3474 cm^{-1} band. This quartz is characterised by a high intensity of the 2.48 eV CL emission (Fig. 5.1, 5.2). The 3474 cm^{-1} absorption band is thermally unstable at temperatures $\approx 450^\circ\text{C}$ (Schneider, 1993). The characteristics of the 2.48 eV CL band and of the Li-associated 3474 cm^{-1} absorption band suggest an association with Li-defects.

Granitic (sample 8, 14) and rhyolitic quartz (sample 11) is characterised by high absorption bands at ~ 3110 and 3220 cm^{-1} . Granitic quartz shows a high number of small fluid inclusions mostly $<1\text{ }\mu\text{m}$ in the measured area. The quartz samples of the Beucha Rhyolite do not contain fluid inclusions. However, the 3110 and 3220 cm^{-1} absorption bands indicate the presence of molecular water in lattice.

Paramagnetic defect centres

The paramagnetic E^{\cdot} , O_2^{3-} , $[\text{AlO}_4]^0$, $[\text{TiO}_4/\text{Li}^+]^0$, and $[\text{TiO}_4/\text{H}^+]^0$ centres were studied at the University Marburg by T. Scherer using EPR spectroscopy. The relative intensities of the defect centre concentration are listed in Table 5.3. The concentration of the paramagnetic defect centres in quartz depends on the number of precursor defects, the post-crystallisation dose rate and the duration of the natural radiation. The centres decay under UV radiation and are stable at temperatures $<100^\circ\text{C}$. The closing temperature varies between 55 and 82°C for the $[\text{TiO}_4/\text{Li}^+]^0$ centre and between 49 and 64°C for the $[\text{AlO}_4]^0$ centre (e.g. Grün et al., 2000). The relative intensities of $[\text{AlO}_4]^0$ as well as $[\text{TiO}_4/\text{Li}^+]^0$ centres systematically increase for hydrothermal quartz (samples 1, 2, 3, 13) granitic quartz (samples 6, 8, 12, 14) and rhyolitic quartz (samples 10, 11, 15), respectively (Fig. 5.16a). The Ti concentration correlates with the absorption intensity of the $[\text{TiO}_4/\text{Li}^+]^0$ centre but there is no correlation between the Al concentration and the intensity of the $[\text{AlO}_4]^0$ centres. High concentrations of $[\text{TiO}_4/\text{Li}^+]^0$ centres are typical for magmatic quartz (Rakov et al., 1991; Agel, 1992; Plötze, 1995). The lack of correlation between Al concentration and paramagnetic Al-defects may be due to the fact that paramagnetic Al-centres are less stable. The $[\text{TiO}_4/\text{H}^+]^0$ centres could not be detected. They are typical for metamorphic quartz (Rakov et al., 1991; Agel, 1992; Plötze, 1995).

The relative concentration of $[\text{AlO}_4]^0$ centres in magmatic quartz shows a positive correlation with the slow decaying component (I_{b1} ; see § 5.2) of the blue 2.79 eV CL emission (Fig. 5.17a). The abundance of O_2^{3-} centres exhibits an association with the fast increasing

component (I_{r2} ; see § 5.2) of the red 1.96 eV CL emission (Fig. 5.17b). This corresponds with the general observation, that the 1.96 eV emission is associated with non-bridging oxygen hole centres (NBOHC) with OH-precursor (e.g. Kalceff and Phillips, 1995). The paramagnetic O_2^{3-} centre is a kind of NBOHC (see chapter 2). Silanol groups ($=Si-O-H$) are favourable precursors O_2^{3-} centres in quartz. Upon irradiation H^+ diffuses away and NBOHC are formed (e.g. O^- , O_2^{3-}) resulting in an increase of the 1.96 eV CL emission.

Table 5.3 List of relative intensity of paramagnetic defect centres determined by EPR spectroscopy.

No	Sample name	Quartz type	ESR intensity of paramagnetic defect centres (a.u.)			
			$[AlO_4]^0$	$[TiO_4/Li^+]^0$	O_2^{3-}	E'-centre
1	megaquartz	hydrothermal	0.38	0	0.422	0.068
2	fissile quartz	hydrothermal	0	0	0	0
3	oil-bearing quartz	hydrothermal	0.691	0	0.68	0.68
4	Schoenfeld Rhyolite	rhyolitic	n.d.*	n.d.*	n.d.*	n.d.*
5	Teplice Rhyolite (TPR2)	rhyolitic	12.77	0.221	1.128	0.719
6	Schellerhau Granite	granitic	11.689	0.948	0.906	0.329
7	Eibenstock Granite	granitic	3.124	0.516	1.57	0.287
8	Aue Granite	granitic	5.003	0.95	1.177	0.171
9	vein quartz	hydrothermal	n.d.*	n.d.*	n.d.*	n.d.*
10	Wachtelberg Rhyolite	rhyolitic	27.94	1.27	0.749	0.439
11	Beucha Rhyolite	rhyolitic	14.03	1.499	0.302	0.801
12	Flossenbuerg Granite	granitic	8.933	0.414	0.604/ 0.682	0.141
13	leucosome quartz	pegmatoid	0.244	0.159	0	0
14	Ramberg Granite	granitic	5.195	0.445	1.365	0.058
15	Weinheim Rhyolite	rhyolitic	11.87	1.505	0.435	0.111

n.d.* - not determined

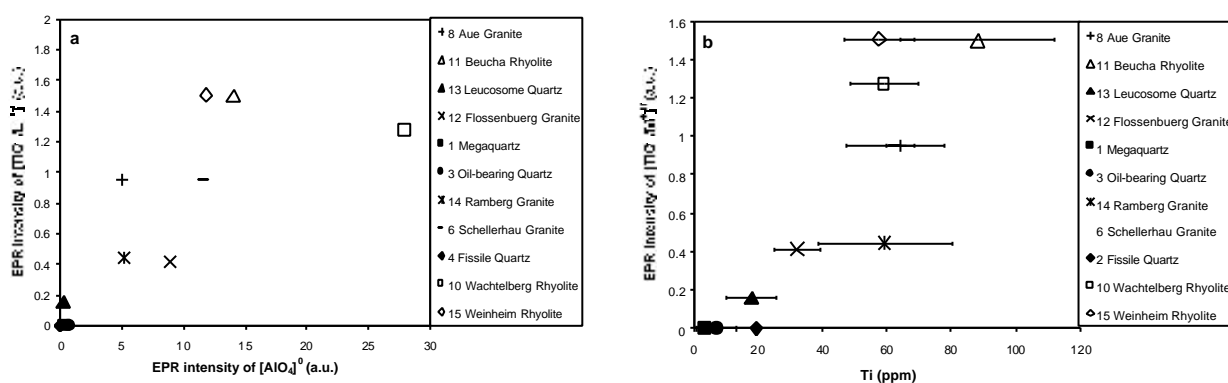


Fig. 5.16 Results of EPR spectroscopy. a - EPR intensity of the $[AlO_4]^0$ vs the $[TiO_4/Li^+]^0$ centre of different quartz types. High temperature formed quartzes exhibit the highest concentrations. b - Ti concentration vs EPR intensity of the $[TiO_4/Li^+]^0$ centre. Quartzes with high Ti content show a high the $[TiO_4/Li^+]^0$ defect concentration.

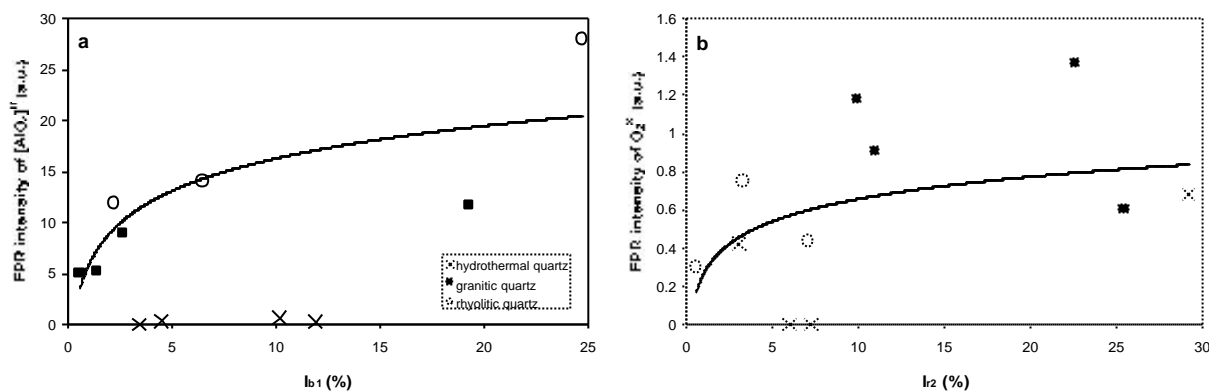


Fig. 5.17 Comparison of intensities of paramagnetic defects and intensity parameters of the 1.96 eV and 2.79 eV CL emission. a - EPR intensity of the $[AlO_4]^0$ vs the slow decaying component (I_{b1} ; see § 5.2) of the blue 2.79 eV CL emission. The regression line was calculated for the magmatic quartzes. b - EPR intensity of the O_2^{3-} vs the fast increasing component (I_{z2} ; see § 5.2) of the red 1.96 eV CL emission.

Overview of CL emission lines of quartz

1.73 ± 0.1 eV emission

The dominance of the 1.73 eV band may be responsible for reddish luminescence (instead of the frequent red-brown CL). The CL typically increases during radiation time. Thermal treatment of some samples results in a significant increase of the intensity at 300°C for 24 h (Fig. 5.8) indicating that the emission can be excited thermally.

The 1.73 eV emission line is caused by the substitutional incorporation of Fe^{3+} into the quartz lattice (Pott and McNicol, 1971; Gorobets et al., 1989; Kempe et al., 1999). Fe^{3+} is an important CL activator even when it is present in low concentration (<50 ppm) in the crystal lattice (Marshall, 1988). The average Fe concentration increases with the quartz formation temperature (Fig. 5.13). It was frequently observed that Fe increases at the grain boundary of magmatic quartz which indicates a high diffusion rate of Fe in the quartz lattice at high temperatures (Fig. 5.11a). However, a correlation between the Fe concentration and the 1.73 eV emission intensity could not be proofed. There are several 3 explanations: 1) the Fe concentration lies mostly near the detection limit and inaccuracies do not allow any correlation, 2) Fe occurs also as a divalent ion which enters interstitial positions (e.g. Lehmann, 1975), 3) the Fe^{3+} can be incorporated into quartz structure also in interstitial positions (e.g. Scala and Hutton, 1976).

1.85 ± 0.1 and 1.96 ± 0.2 eV emission

The dominant peak of the red emission range of most quartzes is given by the 1.96 eV band. The weak 1.85 eV emission is associated with the 1.96 eV band as both emissions show a constant peak area ratio ($1.96 : 1.84 \text{ eV} = 1 : 0.51 \pm 0.17$). The emissions are characterised by an parabolic increase during electron radiation. The only exception is the vein quartz (sample 9), for which no red CL emission was observed. The intensity increase is generally steeper in quartz formed at low temperature and flatter in quartzes in rhyolite, where these lines show already a high initial intensity. The 1.96 and 1.85 eV bands of the rhyolitic quartzes are often very distinct as the neighbouring 1.73 and 2.15 eV emissions normally have low intensities. The emission is slightly influenced by the sample warming during electron radiation (Fig. 5.6). Furthermore the heating at 300°C for 24 h results in an intensity increase of both 1.85 and 1.96 eV bands (Fig. 5.8). This is in agreement with Rink et al. (1993) who observed that radiated rhyolitic quartz phenocrysts show an intense red thermoluminescence band centred at 1.96-2.0.

The concentration of O_2^{3-} centres shows a weak association with the unstable component of the 1.96 eV emission (Fig. 5.17b). This corresponds with the general observation, that the 1.96 eV emission is associated with non-bridging oxygen hole centres (NBOHC) like O_2^{3-} and O^- centres (e.g. Siegel and Marrone, 1981; Kalceff and Phillips, 1995). OH-precursors are the proposed cause for the creation of this NBOHC (e.g. Griscom, 1985; Friebele et al., 1985; Kalceff and Phillips, 1995). Upon irradiation H^+ diffuses away and NBOHC are formed resulting in an increase of the 1.96 eV CL emission. According to Griscom (1985) the paramagnetic E' centre ($\equiv\text{Si}\cdot$) and/or the diamagnetic trapped-electron center ($\equiv\text{Si}:$) are important causes for the emission at 1.96 eV besides the NBOHC. Defects related to structural water have been assumed as possible precursor centres. Koyama (1980) assumed that this emission may originate from hydrogen in the form of OH or adsorbed H_2O in the quartz lattice. The 1.85 eV band is similarly associated with NBOHC (Griscom, 1985; Kalceff and Phillips, 1995). Possible precursors of the NBOHC are peroxy linkages, "strained" silicon-oxygen bonds, and/or hydroxyl groups.

Greenschist facial deformed granitic quartz from the Lachlan Fold Belt (see § 10.7) show a constant or decreasing 1.96 eV and 1.85 eV emissions during electron bombardment. This quartz contains finely dispersed muscovite flakes of up to 0.5 μm in diameter, which are arranged on micro-sliding planes. The flakes are interpreted as products of deformation. They incorporated the stress-induced mobilised structural water of the quartz lattice. Therefore,

nearly no interstitial bonded water occurs in the quartz lattice, which would have caused the rise of red intensity during electron radiation due to the radiolysis of hydroxyl bonds.

Both 1.96 and 1.85 eV emissions do not generally correlate with the Al distribution. High Al concentrations (>1000 ppm) are associated with the 2.79 eV emission (see below) and the 3.26 eV emission (Alonso et al., 1983; Luff and Townsend, 1990; Perny et al., 1992; Gorton et al., 1996). This lack of correlation may be explained as follows: 1) the substitutional position compensated by hydroxyl defects may be occupied also by other ions like Fe³⁺, 2) Al may occur also in interstitial sites (Cohen, 1960), and 3) Al is in part present in the form of micro-inclusions (Blankenburg et al., 1994; Götze et al., 1999).

2.15 ± 0.2 eV emission

The 2.15 eV emission band (yellow) is dominant for granitic quartz (samples 7, 8, 12). It is the only emission band whose intensity remains relatively constant during electron radiation implying a stable luminescence centre. The quartz of the Eibenstock and Aue Granite showing high-intensity 2.15 eV emission exhibit high Mn suggesting that the emission may be caused by Mn.

According to Lysakov (1978) Mn in quartz has characteristic CL at 1.92, 2.23, and 2.6 eV in quartz. The latter peak is caused by the trivalent ion and the other two by the bivalent ion. The 2.15 eV band was observed by Itoh et al. (1990), Remond et al. (1992), Fuchs and Götze (1996) and Götze et al. (1999). Rink et al. (1993) described a thermoluminescence peak centred between 2.14 eV – 2.21 eV in natural quartz of hydrothermal origin. Itoh et al. (1990) proposed that electron radiation of α -quartz generates pairs of E' centres ($\equiv\text{Si}\cdot$) and peroxy radicals ($\equiv\text{Si-O-O}\cdot$) showing luminescence at 2.1 eV as well as self trapped excitons (STE) showing luminescence at 2.8 eV. However, an association of the 2.15 eV and 2.79 eV emission could not be detected. According to Fuchs and Götze (1996) and Götze et al. (1999) the predominance of the 2.15 eV emission of some agates and of hydrothermal quartz is associated with the high concentration of E' centres. In this study a correlation between EPR intensity of the E' centre and the peak area of the 2.15 eV band has not been found.

2.48 ± 0.2 eV emission

Hydrothermal quartz (megaquartz and oil-bearing quartz) exhibit a significant 2.48 eV peak at initial electron bombardment causing a turquoise CL at initial radiation. This emission rapidly decays during the first minute of electron bombardment. The emission is thermally stable up to 300°C, however it is destroyed after heating at 600°C for 24 h. The samples of

hydrothermal quartz (Fig. 5.12a) show a high intensity of the Li-associated 3474 cm^{-1} band. The decrease or disappearance of the Li-H absorption band after heating at 500°C (Schneider, 1993) is in accordance with the presently observed disappearance of the CL emission after 600°C heating (Fig. 5.8). The properties of the 2.48 eV band and of the Li-associated 3474 cm^{-1} absorption bands imply an association of this CL emission with Li-defects (Table 5.4). Demars et al. (1996) established that the UV emission between 3.65 and 3.76 eV correlates with high Al and Li concentrations. Pott and McNicol (1971), Itoh et al. (1988), and Luff and Townsend (1990) proposed that the 2.48 eV band is caused by an impurity defect, but they give different answers about the kind of impurity. Itoh et al. (1988) assumed the 2.5 eV emission band is extrinsic due to the substitutional incorporation of impurity ions; according to Pott and McNicol (1971) the intensity of the band is associated with Mn^{2+} -defects, whereas Luff and Townsend (1990) showed that Ge-doped quartz exhibits a thermoluminescence band at 2.43 eV .

2.58 eV and 2.68 eV emissions

The narrow 2.58 eV emission and the 2.68 eV and the 2.79 eV bands show constant peak area ratios, i.e. $2.68\text{ eV} : 2.58\text{ eV} = 1 : 0.34 \pm 0.08$. The two emission bands are characterised by intensity decay during electron radiation and cause beside the 2.79 eV emission the blue “flash” at initial electron radiation. Contrary to our findings, Gorton et al. (1996) suggested that the 3.26 eV band is responsible for the high initial blue intensity that is visible as a blue “flash”. The 2.68 eV band was observed in crystalline quartz by Kalceff and Phillips (1995) who assume an association of the emission with a STE combined with an E' center. However, the occurrence of the two emissions in all investigated quartzes points to an intrinsic cause.

2.79 \pm 0.2 eV emission

This emission shows a strong intensity decay during the electron radiation and is mainly responsible for the blue “flash” during the first seconds of electron radiation. Heat treatment sometimes leads to the intensification of the blue emission band (Fig. 5.8; sample 14). Vein quartz showing an intense unstable 2.79 eV emission has extremely high Al concentrations. However, no significant correlation between Al concentration and peak area has been found. According to Ramseyer and Mullis (1990) the blue luminescence is related to the positively charged interstitial cations H^+ , Na^+ , Li^+ and K^+ , which compensate Al^{3+} . Ramseyer and Mullis (1990) show that areas with a high Al content ($>1000\text{ ppm Al}$) always exhibit unstable blue luminescence. This luminescence is absent for $\text{Al} < 50\text{ ppm}$. However, they did not find a

simple correlation between the Al content and CL intensity. The relative concentration of $[\text{AlO}_4]^0$ centres in magmatic quartz show a positive correlation with the unstable component of the blue 2.79 eV emission. This observation is in agreement with Nassau and Prescott (1975) who assumed that the $[\text{AlO}_4]^0$ centre is associated with the emission band at 2.85 eV. The general absence of a significant correlation between the Al and the emission intensity of the 2.79 eV band can be explained by the occurrence of Al also in interstitial sites (Cohen, 1960) and/or in form of microinclusions lattice (Flicstein and Schieber, 1974; Blankenburg et al., 1994; Götze and Plötze, 1997). However, the decay of the blue 2.79 eV emission can be explained by radiation-induced release of interstitial cations accelerated by sample warming and charging. Possibly the emission is associated with charge compensating ions of substitutional Al^{3+} .

Table 5.4 Detected CL emission bands of quartz and their possible association with trace elements and defect centres.

Position (eV)	Half width (eV)	Association with trace elements	Association with defect centres
1.73±0.02	0.3±0.02	Associated with Fe-defects (?)	-
1.84±0.01	0.22±0.01	Associated with structural water in form of H^+ , OH^- , and H_2O (especially the unstable component) (?) and partly associated with Al-defects and their interstitial charge compensators (H^+ , Li^+ , Na^+ , K^+ , Fe^{2+}) (?)	Associated with O_2^{3-} centres (?)
1.96±0.02	0.22±0.02	Associated with structural water in form of H^+ , OH^- , and H_2O (especially the unstable component) and partly associated with Al-defects and their interstitial charge compensators (H^+ , Li^+ , Na^+ , K^+ , Fe^{2+})	Associated with O_2^{3-} centres
2.15±0.02	0.38±0.01	Associated with Mn-defects (?)	-
2.47±0.02	0.30±0.03	Associated with Li-defects	Associated with Li-H defects
2.58±0.01	0.18±0.005	-	Intrinsic defect (?)
2.68±0.01	0.23±0.01	-	Intrinsic defect (?)
2.79±0.01	0.26±0.01	Associated with Al-defects and their interstitial charge compensators (H^+ , Li^+ , Na^+ , K^+ , Fe^{2+})	Associated with $[\text{AlO}_4]^0$ centres
2.96±0.015	0.30±0.02	Associated with Ti-defect structures	Associated with $[\text{TiO}_4/\text{Li}^+]^0$ centres

2.96 ± 0.2 eV emission

This band represents the more stable part of the blue CL emission and is characteristic for rhyolitic quartz (sample 5, 15) as well as for granitic quartz (sample 7, 12, 14; Fig. 5.1, 5.3). A good correlation between the emission intensity and Ti distribution was found (Fig. 5.14). Heating at 600°C for 24 h results in the intensification (sample 15) as well as the creation (sample 1) of the 2.96 eV band after (Fig. 5.8, 5.9).

Rink et al. (1993) observed thermoluminescence emission at 2.85-2.95 eV for magmatic quartz. Kalceff and Phillips (1995) assumed that the origin of the 2.95 eV emission is possibly related to irradiation producing intrinsic defects. Koyama (1980) observed blue CL in carbon-implanted SiO₂. Like Ti⁴⁺ carbon enter the substitutional position in the SiO₄ tetrahedra. Although the Ti content closely correlates with the 2.96 eV emission, it is not clear whether Ti is a CL activator or sensitizer (Table 5.4).

6 Genetic significance of CL structures and trace element distribution

6.1 Impurity uptake during quartz crystallisation in silicate melts

The rhyolites (samples 4, 5, 10, 11, 15) as well as a number of the sampled granites (samples 6, 7, 8, 14) contain euhedral quartz phenocrysts showing a CL-contrasted complex growth pattern (Fig. 5.11, 6.1, 6.2a-f, 7.6; Plate 1). The euhedral phenocrysts of granites are recognisable only by using CL because they are overgrown and embedded in a homogeneous anhedral quartz phase. The existence of euhedral quartz phenocrysts in granites showing CL-contrasted growth textures is currently not known to be common and was described in only a few cases (Frentzel-Beyme, 1989; Seltmann, 1994; D'Lemos et al., 1997; Müller and Behr, 1997). The questions arises if this granitic phenocrysts are comparable phenocrysts occurring in rhyolites and if they represent a similar crystallisation environment.

A main result of the trace element analysis is that the stable blue CL of the phenocrysts correlates with high Ti concentrations and that the variation of Ti is mainly responsible for the contrasting of the magmatic zoning of the quartz phenocrysts (see chapter 7 and 9). Caused by its high field strength ($F = 1.04$) Ti^{4+} can substitute Si only at high temperatures. High Ti concentrations in macroscopically rutile-free quartz generally indicate formation temperatures $\approx 500^{\circ}C$ (Blankenburg et al., 1994). High Ti concentrations are also typical for quartz in granulites (Kerkhof and Müller, 1999). To understand the variation of the Ti concentration in quartz phenocrysts the growth textures were classified according their structure. The classification of growth zoning is necessary to distinguish between zoning caused by self-organised growth and zoning caused by physico-chemical changes of external factors such as temperature, pressure and magma composition (e.g. Bottinga et al., 1966; Allègre et al., 1981; Shore and Fowler, 1996). The zoning caused by external factors is of great interest for the reconstruction of the crystallisation history of felsic melts (magma storage, ascent, mixing, emplacement, and cooling rate) which will applied in the in the chapters 7-10.

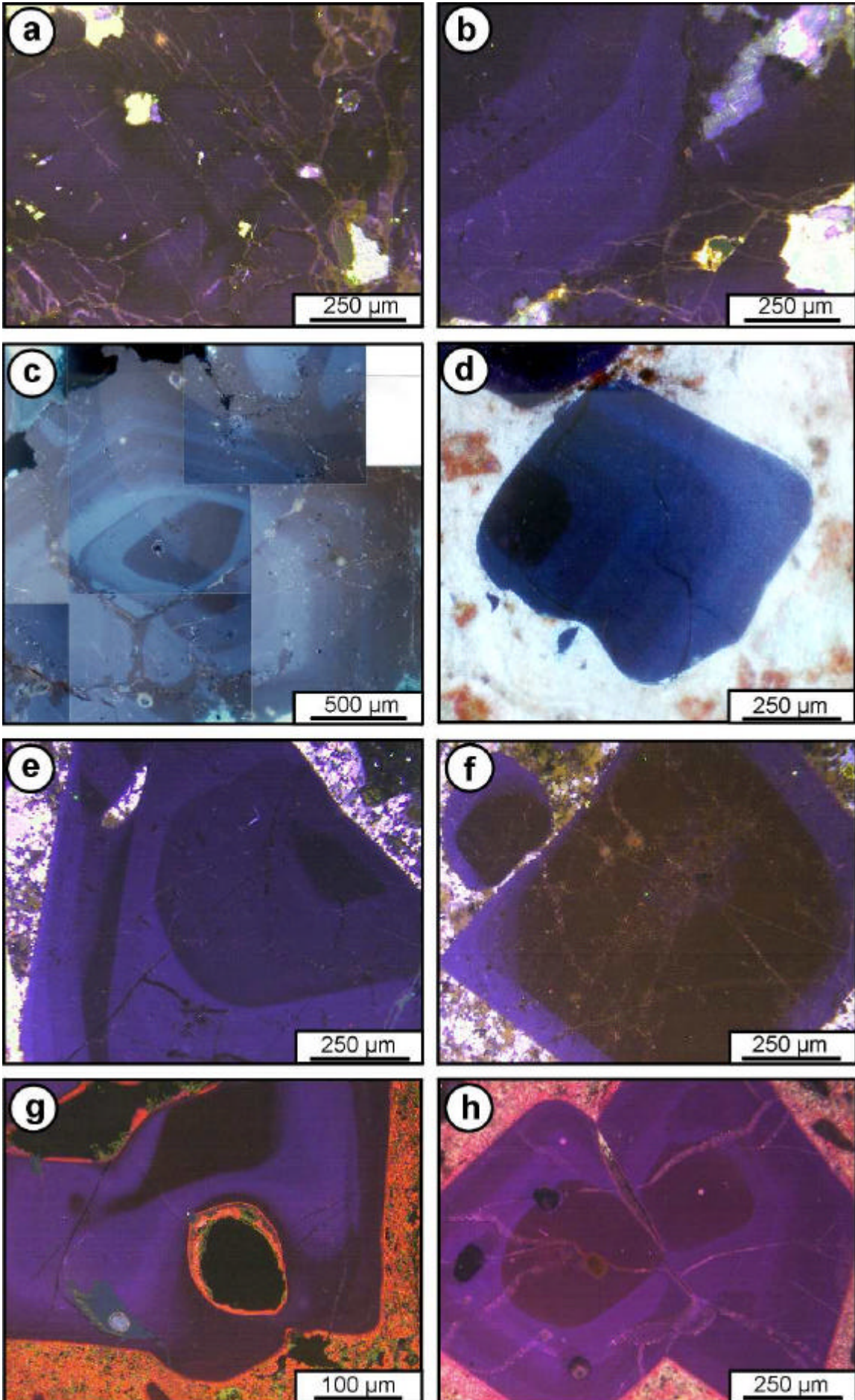


Plate 1 CL images of magmatic quartz. a – Quartz of the Flossenbuerg Granite (sample 12) showing a weak red-brown CL and a dense network of healed cracks. b – Edge of a zoned quartz phenocryst with blue CL overgrown by red-brown luminescent matrix quartz (Schellerhau Granite, sample 6). c – Quartz phenocryst of the Schellerhau Granite with complex growth pattern overgrown by red-brown luminescent anhedral matrix quartz. d - Zoned quartz phenocryst of the Teplice Rhyolite (sample 5). Resorption of the phenocryst surface causes the truncation of pre-existing growth zones. Note the small quartz fragments around the phenocryst which indicate a mechanical abrasion during transport in the melt. e - Zoned quartz phenocryst of the Teplice Rhyolite. f – Zoned quartz phenocryst of the Teplice Rhyolite with red-brown luminescent core. g – Edge of a zoned quartz phenocryst of the Weinheim Rhyolite (sample 15) with a melt inclusion. The zoning fits the shape of the melt inclusion (black with red rim). h - Zoned quartz phenocryst twin of the Weinheim Rhyolite which exhibits resorpted red-brown luminescent cores, melt inclusions (black), and healed cracks (pink lines).

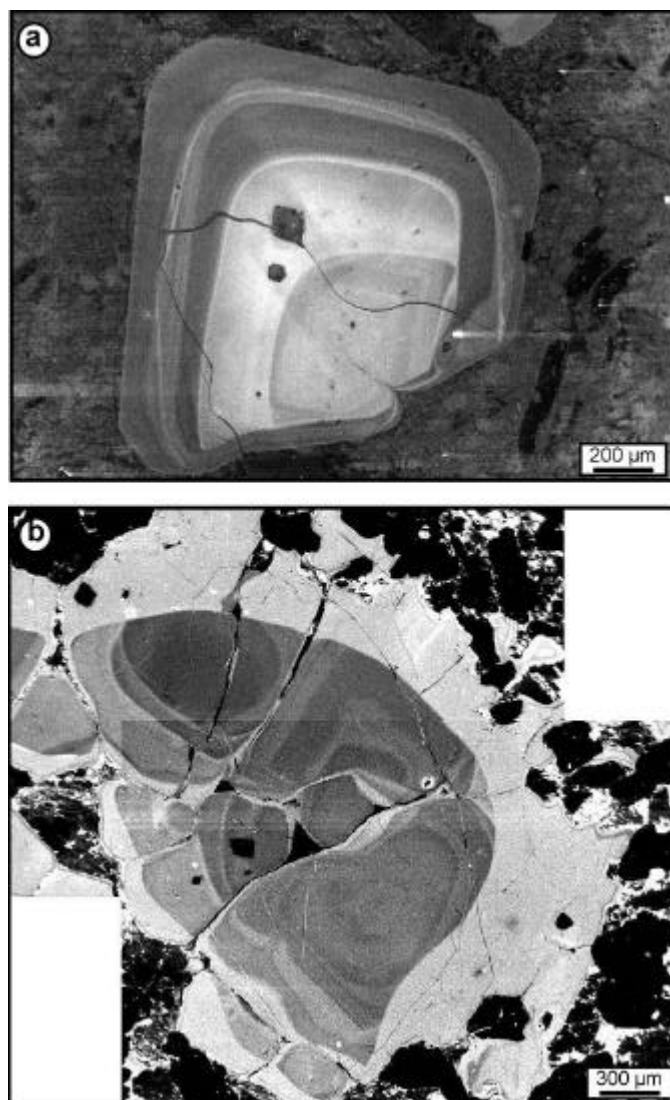


Fig. 6.1 CL images of rhyolitic quartz phenocrysts recorded with a JEOL CLD40 R712 detector. a – Phenocryst from the Weinheim Rhyolite (sample 15). b – Phenocryst from the Beucha Rhyolite (sample 11). Note the anhedral, unzoned, bright quartz phase which overgrows the resorpted core with complex zoning pattern.

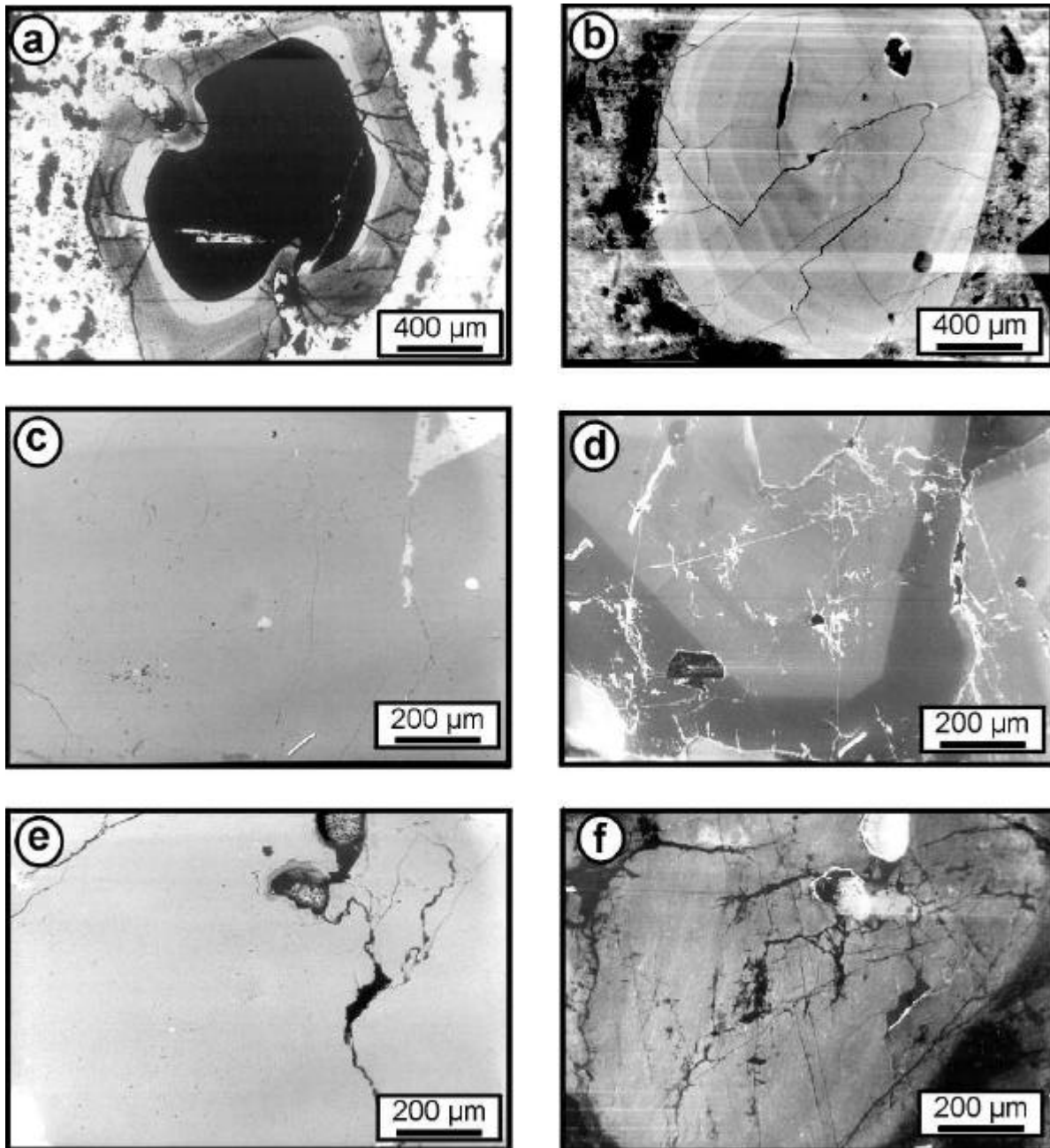


Fig. 6.2 CL and BSE images of magmatic quartz. The CL images were recorded with the S20 Extended detector. a – Phenocryst of the Wachtelberg Rhyolite showing a red-brown, Ti-depleted core. b – Phenocryst of the Schoenfeld Rhyolite with bright blue CL. c – BSE image of quartz in the Eibenstock Granite. d – CL image of the same area as (c) showing an euhedral zoned core overgrown by an anhedral, red luminescent quartz phase without zoning. The CL intensity of secondary quartz have been turned from low CL intensity to high CL intensity after 5 min electron radiation (bright patchy areas within the crystal). e - BSE image of quartz in the Ramberg Granite. f - CL image of the same area as (e) showing a very weakly contrasted phenocryst (bright) with faint growth zoning. The granitic quartz in figures d and f exhibits a number of secondary CL structures.

The development of growth zoning during magmatic crystallisation is described by a number of models (e.g. Sibley et al., 1976; Anderson, 1984; Fowler, 1990) that have been derived from the growth zoning of plagioclase. We apply these models to the crystallisation of magmatic quartz having a very similar growth zoning as plagioclase. Below an interpretation of growth textures in quartz phenocrysts is given, based on our observations and the present level of knowledge, to explain the variations of impurity uptake in magmatic quartz. The compilation of growth textures is illustrated in Fig. 7.1 (chapter 7).

During crystallisation of a mineral four processes are competing and the overall growth rate-controlling process is the slowest one: 1) the reactions occurring at the crystal-melt interface, 2) the bulk diffusion of components in the melt close to the interface, 3) the production and dissipation of the latent crystallisation heat at the interface, and 4) the relative flow of the melt with respect to the interface. The latter two are not critical since heat diffusivities are one to several orders of magnitude higher than mass diffusivities (Dowty, 1980) and the crystal settling effects in a magma chamber are small for viscous silicate melts. Therefore, processes 1) and 2) control are the main parameters controlling the crystal growth rate. A crystal can grow only if the thermodynamic variables for the formation of that phase exceed the equilibrium conditions. This overstepping (undercooling, overheating, supersaturation) provides energy by which nuclei are formed and crystal growth is sustained. The nuclei provide sinks to which the crystallising components diffuse. The distance over which elements are transported by diffusion depends on the diffusion rate and time.

The microscopic topography of individual growth zones is a relic crystal-melt interface and is indicative for disturbances of growth and diffusion rates during crystallisation. These parameters depend on the melt composition, crystal transport in the melt (e.g., convection), the ascent velocity of the melt, and pressure- and temperature variations. These criteria regulate the type and quantity of trace elements, few of which are CL-activators. Thickness and frequency of the zones are directly related to the physical and chemical melt properties. The diffusion rate in the melt controls the compositional variation and width of the zoning. The higher the diffusion rates, the less are the compositional differences in trace element content in the quartz. Concentration gradients develop in the melt when the growth rate exceeds the diffusion rate, and in the solid when the reaction rate of crystals with the liquid is lower than the growth rate (Sibley et al., 1976). The development of growth zoning during magmatic crystallisation was described by a number of models (e.g. Sibley et al., 1976; Anderson, 1984) that have been derived from the zonal structure of plagioclase. We apply

these models to the crystallisation of magmatic quartz, which shows very similar zonal growth as plagioclase.

Major discontinuities in the zoning (50 - 1000 μm width) being non-periodic and showing a significant change of the luminescence colours result in physico-chemical changes of external factors (“extrinsic” according to Shore and Fowler, 1996) such as temperature, pressure and magma composition (Bottinga et al., 1966; Allègre et al., 1981). Bottinga et al. (1966) defined the non-periodic zones as *compositional zoning*, and Allègre et al. (1981) called them *stepped zoning*. Depending on the type of the physico-chemical change (degassing, magma mixing or ascent) the trace element concentrations, mostly represented by variations of Ti and sometimes of Al, show an abrupt change (see chapter 7).

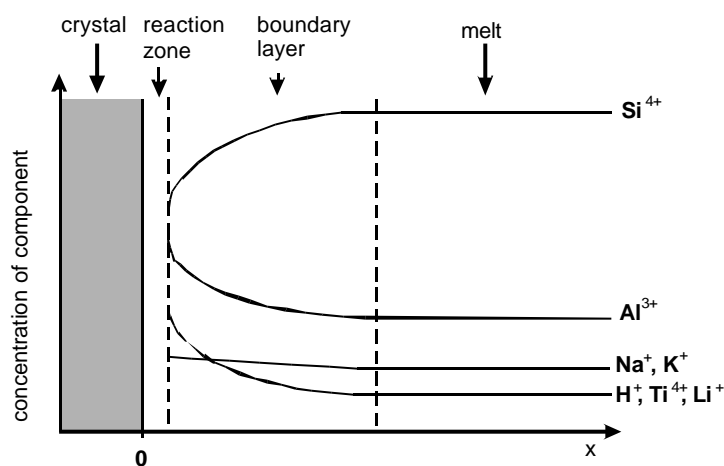


Fig. 6.3 Model system showing schematic concentrations of relevant species versus distance from the surface of quartz crystal in melt. The very low Na^+ and K^+ gradient is due to its high diffusion coefficient (after Hess 1989).

The *fine oscillatory zoning* (2 - 20 μm width) within the step zones can be explained by a self-organised (“intrinsic” according to Shore and Fowler, 1996) diffusion-controlled mechanism on the crystal-melt boundary layer and plays a role exists in a number of models proposed by several authors (Sibley et al., 1976; Haase et al., 1980; Allègre et al., 1981; Loomis, 1982; Simakin, 1984; Pearce, 1993). Oscillatory growth zones form very slowly, at low degrees of undercooling and oversaturation under near-equilibrium conditions. This is possible only when the crystallising system on the solid-liquid interface is not disturbed, i.e. thus the melt should not convect (Allègre et al., 1981). The self-organisation in the crystal-melt reaction zone and boundary layer can be explained by the following model (e.g. Allègre et al., 1981; Fig. 6.3): Saturation of silica in the reaction zone increases the quartz growth rate. The increasing growth rate results in the decrease of silica concentration if the growth rate exceeds the diffusion rate of silica. Simultaneously, quartz-foreign elements are accumulated in the reaction zone and boundary layer. The high growth rate favours the incorporation of impurities due to the change of planar to the cellular interfaces with rather high specific free

energy. The growth rate will slow down when quartz growth is so fast that silica becomes depleted in the reaction zone and boundary layer. Consequently, the diffusion rate becomes the dominant crystal growth controlling process. The growth rate starts to rise again as soon as the silica in the reaction zone has been recovered. Investigations on natural plagioclase by Greenwood and McTaggart (1957) and Wiebe (1968) confirm that oscillation zones of crystals grown from the same melt and formed by self-organising character of processes cannot be correlated. Physical or chemical changes in the bulk magma are not required to develop oscillation zones. The self-organised growth causes only slight variations of Ti upatke.

Wavy surfaces are sometimes observed between the straight-bordered growth zones. They are characterised by convex inlets which are opposed to the growth direction. In contrast to resorption surfaces which are resulted in sharp truncation of the regular zoning and rounded crystal corners (e.g. Shore and Fowler, 1996) the inlets of the wavy surface are much smaller and extend maximal 20 μm in the growth zones and do not cut older zones or round-off corners. The subsequent growth zones are rectilinear bordered again and parallel to the euhedral crystal habit. This feature is in contrast to the wavy zoning which is described for plagioclase by Pearce and Kolisnik (1990), where the subsequent growth zones keep the wavy structure. The wavy zones of quartz are interpreted as a small scale diffusion front caused by rapid variation of the melt temperature and/or composition leading to changes of CL properties developed during crystal growth.

Discussions about the distinction of *resorption surfaces* and *growth impediments* in quartz phenocrysts have been controversial (Kozłowski, 1981; Harris and Anderson, 1984). Laemmlein (1930) first recognised and described lobate depressions at the quartz crystal surface as growth impediments. This result is in accordance with our CL observations which show clearly that the zoning around lobate depressions, mineral-, and melt inclusions adapts to the shape of the impediments. In contrast, resorption surfaces cut pre-existing growth zones. Growth impediments are caused by immiscible liquids, vapor bubbles, molten sulfide or fluid-rich melt droplets which stick on the crystal surface, hinder the crystal growth and result in lobate depressions and entrapments (Kozłowski, 1981; Donaldson and Henderson, 1988; Lowenstern, 1995). The resorption (melting) of quartz surfaces is due to SiO_2 -undersaturation of the melt that may be caused by increase in temperature, isothermal depressurisation or magma mixing. Crystals may undergo rounding due to chemical interaction (melting) and mechanical abrasion during transport in the melt. The occurrence of resorption which results in strong rounding of the quartz crystals is in accordance with the

rapid ascent of granitic melts by dyke formation as found by Holtz and Johannes (1994) and Johannes and Holtz (1996).

The presence of *skeletal (dendritic) growth* indicates supercooling and the consequent decrease of the diffusion/growth rate. Here, the compositional gradient on the crystal-melt interface develops, but the planar crystal-melt interface becomes unstable and changes to cellular and dendritic growth. This type of crystal growth results in skeletal (dendritic) crystal morphologies (Kirkpatrick, 1981; Fowler, 1990).

The growth pattern in rhyolitic and granitic quartz phenocrysts are similar indicating a similar crystallisation environment. Flick (1984; 1987) describes rhombohedral α -quartz phenocrysts from the Weinheim Rhyolite (sample 15). Assuming a typical solidus of a rhyolitic melt of 900-950°C, a crystallisation pressure of at least 13 kbar is necessary for α -quartz crystallisation (Flick 1987). This pressure corresponds with a formation depth of phenocrysts in this rhyolite of about 40 km assuming a geothermal gradient of 20/25°C/km. Thomas (1992) calculated the depth of quartz phenocryst crystallisation of granites of the Erzgebirge (e.g. Eibenstock Granite) of up to 21 km provided by microthermometric studies of silicate melts. Our observations and the two calculations of the crystallisation depth show that euhedral quartz phenocrysts in rhyolites as well as granites exhibiting blue CL-contrasted growth zoning represent a low to mid-crustal crystallisation environment.

Like shown above except for the oscillatory zoning all growth textures are caused by physico-chemical changes of external factors such as temperature, pressure and magma composition which result in the abruptly change of Ti concentration. In § 9.8 is shown that the Ti content in quartz phenocrysts increases with increasing growth rate. Quartz phenocrysts frequently show a Ti depletion in the red/red-brown luminescent crystal core (sample 5, 6, 10, 15) indicating a slow growth rate during the early crystallisation stage (Fig. 6.2a).

6.2 Impurity uptake during quartz crystallisation in aqueous solution

Hydrothermal quartz shows similar growth patterns as magmatic quartz but the compositional zoning is more dominant than the self-organised oscillatory zoning. This indicates crystallisation in a more frequently disturbed (open) system. Resorption (solution) surfaces observed in magmatic quartz and cutting pre-existing growth zones do not occur in hydrothermal quartz. This observation can be explained by the low solubility of Si_2O in water which results only in weakly resorbed (solved) crystal surfaces that can not be distinguished

from unsolved surfaces. A matter of discussion is, if a crystal surface represents generally a solution surface. A characteristic feature of hydrothermal quartz is the so-called *sector zoning* (e.g., Siebers, 1986) which has been not observed in magmatic quartz.

As shown in chapter 6 the contrasted zoning of hydrothermal quartz was explained by the distribution of Al-defects. Therefore, the present discussion focuses on the incorporation and distribution of Al^{3+} (and to lesser extend also Fe^{3+}) and their charge compensating ions Li^+ , H^+ , Na^+ , Fe^{2+} , K^+ . Ti, which may cause CL zoning of magmatic quartz phenocrysts is nearly absent in hydrothermal quartz. This can be explained by the following considerations: 1) The high field strength of Ti^{4+} allows the to substitution of Si^{4+} only at temperatures $>500^{\circ}C$ (Blankenburg et al., 1994), 2) the supply of Ti is very low in natural hydrothermal solutions, and 3) the uptake of Ti of >50 ppm is limited by the stability PT-field of the α -quartz.

Generally, the incorporation of trace elements in hydrothermal quartz depends on the growth direction, growth velocity, the solution chemistry, and the crystallisation pressure and temperature (Brown and Thomas, 1960; Cohen, 1960; Bambaer, 1961; Poty, 1969; Siebers et al., 1984; Siebers and Klapper, 1984; Siebers, 1986; Pankrath 1988). The quartz growth kinetic in an aqueous solution is similar to the processes in silicate melt and can be divided into 5 stages:

- 1) Solution of silica in the form of complexes
- 2) Transport of the complexes into the crystal boundary layer and reaction zone of the growing crystal by diffusion and convection
- 3) Dissociation of the complexes, and adsorption of the complex components on the crystal surface; desorption and removal of water and quartz-foreign elements from the reaction zone
- 4) Surface diffusion of the components to energetically favourable places
- 5) Incorporation (reaction) into the crystal and diffusion of the reaction heat.

In order to understand the processes in the crystal-fluid reaction zone and boundary layer in aqueous solutions Siebers (1986) proposed the following model: At the crystal surface a equilibrium develops between diffusion and boundary layer processes (Fig. 6.4). The thickness of the boundary layer depends on the diffusion coefficient of the reaction partners at the crystal surface. The thermal diffusion coefficient of the heat which is produced in the reaction zone is much higher than the diffusion coefficients of the substances. Therefore, the reaction heat does not effect reaction and growth processes. The oversaturation of the reaction partners increases with the distance from the reaction zone. The concentration gradient in the boundary layer is the driving force of the reaction and growth rate. Therefore, the height of

growth mounds at the basis c (0001) corresponds to the thickness of the boundary layer which can reach several millimetres (Jackson, 1979). In comparison to the crystal-melt interface the crystal-liquid interface is generally more sensitive for concentration variations than temperature variations (Siebers, 1986).

Precondition for impurity incorporation in quartz is that the impurity element is dissolved in the aqueous solution as a complex which can be transported. The dissolution rate and the ability of forming complexes depend on the element concentration of the solution, the pressure, temperature, redox potential, and pH (e.g. Siebers, 1986). Al can be fixated on the quartz surface if it is represent as aqueous tetrahedrally coordinated species $[Al(OH)_4]$ (Merino et al., 1989). This species occurs in aqueous solutions with $pH > 5$ (for $T = 100^\circ C$). According to Merino et al. (1989) and Pankrath (1988) high amounts of Al (> 2000 ppm), Li, Na and low H concentrations in hydrothermal quartz may result from crystallisation in a high-pH aqueous solution. These authors assumed that the pH of the solution is beside the crystal growth rate the main controlling factor in the uptake of Al and responsible for the large variation of Al in hydrothermal quartz.

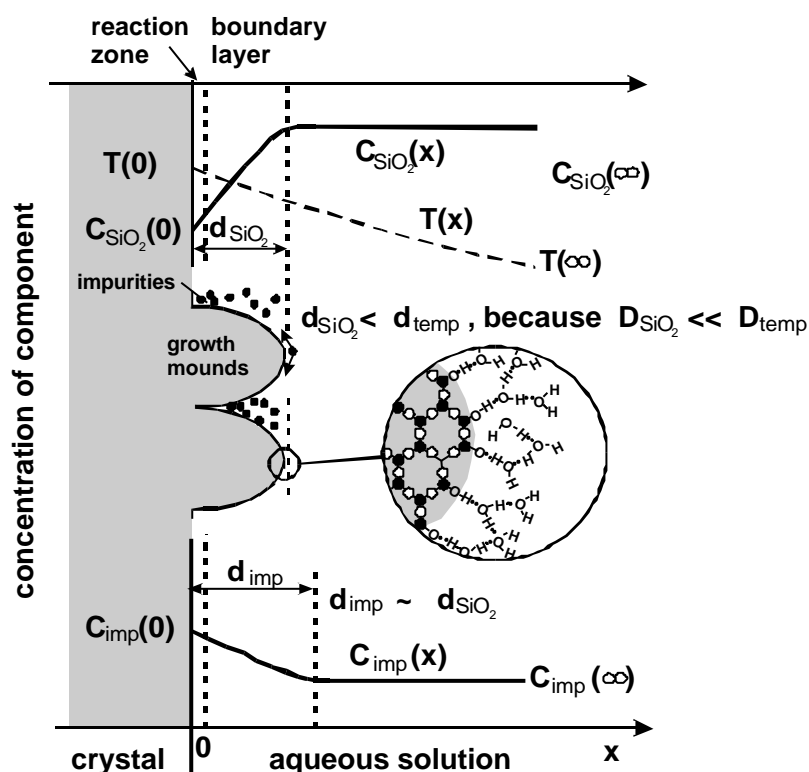


Fig. 6.4 Model system (modified after Siebers 1986) showing schematic concentrations c of relevant components versus distance from the surface of quartz crystal in solution during diffusion-controlled growth. The relative thickness of the boundary layer d of component is controlled by its diffusion coefficient D . The development of growth mounds favours the impurity segregation. The sketch in the cycle show the idealised crystal-fluid reaction zone in pure water.

The Al concentration of the hydrothermal quartz (sample 9) differs between the rhombohedral faces z (~4500 ppm) and r (~3300 ppm). The different Al concentrations of different growth directions cause the sector zoning observed by CL (Fig. 6.11c). The probability of Al^{3+} uptake is controlled by different crystal structural and crystal chemical properties of the surfaces of the growing crystal. For these different surfaces, the probability of Al uptake is higher for z (0111) faces and lower in r (1011) faces. According to the Periodic-Bond-Chain (PBC) theory after Hartmann (1978) the crystal faces of quartz can be distinguished into K-(kinked) and F-(flat) faces. Atomic flat F-faces are the m (1010), r (1011), and z (0111) faces. The basis c (0001) is an atomic rough K-face. The PBC theory can not differentiate between the surfaces of r (1011) and z (0111). The K-face is more reactive because of the high number of free bonds. At this face foreign ions are preferably adsorbed. The F-faces remains flat during higher growth rate whereas the roughness of the K-face c (0001) increases. An increasing growth rate results in a drastic increase of the impurity uptake at the rough K-face c (0001) (e.g., Martin and Armington, 1983). The increase of Al uptake on the F-face z (0111) with increasing growth rate occurs at temperatures above 400°C. Below 400°C the relationship between Al uptake and growth rate becomes inverted (Tsinober and Kamentsev, 1964; Rumyantsev and Novozhilov, 1980). Siebers (1986) proofed that the impurity concentration decreases from c (0001), m (1010), r (1011), to z (0111). The PBC theory cannot explain the different distribution coefficients of foreign ions at m (1010), r (1011), and z (0111). The distribution coefficient of foreign ions on the different faces depends also on the growth rate, temperature, degree of saturation, and growth mechanism (Siebers, 1986). The compositional differences between F and K-faces disappear at higher temperatures near the solidus. During high temperature crystallisation the crystal-fluid interface undergoes a drastic increase of roughness. Close to the melting temperatures all faces becomes rough and take up foreign ions in similar portions. That explains why sector zoning is not observed in magmatic quartz. The extremely high Al in hydrothermal quartz up to 5000 ppm (sample 9) gives reason to assume that Al is not only structurally incorporated, but also as impurity clusters or inclusions (Flicstein and Schieber, 1974; Blankenburg et al., 1994). Götze et al. (1999) showed that the content of bulk trace Al is higher than the structurally incorporated Al calculated from saturated paramagnetic Al centres. Mullis and Ramseyer (1999) determined up to 12000 ppm Al in fissure quartz from the Alps. Caused by the larger ion radius of Al^{3+} in comparison to Si^{4+} such high amounts of structurally incorporated Al^{3+} should cause an extreme deformation and weakening of the quartz lattice. Pfenninger (1961) described impurity entrapment in the form of micro-inclusions and gave the following explanation: The oversaturation of silica

results in diffusion-controlled crystal growth and higher growth rates. At these rates the surface diffusion is too low to organise a planar face growth and cellular growth becomes dominant. Cellular growth results in the development of defect channels which may be filled with foreign elements. These defect channels, 20 - 50 nm in diameter, are parallel to the c-axis and surrounded by disordered SiO₂ boundary layers (Fig. 6.5). They start to grow at the structural channels due to the stepwise bond lacking between the tetrahedra. The competition between impurity segregation and lateral diffusion results in a broadening of the defect channels which finally may result in dendritic growth.

The dynamics of processes at the atomic boundary layer (4-6) are not fully explained, because the structure of the quartz surface is unknown. It has been assumed that free bonds of the surface oxygen are compensated by H⁺ (e.g., Anderson and Wickersheim 1964, Gallei and Parks 1972, Kuznetsov and Lobachev 1973). H₂O is removed during the uptake of dissolved SiO₂ complexes. The Si-OH bond layer is followed by polymolecular adsorbed H₂O molecules (Fig. 6.4). This “quasi-crystalline” layer interacts with the dissolved complexes.

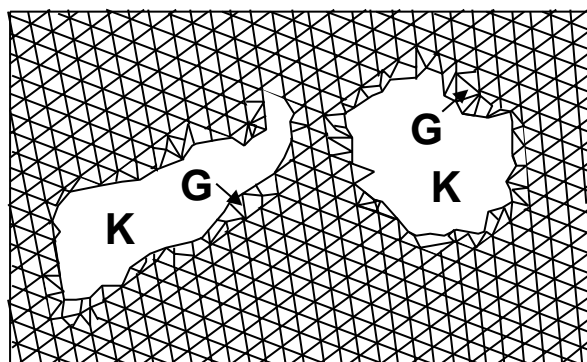


Fig. 6.5 Idealised model of hollow defect channels K and the disordered boundary layer G according to Pfenninger (1961). Section vertical to c-axis.

The criteria which control the uptake of Al³⁺ and Fe³⁺ and its charge compensating ions Li⁺, H⁺, Na⁺, Fe²⁺, K⁺ into the lattice of hydrothermal quartz can be summarised as follows:

- 1) Impurity concentration differs systematically between growth directions and decreases from c (0001), m (1010), r (1011), to z (0111).
- 2) The increase of the growth rate stimulates the impurity uptake at the K-face c (0001). This is valid only at temperatures >400°C for the F-face z (0111). Below 400°C the impurity concentration decreases with increasing growth rate.
- 3) Impurity uptake is controlled by the pH of the aqueous solution. High pH (≈5) of an aqueous solution results in high Al concentrations in quartz.
- 4) The presence of the charge compensating ions H⁺, Li⁺, Na⁺, and K⁺ stimulates the Al³⁺ and Fe³⁺ uptake.

Dennen et al. (1970) proposed a geothermometer based on the incorporation of Al in hydrothermal quartz as a function of the formation temperature. However, the multiple criteria which control the Al uptake show that the Al concentration cannot be directly used as a geothermometer.

6.3 Secondary CL structures and processes resulting in modification of defect centres

Quartz may show a number of secondary structures made visible in CL which formed after growth of the host crystal by retrograde processes. The secondary CL structures are principally formed by a number of processes: 1) micro-cataclasis followed by healing (dissolution-precipitation), 2) diffusion, and 3) α -radiation. These processes result in the modification of defect centres in the quartz lattice or in the formation of new quartz. The secondary structures may show reduced or lower defect centre contents or reversely defect centres are induced. The secondary CL structures have been grouped according their defect centre content.

Secondary CL structures with reduced defect centres

Secondary structures with reduced defect centre content are healed veinlets, healed irregular domains, and patchy halos of secondary quartz around fluid inclusions. They are distinguished by weak red-brown or no CL. This weak CL is indicative of lower contents of activator elements and/or intrinsic defects.

Trans-granular *veinlets and irregular domains* of up to several hundreds micrometres wide have been observed. The veinlets are completely healed, or they contain fluid inclusions. Some samples (Megaquartz, Schellerhau Granite) show different veinlet generations of (Fig. 6.6e, f). Thin concentric and radial, healed micro-cracks are typical for rhyolitic quartz phenocrysts (Fig. 6.2a, b). In this case the cracks are interpreted as thermally induced contraction cracks formed due to rapid cooling during effusion. Dissolution-precipitation (healing) results in veinlets and domains of secondary quartz along micro shear zones, grain edges, grain and subgrain boundaries (§ 10.7).

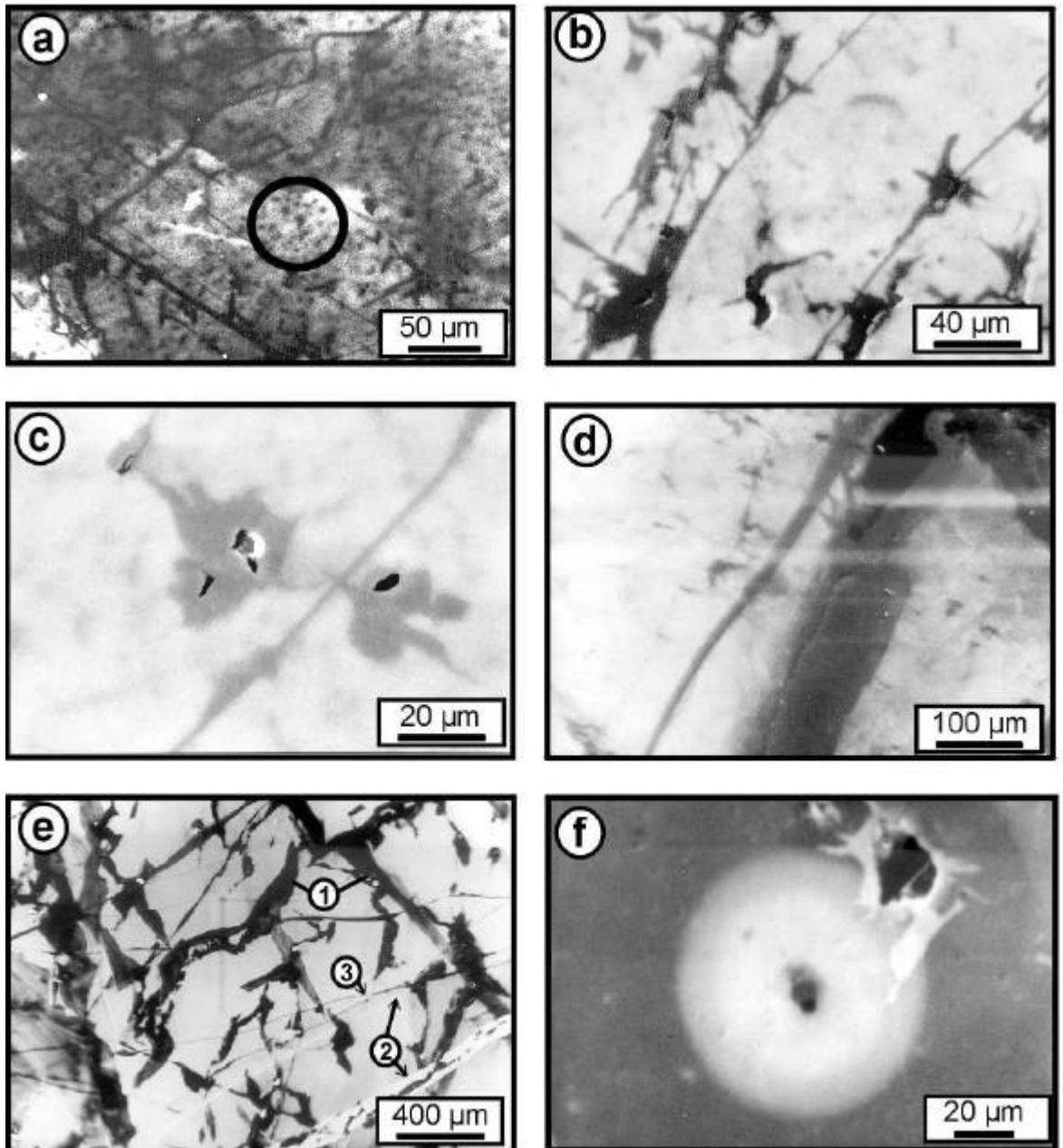


Fig. 6.6 SEM-CL images of secondary CL structures in quartz. a – Non-luminescent spots (easily visible in the cycle) in quartz of the Flossenbuerg Granite. b – Patchy halos of secondary quartz around fluid inclusions connected by sub-parallel healed micro cracks (Flossenbuerg Granite). c - Combination of SEM-CL and BSE images showing the residual porosity of the former fluid inclusions (black “holes”; Flossenbuerg Granite). d – Healed veinlet in the quartz of the Sunset Hills Granite/Lachlan Fold Belt (see chapter 10). The wider veinlet is not completely healed. e – The hydrothermal megaquartz shows a dense network of healed cracks and domains of different ages. Three populations can be distinguished: 1) healed domains with weak CL following fluid inclusion trails. 2) Bright luminescent, linear trails some of which overprint the population (1). 3) Linear, thin cracks healed with weak luminescent quartz. f – Light circular halo around a zircon. The radius of halo is $\sim 40 \mu\text{m}$. The halo is subdivided into a brighter inner zone ($\sim 25 \mu\text{m}$) and a outer zone ($\sim 15 \mu\text{m}$) (Schellerhau Granite).

Particularly in quartz formed at high temperatures *patchy halos of secondary quartz around fluid inclusions* were observed. These and similar structures have been observed since about one decade (Frentzel-Beyme, 1989; Behr, 1989; Kerkhof and Müller, 1999). In the following part the characteristics and formation mechanics of the halos are discussed in more detail. The understanding of the formation of this structures is important for the interpretation of fluid inclusion data. Magmatic quartz crystals typically contain red to red-brown luminescent, patchy halos of secondary quartz around fluid inclusions, connected by healed sub-parallel trans-granular micro-cracks of <5 µm wide (Fig. 6.6c). This structures are frequent in granitic quartz and less common in rhyolitic phenocrysts. The secondary quartz has the same crystallographic orientation as the host quartz indicating. The CL intensity of the secondary quartz increases during 2-10 min electron radiation using high beam power densities >10⁴ W/cm² (Fig. 6.2d). The halos of secondary quartz are depleted in trace elements (Li, Al, K, and Ti) compared to the host quartz (see § 10.7). Sometimes, the host crystal around the secondary quartz is enriched particularly in Fe and Ti (Fig. 5.11c). These elements are probably released from the secondary quartz.

Decrepitation experiments of fluid inclusions with halos of secondary quartz showed that they hold anomalously high fluid pressures on heating (Müller, 1995). Bodnar et al. (1989) showed that the internal pressure required to initiate decrepitation of fluid inclusions in quartz is inversely related to inclusion size according to the equation: internal pressure (kbar) = 4.26 • D^{-0.423}, where D is the inclusion diameter in microns. Figure 6.7 shows this relationship between decrepitation pressure and fluid inclusion diameter (line) within a range (hatched area) after Bodnar et al. (1989). The data measured for the pegmatite quartz of Pleystein and Kreuzstein and Pfahl quartz (Oberpfalz, Germany) plot in the hatched area. On the other hand the data of the Rozvadov Granite (Oberpfalz, Germany) show extremely high decrepitation pressures. The fluid inclusions of this rock exhibit halos of secondary quartz, whereas the pegmatites and Pfahl quartz do not.

The specific features of secondary quartz around fluid inclusions allow us to establish a model for the mechanism of fluid inclusion decrepitation and modification, whereby three stages can be distinguished (Fig. 6.8).

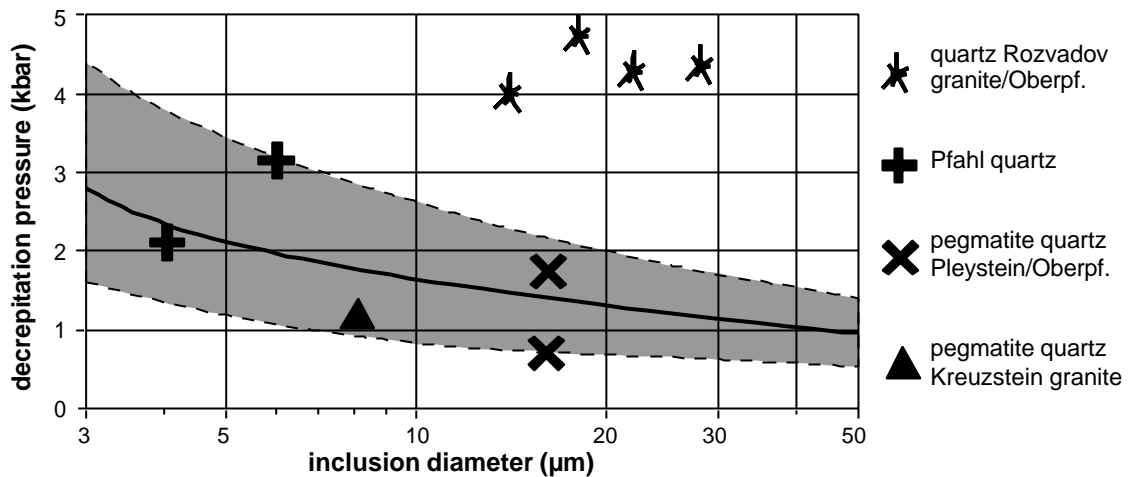


Fig. 6.7 Relationship between decrepitation pressure and inclusion diameter after Bodnar et al. (1989). According to Bodnar et al. (1989) data should plot in the hatched area like the fluid inclusions of the pegmatites and the Pfahl quartz from the Oberpfalz/Germany. The fluid inclusions in the quartz of the Rozvadov Granite showing halos of secondary quartz around fluid inclusions hold anomalously high fluid pressures on heating (Müller, 1995).

In the first stage *mass decrepitation of fluid inclusions (micro-crack formation)* may occur. Simultaneous decrepitation of fluid inclusions is assumed, because in the present samples the halos are connected with one generation of healed micro-cracks. Mass decrepitation may be induced by differences between fluid pressure and lithostatic pressure e.g. during uplift (isothermal decompression). The α/β -transition causes an anisotropic contraction of 0.86 vol.% vertical to the c-axis and 1.3 vol.% parallel to the c-axis and induces stress within individual grains (e.g. Blankenburg et al. 1994) and subsequently may also trigger mass decrepitation. Dissolution-precipitation initiated by shearing leads to the healing of the micro cracks.

In the second stage the *defect-poor quartz grows at the cost of the host quartz and releases or replaces defect centres*. The formation of defect-poor quartz at the cost of the defect-rich host quartz is explained by the displacing of atoms along the phase boundary of the quartz with higher defect density so that the atoms fit to the lattice of the quartz with low defect density (e.g. Passchier and Trouw, 1998; Stünitz, 1998). This results in local displacement of the phase boundary (between the new quartz and the host quartz) and the growth of the more pure crystal at the cost of more disordered neighbour. The process reduces the internal free energy of the crystals involved and causes the release and replacement of defect centres, which are enriched in the grow front.

In conclusion, the formation of secondary quartz around fluid inclusions is explained by a reconstituting process of the host crystal and represents a structural transformation, whereby the crystallographic orientation is preserved.

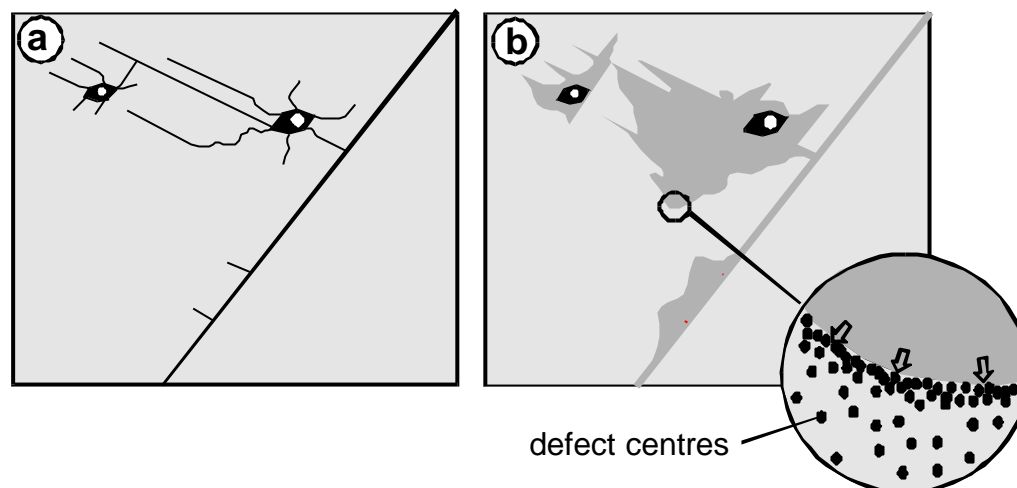


Fig. 6.8 Model of formation of halos of secondary quartz around fluid inclusions. a – first stage: mass decrepitation of fluid inclusions (micro-crack formation). b – second stage: defect-poor quartz grows at the cost of the host quartz and releases or replaces defect centres.

Secondary CL structures with induced defect centres

Secondary CL structures with induced defect centres are halos around radioactive inclusions, diffusion rims along grain boundaries and micro-cracks, and non-luminescent spots in granitic quartz. Natural α -radiation and trace element diffusion cause the modification and formation of defect centres in quartz.

Some samples show round *halos around radioactive inclusions* with pinkish/yellowish white CL (Fig. 6.6b). Natural α -radiation of radioactive micro-inclusions (zircon, monazite) results in damage of the crystal structure (metamictisation). The radius of halos is typically $\sim 40 \mu\text{m}$. Each halo is subdivided into a brighter inner zone ($\sim 25 \mu\text{m}$) and an outer zone ($\sim 15 \mu\text{m}$). The radius of $\sim 40 \mu\text{m}$ corresponds to the interaction radius of the α -particles in quartz (Owen, 1988). Similar bright CL was also observed in hydrothermal quartz (sample 1) along open cracks, indicating that quartz lattice damage was produced by α -radiation from radioactive components of the migrating fluid.

In magmatic quartz *diffusion rims* at grain boundaries (grain boundary alteration) frequently occur at the grain contacts between quartz and plagioclase or biotite (see § 10.7). The diffusion rims show the enrichment of Fe, Al, and K. Fe may diffuse up to $400 \mu\text{m}$ into the

quartz. The Fe enrichment at the grain boundaries not always results in the change of the CL colour (Fig. 5.11c). This observation may be explained by the fact that Fe occurs as divalent and trivalent ions. The diffusion rims in magmatic quartz are explained by solid state diffusion of trace elements at high (sub-solidus) temperatures.

Particularly in granitic quartz radiation-induced *non-luminescent spots* were observed. Weak luminescent spots up to 5 μm in size developed during electron radiation in granitic quartz (sample 7, 8, 12, and 14; Fig. 6.6a). The radiation-induced spots are interpreted as aggregations of aqua complexes with a gel-like disordered structure, i.e. regions with a high local concentration of H_2O and substitutional Al with one or more OH groups attached in a locally disordered network. Stenina et al. (1984) described similar spots developed during electron radiation and identified these structures as amorphous (non-crystalline) micro-areas using TEM imaging. The electron radiation results in the release of molecular water from the aqua complexes (see § 2.2). H^+ ions migrate along weak donor-acceptor and hydrogen bonds of the aqua complex defects. As a consequence oxygen may migrate due to the radiation-triggered redistribution of Si-O and $\text{M}^{\text{m}+}$ -O bonds (Stenina et al., 1984; Gritsenko and Lisitsyn, 1985). At the defective places the following reaction occurs: $\text{O}^{2-} + 2\text{H}^+ \rightarrow \text{H}_2\text{O}$. Here water bubbles may develop. Heggie (1992) showed that microcracks by producing radicals facilitate the migration of water. In this case “water” moves through SiO_2 matrix in the dissociated form. Heat-treatment experiments (500°C for several hours) showed that the aqua complexes homogenised into the lattice and structural water converts to non-bound form and creates micro bubbles (e.g. Griggs, 1967; Brunner et al., 1961; Bambauer et al., 1969; McLaren et al., 1983; Stenina et al., 1984). These bubbles of heat-treated quartz arise as a result of the thermal-induced break down of $2[\text{SiO}_3]^{--}\text{O}-\text{H}-\text{H}$ bonds and the following H^+ migration along the weak bonds of the lattice. The gel like defect structures were incorporated during crystallisation. The frequent occurrence of these spots in anhedral granitic quartz (matrix quartz) reflects “wet” conditions during crystallisation whereas rhyolitic and granitic quartz phenocrysts does not show spots indicating “dry” crystallisation conditions.

In summary, trace elements in quartz are largely redistributed during retrograde processes. Non-luminescent spots and secondary quartz around fluid inclusions are frequently in granitic matrix quartz and less common or lacking in rhyolitic phenocrysts. The frequent occurrence of spots caused by gel-like defect structures in anhedral granitic matrix quartz reflects “wet” conditions during crystallisation, whereas rhyolitic and granitic quartz phenocrysts does not show spots indicating “dry” crystallisation conditions. Rhyolitic phenocrysts are mostly fluid

inclusion free, whereas granitic phenocrysts frequently show halos of secondary quartz around fluid inclusions as a result of a overprinting by late-magmatic volatiles.

7 Application of Cathodoluminescence to Magmatic Quartz in a Tin Granite – Case Study from the Schellerhau Granite Complex, Eastern Erzgebirge, Germany

(this chapter has been published in *Mineralium Deposita*, vol. 35, pp. 169-189, 2000, co-authors: R. Seltnann and H.-J. Behr)

7.1 Abstract

A model of the cooling history of tin-bearing granitic magma forming the Schellerhau granites (Eastern Erzgebirge, Germany) is shown on the basis of quartz textures. Similar grain size, similar grain habit and correlatable growth textures of phenocrysts in different granite varieties give proof of a common crystallisation history before the melts of the Schellerhau granite varieties were intruded. Four nucleation events occurred during crystallisation in different crustal levels between about 20 and 1 km depth. The parental melt of the Schellerhau granites is interpreted to have contained <2.5 wt.% H₂O originally. The water content of the melt during the subvolcanic intrusion stage amounted to more than 5 wt.% and characterises highly evolved residual melts that enable the formation of tin deposits. This paper contributes to a better understanding of the development and behaviour of fractionated tin-bearing granitic melts, and links quartz cathodoluminescence (CL) with microanalytical studies.

7.2 Introduction

MacLellan and Trembath (1991) developed a quantitative model for evaluating the cooling history of a granitic magma on the basis of quartz textures. The relative chemical and structural stability of quartz is responsible for the conservation of quartz generations of different size, habit and structural state in granites and rhyolites. In contrast the chemical composition of feldspar changes during cooling because it is in equilibrium with melt. Therefore quartz morphology provides reliable information about the cooling history of granitic melts.

In this paper we report about the application of cathodoluminescence (CL) microscopy to distinguish different quartz generations in the Schellerhau tin granites. CL is used to illustrate

the growth textures of quartz. However, it is not the aim of this paper to provide a detailed explanation of the complex causes of luminescence in quartz. The CL of quartz results from substitutional and interstitial incorporation of trace elements and from different types of intrinsic and extrinsic defect centres in the quartz lattice (e.g. Ramseyer et al., 1988). Consequently, the luminescence behaviour is a complex function of the concentration of trace elements which may act as CL activators, like Al, Fe and Ti, or as quenchers. The CL is related to the conditions of mineral crystallisation, and alteration and of natural γ - and α -radiation. The analysis of the luminescence spectra makes it possible to quantify the emission properties of single grains. The scanning electron microscope cathodoluminescence (SEM-CL) facilitates high resolution of intragranular growth textures of magmatic quartz. Zoning within quartz is normally invisible by conventional optical microscopy and rarely documented by quantitative analysis. We also determined trace element concentrations in quartz using the electron microprobe. In addition, the detailed analysis of quartz texture and size distribution was carried out. The intragranular growth textures, the quartz framework and the grain size distribution yield important information on the nature and evolution of the melt from which the crystal grew. Plots of maxima of grain size distributions for a single mineral indicate bursts of nucleation which are caused by a high degree of melt undercooling (Dowty, 1989).

In the following is given a short introduction in the general interpretation of growth textures, based on the present level of knowledge. A general compilation of observable growth and resorption textures is illustrated in Fig. 7.1.

The different primary growth textures represent disturbances of growth and diffusion rates during crystallisation. Growth and diffusion rates depend on melt composition, crystal transport in the melt (e.g., convection) and ascent velocity of the melt and related pressure and temperature changes. These criteria regulate type and quantity of defects, few of which are luminescent active and incorporated into the quartz lattice. Wavelength and amplitudes of individual zones are directly related to the physical and chemical melt properties. The

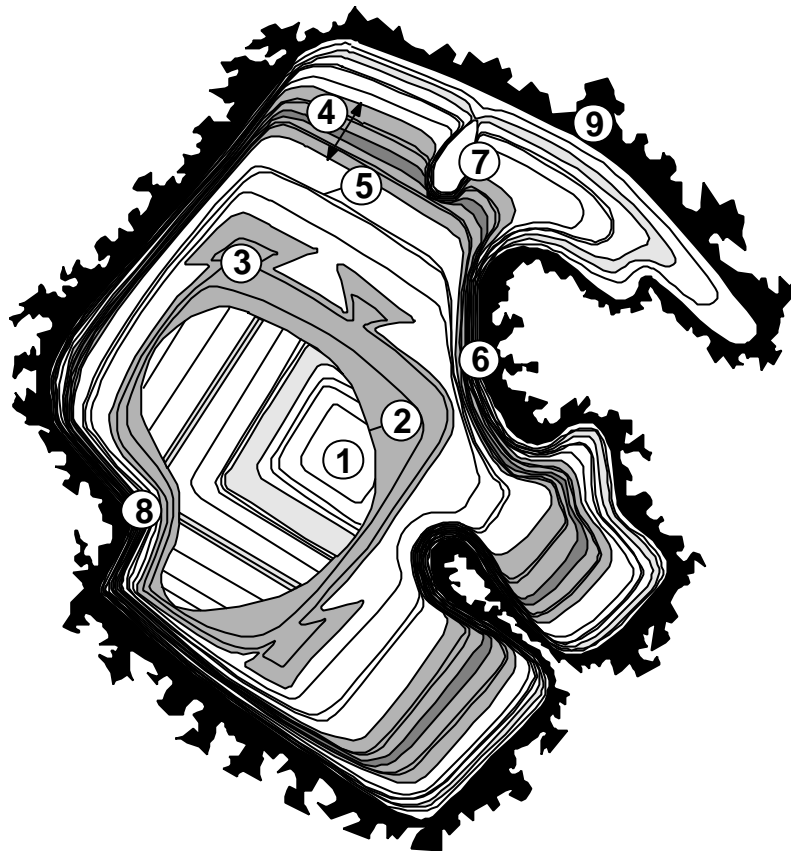


Fig. 7.1 Synoptical scheme of primary growth textures in magmatic quartz phenocrysts with a diameter of 1 to 5 mm contrasted by SEM-CL. 1 - Nucleation of hexagonal β -quartz or rhombohedral α -quartz; 2 - Resorped surface; 3 - Skeletal growth; 4 - Step zoning (50 - 1000 μm); 5 - Oscillation zoning (2 - 20 μm); 6 - Growth impediment; 7 - Inclusion (entrapment) of melt or a bubble; 8 - Growth impediment caused by adjacent phenocrysts; 9 - Rim of anhedral quartz of the final magmatic crystallisation.

diffusion rate in the melt controls the compositional variation and width of the zoning. The higher the diffusion rates, the less compositional differences occur in the quartz. Concentration gradients develop in the melt when the growth rate exceeds the diffusion rate, and in the solid when the reaction rate of crystals with the liquid is lower than the growth rate (Sibley et al., 1976).

The development of growth zoning during magmatic crystallisation is described by a number of models (e.g. Sibley et al., 1976; Anderson, 1984) that have been derived from the zonal structure of plagioclase. We apply these models to the crystallisation of magmatic quartz having a very similar zonal growth as plagioclase.

Major discontinuities in the zoning (50 - 1000 μm width) being non-periodic and showing a significant change of the luminescence colours result in physicochemical changes of external factors (“extrinsic” acc. to Shore and Fowler, 1996) such as temperature, pressure and magma

composition (Bottinga et al., 1966; Allègre et al., 1981). Bottinga et al. (1966) defined those zones as *compositional zoning*, and Allègre et al. (1981) called them *stepped zoning*.

The *fine oscillatory zoning* (2 - 20 μm width) within the step zones is explained by a self-organised (“intrinsic” acc. to Shore and Fowler, 1996) diffusion controlled mechanism on the crystal-melt boundary layer and exists in a number of recent models (Sibley et al., 1976; Haase et al., 1980; Allègre et al., 1981; Loomis, 1982; Simakin, 1984; Pearce, 1993). Oscillatory growth happens very slowly at low degrees of undercooling and oversaturation. It may only take place when the crystallising system is not disturbed on the solid-liquid interface, thus the melt should not convect (Allègre et al., 1981). Investigations on natural plagioclases by Greenwood and McTaggart (1957) and Wiebe (1968) confirm that oscillation zones of crystals grown from the same melt cannot be correlated due to the self-organising character of the process. To develop oscillation zones physical or chemical changes in the bulk magma are not required.

Discussions about the distinction of *resorption structures* and *growth impediments* in quartz phenocrysts have been controversial (Kozłowski, 1981; Harris and Anderson, 1984). Laemmlein (1930) first recognised and described lobate depressions at the crystal surface as growth embayments. The fact that these are growth impediments may be recognised because the zonation adapts to the shape of the embayments. In contrast, resorption surfaces cut pre-existing zones. Growth impediments are caused by immiscible liquids, vapor bubbles, molten sulfide or fluid-rich melt droplets which stick on the crystal surface, hinder the crystal growth and result in lobate depressions and entrapments (Kozłowski, 1981; Donaldson and Henderson, 1988; Lowenstern, 1995). The resorption (melting) of quartz surfaces is due to SiO_2 -undersaturation of the melt which may be caused by increase in temperature, isothermal depressurisation or magma mixing. Crystals may undergo a rounding due to thermal weakening, chemical interaction and mechanical abrasion even during transport in the melt. The occurrence of resorption which results in strong rounding of the quartz crystals is in accordance with the rapid ascent of granitic melts by dyke formation as found by Holtz and Johannes (1994) and Johannes and Holtz (1996).

The presence of *skeletal growth* indicates supercooling and a related decrease of the ratio of diffusion rate/growth rate. In such cases compositional gradients on the crystal-melt interface develop, planar crystal/melt interfaces become unstable and the growth results in skeletal morphology (Kirkpatrick, 1981; Fowler, 1990).

As object of studies we have chosen the *Schellerhau Granite Complex (SGC)* in the Eastern Erzgebirge/Germany. It has been studied by Pälchen and Ossenkopf (1967), Helbig and Beyer (1970), Seim et al. (1982), Just et al. (1987), and Schilka and Baumann (1996) so that an extensive state of knowledge based on mapping, availability of drill cores and resulting chemical and petrographical data exists. The pluton was studied by the authors across a vertical sampling profile of about 1000 m using the relief differences of up to 300 m caused by erosion and dislocations, and available drill cores of depths of up to 1000 m (drilling Niederpöbel 1/58, Helbig and Beyer, 1970). On the basis of the collected data, we present a model of the quartz crystallisation history of the Schellerhau granite magma.

7.3 Analytical methods

Cathodoluminescence (CL) microscopy has been used to visualise growths and alteration structures in quartz. Two instruments for CL studies of polished thin sections were used. The analyses of the luminescence colours (optical CL) were carried out on a hot-cathode-luminescence-microscope (Neuser et al., 1995) at the University of Göttingen. Thin sections were coated with a carbon layer and were bombarded with electrons with an energy of 14 keV and a filament current of 0.17 mA. The electron beam (4 mm cross section) and the sample were maintained in vacuum conditions of 10^{-5} mbar. The spectral response of the luminescence was recorded by a TRIAX 320 spectrometer with a 100 lines/mm grating for the emission spectra from 1.3 to 3.1 eV. The single emission bands 2.79 eV and 1.96 eV were measured with the Monochromator at a speed of 10 mm/min using the CL-microscope after Zinkernagel (1978) (10 keV, 0.25 mA). The scanning electron microscope model Geoscan 250-MK3 with a CL detector (SEM-CL) was used for black-and-white images of the internal growth and secondary structures of the quartz grains. The voltage was 15 keV and the current 5 to 15 nA. Dark contrasted areas in quartz produced by SEM-CL correspond to red to reddish brown CL-colours of the optical CL. Light areas correspond to blue to violet colours.

The trace element concentrations in quartz were determined by wavelength-dispersion analysis on the *JEOL JXA 8900 electron microprobe* operating at 15 kV and 70 nA with a beam diameter of 5 μm . Analyses were performed for Al, Ti, Mn and Fe. The calculated detection limits ranged from <25 ppm for Al, <17 ppm for Ti, <26 ppm for Mn to <23 ppm for Fe with a confidence level of 95%.

The application of the *lacquer peel method* (Behr, 1966) enables detailed analyses of the quartz framework (Müller and Behr, 1997). This technique, usually applied to carbonates, is used here to visualise the quartz textures. The peels are produced by treating the surfaces of polished samples with a 40% HF solution. The corroded surface is covered with several lacquer layers. After drying, the lacquer film is pulled off and used as a negative for black-and-white photos. Quartz appears black and feldspar and mica white or grey on the photos.

Grain size analyses were carried out in thin sections and in hand specimen. The length and width of quartz grains (≤ 1 mm) in the thin sections was measured using a defined raster, determined through the grain size. The distance between the points of the raster corresponds to the average grain diameter. Quartz grains larger than 1 mm were measured by micrometer on polished hand specimens (15 x 15 cm). The grain size was calculated from the average of its length and width.

7.4 Geology and geochemistry of the SGC

Geological setting

The SGC belongs to the highly evolved younger granite group of the Erzgebirge batholith (Tischendorf and Förster, 1990; Stemprok, 1993; Förster and Tischendorf, 1994; Seltmann, 1994). Neoproterozoic gneisses of the metamorphic basement and volcano-sedimentary rocks of the Altenberg-Teplice caldera form the host rocks (Fig. 7.2).

Late-collisional extensional tectonics and collapse of the Variscan orogen controlled during the Upper Carboniferous the block and graben tectonics in the area, caldera formation with pre-dominantly ignimbritic rhyolites and porphyritic microgranites, and finally the post-tectonic multiple intrusion of tin granites of the SGC into a subvolcanic level. Uplift, faulting, block tilting and erosion took place mostly in Permo-Silesian and Cenozoic times and formed the recent morphology. NW- and NE-striking faults with vertical dislocations of several hundred metres form the SGC as horst and as a result some deeper pluton parts are uncovered by erosion. The SGC crops out at about 13 km² as a NW-SE elongated body roughly bounded in the north-eastern part by the Weisseritztal fault and in the south-western part by the

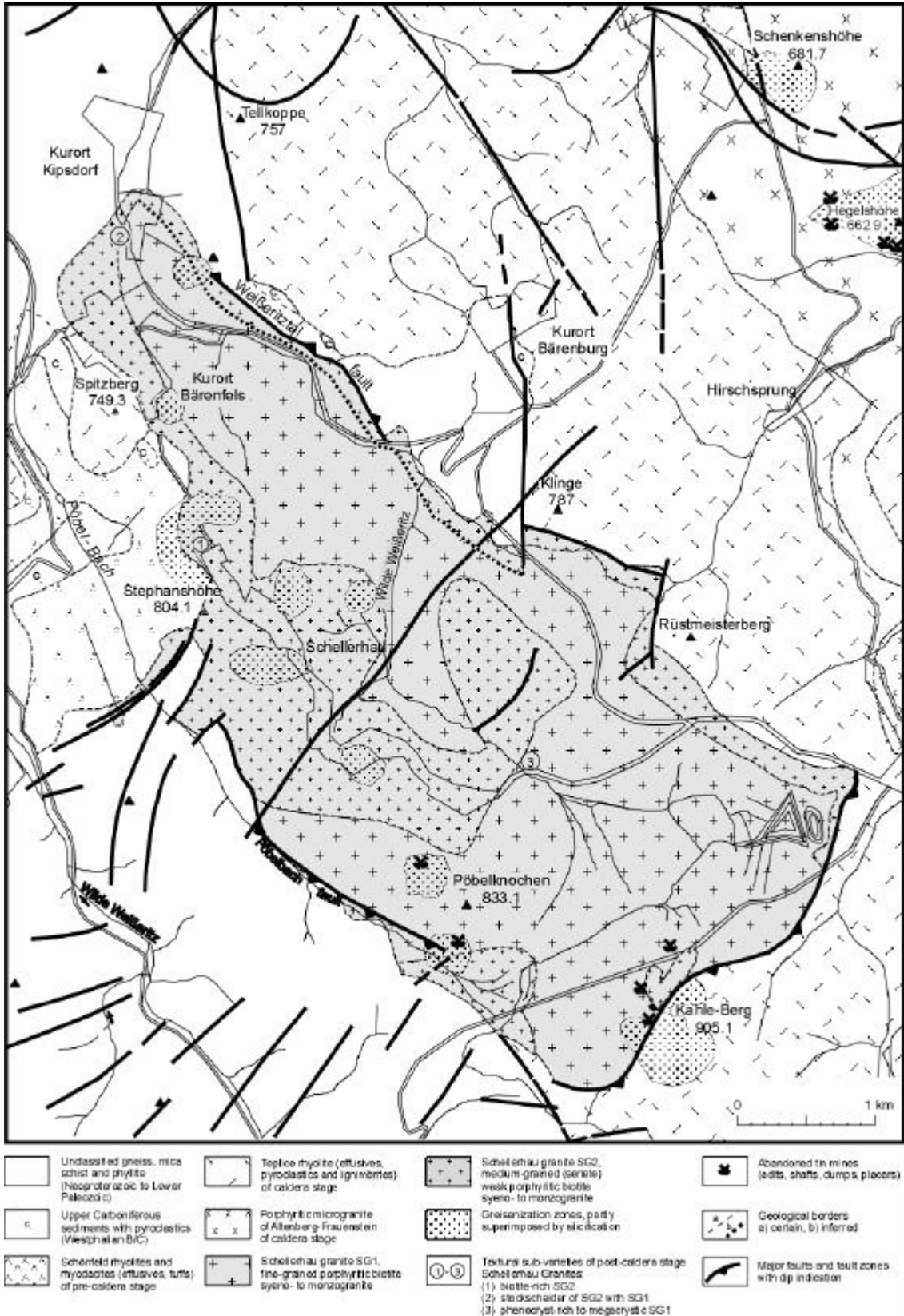


Fig. 7.2 Geological sketch map of the Schellerhau granite massif and its geological setting in the Altenberg-Teplice caldera, Eastern Erzgebirge (without Cenozoic).

Pöbelbach fault (Schilka and Baumann, 1996). These marginal fault zones indicate within the structural pattern of the Altenberg-Teplice caldera a NW-striking sinistral strike-slip movement and north-east directed extension controlling in the post-caldera stage the post-tectonic SGC intrusion. Faults intersecting the SGC are either post-intrusively reactivated or newly formed as indicated by their hydrothermal mineralisation of different ages ranging from Upper Carboniferous to Cenozoic.

According to gravimetry data and geochemical studies of drill cores, granites of the SGC type form the mostly hidden Eastern Erzgebirge partial pluton (Tischendorf, 1964). This NNW-striking hidden granite ridge reaches from Dippoldiswalde in the north to Zinnwald in the south with ca. 10 km east-west extension. To the south, in the Czech part of the Erzgebirge, the chemically and texturally similar Preisselberg-Cinovec granite (Stemprok et al., 1994) forms the continuation of this granite ridge.

Phasing

The SGC is characterised by the intrusion sequence of porphyritic (SG1) to weakly-porphyritic (SG2) *biotite syeno- to monzogranites*, and mostly seriate *albite granites* (SG3). The SG1, SG2 and SG3 rocks of the SGC represent individual stages (phases) of a multiple granite intrusion as indicated by field evidence.

The SG1 forms the central and upper part of the SGC and occupies about 2/3 of the SGC at the recent surface. Locally, the SG1 exhibits a marginal facies characterised by the most primitive composition within the SGC that is due to porphyritic texture and muscovite-bearing similar to the “intermediate granites” (IG, “Zwischengranite” type Walfischkopf, Lange et al., 1972; Stemprok, 1986) of the Western Erzgebirge. Variants of that SG1 variety of the SGC also occur in the multiple intrusions of tin granites at Sadisdorf and Sachsenhöhe. The textural variability of the marginal facies of the SGC also includes so-called two-phase textures (Cobbing et al., 1992; Seltsmann and Stemprok, 1994) where crystals/crystal mush of an earlier SGC intrusion and cooling stage either underwent fluidisation at intrusive contacts or were infiltrated along grain margins but not resorbed by low-viscosity melt batches of a subsequent intrusion stage. The older phenocrysts exhibit sharp contacts to the surrounding groundmass of that second stage.

The SG2 intruded the SG1 along its margins probably due to cauldron subsidence effects in the post-caldera stage of the Altenberg-Teplice crustal unit. The SG2 occupies about 1/3 of the SGC surface. There is field evidence that SG1 enclaves occur in SG2 (locality Paradies-Fundgrube), SG2 dykes cross-cut SG1, and there are sharp intrusive contacts with

stockscheiders and chilled margins of the younger phase against the earlier phase (northern SGC flank at Kipsdorf SG2/SG1, southern SGC flank at Kahleberg SG2/SG1, drill cores SG3/SG1 and SG3/SG2).

The albite granites (SG3) occur as fine- to medium-grained porphyritic and seriate varieties. They were found in most of the drillings as flat igneous layers of up to several ten metres thickness intercalated with SG1 and SG2 units characterising the SGC as sheeted laccolite body. Small SG3 dykes cross-cutting the earlier granite phases SG1 and SG2 provide evidence for magmatic origin of SG3 and against its interpretation as metasomatic zones. Exploratory excavations near the former New Galgenteich quarry exposed a small SG3 dyke with sharp igneous contacts to the SG2 (F. Schiemenz, pers. comm.). The occurrence of fluid saturation textures (miarolitic cavities, micrographic quartz/K-feldspar intergrowth) reflects the high fractionation degree of the SG3 melt.

The genetical position of alkali feldspars, especially the occurrence of sugar-grained albites, remains unsolved and is controversially discussed for similar rocks (Beus et al., 1962; Schwartz, 1992; Stemprok, 1993). Regardless of many subsolidus features caused by deuteric alteration and post-magmatic fluid-rock reactions, we classify the SG3 rocks as to be of predominantly magmatic origin (Just et al., 1987; Seltmann et al., 1992) as they are characterised by snowball quartz that is bearing melt inclusions (R. Thomas, pers. comm.). These melt inclusions show features of trapped silicate melt similar to those studied in topaz-bearing granites from Karelia (Poutiainen and Scherbakova, 1998) and do not link to the interpretation of crystallised silica colloid trapped as a hydro gel during greisenisation as described from a Cornish topaz granite (Williamson et al., 1997). The snowball quartz contains also inclusions of late-magmatic matrix albite. Many SGC samples underwent supplementary metasomatic albitisation (Haapala, 1997) and therefore only relics of the primary texture and structural relationships allow to identify the original granite type.

Within the Eastern Erzgebirge, marginally to the SGC, a series of stock-like granites (Altenberg, Sadisdorf, Sachsenhöhe, Zinnwald, Preisselberg), each with 1-5 km² outcrop size at the recent surface, form as multiple intrusions cupola-shaped elevations of the hidden pluton. These stocks we interpret as channelised products of evolved melt batches and the accompanying ore-forming greisen fluids as originated from deeper parental magmas. They are, similar to the SG1 to SG3 sequence, composed of rock types with fine-grained porphyritic via medium-grained equigranular syeno- to monzogranites to seriate albite granites. The granite elevations represent the country rocks for endocontact tin mineralization of the greisen type. Numerous drillings made in the area between Cinovec (Zinnwald) and

Krupka on the Czech side where granites were continuously followed in the drill cores appear equivalent to those found in the SGC. Our studies confirm the evolution series of protolithionite, zinnwaldite and lepidolite granites such as described as upward sequence from the deep drilling at Cinovec (Stemprok and Sulcek, 1969; Rub et al., 1997).

Due to the recent erosion level of the SGC of estimated ca. 500-1000 m (Schust, 1980, Spengler, 1949), any mineralised cupolas or elevations over the Schellerhau granite body were eroded. Greisen occurrences within the SG1 (Fig. 7.1) represent either the root zones of eroded tin mineralization or are exogreisens of hidden intrusions of SG2 and SG3 intruding at depth the SG1.

Geochemistry

The SG1, SG2 and SG3 rocks chemically represent the suite of P-poor, Li-F-enriched series of leucogranites that exhibit some distinct A-type tendency (Förster et al., 1995; Breiter et al., 1999). The latter are weakly peraluminous ($A/CNK \leq 1.2$), enriched in HREE, Y, Th, Hf, Zr, Sc, Nb, Ta, and U and display elevated abundances of Rb, Li, F, and Sn (Förster et al., 1996) increasing from SG1 to SG3. There is only a moderate chemical contrast between the SG1 and SG2 rocks. The SG3, however, exhibits in distinction to the SG1 and SG2 the chemical and petrographic patterns of alkali feldspar leucogranites (Table 7.1). The SG3 rocks are more highly evolved as also shown by the decreased Zr/Hf and Y/Ho values. Its modal composition (Table 7.2) is due to feldspathisation different to that of the SG1 and SG2 rocks. Topaz occurs mostly poikiloblastic and was classified in Table 7.2 as of secondary nature but in few cases primary magmatic topaz exists in the SGC rocks (R. Thomas, pers. comm.).

The SG1, SG2 and SG3 rocks are interpreted as products of in-situ fractionation of a magma derived from a common deep-crustal parental magma. The chemical and textural specifics of the SG3 rocks were produced when the rock underwent deuteric alteration, and only in few cases (drill cores) the primary textural and chemical features were preserved.

Table 7.1 Chemical analyses of major and trace elements from representative SGC samples.

Number, Granite	Sh-22 (SG1)	# 16 (SG2)	Sh-32 (SG2)	Sh-18 (SG3)
Locality	Abandoned mine Paradies-Fdgr.	Abandoned mine Paradies-Fdgr.	From drill core near Kipsdorf	295m depth, drill core at Kipsdorf
Texture	Very fine-grained, weakly porphyritic, phenocryst-poor	Medium-grained (altered), seriate, weakly porphyritic.	Medium-grained equigranular (slightly altered)	Fine- to medium-grained seriate, albitized
SiO ₂ , wt. %	75.13	72.93	71.91	69.29
TiO ₂	0.057	0.094	0.068	0.022
Al ₂ O ₃	12.60	13.84	14.64	16.97
Fe ₂ O ₃	0.89	1.69	1.25	0.74
MnO	0.02	0.05	0.033	0.09
MgO	0.06	0.17	0.07	0.02
CaO	0.50	0.71	0.92	0.11
Na ₂ O	3.31	3.47	3.91	6.96
K ₂ O	5.33	5.09	4.64	4.09
P ₂ O ₅	0.02	0.04	0.036	0.03
H ₂ O ⁺	0.86	0.72	0.98	0.87
CO ₂	0.05	0.10	0.12	0.15
Li ₂ O	0.037	0.075	0.164	0.016
F	0.51	0.82	1.41	0.12
-O=F	-0.21	-0.34	-0.59	-0.05
Total	99.16	99.45	99.56	99.43
Sn, ppm	18	402	164	42
Nb	51	40	75	72
Rb	782	929	1297	1115
Sr	8.53	34.0	32.1	19.2
Ba	86.9	798	105	83.8
Cs	29.7	40.2	62.4	16.7
Zr	140	121	84.2	40.1
Hf	8.11	7.53	6.71	8.28
Pb	39	413	18	6.9
Th	58.1	39.5	24.9	9.29
U	15.0	17.6	20.8	3.33
Y	103	89.6	44.5	1.55
La	15.8	35.5	26.1	1.14
Ce	32.4	85.3	69.0	2.44
Pr	5.22	11.2	8.55	0.26
Nd	19.0	37.4	25.3	0.70
Sm	6.11	10.3	6.85	0.24
Eu	0.063	0.195	0.12	<0.02
Gd	8.47	10.7	6.01	0.24
Tb	1.94	2.27	1.36	0.06
Dy	14.3	15.4	9.54	0.38
Ho	3.24	3.25	1.99	0.08
Er	10.6	10.5	6.95	0.30
Tm	1.73	1.89	1.42	0.08
Yb	12.0	12.8	11.4	0.93
Lu	1.80	1.97	1.71	0.15
Y/Ho	31.7	27.5	22.4	20.7
Zr/Hf	17.2	16	12.5	4.8

Notes on analytical methods: Oxides, Nb, Sn by XRF, Li by ICP-AES, F by ISE, other trace elements by ICP-MS. Details on analytical conditions and accuracy are available on request from RS. H₂O⁺ not determined. Sample #16 bears little galena.

Table 7.2 Modal mineral composition of representative samples of the SGC.

Samples	Sh-22 (SG1)	# 16 (SG2)	Sh-32 (SG2)	Sh-18 (SG3)
<i>Characteristics</i>	Very fine-grained, weakly porphyritic, phenocryst-poor	Fine-to medium-grained (altered), seriate, weakly porphyritic	Medium-grained, equigranular (slightly altered)	Fine- to medium-grained seriate, albitized
PRIMARY MINERALS: PHENOCRYSTS and GROUNDMASS, vol. %				
<i>Quartz</i>	31.7	30.7	23.6	19.7
<i>K-feldspar</i>	35.8	32.2	30.3	15.3
<i>Albite (An<5 vol.%) (Afs), estim. portions</i>	6.3	5.0	13.0	14.9
<i>Albite-Oligoclase (Plagiocl. An>5 vol.%)</i>	14.2	15.0	13.9	-
<i>Li-mica (Protolithionite to Zinnwaldite)</i>	3.4	3.0	9.0	4.9
<i>Accessories (Titanite, Rutile, Monazite, Zircon, Thorite, Apatite, ...)</i>	0.1	0.8	0.1	0.1
<i>Opaque (Ore) Minerals: Ilmenite, Sulphides</i>	0.1	0.1	0.1	0.1
SECONDARY MINERALS, vol. %				
<i>Albite (Afs, An <5 vol.%)</i>	3.3	6.3	3.0	38.1
<i>Mica from veinlets</i>	-	0.6	-	-
<i>Sericite (\pm Hydrosericite)</i>	4.4	3.6	2.5	6.3
<i>Muscovite</i>	0.1	0.5	-	-
<i>Kaolinite</i>	0.1	1.6	1.5	-
<i>Fluorite</i>	0.3	0.7	0.8	0.6
<i>Topaz</i>	0.2	0.2	2.1	-
<i>Carbonate</i>	-	0.4	-	-
<i>SUM, vol. %</i>	100.0	100.1	99.9	100.0

7.5 Textural studies

The quartz texture of the SG1

The grain size maxima of quartz in the phases and varieties of the Schellerhau granite massif (Figs. 7.3 and 7.4) help to reconstruct the multiphase intrusion and crystallisation history of the pluton. We focussed in our study on SG1 and SG2 phases of the SGC since these are the only ones well exposed at the surface, whereas the afs-rich SG3 varieties are predominantly represented by a few drill cores and are mainly characterised by secondary (recrystallisation) structures which overprint and remove the primary ones.

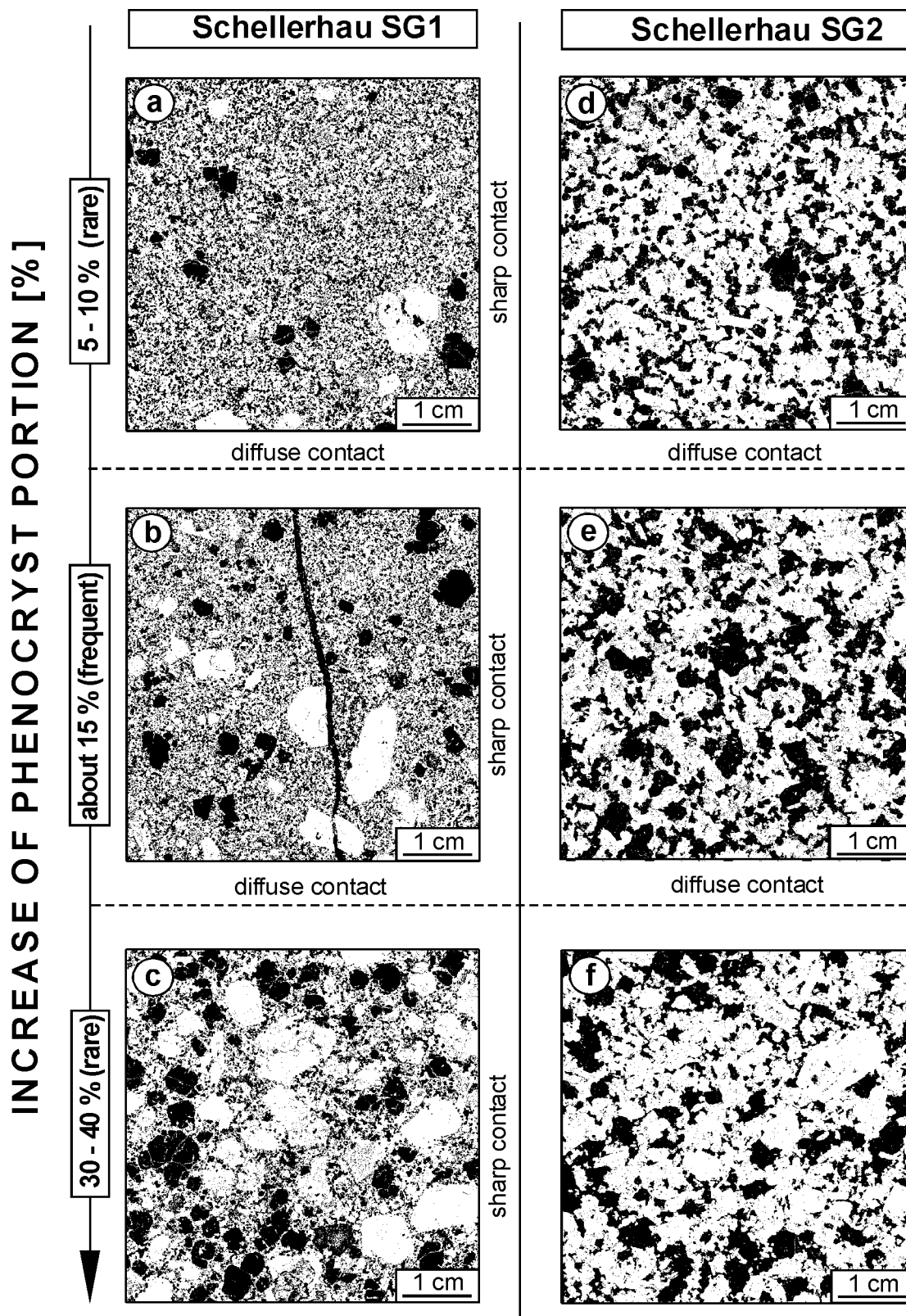
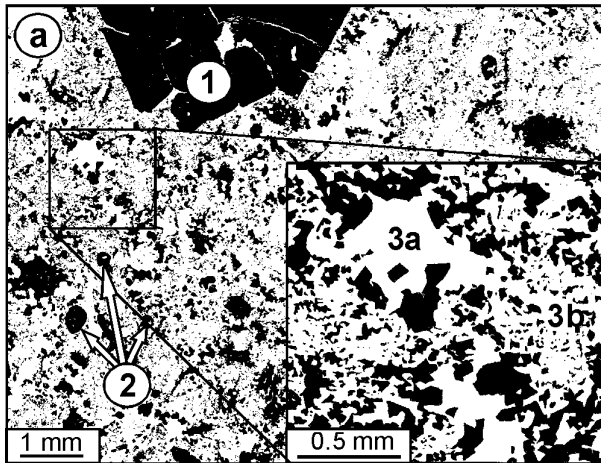
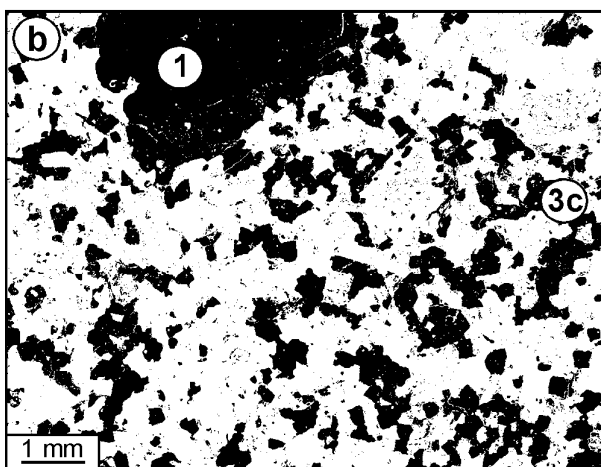
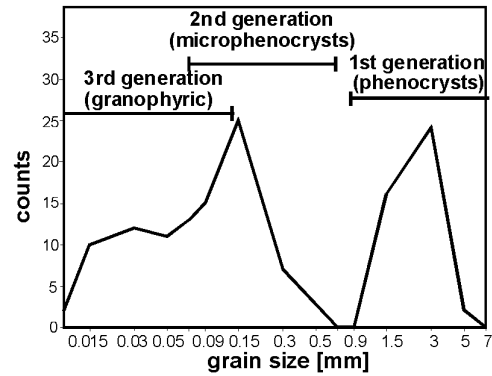


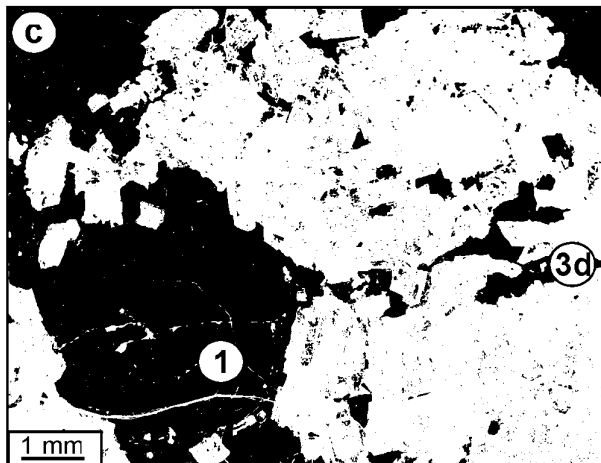
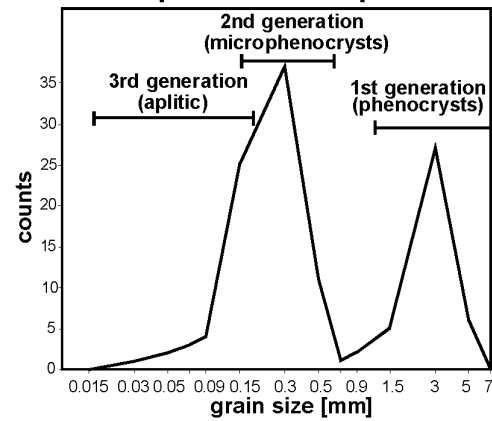
Fig. 7.3 The phenocryst portion of textural varieties of the SG1 and SG2, illustrated by black-and-white prints of lacquer peels. Quartz appears black and feldspars grey or white. The phenocryst portion varies between 5 to 40%; the portion of 15% is most frequent and common.



porphyritic SG1 with microgranophytic matrix quartz and interconnected miarolitic texture



porphyritic SG1 with aplitic matrix quartz



weak porphyritic SG2 with anhedral matrix quartz

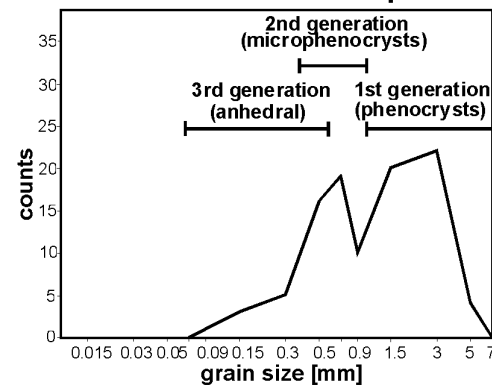


Fig. 7.4 Grain size maxima, shapes and distributions of quartz crystals in the SG1 and SG2. A maximum in the grain size distribution in a magmatic rock indicates a burst of nucleation caused by a high degree of melt undercooling. The texture is contrasted by black-and-white prints of laquer peels. The quartz appears black and the feldspar grey or white. 1 - quartz phenocrysts (1st generation); 2 - quartz microphenocrysts (2nd generation); 3a - granophytic quartz in miaroles; 3b - microgranophytic quartz (3rd generation); 3c - isometric aplitic quartz (3rd generation); 3d - anhedral quartz (3rd generation).

The *phenocrysts* of the early quartz generation (1st generation) are large, 1.5 to 6 mm idiomorphic hexagonal dipyrarnidal crystals with hexagonal prism faces (β -quartz). The median grain size of SG1 quartz phenocrysts is 2.3 mm. The large feldspar phenocrysts (up to 2 cm long) are surrounded by microgranophyric intergrowths with quartz. The “typical” SG1 rocks contain a portion of ca. 15 vol.% phenocrysts (5% quartz + 10% feldspar, less than 1% mica). Phenocryst portions below 12 vol.% and more than 18 vol.%, resp., are rarely represented and occur only in the southern part of the Schellerhau granite (Pöbelknochen and Seifenbusch area, Schilka and Baumann, 1996). The Pöbelknochen (elevation 833 m) represents the uppermost part of the Schellerhau granite massif in the studied vertical profile. The matrix quartz, we call it later 3rd generation, exhibits variable shape. The major portion of the granite is characterised by *aplitic matrix quartz* which contains small crystals (0.02 - 0.2 mm) that are anhedral and more or less isometric. They surround the small euhedral feldspar crystals as clusters or networks or occur as overgrowths on quartz phenocrysts. Crystals (< 0.1 mm) are often in granophyric intergrowths with feldspar. The matrix quartz is in a microgranophyric intergrowth with feldspar especially in the upper 30 m of the cupola region of the locality Pöbelknochen. This texture is superimposed by *interconnected miarolitic texture* (IMT, Candela and Blevin, 1995). The IMT consists of micropegmatitic miaroles that form 3-dimensional interconnected networks (Fig. 7.4). The size of the druses and miaroles ranges from 0.2 mm to pegmatitic cavities of several cm size. Below 800 m elevation the microgranophyric texture of the matrix quartz continuously changes into aplitic texture and the IMT disappears. In the deeper parts, the IMT occurs only rarely and is developed 2-dimensionally exclusively along early fractures that were filled by residual melt portions (locality Paradies-Fundgrube).

Supported by the small grain size of the miarolitic matrix, another quartz type could be detected at the Pöbelknochen locality. However in contrast to the phenocrysts, these *microphenocrysts* are euhedral, hexagonal dipyrarnids of only 0.1 to 0.5 mm size, and are homogeneously distributed within the matrix. They are mantled by matrix quartz, similar to the phenocrysts, and are classified as 2nd quartz generation. The percentage of this frequent grain generation is difficult to determine. For example, the miarolitic SG1 rocks contain 5 to 7 vol.% of this 2nd quartz generation. It may be assumed that this generation is represented also within the aplitic type. However, due to the small grain size it is not distinguishable from the aplitic grains in studies of the lacquer peels and thin sections.

Hydrothermal quartz is well distinguishable from the above described primary magmatic quartz. Based on postsolidus recrystallisation textures (metasomatic overprint and blasteses),

visible CL zonation, and dark red-brown luminescence, those metasomatic quartz textures formed by hydrothermal processes could be excluded from this study.

The quartz texture of the SG2

The SG2 exhibits a weak hiatalporphyritic texture (Figs. 7.3 and 7.4) that was described in the past as homophan (Pälchen, 1968) or equigranular (Schilka and Baumann, 1996). However, the grain size distribution shows a significant hiatus between the both maxima at 0.7 mm and 3 mm. The median grain size of the SG2 quartz phenocrysts (1st generation) is 2.6 mm (the corresponding value in the SG1 for the 1st quartz generation is 2.3 mm). The most frequent phenocryst portion amounts to 15 vol.% as in SG1 (5 % quartz + 10% feldspar). Variations in comparison to the “normal” type are situated only in the southern part of the granite massif near the locality of Seifenbusch. The mine dumps of the abandoned “Paradies-Fundgrube” contain SG2 varieties with up to 35 vol.% phenocryst portions (quartz + feldspar), and others with less than 10 vol.%. The role of the 2nd quartz generation may be similar to that in the SG1. The anhedral matrix quartz (3rd generation) of the SG2 was feeding the irregular cavities between the subhedral to euhedral feldspar crystals and envelopes the quartz phenocrysts.

The quartz texture of the SG3

The textures of the granite phases succeeding SG1 and SG2, in the following summarized as SG3, are heterogeneous, aberant and show no or only few similarities to the previously described textural types (Fig. 7.5). Numerous leucocratic SG3 phases and varieties, hiatalporphyritic, seriate, equigranular and aplitic ones, are, in general, characterised by an alkali feldspar-rich matrix. Within the matrix composed of euhedral, microcrystalline albite plates (20 - 600 µm) occur micropoikilitic, amoebic and snowball-like quartz *phenoblasts* of different size (0.3 - 5 mm). These belong to magmatic-hydrothermal transition processes and form a 4th quartz generation that is grown in a highly viscous crystal mush with a low portion of residual melt in coexistence with fluids exsolved from the melt. Albite has been clearly determined as the liquidus mineral as it forms inclusions in all the other rock-forming minerals. Small isolated K-feldspar phenocrysts have irregular grain boundaries. The quartz crystals contain numerous euhedral albite crystals that also typically occur in the matrix. The irregular grain boundaries of the quartz, surrounding the albite crystals of the matrix, support the idioblastic growth. Partially, the quartz grains show euhedral shape due to occurrence of idioblastic growth creating textures characteristic of highly fractionated Sn-bearing granites (Cobbing et al., 1992; Müller and Behr, 1997; Beskin et al., 1994).

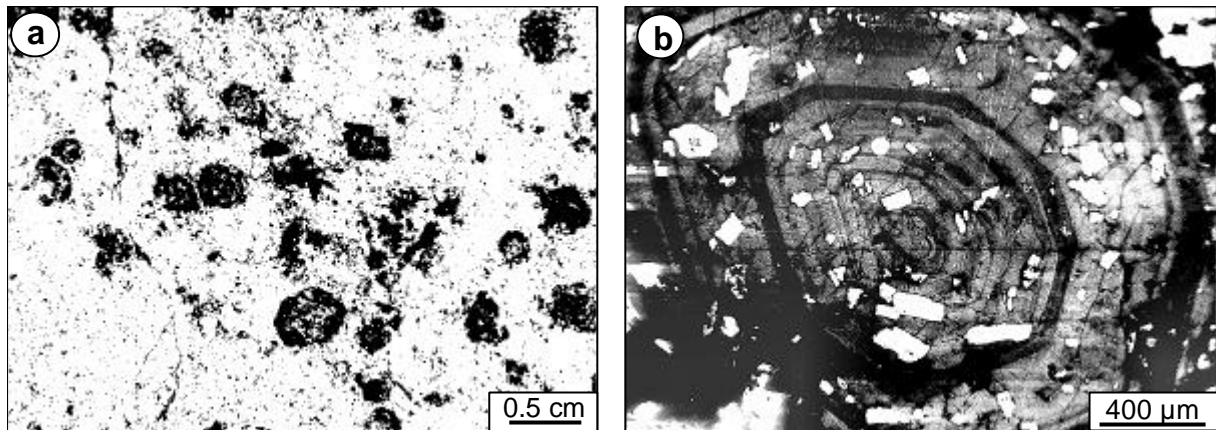


Fig. 7.5 The quartz phenoblasts (4th generation) of the SG3. a - Porphyroblastic texture of the SG3. Quartz is black and feldspar white; b - SEM-CL image of the idioblastic, micropoikilitic snowball quartz of the SG3. The CL and the growth textures are different from that of the phenocrysts and microphenocrysts. The zoning follows the shape of trigonal α -quartz (combination of the hexagonal prism m and the rhombohedrons r and z).

7.6 CL properties of the quartz in the SGC

CL colours

The detected emission spectra (1.3 - 3.1 eV) of the SGC quartz generations are composed of two broad emission bands: blue (2.6 - 3.1 eV) and red (1.75 - 2.2 eV). In addition, an infra-red emission band with low intensity occurs between 1.3 to 1.5 eV. The blue emission (2.6 - 3.1 eV) centred around 2.79 eV is characterised by very high intensity at initial electron bombardment being a typical feature of natural quartz (e.g., Ramseyer and Mullis, 1990). The initial intensity drops by 1/2 to 1/3 after a few seconds (unstable CL) and is stabilised after 30 to 120 s of electron bombardment (stable CL). A slight decrease or nearly constant intensity was observed. The removal of those defects that are luminescence active in the blue emission range is forced in the crystal lattice caused by electron bombardment (γ -radiation) and the related warming of the sample to 70° to 90°C. Alonso et al. (1983) and Gorton et al. (1996) detected three (2.82, 2.92, 3.26 eV) and four (2.48, 2.76, 2.95, 3.18 eV) bands in the blue emission range, respectively. Gorton et al. (1996) suggested that the 3.26 eV band is responsible for the high initial blue intensity that is visible as a blue “flash”.

In contrast to the blue emission, the red emission (1.75 - 2.2 eV) is centred around 1.96 eV and shows an intensity minimum at initial electron bombardment that is flat or exhibits a steep parabolic increase during radiation duration of several minutes. However, the decrease of blue and the increase of red emission are two independent processes because it was observed in

deformed quartz that the red emission remained constant whereas the blue one decreased (authors' unpubl. data).

After subsidence of the initial blue emission, the morphologically-distinct quartz generations of the SGC show different luminescence colours from bright blue to violet to dark red-brown. There are three different luminescence types of quartz in SG1 and SG2 rocks. Nearly all phenocrysts in the SG1 and SG2 sections, exhibit a weak luminescent, dark red-brown phenocryst core. This is surrounded by 100-1000 μm broad, in shades of a blue and violet luminescent phenocryst ongrowth zone. The phenocrysts show an outermost ongrowth zone formed by homogeneous matrix quartz with unstable red-brown luminescence. The spectral analysis of the red-brown luminescent phenoblasts of the SG3 was not feasible due to the high density of feldspar inclusions.

The luminescence spectra at 1.3 to 3.1 eV of these three types show different ratios of red versus blue emission peak areas. The ratio in the phenocryst core is 3.5, in the blue zone 1.4, and in the matrix quartz 2.8. The red-brown luminescent phenocryst core is characterized by a minor concentration of stable blue luminescent defect structures and accompanied by a low red emission intensity, that only slightly increases during continued radiation. In contrast, the blue luminescent quartz exhibits a much higher stable blue luminescence and also a low and slightly increased red emission. The intensity of the blue luminescence of the matrix quartz lies near those of the red core, but the high red intensity is characterised by a steep rise. Consequently, the CL of the two phenocryst luminescence types is more stable during electron radiation than the CL of the matrix quartz.

The infra-red emission between 1.3 to 1.5 eV behaves similar to the red emission, the intensity increases with treatment (electron bombardment) time. The intensity of this emission peak is lower than the blue and red emissions, and it varies strongly within quartz grains that are visible as homogeneous.

Primary growth textures

The phenocrysts and microphenocrysts of the SG1 and SG2 show distinctive growth zonations (Figs. 7.6, .7.7 and 7.8), as is normally more common for rhyolitic phenocrysts (e.g.

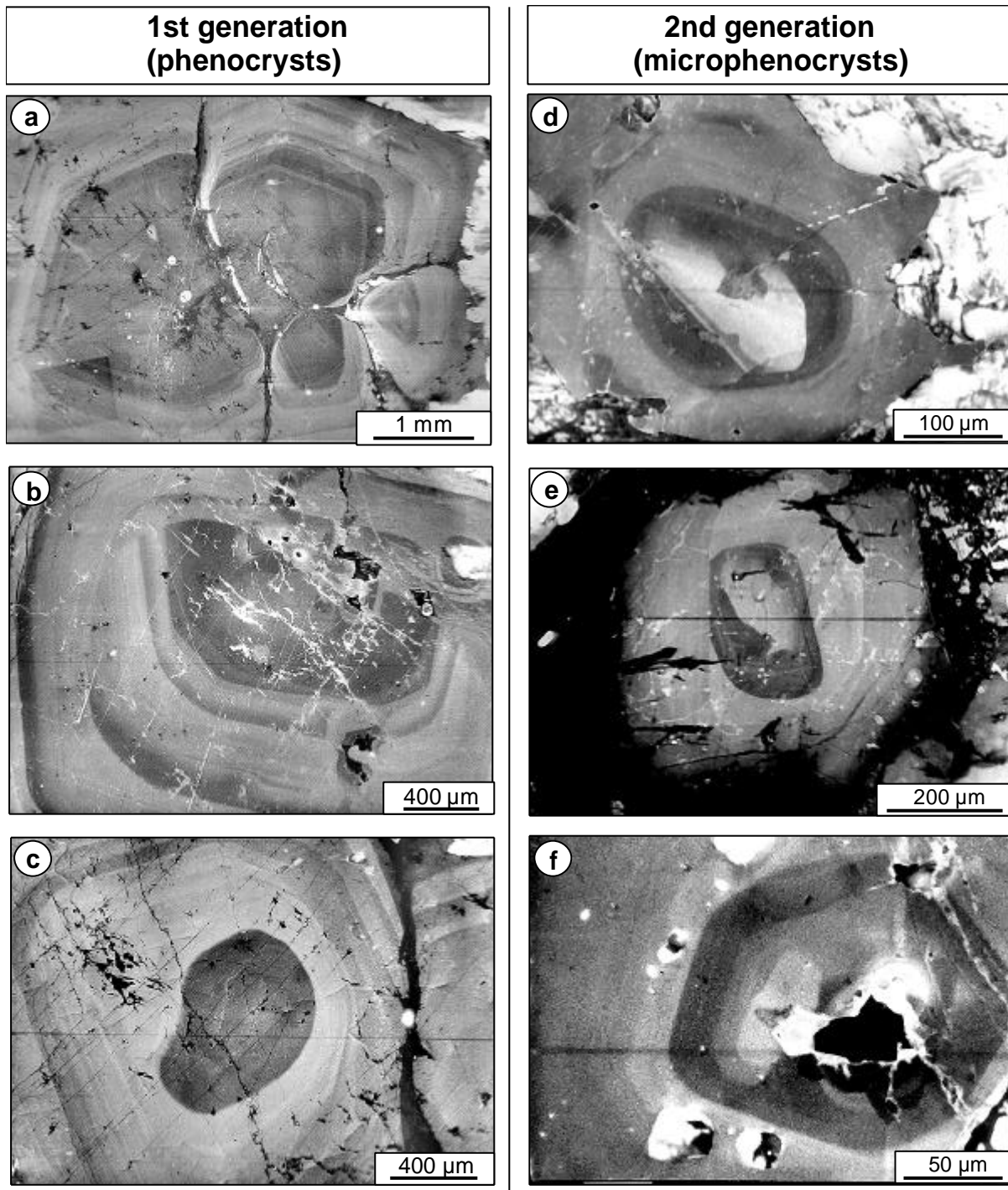


Fig. 7.6 Quartz growth textures contrasted by SEM-CL in the 1st generation (phenocrysts) and in the 2nd generation (microphenocrysts) of the SG1 and SG2; a - hexagonal dipyramidal phenocryst with hexagonal prism faces (β -quartz) (SG1); b - microphenocryst (SG1) with anhedral ongrowth rim; c - phenocryst (SG2) with different resorbed surfaces; d - microphenocryst (SG2); e - phenocryst with rounded (resorbed) core (SG2); f - microphenocryst nucleation on K-feldspar (black) (SG2).

Laemmlein, 1930; Schneider, 1993; Watt et al., 1997). The existence of euhedral quartz phenocrysts in granites showing CL-contrasted growth textures is currently not known to be common and was described in only a few cases (Frentzel-Beyme, 1989; Seltmann, 1994; D’Lemos et al., 1997; Müller and Behr, 1997). The detailed analysis and comparison of growth textures of ca. 40 phenocrysts and 50 microphenocrysts in SG1 and SG2 allow the correlation of significant growth textures indicating a common crystallisation history.

All phenocrysts of the SG1 and SG2 exhibit a dark red-brown luminescent rounded or globular core (zone 1). Internally, the dark core zone does not show contrasted growth textures. Weakly contrasted growth zones occur exclusively in the marginal zone (zone 1a). The crystals used tiny mica, albite or orthoclase crystals as nuclei. Large crystal nuclei (e.g., mica and K-feldspar) often serve as growth centers for two to five quartz crystals simultaneously, and growth impediments are typical (Fig. 7.6a). Such grain clusters may break up during magma flow, leading to single grains, showing different growth rates in the various growth directions. In the case of small nuclei, isolated crystals develop.

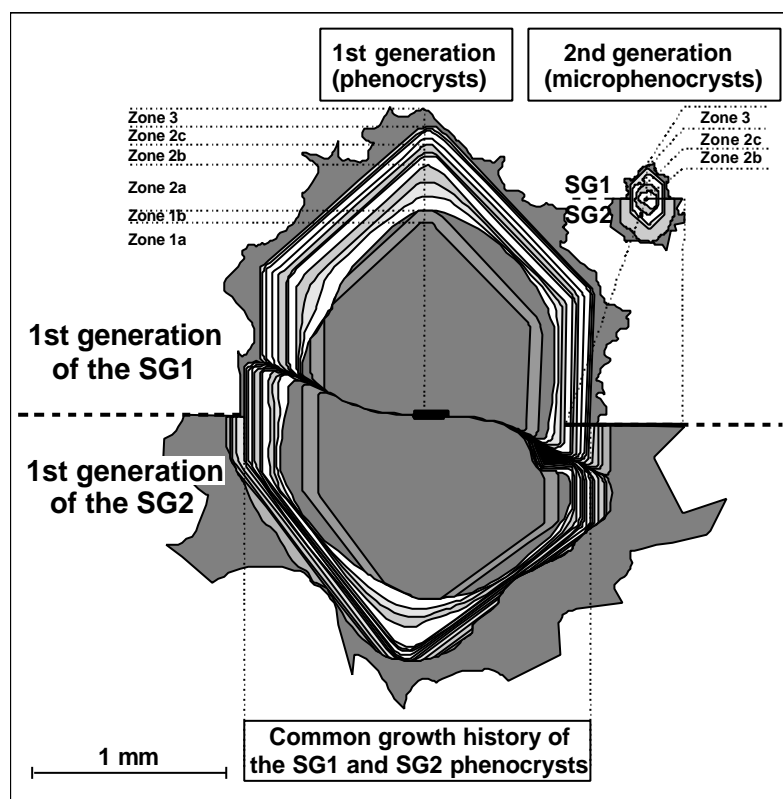


Fig. 7.7 Schematic representation of quartz growth textures contrasted by SEM-CL and their correlation with the 1st generation (phenocrysts) of the SG1 and SG2. Two different euhedral quartz generations continue to grow simultaneously with the beginning of microphenocryst growth in the step zone 2b. The subordinate zones 2a, b and c are characterised by a gradual change from bright blue to violet luminescence. Both the phenocrysts and microphenocrysts are hexagonal dipyrmidal β -quartz crystals with hexagonal prism faces.

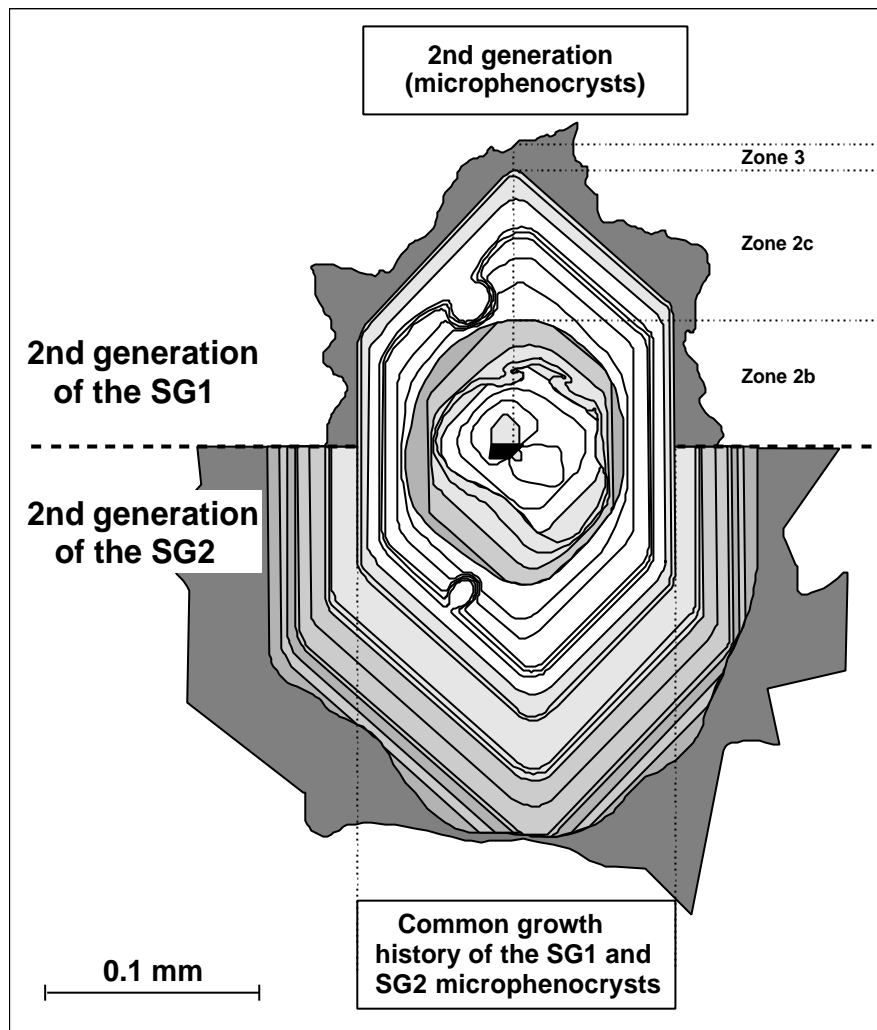


Fig. 7.8 Schematic representation of quartz growth textures contrasted by SEM-CL and their correlation with the 2nd generation (microphenocrysts) of the SG1 and SG2. The frequent impediments of the zone 2c were caused by vapour bubbles that stuck to the crystal surface and hindered the growth.

The stage of red-brown growth ends with resorption (rounding) (Figs. 7.6b, c). The evidence of resorption is the cutting of zonations of zone 1a. The degree of resorption differs strongly in the individual crystals, and most of the euhedral crystals develop a globular shape. This is succeeded by a blue to violet growth zone (zone 2) that may be subdivided into three sub-zones (2a, b and c). Internally, these sub-zones show a gradual transition from bright blue to violet. Within the sub-zones are oscillatory zonations of 2 to 20 μm thickness. Zone 2 may have up to three subordinated resorption phases, where the resorption is only slightly developed and is not detectable in each crystal. The oscillatory zonation of zone 2 in the SG1 phenocrysts disappears in the direction of the red-brown luminescent rim (3rd generation, zone

3). In contrast, zone 2 in the SG2 phenocrysts is disturbed by resorption. This is followed by a homogeneous red-brown anhedral growth rim.

In addition to the 1st generation of quartz phenocrysts, the 2nd generation of euhedral quartz (microphenocrysts) occurring in the miarolitic SG1 (Figs. 7.4 and 7.8) exhibits clearly-contrasted growth textures with oscillatory zones of $\geq 2 \mu\text{m}$. The growth textures belonging to different crystals may be correlated as genetically-linked generations. The nucleation of the second generation can be reconstructed in detail (Fig. 7.6d-f). Exclusively, tiny K-feldspar crystals serve as crystallisation centre for quartz that started growing simultaneously at many places on the feldspar surfaces. With increasing size the growing crystals touch and unify to a single crystal. It is significant that these crystals of the 2nd generation do not show the growth impediments that usually develop during growth of neighbouring crystals (such as phenocrysts of 1st generation). The crystals of the 2nd generation could grow in the melt unimpeded and have only few small lobate impediments. Consequently, the crystals accumulated in a later crystallisation stage to intergranular clusters that are situated among the feldspars and form net-like envelopes around the feldspar crystals as visible by CL (Fig. 7.9). The crystal growth begins with bright blue luminescent quartz which merges into violet during further growth. This growth stage is accompanied by an early simultaneous resorption and by a subsequent distinct resorption stage (Fig. 7.6d-f). The overgrowth zone changes from bright blue to violet again. Within this zone lobate impediments often occur. Such structures could not be observed in large phenocrysts of the 1st generation. Marginally, the SG1 microphenocrysts lose their zonal structure and merge into homogeneous, dark red luminescent, anhedral growth rims. In contrast, the marginal zone of the SG2 quartz concludes with resorption, similarly to the SG2 phenocrysts. Finally, the SG2 microphenocrysts show ongrowth of a homogeneous, red-brown luminescent anhedral generation (3rd generation, zone 3).

The average grain size of the microphenocrysts (0.07 - 0.6 mm, Fig. 7.4) is lower in the SG1 than in the SG2 (0.3 - 0.9 mm). The comparison of grain size maxima of the miarolitic SG1 (0.15 mm) with the aplitic SG1 (0.3 mm) shows that the grain size of this generation increases in the aplitic SG1. The CL observations allow the conclusion that this increase of grain size is caused by a broader anhedral growth rim in the aplitic facies. In contrast, the grains of the miarolitic variety exhibit either no or very thin growth rims. Thus, the measured average grain size of the miarolitic variety represents the “true” size of the SG1 microphenocrysts.

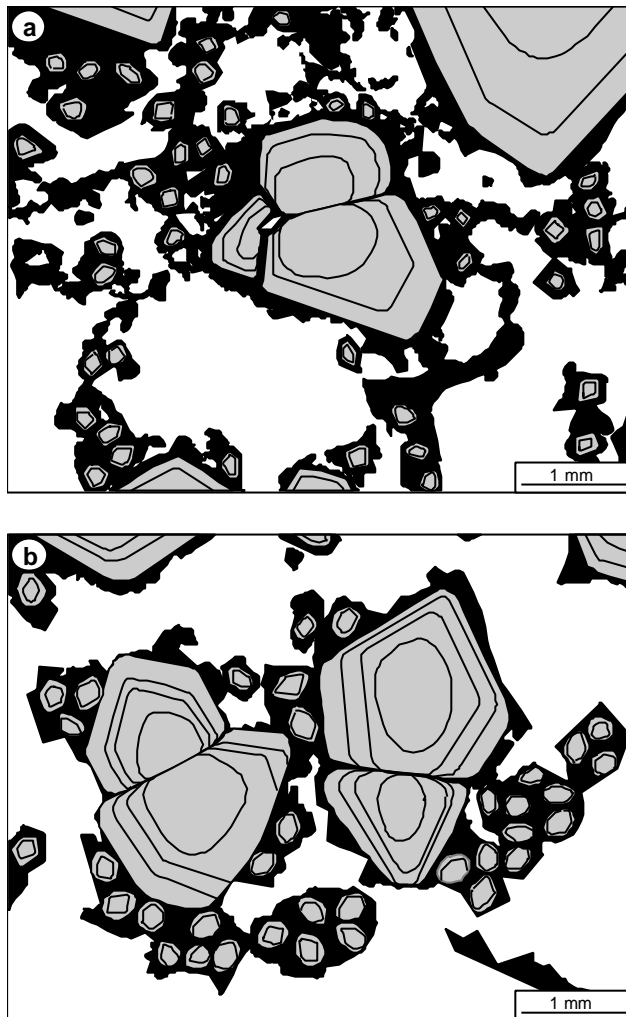


Fig. 7.9 Distribution of the 1st (large grey grains), 2nd (small grey grains) and 3rd generation (black) in the quartz framework a) of the SG1 and b) of the SG2 in thin section images.

Although the euhedral 1st and 2nd generations show different grain size range, it is justified to correlate their growth textures. The microphenocrysts have initial growth during the growth of zone 2b of the phenocrysts. Both exhibit the same resorption events, but the resorption is more strongly developed in the microphenocrysts. In exceptional cases, individual crystals form sub-generations between 1st and 2nd generations. These are phenocryst fragments that formed by brittle failure during magma flow and that later continued to grow separately (Fig. 7.6a). According to habits, internal zonation and luminescence behaviour, the 1st and 2nd generations of quartz phenocrysts are similar or identical to those in rhyolites (Schneider, 1993). This observation characterises the original SGC melt as dry felsic (rhyolitic) magma. The growth zoning of phenoblasts of the SG3 (4th generation, Fig. 7.5) shows no similarities to the zoning in the phenocrysts and microphenocrysts of the SG1 and SG2 and develops obviously under magma-hydrothermal transitional conditions when the melt is degassing. It is clearly distinguishable from the postsolidus rearrangements by hydrothermal fluids as outlined above. The phenoblasts consist of sharp-bordered, homogeneous, bright grey and

dark grey contrasted zones (2 μm to 200 μm). Resorption surfaces which resulted in rounding of the crystals cannot be detected. The zoning follows the shape of trigonal α -quartz (combination of the hexagonal prism m and the rhombohedrons r and z). Growth impediments occur around the feldspar inclusions, but the impediments do not form large lobate textures like those in the microphenocrysts.

Secondary CL structures

Primary growth textures and secondary CL structures are distinguished by characteristic features because primary textures were developed during crystallisation and secondary structures formed after growth. Secondary structures overprint and delete primary ones. Cataclasis of crystals (cracks, decrepitated inclusions) cause recrystallisation of quartz that shows different CL characteristics due to formation under different conditions.

Almost all quartz crystals contain dark red-brown luminescent, star-like structures along thin microcracks (< 3 μm). These structures are healed decrepitation traces of micro-inclusions. The ruptures that connect the decrepitation halos can be explained by cooling-induced thermal stresses at grain scales, especially during incoherent β -/ α -transition and isothermal uplift (Sprunt, 1979; Behr, 1989). In the case of dense networks of microcracks a fracture pattern of dark contrasted polygons develops (Figs. 7.6e and 7.10).

White to light gray contrasted structures veining the grains in high intensity are conspicuous in these samples (Fig. 7.6b). Their distribution is inhomogeneous; some single grains are extremely veined and others not. These structures are stable at extended electron bombardment and are rooted in inclusions and neighbored crystals of K-feldspar. The quartz develops white rims at its grain boundaries with K-feldspar. The veins use the decrepitation structures and partially overprint them. All quartz types show light halos around radioactive inclusions.

In addition to thin CL contrasted microcracks (< 3 μm) that connect the decrepitation traces, larger transgranular microshear zones (to 100 μm) showing distinct brecciation of the host quartz occur (Fig. 7.6c). The healed cracks, that are only visible by CL are related to heat generated by friction of crystals in the melt and to post-magmatic deformation.

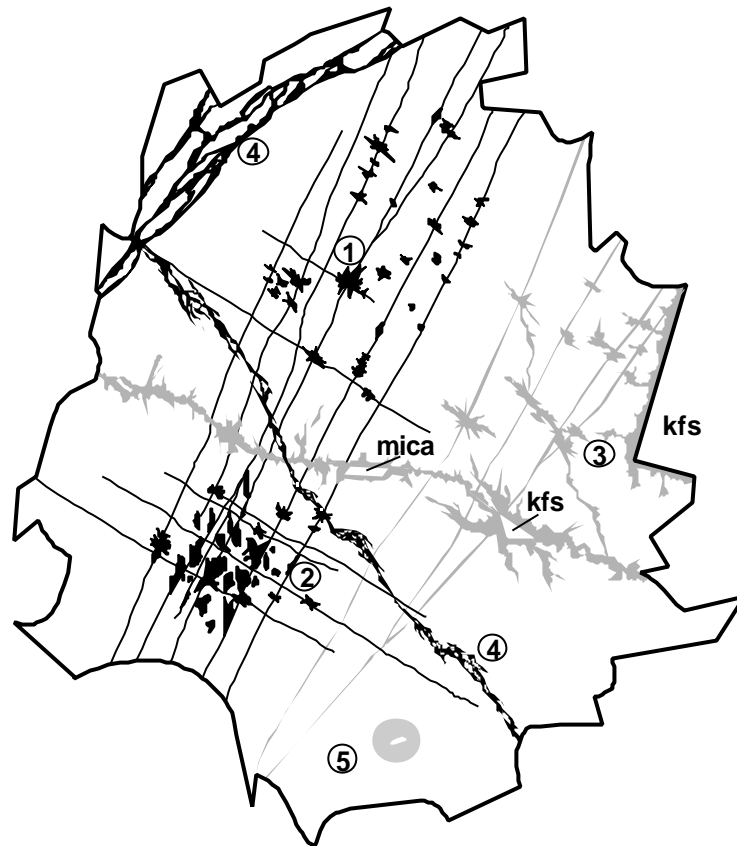


Fig. 7.10 Synoptical scheme of secondary structures contrasted by SEM-CL. 1 - star-like decrepitation traces around fluid inclusions connected with microcracks; 2- pattern of polygons associated with a dense network of microcracks; 3 - light grey contrasted structures rooted in inclusions and neighbored crystals of K-feldspar; 4 - microshear zones; 5 - round halos around radioactive inclusions.

7.7 Relationships between CL and trace element distribution in quartz of the SGC

Different trace element contents in the quartz generations and the heterogeneous incorporation of trace elements in zoned crystals reflect changes of growth conditions like temperature, pressure and composition of the melt. One aim of this work was to determine the trace-element contents of the different quartz generations and their distribution in the zoned phenocrysts, to search for correlations between the CL behaviours and Al, Ti, Fe and Mn.

High Al concentrations occur in the red brown luminescent matrix quartz as a short-lived, intensive initial blue (Figs. 7.11a, c and 7.12). In contrast, the quartz phenocrysts and the quartz of the healed microcracks with blue CL and relative stable red-brown, respectively, contain low Al concentrations. Alonso et al. (1983), Perny et al. (1992), Kalceff and Phillips (1995) and Gorton et al. (1996) suggested that the 3.1 – 3.25 eV emission band correlates with Al of the compensated centres and causes the unstable portion of the blue CL. However, the

investigated quartz shows a decrease of the entire measured blue emission range (2.6 – 3.1 eV) with maximum at 2.79 eV.

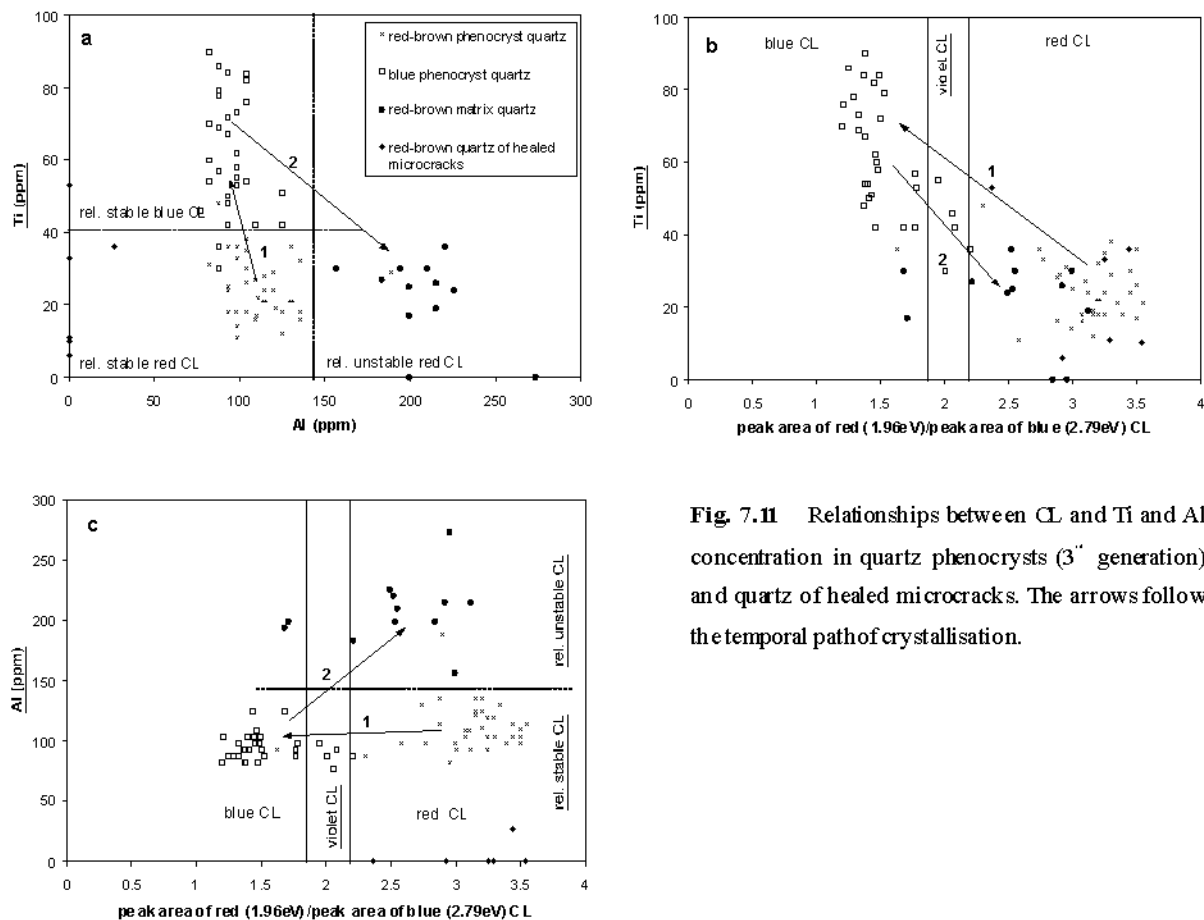
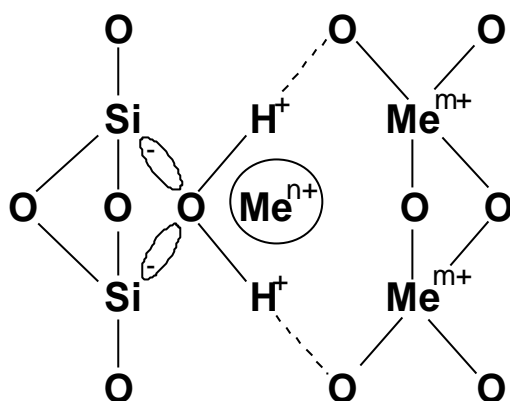


Fig. 7.11 Relationships between CL and Ti and Al concentration in quartz phenocrysts (3rd generation) and quartz of healed microcracks. The arrows follow the temporal path of crystallisation.

Numerous studies of natural and synthetic quartz by electron paramagnetic resonance (EPR) and optical absorption showed that Al^{3+} (M^{3+}) as the most characteristic impurity element of quartz substitutes Si^{4+} in the silicon-oxygen tetrahedra of the regular lattice and Li^+ , Na^+ , K^+ , Fe^{2+} and H^+ (M^{n+}) as ion-compensators enter interstitial positions. The infrared absorption spectra of natural quartz crystals often exhibit sharp, dichroic absorption peaks between 3000 and 3740 cm^{-1} which are associated with hydrogen and hydroxyl acting as a charge compensator of Al^{3+} and of M^{n+} (e.g. Brunner et al., 1961; Kats, 1962; Bambauer et al., 1963). Maschmeyer and Lehmann (1983) gave a first model for the association of Al and hydroxyl in quartz where two OH groups are neighbouring the substitutional M^{3+} (Al^{3+} , Fe^{3+} ...) and interstitial M^{n+} . Stenina et al. (1988) showed on the basis of transmission electron microscopy, X-ray microanalysis and EPR that the trace M^{3+} cations replacing Si^{4+} in oxygen tetrahedra are related to compensating M^{n+} ions and form parts of aqua complexes and clusters as follows:



Scheme 1

The greater part of the structural water, Al-, Li- and Na-ions of hydrothermal and magmatic quartz are incorporated in such aqua complexes. These defect structures are primary and are built into the lattice during crystallisation. Consequently the uptake of M^{2+} and M^{n+} in magmatic quartz is controlled by the presence of water in the melt. The structural water bounded as Si---O-H-H traps scattered electrons during radiation and the bounds are ruptured (McLaren and Phakey, 1966; Maschmeyer and Lehmann, 1983; Stenina et al., 1984). The radiation-induced reaction results in the development of paramagnetic E' centres ($\equiv\text{Si}\cdot$) and/or diamagnetic trapped electron centres ($\equiv\text{Si}:$) which are beside the non-bridging oxygen hole centres (Si-O \cdot) the cause for the emission at 1.96 eV (Griscom, 1985). This process is visible by CL where the formation of point defects of red-brown CL ($<1\mu\text{m}$) takes place in water-rich pegmatitic and granitic quartz during electron bombardment (e.g. Behr, 1989; Schneider, 1993). Nevertheless, the mechanism of transformation is not clearly yet. The higher the content of interstitial molecular water and of associated Me^{n+} and M^{3+} ions in the magmatic quartz the steeper is the intensity increase of red CL during the electron bombardment. Furthermore, the different quartz luminescence types of the SGC reflect the water content of the melt: dry ("rhyolitic") conditions during the nucleation and growth of the red-brown phenocryst core, more wet conditions during the blue phenocryst growth and, finally, wet ("granitic") conditions during the granite emplacement and crystallisation of the 3rd generation. The low Al concentration in the phenocrysts is presumably caused by the limited water supply in the melt. This conclusion confirms Thomas (1994) who determined water contents of melt inclusions of Erzgebirge granites in the range of 2.9 to 8.0 eq. wt. %. These melt inclusions represent the early and late stages of quartz crystallisation, respectively.

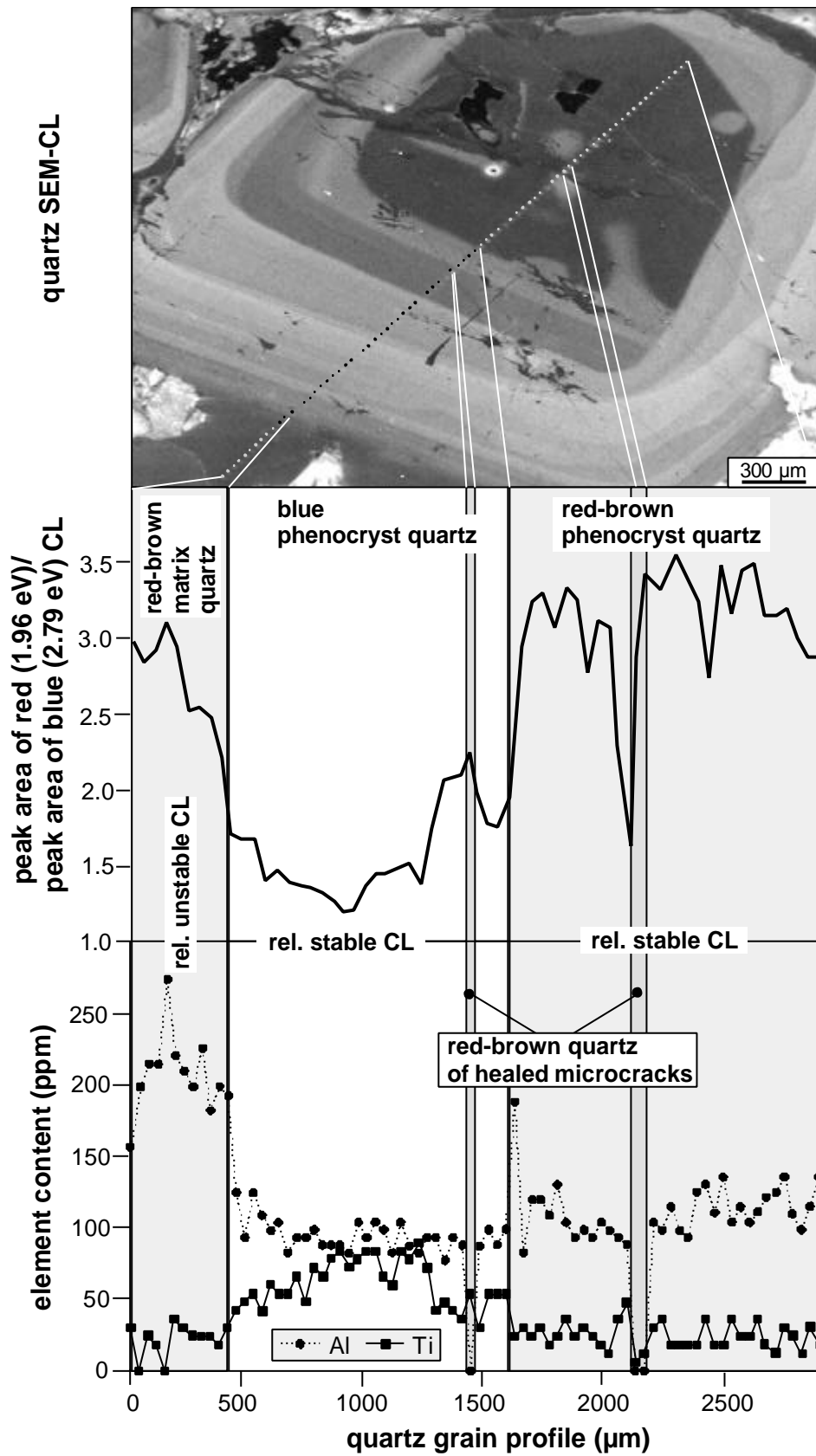


Fig. 7.12 SEM-CL profile across a zoned quartz phenocryst showing the Al and Ti concentration and the ratio of the red and blue emission peak areas.

In contrast to the M^{3+} and M^{n+} the substitutional M^{4+} ions (mostly Ti^{4+}) create relatively stable defect centres without interstitial charge compensators. The blue luminescent quartz of the phenocrysts and microphenocryst shows a strong enrichment of Ti. In contrast the stable red-brown CL of the phenocryst and crackling structures and the unstable red-brown CL of matrix quartz exhibit low Ti concentrations. The high intensity of the stable blue luminescence correlates with Ti-related defect centres (Figs. 7.11a, b and 7.12). These observations are also supported by Kerkhof et al. (1996) and Bruhn et al. (1996). It remains unsolved if the Ti functioned as CL activator or sensitizer (J. Götze, pers. comm.). The dark red-brown luminescent quartz of the healed microcracks and of the decrepitation halos is depleted in Al and Ti (Figs. 7.11a-c and 7.12).

Iron and manganese concentrations of all CL types are below the detection limit of 23 and 26 ppm, respectively.

7.8 A multistage quartz crystallisation model of the SGC

Early phenocryst crystallisation

Initially, nuclei developed in the melt during growth as hexagonal dipyrramids (β -quartz). Such crystals are formed at low values of undercooling ΔT_i (Kirkpatrick, 1975; Allègre et al., 1981; Swanson and Fenn, 1986; MacLellan and Trembath, 1991). The value of ΔT_i is the difference between the liquidus temperature and crystallisation temperature. At such conditions, the nucleation rate is low (Swanson, 1977), and only a limited number of nuclei may be formed in the melt.

The nucleation of quartz crystals of the 1st generation, and 2nd generation, as well took place in few cases on growth centres that are formed by tiny K-feldspar, albite and mica crystals. Their joint occurrence allows to interpret them as microenclaves that are in disequilibrium with the melt. Especially the alkali feldspar residues are often corroded until nearly complete resorption.

The euhedral habit of the phenocrysts seems to indicate unimpeded crystallisation in the melt, maybe due to high charge potential. The hexagonal habit of the zoning (β -quartz) indicates that the phenocrysts crystallised at about 750 °C (7 kbar; Yoder, 1950) and that the melt shows a H_2O -content of <2.5 wt% (Johannes and Holtz, 1996). Evidence for possible maximum depths of first nucleation for crystallisation of Erzgebirge tin granites is provided by microthermometric studies of silicate melt inclusions in quartz phenocrysts (Thomas,

1992), which indicate the depth of magma formation of up to 21 km (Fig. 7.13). The results of melt inclusion studies (Thomas, 1994) on granitic quartz form a p-T-t path that tracks the entrapment of melt during quartz growth in different stages of magma uprise at various crust levels. This synoptical information based on a few hundreds of inclusion data reflects the stages of melt evolution. To reconstruct in detail from which defined growth zone of a single quartz phenocryst an individual melt inclusion was measured requires application of more sophisticated methods (oriented sections, CL, SIMS).

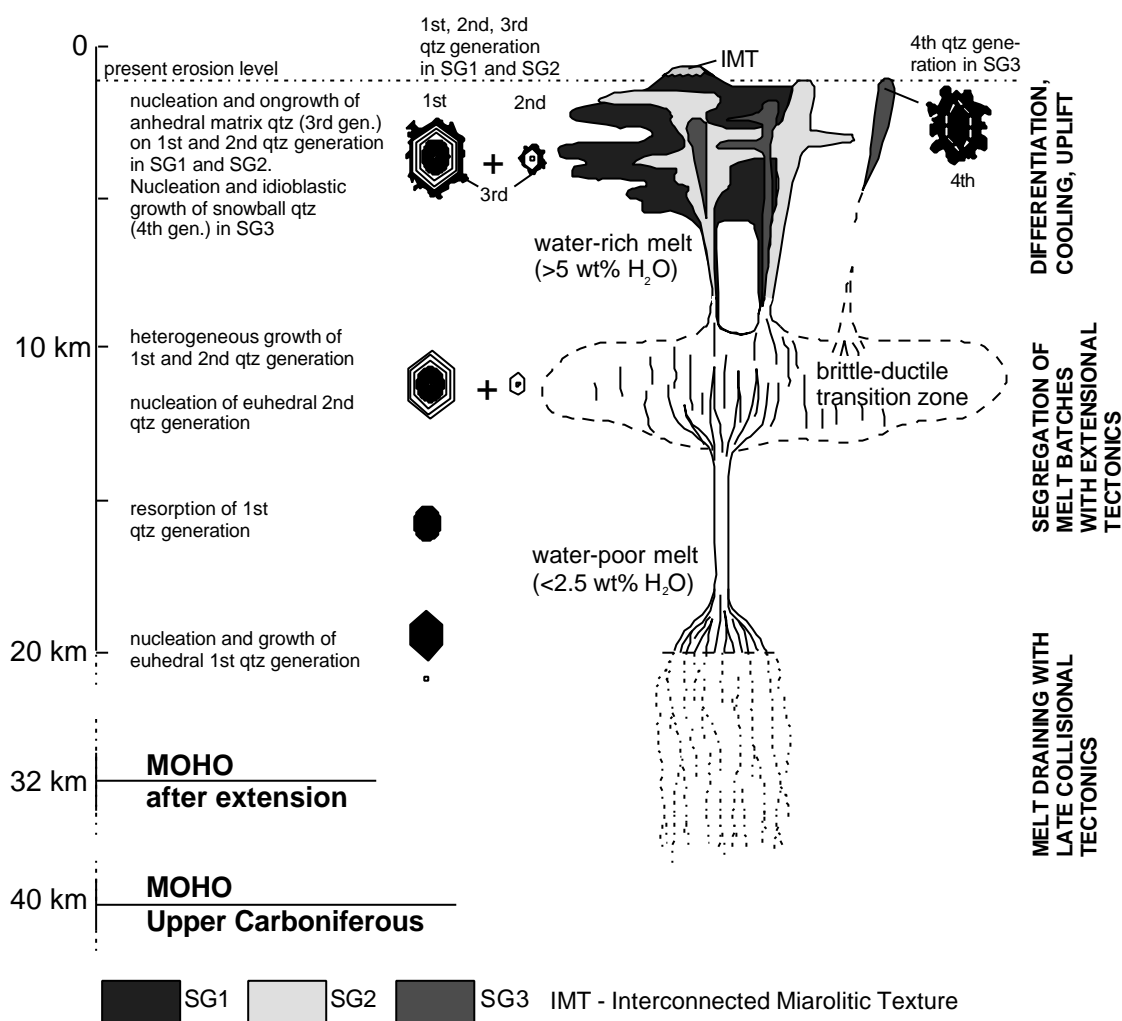


Fig. 7.13 The quartz crystallisation model of the Schellerhau granites. Scheme shows nucleation, growth and resorption of four different quartz generations at its formation depths and resulting growth patterns. The evolution scheme of the SGC considers melt generation from the lower crust under decompressional, late collisional tectonics of the Variscan orogen in the Upper Carboniferous. Extensional tectonics control the segregation of melt batches and multiphase intrusion of SG1, SG2 and SG3 into a subvolcanic level.

Weakly CL contrasted growth zones developed only during the final stage of initial growth (*red-brown luminescent* core zone 1, Fig. 7.7). These may be either self-organised (oscillative) growth zones or zones disturbed by disequilibrium with the melt. The growth of zone 1 ended abruptly by strong resorption of the initial crystallisation stage. Rapid, isothermal ascent of the magma into higher crust levels explains the resorption that produced rounded crystals (Holtz and Johannes, 1994). There is no evidence for magma mixing, neither from the chemical evolution of the intrusion sequence nor from the element profiles in the feldspars (authors' unpubl. data).

The growth of the *blue luminescent zone* begins (zone 2) in a higher crust level, at weakly-undercooled melt conditions (Fig. 7.13). The euhedral unimpeded growth continues, with the distinction, that periodic, fine laminae, 5 - 20 μm broad oscillatory zones form in the 300 to 1000 μm broad zone 2.

Cyclic, self-organising oscillation growth is only possible when the melt cannot convect and the chemical bulk composition remains constant. Despite the obvious homogeneity of the blue growth zone a number of events are documented that possibly reflect changes of the melt conditions (Figs. 7.9 and 7.13):

1. Within zone 2 occurs three times the gradual change from bright blue to violet. These sub-zones (2a, b and c) stop abruptly and the next zone starts growing with bright blue CL.
2. A second nucleation stage, that begins with the growth of zone 2b in the phenocrysts occurs. Crystallisation of the 2nd euhedral quartz generation (microphenocrysts) starts (Fig. 7.7, 7.13). The second nucleation stage requires a change in temperature/pressure conditions (Sibley et al., 1976).
3. Furthermore, up to three subordinated resorption stages develop. Only one of them coincides with the abrupt change of violet to blue luminescence (border of zone 2b to 2c). The other two resorptions are situated within the zones 2a and 2b, respectively. The latter resorption stages are more clearly developed in the microphenocrysts than in the phenocrysts.
4. Also obvious are frequent lobate impediments occurring in the zone 2c, especially of the microphenocrysts (Fig. 7.8). The impediments may be caused by vapour bubbles which stuck to the crystal surface and hindered growth. The bubble formation may be explained by depressurisation (degassing) and related foaming (1st boiling of melt) prior to the main intrusion.

The equilibrium of the bulk melt in the reservoirs, that is responsible for the blue luminescent zones, occurred for a long time, and was only slightly disturbed. Stepwise ascent along short distances or convection may be the cause of weak undercooling in the melt. The initiation of growth of the microphenocrysts of zone 2b caused two different euhedral quartz generations that continue to grow simultaneously. The nuclei of the microphenocrysts surrounding one and the same crystallisation centre unify themselves during continued growth to one single crystal which contrasts with the nucleation behaviour of the 1st quartz generation. This may be due to lower charge potential of the 2nd quartz generation.

Melt separation, intrusion, and main crystallisation of SG1, SG2 and SG3

Generally, the 1st and 2nd quartz generations of the SG1 and SG2 have a common crystallisation history as outlined above. Only during the growth of zone 2b, the SG1 melt separated from deeper located melt reservoir and intruded at a subvolcanic level. The microgranophyric and aplitic matrix quartz, both of which crystallised in the intrusion level, represent as 3rd generation (zone 3) the final crystallisation. The textures indicate extreme nucleation, low growth rates and that the melt was strongly undercooled (Swanson and Fenn, 1986). MacLellan and Trembath (1991) show, that porphyritic textures in which quartz occurs as unit of phenocrysts and aplitic matrix grains (Kirkham and Sinclair, 1988) are textures of rapid cooling. Granophyric intergrowths in the groundmass and matrix quartz overgrowing the phenocrysts are common. Consequently, the quartz phenocrysts were already present, when the matrix and granophyric quartz crystallised. In addition to the textures, the geomorphological and stratigraphic considerations of Spengler (1949) and Schust (1980), who concluded a ca. 1,000 m thick cover at the time of intrusion, support the subvolcanic nature. Geothermobarometric data give a paleo-intrusion level of the various tin granites of the Erzgebirge between 200 and 3,000 m (Seltmann et al., 1992).

The locality *Pöbelknochen* (833 m) represents the roof of the Schellerhau massif. There are diffuse contacts between “normal” SG1 rocks (with 15% phenocrysts) and local zones of SG1 variations with extremely variable phenocryst content. We interpret the latter rocks as result of highly dynamic magma near the intrusion centre. Possible interpretations include mixing of forerunner marginal and main phase magma in the immediate roof parts of the intrusion, or magma schlieres with variable phenocryst content, or melt batches intruding subsequently to the normal SG1 emplacement. Except for the marginal intrusive endocontacts, only at *Pöbelknochen* few xenoliths of the metamorphic cover are incorporated in the granite body. The interconnected miarolitic texture (IMT) found at *Pöbelknochen*

clearly developed in the granite variety with microgranophyric matrix quartz of SG1 (0.01 - 1 mm). It represents a snapshot of a special type of volatile-phase permeability that occurs in the upper part of granite complexes (Candela and Blevin, 1995). The volatile phase was enriched beneath the impermeable roof of the intrusive body, infiltrated earlier crystallised marginal granite intrusion phases and reacted with the crystallising magma itself. The roof impermeability was formed through rapid cooling (and pressure release quenching, resp.) when the granite melt intruded zones of sharp thermal gradient that is developed best at subvolcanic crustal levels (Seltmann, 1994). The IMT disappears beneath the top of the Pöbelknochen and merges into aplitic texture. Towards deeper parts of this elevation, the IMT is developed only along a few joints that were used after their opening as fluid pathways. Feldspar phenocrysts are surrounded by granophyric intergrowths with quartz caused by undercooling due to degassing of magmatic vapour phase and related pressure release. The locality might represent according to gravity data (Tischendorf, 1964), the central part of the NNW striking intrusion axis and, moreover, the fluid-enriched carapace above the intrusion centre.

Because the 1st and 2nd quartz generations were resorbed in SG2 but not in SG1 (Figs. 7.7 and 7.8), we conclude that the melt/crystal ratio remained nearly constant in SG1. The resulting slope of the P-T path of the SG1 melt ascent should run along the liquidus curve or be more flat in response to the water content of the melt (Holtz and Johannes, 1994; Johannes and Holtz, 1996).

After the SG1 melt portion separated from the deeper reservoir, the remaining phenocrysts continued to grow to another 10 to 15 vol.% and the microphenocrysts of the 2nd generation increase their volume by 100 vol.% until the SG2 melt separated from the reservoir and intruded the subvolcanic level that was earlier reached from the SG1 portion. Based on the extreme degree of phenocryst rounding, the melt/crystal ratio must have increased and the ascent was nearly isothermal. The anhedral matrix crystals are in comparison to the SG1 less but larger (0.08 - 0.6 mm), and indicate medium to low undercooling (Swanson and Fenn, 1986). The SG2 could use the intrusion path of the SG1 as is indicated by the spatial distribution of the SG2 along the SG1 flanks and that at depth the SG2 is situated parallel to the SG1 intrusion axis. Because the magma of the SG1 intrusion pre-heated the intrusion level and formed a thermal barrier by rapid cooling of its roof, the cooling of SG2 occurred more slowly as indicated by the seriate to equigranular textures of the latter. Chilled margins at some contacts and sharp borders of SG1 fragments within SG2 provide evidence that the SG1 was already fully crystallised when the SG2 intruded. It is postulated that the intrusion of both

granites occurred in the period of crustal uplift and rapid erosion so that the crystallisation process happened within changing p-T gradients.

The SG3 represents the end member of the geochemical differentiation of the Schellerhau granite massif. Despite its geochemical and genetical relations with SG1 and SG2, the SG3 does not show textural similarities. Geochemical evidence (REE patterns, Zr/Hf) indicates that the melt originated from the same reservoir. But, texturally, the phenocrysts of the 1st and 2nd generations are missing as expected. The sealed amoebic grain boundaries of snowball quartz (4th generation) show replacement and idioblastic growth with entrapment of numerous matrix crystals. The crystallisation of this phenoblastic quartz type occurred in the last stage of crystallisation representing the fluid-saturated, highly-evolved alkali feldspar-rich residual melt. Oscillations of rapidly increased velocity of quartz growth enabled zonal entrapment of albite. At slow growth velocity quartz “snowplowed” the albite tablets in the melt and albite-free zones of quartz were developed. This crystallisation stage is representing the magma-hydrothermal transition when the melt is becoming highly viscous after releasing its magmatic vapour phase (magma degassing due to hydraulic fracturing).

The trigonal habit of the zoning (α -quartz) indicates that the phenoblasts crystallised at <600°C (<1kbar). The phenoblasts which crystallised in the subvolcanic level indicate a late-stage H₂O-content of >5 wt% in the melt (Yoder, 1950; Thomas, 1994; Johannes and Holtz, 1996).

The quartz phenoblasts and hydrothermal greisen quartz cannibalised more or less the older quartz generations, thus reflecting the intense late- to post-magmatic fluid-rock reactions that are closely related to tin mineralisation and deuteric alteration.

7.9 Summary

The application of cathodoluminescence combined with grain texture and grain size analysis facilitates the identification of four quartz generations in the SG1, SG2 and SG3: ① large ($\varnothing=2.3$ mm) euhedral hexagonal dipyrmidal zoned *phenocrysts* (1st generation); ② hexagonal dipyrmidal zoned *microphenocrysts* (2nd generation) ($\varnothing = 0.2$ mm); ③ *matrix quartz* (3rd generation) developed *aplitic and miarolitic* ($\varnothing=0.1$ mm) in the SG1 and *anhedral* ($\varnothing=0.3$ mm) in the SG2; and ④ zoned, micropoikilitic, amoebic and snowball-like quartz *phenoblasts* (0.3 - 5 mm) (4th generation) in the SG3. One maximum of a grain size

distribution plot represents one quartz generation and indicates a burst of nucleation which was caused by a melt undercooling event.

The same grain size, grain habit and the correlatable growth textures of the phenocrysts and microphenocrysts in the different granite varieties give proof of a common crystallisation history until the melts of the three granite varieties SG1, SG2 and SG3 were separated and intruded. Four nucleation events occurred during crystallisation at different crustal levels between about 20 and 1 km depth.

The stable blue CL of the phenocrysts correlates with high Ti concentrations. The unstable blue as well as the unstable red CL are controlled by aqua complexes in the form of $2\text{SiO}_3\text{-H}_2\text{O-M}^n\text{+}2\text{M}^{3+}\text{O}_4$, where M^{3+} is mostly Al^{3+} and M^n mostly H^+ , Li^+ and Na^+ . The slight increase of the red emission intensity during electron bombardment reflects dry conditions during the nucleation and the early crystallisation stage. The steep increase reflects more wet conditions during the granite emplacement and crystallisation of the 3rd generation. The Schellerhauer granite melt is interpreted as one with a dry „rhyolitic“ early stage, due to the euhedral zoned β -quartz phenocrysts formed in water-poor conditions with <2.5 wt% H_2O in the melt and at temperatures about 750°C. The water content of the melt increases during the further development until the melt assumes granitic properties. The 4th quartz generation (snowball quartz) which crystallised in the subvolcanic level indicates a H_2O -content of >5 wt% in the melt and temperatures <600°C. Due to the highly-reactive fluids exsolved in late magmatic stages from the melt, the quartz and feldspar phenocrysts of 1st and 2nd generations were cannibalised and only a few relics of K feldspar remained.

The application of CL is a very helpful and irreplaceable tool for the reconstruction of the crystallisation history of granitoid melts in connection with other methods such as trace-element geochemistry, grain texture and grain size analysis.

8 The genetic significance of snowball quartz in highly fractionated tin granites of the Krušne Hory/Erzgebirge

(this chapter has been published in “Mineral Deposits: Processes to Processing” edited by Stanley et al., Balkema, pp. 409-412, 1999, co-author: R. Seltmann)

8.1 Abstract

Snowball-textured quartz phenoblasts are magmatic-hydrothermal fluid saturation textures and occur widespread in highly evolved alkali feldspar and topaz-bearing granites. They are characterised by zonal arrangement of entrapped matrix minerals (albite, K-feldspar, mica) alternating with inclusion-free zones. Case studies from the Schellerhau and Podlesi granites (Erzgebirge/Krušne Hory) showed a crystallisation sequence albite – K-feldspar – Li-mica – snowball quartz. If the growth velocity increased rapidly, beside silicate melt drops also predated and simultaneously formed matrix minerals were overgrown and trapped in the quartz. CL and growth zoning studies indicate a kinetically caused increase of the growth velocity with crystal size in a nearly non-convecting crystal mush. Wavy zones of snowball quartz are interpreted as products of small scale diffusion fronts which lead to the change of CL properties developed during the crystal growth and caused by rapid variation of the melt conditions.

8.2 Introduction

Snowball-textured quartzes in granitic rocks are ellipsoidal phenoblasts up to 1cm in size. They are characterised by zonal arrangement of entrapped matrix minerals (albite, K-feldspar, mica) alternating with inclusion-free zones (Figs. 8.1 – 8.2a).

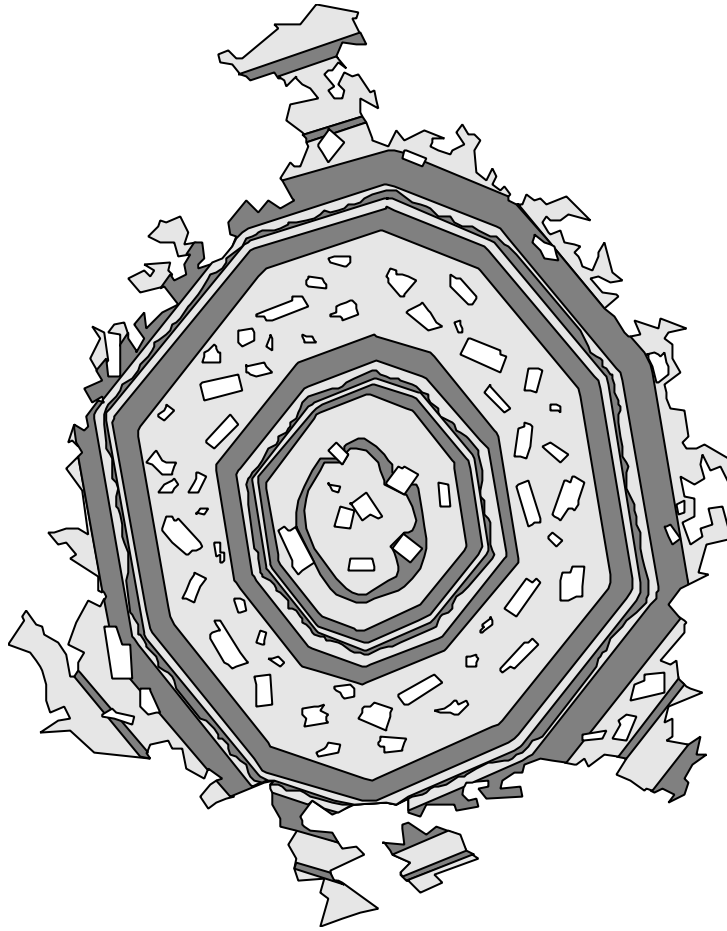


Fig. 8.1 Synoptical scheme of CL-contrasted growth textures in snowball quartz as observed in the Schellerhau SG3 granite and in the Podlesi dyke granite. Quartz crystal size is usually 1 mm up to 1 cm.

Regardless the genetically totally different formation mechanism, these late-magmatic textures have some phenomenological similarities to metamorphic blastesis products also called snowball texture for which the term was first used when crystals grow under shear stress and other minerals were entrapped during rotational deformation.

The snowball texture is typical for highly evolved alkali feldspar and topaz-bearing granites world-wide and its origin is controversially discussed. It is considered to be either metasomatic (e.g. Beus et al., 1962; Sonyushkin et al., 1991), or magmatic in origin (Kovalenko, 1977; Renno, 1997; Poutiainen and Scherbakova, 1998).

Snowball-textured quartz occurs also in the roof of late Variscan tin-bearing alkali feldspar granite stocks of the Krušné Hory/Erzgebirge. For textural, cathodoluminescence (CL) and trace element studies on snowball quartz were chosen the third intrusion stage SG3 of the Schellerhau granite complex (Eastern Erzgebirge/Germany; Müller et al., 1999) and the Podlesí dyke granite (Western Krušné Hory/Czech Republic; Breiter et al., 1997). These

highly evolved, Li-F-enriched alkali feldspar leucogranites belong to the younger granite group and are connected with the Sn-W mineralization of the Krušné Hory/Erzgebirge (Seltmann, 1994). The rocks are emplaced as small stocks, sills and dykes at shallow crustal levels (formation pressure <1kbar).

8.3 Petrography and texture

The texture of the alkali feldspar granites is characterized by porphyritic snowball quartz and K-feldspar, and fine-grained euhedral albite tablets which form the main portion of the matrix. The quartz are between 2 - 5 mm and 0.2 – 1.5 mm in diameter in the Schellerhau SG3 granite and Podlesi dyke granite, respectively. In the Podlesi dyke granite, where snowball quartz and K-feldspar have nearly the same size as the matrix albite, the porphyritic texture shifts into a fine-grained one. The snowball quartz shows continuous growth into the matrix quartz, recognizable by the ramified, amoebic grain boundaries, and penetrates the matrix. Up to 90 vol.% of the modal quartz is accumulated in the snowballs. The crystals contain zonally enriched inclusions of the matrix minerals, such as corroded K-feldspar, mica, metamictic zircon, apatite and above all albite. Furthermore, in many cases fluid and melt inclusions occur. The entrapped albite tablets are often arranged with their long axis parallel to the zoning. Large number of albite tablets envelope the phenoblast edge indicating that the quartz put off the albite tablets during the growth. If the growth velocity increased rapidly the albite and other matrix minerals were overgrown and trapped in the quartz. The general crystallisation sequence is: albite – K-feldspar – mica – snowball quartz.

8.4 CL and growth zoning

The investigated snowball quartz have a red-brown luminescence with weak intensity. The CL spectra show a dominance of the red emission centred at 1.96 eV and low intensity of the blue emission centred at 2.79 eV. During the electron radiation the red emission increases whereas the blue emission decreases visible by the blue “flash” at the first seconds of radiation.

The phenoblasts contain CL-contrasted growth zoning which is visible by using the SEM-CL with 15 kV and a current of 15 mA (Figs. 8.1-8.2). The first growth zones show spherical

shape which changes during the subsequent growth into rectilinear bordered zones with α -quartz habit. The zones have variable width from 2 to 200 μm . Growth impediments around albite inclusions are recognizable as the zoning fits the shape of the obstruction (Fig. 8.2b).

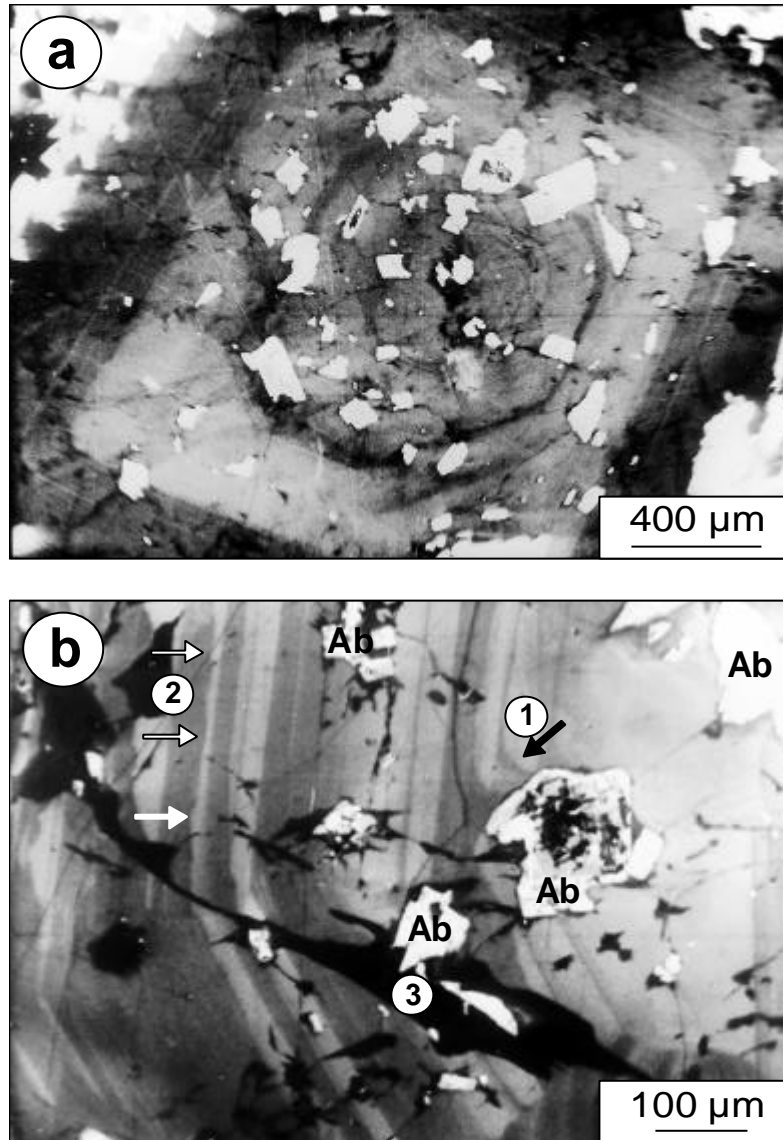


Fig. 8.2 SEM-CL images of snowball quartz of the Schellerhau SG3 granite. a) Snowball quartz with a large number of albite inclusions (white); b) Detail of a snowball quartz showing growth impediments around albite (Ab) inclusions (1), wavy zoning (2), and stress-induced recrystallised quartz (black) around mineral inclusions (3).

These impediments are well developed in the crystal core and are smaller and indistinct in the direction to the crystal edge. This indicates a general increase of the growth velocity with growing crystal size. Between the straight bordered growth zones wavy surfaces occur. They are characterized by convex inlets which are opposed to the growth direction. In contrast to resorption surfaces which are resulted in sharp truncation of the regular zoning and rounded crystal corners (e.g. Shore and Fowler, 1996) the inlets of the wavy surface are much smaller and extend maximal 20 μm in the growth zones and do not cut older zones or round-off corners. The subsequent growth zones are rectilinear bordered again and parallel to the euhedral crystal habit. This feature is in contrast to the wavy zoning which is described in plagioclase by Pearce and Kolisnik (1990) where the subsequent growth keeps the wavy texture. The wavy zones of snowball quartz are interpreted as a small scale diffusion front which lead to the change of CL properties developed during the crystal growth and caused by rapid variation of the melt conditions. The zoning continues into the amoebic crystal margin and into the matrix quartz without changes of the CL properties. Consequently, at least the rims of snowball quartz and the matrix quartz represent one and the same quartz generation. The zoning pattern indicates that the snowball quartz crystallised in-situ without significant magma movement. The tension anisotropy of quartz caused the stress-induced recrystallisation of non-luminescent secondary quartz around albite inclusions (Fig. 8.2b).

8.5 Trace elements

The CL of quartz results from substitutional and interstitial incorporation of trace elements like Al, Fe and Ti and from different types of intrinsic and extrinsic defect centres in the quartz lattice. K and Na were measured to distinguish the Al originated from mineral inclusions from that of the host quartz.

Both, the Schellerhau and the Podlesi snowball quartz, are characterised by in average low Ti concentration of 20 ppm (Figs. 8.3a - 3b). In contrast, the quartz has a variable and mostly high Al content. Near the contact to albite the Al, Fe and Ti content increases caused by diffusion (Fig. 8.3b).

The measured trace elements show no correlation with CL zoning. This is in contrast to rhyolitic phenocrysts where Ti is mainly responsible for the contrasting of the magmatic zoning (Müller et al., 1999). The dominance of red luminescence centered at 1.96 eV

associated with a steep increase during electron radiation indicates high content of Si-OH bonds and molecular water in the quartz lattice (Kalceff and Phillips, 1995).

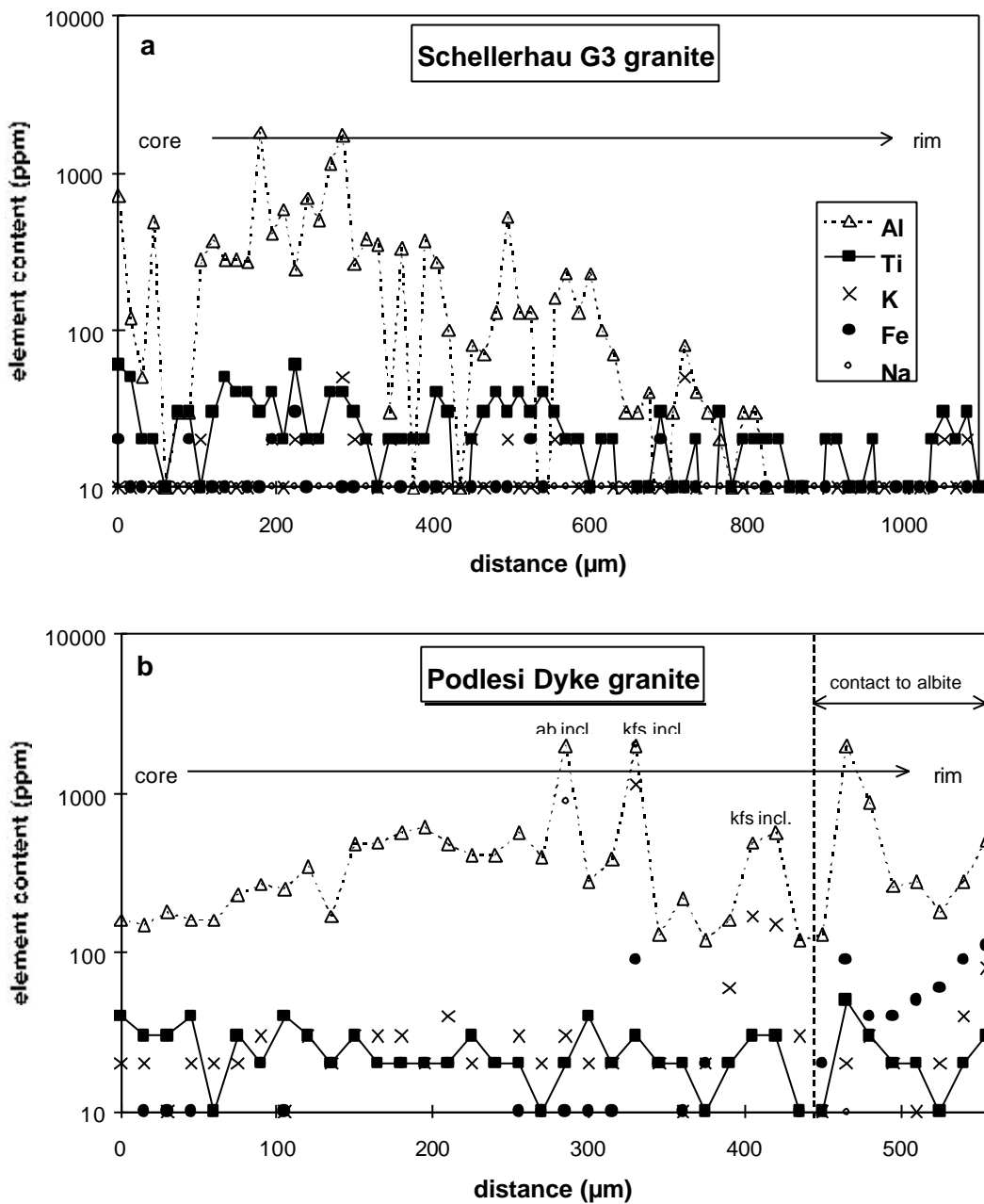


Fig. 8.3 Trace element profiles of snowball quartz of the Schellerhau SG3 granite (a) and the Podlesi dyke granite (b) using electron microprobe.

8.6 Conclusions

The habit and zoning pattern, the arrangement of the enclosed and neighbouring albites and the occurrence of melt inclusions indicate a growth of the snowball quartz in a nearly non-convecting crystal mush. On the other hand, the trigonal habit of the zoning indicates crystallisation temperature of $<600^{\circ}\text{C}$ (at $<1\text{kbar}$). The zoning and CL properties of the snowball quartz show magmatic as well as hydrothermal features.

According to Holten et al. (1997) the observed zoning texture of the snowball quartz mostly reflects an external fluctuation in open systems and is not a product of self-organising growth. The irregular zoning is explained due to periodic degassing during melt cooling in the granite roof (Plimer, 1987).

Due to the highly reactive fluids exsolved in late magmatic stages from the melt, obviously the quartz and feldspar phenocrysts of the early crystallisation stages were cannibalised and mainly resolved.

Consequently, snowball quartz is a textural indicator for fluid-saturated, F-Li-enriched melts of alkali feldspar granites with subvolcanic (shallow) emplacement (Pitfield et al., 1990). Furthermore, it serves as indirect indicator for tin-tungsten mineralisation related to such melts.

9 Cathodoluminescence (CL) of magmatic quartz: Applications to topaz granites from the Hub Stock (Slavkovský Les Mts., Czech Republic)

(this chapter has been submitted to Terra Nova, co-author: M. René and H.-J. Behr)

9.1 Abstract

Topaz-bearing granites from the Hub Stock, hosting the Sn-W deposit Krásno (Slavkovský Les Mountains, Czech Republic), form a stock structure in the SW part of the Krušné Hory/Erzgebirge Batholith. CL facilitates the discrimination of three magmatic quartz generations within these granites, which has given new insights into the textural evolution of felsic igneous rocks. Two phenocryst generations exhibit complex growth zoning with dominant blue CL, similar to those generally found in phenocrysts from rhyolites. They represent a water-poor (<2.5wt% H₂O) “rhyolitic” crystallisation environment in the lower and middle crust. Variation of Ti is mainly responsible for the contrasting magmatic zoning pattern in quartz phenocrysts. Furthermore, the Al/Ti ratio measured by EPMA can be used to distinguish quartz phenocrysts from different magma sources. Unzoned matrix quartz crystallised during and after subvolcanic melt emplacement and overgrew the older phenocryst generations. From the high Al content and the dominance of the unstable red 1.96 eV CL emission, which is associated with hydroxyl defects and adsorbed H₂O in the lattice, it is suggested that the matrix quartz grew in a residual “granitic” melt with higher water content.

9.2 Introduction

Electron-excited luminescence, or cathodoluminescence (CL), is a sensitive method for revealing growth zoning, alteration patterns, grain shapes and different generations of quartz, which are not distinguishable in transmitted or polarised light (e.g. D’Lemos et al., 1997; Watt et al., 1997; Müller et al., 2000). CL colour and intensity in quartz are generally

controlled by activator and sensitise elements (extrinsic lattice defects) like Al, Ti, Fe, Mn, Ge, Li, Na, and H and intrinsic defects (e.g. oxygen and silicon vacancies) (e.g. Sprunt, 1981; Waychunas, 1988; Perny et al., 1992; D'Lemos et al., 1997; Pagel et al., 2000). Al^{3+} , Ti^{4+} , Fe^{3+} , and Ge^{4+} substitute for Si^{4+} and the cations H^+ , Li^+ , Na^+ , Fe^{2+} , and Mn^{2+} function as compensators of the electric charge at interstitial positions (e.g. Bambauer, 1961; Lehmann, 1975; Lehmann and Bambauer, 1973; Maschmeyer and Lehmann, 1983; Weil, 1984). Earlier studies showed a large variation in the trace element content within quartz crystals as well as of quartz crystals from different environments (e.g. Stuttner and Leininger, 1972; Schrön et al., 1988; Blankenburg et al., 1994; Müller, 2000). Spatial variations of CL properties reflect structural and chemical variations within crystals, which are related to crystal growth zones. These variations are caused by fluctuations in growth and diffusion rates in the melt through the crystal-melt boundary layer. Growth and diffusion rate are controlled either by self-organising intrinsic mechanism or an extrinsic mechanism involving physical or chemical changes within the bulk system, such as crystal settling, large-scale convection, magma mixing, ascent velocity and related temperature and pressure changes (e.g. Sibley et al., 1976; Shore and Fowler, 1996), but the problem is to relate the different patterns of zoning to specific genetic processes.

Despite considerable benefits of the phenomenological investigation of the CL of quartz, the relationship between CL properties, trace elements, and petrogenesis is far from being solved. This study is focused on magmatic quartz from the topaz-bearing granites of the Hub Stock hosting the Krásno Sn-W deposit (Slavkovský Les Mountains, Czech Republic). The aim of this study is to explain the causes of the CL of magmatic quartz and to determine the petrological significance of trace element distribution, quartz CL, and of textures visible in CL. Combination and comparison of the CL studies with micro-analytical results (EPMA) has been given new insights into the origin, emplacement, crystallisation, and textural evolution of fractionated Li-F-enriched melts and provide an information link between simplified systems of theory and experiment, and the complexities of natural processes.

9.3 Geological setting

The Krušné Hory/Erzgebirge batholith that extends over an area of about 6000 km², belongs to the largest Variscan granite bodies in the Bohemian Massif (Fig. 9.1). Topaz-albite granites that usually form granite stocks are traditionally related to the younger intrusive complex (YIC) of the Krušné Hory/Erzgebirge batholith (Lange et al., 1972; Fiala 1968). However, the topaz-albite granites of the Hub Stock form part of a complicated stock structure of topaz-albite granites, which are associated with the upper part of the Krásno Sn-W ore deposit (Jarchovský et al., 1994; René, 1998). Topaz-albite granites in this part of the Slavkovský les Mts. are part of the Krudum massif that forms a relatively independent magmatic body on the SW margin of the Karlovy Vary pluton. The emplacement of the granite stock was associated with intensive tectonic deformation of slightly migmatized biotite paragneisses in the overlying pre-Variscan basement. Intrusion breccias described in detail by Jarchovský and Pavlu (1991) and Seltmann et al. (1992) occur in the upper part of the Hub stock and are cemented by topaz-albite microgranites.

Topaz-albite granites of the Hub stock are mostly medium-grained varieties locally accompanied by fine-grained porphyritic topaz-albite granites with characteristic quartz and K-feldspar phenocrysts. The temporal relationship between the medium-grained and fine-grained porphyritic granites cannot be interpreted unambiguously. The contact of both varieties has a tectonic character in some cases and an intrusive character in the other, either gradually passing from one variety to another or linked with the origin of a small coarse-grained zone on the contact of both varieties. The two textural varieties may represent different granitic facies of approximately the same age, the origin of which was controlled by local pressure conditions during emplacement and crystallization (René, 1998)

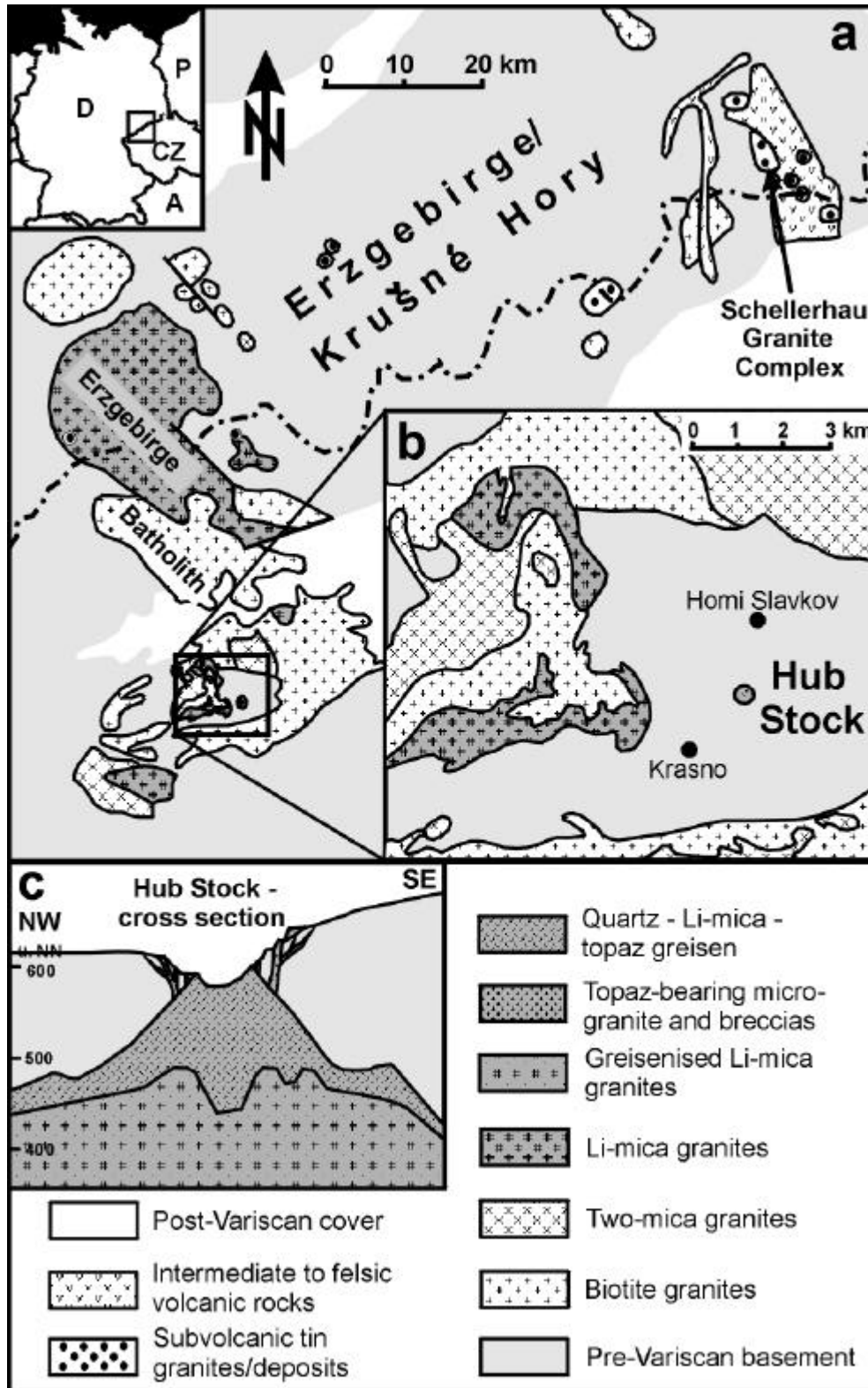


Fig. 9.1 Geological setting of the Hub stock. (a), (b) Geological map of the Krušné Hory/Erzgebirge with the distribution of granite types and the position the Hub stock. (c) Simplified cross-section through the Hub stock according to Jarchovský (1998).

9.4 Petrography

The porphyritic topaz-albite granitic rocks (sample Ju-10) have a fine-grained equigranular groundmass (50 - 100 μm) of anhedral quartz, albite (An_{03-05}), K-feldspar, Li-mica, topaz, muscovite, and accessory minerals (fluorite, cassiterite, apatite, zircon, hematite, sulphides). The megacryst population is dominated by bipyramidal quartz (1.5 - 3 mm), platy Li-mica, and sparse K-feldspar up to two centimetres in size.

Topaz-albite microgranites (sample Ju-20) found in the upper part of the Hub stock, that form the matrix of the intrusion breccias, are aplitic (grain size: 200-500 μm) and rarely porphyritic. The microgranitic rocks include K-feldspars several millimetres in size as well as bipyramidal quartz (1.5 - 3 mm). The groundmass of the microgranitic rocks is composed of anhedral quartz, albite, Li-mica, K-feldspar, and primary topaz.

The application of CL facilitates the identification of a third magmatic quartz population beside the large phenocrysts (qz1) and the matrix quartz (qz3) in both granite varieties (Fig. 9.2a, b). Like the large phenocrysts, this population is 300 – 700 μm in size and exhibits a dipyramidal β -quartz habit and growth zoning. Each phenocryst population forms a maximum in the grain size distribution plot: qz1 at 2 mm and qz2 at 0.4 mm. In the following we call this population microphenocryst (qz2). Both the phenocrysts and microphenocrysts are overgrown by younger matrix quartz.

9.5 Methodology

CL investigations were carried out using a hot-cathodoluminescence-microscope (Neuser et al., 1995) with 14keV energy and filament current of 0.18 μA . CL spectra were recorded with a triple-grating (100, 1200, and 1800 lines/mm) spectrograph TRIAX 320 provided with a liquid N_2 -cooled Charge Coupled Device (CCD) camera. The system is well suited to applications with very low signals such as the CL of quartz. The 100-lines/mm grating was used to detect the emitted spectra between 400 and 950 nm (3.1 and 1.4 eV), whereas the 1200 lines/mm grating provided high-resolution spectra of 70 nm width sectors. The latter allowed the determination of the exact position of the single CL emission bands. For the quantification of the CL spectra were resolved by best fitting with Gaussian curves.

The application of a microprobe (EPMA) equipped with a CL detector (SEM-CL) facilitates the analysis of trace element distribution in relation to the CL textures. Trace element abundances of Al, Ti, K and Fe in quartz were determined using a JEOL JXA 8900 electron

microprobe fitted with a wavelength dispersive detector and with a CL detector (CLD40 R712). Raw analysis were converted into concentrations, after making appropriate matrix corrections using the phi-rho-z method of Armstrong (1991). The main advantages of the EPMA are the high spatial resolution of $\sim 5 \mu\text{m}$ and the capability of combining microanalytical analysis with CL and BSE imaging on the same area. The CL detector provided monochromatic (grey scale) images of the growth zones and alteration patterns within individual quartz crystals. Trace element measurements were carried out as line scans yielding distribution profiles. CL imaging was performed prior to and after EPMA analysis. In this way the measurement points in relation to the CL textures can be exactly located. The grey scale profiles along measured trace element profiles within quartz crystals are processed from the SEM-CL images using the software Optimas 6.0. Dark contrasted areas of quartz SEM-CL images correspond to red to reddish brown CL-colours and bright areas correspond to blue to violet colours. Quartz contains trace elements of very low concentrations so that quantification by EPMA poses a major difficulty. For high precision and sensitivity, a high beam current of 120 nA, beam diameter of $7 \mu\text{m}$, and a counting rate of 10 min per analysis (i.e. 180 s per element) were chosen. Detection limits were calculated for each trace element profile with a confidence level of 95% on the basis of the standard deviation obtained from 12 background measurements (Plesch, 1982). Detection limits are 56 ppm for Al, 9-16 ppm for Ti, 8 ppm for K, and 11-18 ppm for Fe.

There are several reasons why the concentrations of Al, Ti, K and Fe were determined. Al^{3+} and Ti^{4+} are the most frequent trace elements in quartz, which substitute for Si^{4+} (e.g. Bambauer, 1961; Dennen, 1965; Weil, 1984; Blankenburg et al., 1994) and may have a strong influence of the CL of quartz (e.g. Ramseyer and Mullis, 1990; Perny et al., 1992; Müller et al., 2000). K^+ was chosen as representative of the interstitial ions, because the detection limit of Na (~ 80 ppm) was higher than the concentration and the ultra-light element Li cannot be measured by EPMA. Fe and Mn are important CL activators and quenchers in silicates and enter interstitial (Fe^{2+} and Mn^{2+}) and substitutional (Fe^{3+} and Mn^{3+}) positions (Marshall, 1988). However, the concentration of Mn was far below the detection limit (~ 12 ppm).

9.6 Quartz CL colours and growth patterns

The application of CL facilitates the identification of three magmatic quartz generations in the two granite varieties: euhedral zoned phenocrysts (qz1), euhedral zoned microphenocrysts (qz2), and anhedral unzoned matrix quartz (Fig. 9.2a and b). The growth zoning in the phenocrysts (qz1 and qz2) is contrasted by different shades of blue, violet, and red-brown CL and include stepped (compositional) and oscillatory zoning with β -quartz habit, resorption surfaces, and growth impediments (Kozłowski, 1981; Schneider, 1993; Müller et al., 2000; Fig. 9.2c, d and e). Characteristic is the presence of fine-scale oscillatory zoning (2 - 20 μm width) within super-ordinate stepped zoning (50 - 1000 μm width). The analysis of the growth zoning shows, that the nucleation and growth of the microphenocrysts (qz2) begins with the growth of the outer step zone of qz1 (Fig. 9.2a, b).

The existence of euhedral quartz phenocrysts in granites showing CL-contrasted growth zoning is currently not known to be common and was described in only a few cases (Seltmann, 1994; D'Lemos et al., 1997; Müller et al., 2000). Furthermore, the growth zoning of these granitic phenocrysts is similar to growth zoning of phenocrysts observed in Permian-Carboniferous rhyolites of the Erzgebirge (Fig. 9.2f). In contrast the matrix quartz (qz3) overgrowing qz1 and qz2 is free of growth zoning and exhibits a red-brown CL.

Quartz formed during post-magmatic or late-magmatic alteration is easily distinguishable from the above-described magmatic quartz. Based on postsolidus recrystallisation textures (fluid saturation textures, grain blasteses, cannibalising; e.g. Müller and Seltmann, 1999), and dark red-brown luminescence, those metasomatic quartz textures formed by hydrothermal processes could be excluded from this study.

9.7 Quartz CL spectroscopy and trace element distribution

The spectral response of the CL of quartz in the range of visible light is characterised by 9 emission bands between 1.7 – 2.2 eV (red) and 2.4 – 3.1 eV (blue) (Fig. 9.3, Table 9.1). The intensity of the emission bands changes with the exposure time of electron radiation, whereby the blue emission decreases and the red emission increases, indicating the decay and creation of luminescence centres,

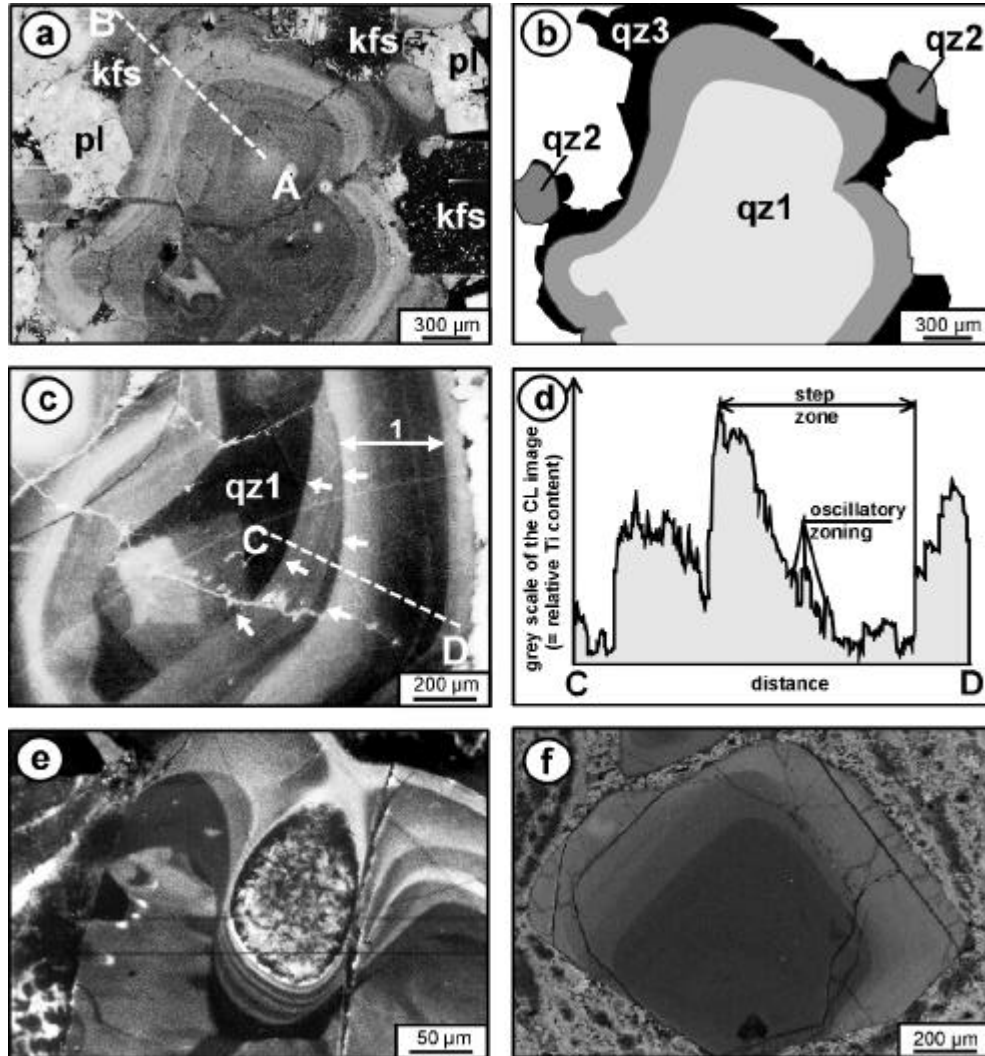


Fig. 9.2 SEM-CL images of quartz phenocrysts from the Hub stock topaz-bearing granites (Slavkovský Les Mts.). (a) Zoned quartz phenocryst (qz1, Ju-20). The line A-B shows the position of the trace element profile in figure 9.4a, c, and e. (b) Scheme of the three quartz generations, which are distinguishable in the SEM-CL image (a): zoned phenocryst (qz1), zoned microphenocrysts (qz2), and the matrix quartz (qz3) developed as ongrowths on qz1 and qz2. The nucleation and growth of qz2 begins with the growth of the outer step zone of qz1. (c) Zoned quartz phenocryst (qz1, Ju-20). The stepped zones (1) are truncated by resorption surfaces (arrowed) and overlain by the sub-ordinate oscillatory zoning. Three large scale resorption events are recorded in the zoning pattern. (d) Grey scale profile through the quartz phenocryst in figure 3c. High grey scale corresponds to blue CL and low grey scale to red-brown CL. Within a stepped zone the grey scale (blue CL) tendentially decreases in the growth direction. The grey scale correlates with the Ti distribution (see Fig. 9.5a). (e) Quartz phenocryst showing growth impediments. The zoning fits the shape of the impediment caused by immiscible melt, vapour phases or minerals which stick onto the crystal surface during growth. During further growth the impediment becomes enclosed. (f) Zoned quartz phenocryst from the Wachtelberg Rhyolite (Eastern Erzgebirge). The zoning pattern of rhyolitic phenocrysts is similar to the zoning occurring in the phenocrysts of the Hub stock granites.

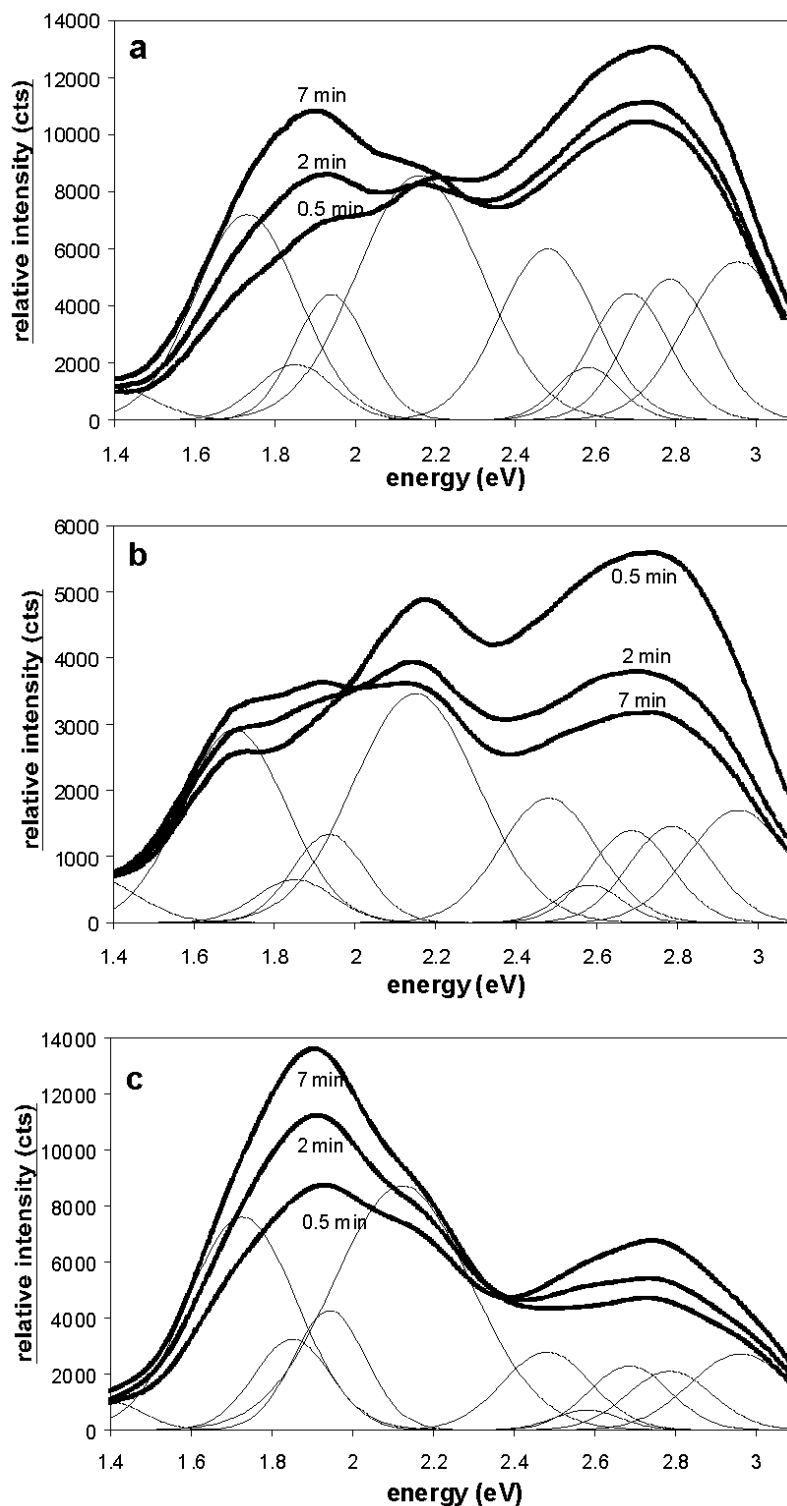


Fig. 9.3 CL spectra of (a) violet luminescent phenocryst quartz of sample Ju-10, (b) violet luminescent phenocryst quartz of sample Ju-20, and (c) red-brown luminescent matrix quartz (Ju 10). The spectra were recorded after 30 s, 2 min, and 7 min electron radiation. The 7-min-spectra are fitted with Gaussian curves. Each Gaussian curve represents a single emission band.

Table 9.1 CL emission bands between 1.4 and 3.1 eV observed in the magmatic quartz of the topaz-bearing granites from the Hub stock and their identification (NBOHC - non-bridging oxygen hole centre; STE - self-trapped exciton)

CL band position (eV)	Half width (eV)	Identification	Reference
1.73±0.02	0.3±0.02	substitutional Fe ³⁺	Pott and McNicol (1971)
1.84±0.01	0.22±0.01	Associated with NBOHC with Si--O and peroxy linkage precursor or ≡Si: centre	Stevens Kalceff and Phillips (1995)
1.96±0.02	0.22±0.02	Associated NBOHC with –OH precursor	Stevens Kalceff and Phillips (1995)
2.15±0.02	0.38±0.01	STE associated with Ge	Luff and Townsend (1990)
2.47±0.02	0.3±0.03	Impurity	Itoh et al. (1988)
2.58±0.01	0.18±0.005	Associated with Al ³⁺ -defect structures STE	Nassau and Prescott (1975) Remond et al. (1992)
2.68±0.01	0.23±0.01	STE Associated with Ti-defect structures	Stevens Kalceff and Phillips (1995) Marfunin (1979)
2.79±0.01	0.26±0.01	Oxygen related centre	Hagni (1987)
2.96±0.02	0.3±0.02	Associated with Ti-defect structures	This study

respectively. The CL colours are more unstable in the matrix quartz than in the phenocrysts. The CL signal obtained from phenocrysts within both granitic varieties is similar, whereas the CL spectra of the matrix quartz show a dominance of the red emission (Fig. 9.3).

The comparison of CL emission band and trace elements revealed the following:

- Growth zones with blue CL show high Ti concentrations up to 70 ppm (Fig. 9.4a and b). We found that the blue CL emission at 2.96 eV is associated with Ti (Fig. 9.5a). From this observation we conclude, that variations in Ti are mainly responsible for the magmatic zoning pattern within these quartz phenocrysts. The 2.96 eV band is beside the 2.47, 2.58, 2.68, and 2.79 eV one of five bands of the blue emission range. Generally, crystallisation

temperatures $>500^{\circ}\text{C}$ are necessary for the substitution of Si^{4+} through Ti^{4+} caused by the high field strength of Ti^{4+} ($F = 1.04$; Blankenburg et al., 1994). However, it is generally not clear whether Ti is a CL activator or sensitizer (Marshall 1988, Götze 2000).

- Phenocryst quartz (qz1 and 2) shows an Al content between 170 and 270 ppm, whereas matrix quartz (qz3) has higher concentrations between 250 and 370 ppm (Fig. 9.4c and d). Al concentrations >400 ppm correlate with K concentrations >30 ppm indicating the contamination of the analysis by feldspar microinclusions. Al generally behaves in an opposite way to Ti with abundances being low in the blue and higher in the red-brown luminescent quartz especially in the matrix quartz (qz3; Fig. 9.5b). In contrast Ramseyer and Mullis (1990) and Perny et al. (1992) assume that the high Al and Li concentrations are the cause of the blue CL of hydrothermal quartz. According to Siegel and Marrone (1981), Griscom (1985), and Stevens Kalceff and Phillips (1995) the red CL emission around 1.96 eV is related to OH⁻ and/or adsorbed H₂O. The increase of the emission during electron radiation is explained by radiolysis of hydroxyl groups and/or adsorbed H₂O of the quartz lattice, which leads to the formation of non-bridging oxygen hole centres (NBOHC). Hydroxyl groups and adsorbed H₂O acting as charge compensator of Al^{3+} forming $[\text{2SiO}_3\text{-H}_2\text{O-M}^+\text{2AlO}_4]$ defects, where M^+ is a combination of Li, K, and Na ions (Bambauer et al., 1963; Maschmeyer and Lehmann, 1983; Kronenberg et al., 1986; Stenina, 1995). This association of Al and hydroxyl groups and/or adsorbed H₂O may explain the weak correlation of Al with the red emission.
- The Fe content varies predominantly between 10 and 30 ppm (Fig. 9.4e and f). It was observed that Fe increases towards the grain boundary up to 260 ppm indicating a high diffusion rate of Fe in the quartz lattice. This grain rim shows no change in CL properties. Pott and McNicol (1971) and Kempe et al. (1999) found that high Fe^{3+} causes the 1.73 eV CL emission. However, in our samples we found no correlation between the Fe concentration and the 1.73 eV band intensity. The lack of correlation may be explained by the fact that Fe occurs as divalent and trivalent ions.
- Weak to non-luminescent, post-magmatic (secondary) quartz is depleted in Ti, Al, Fe and K (Fig. 9.5a and b).

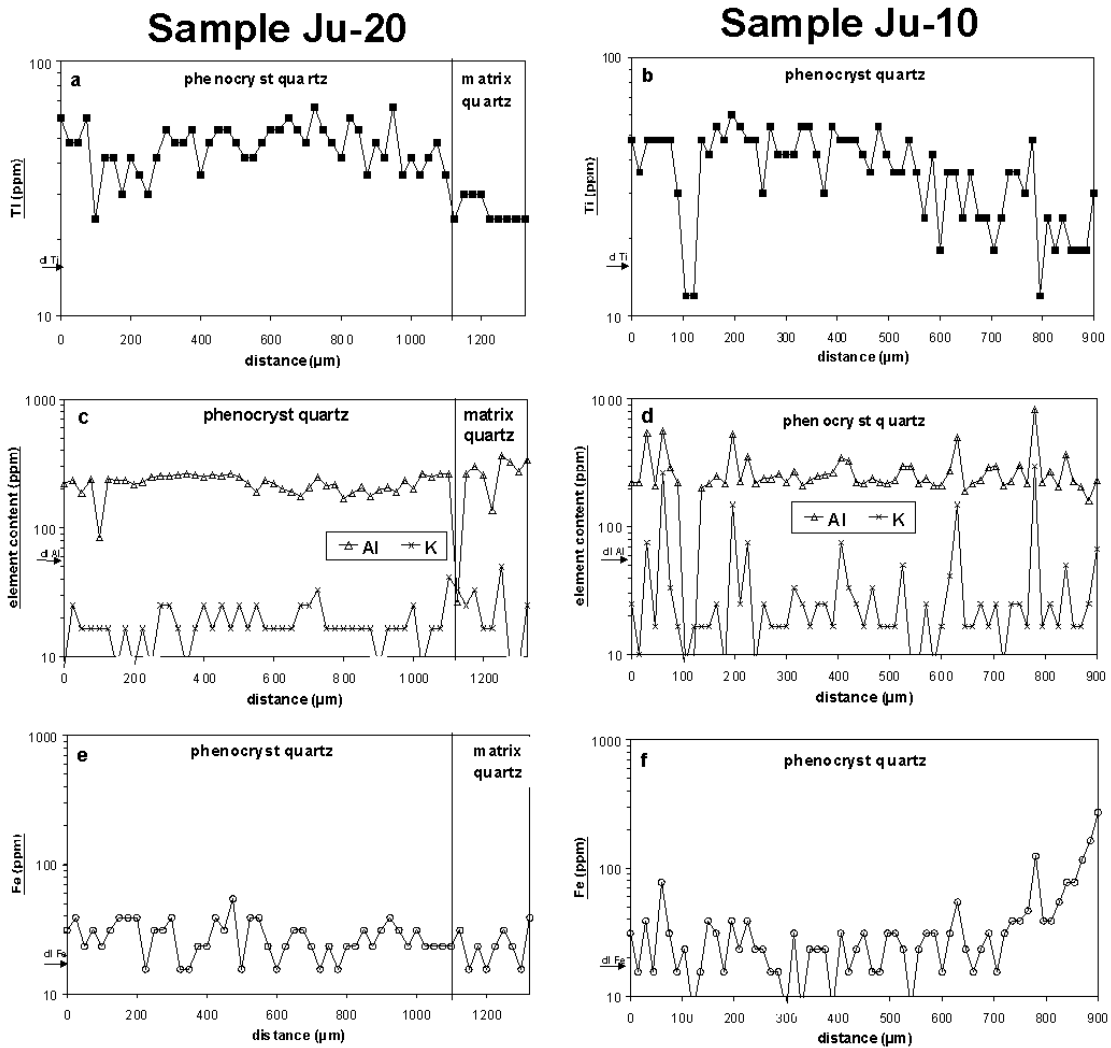


Fig. 9.4 Trace element profiles of quartz of the topaz granites from the Hub stock. Lower Ti and higher Al are characteristic for the matrix quartz. High Al (>400 ppm) correlates with K indicating analysed micro-inclusions of feldspar. The steep increase of Fe near the grain boundary to plagioclase demonstrates the high diffusion rate of Fe in the quartz lattice. Secondary (post-magmatic) quartz between 100 and 130 µm in (b), (d), and (f) is depleted in Ti, Al, Fe and K. The arrows at the axis of ordinates mark the detection limits (dl).

9.8 Discussion

Topaz-bearing granites of the Hub stock hosting the Krásno Sn-W ore deposit contain three generations of magmatic quartz represented by phenocrysts (qz1), microphenocrysts (qz2), and matrix quartz (qz3) indicating multiple crystallisation and contrasting crystallisation environments.

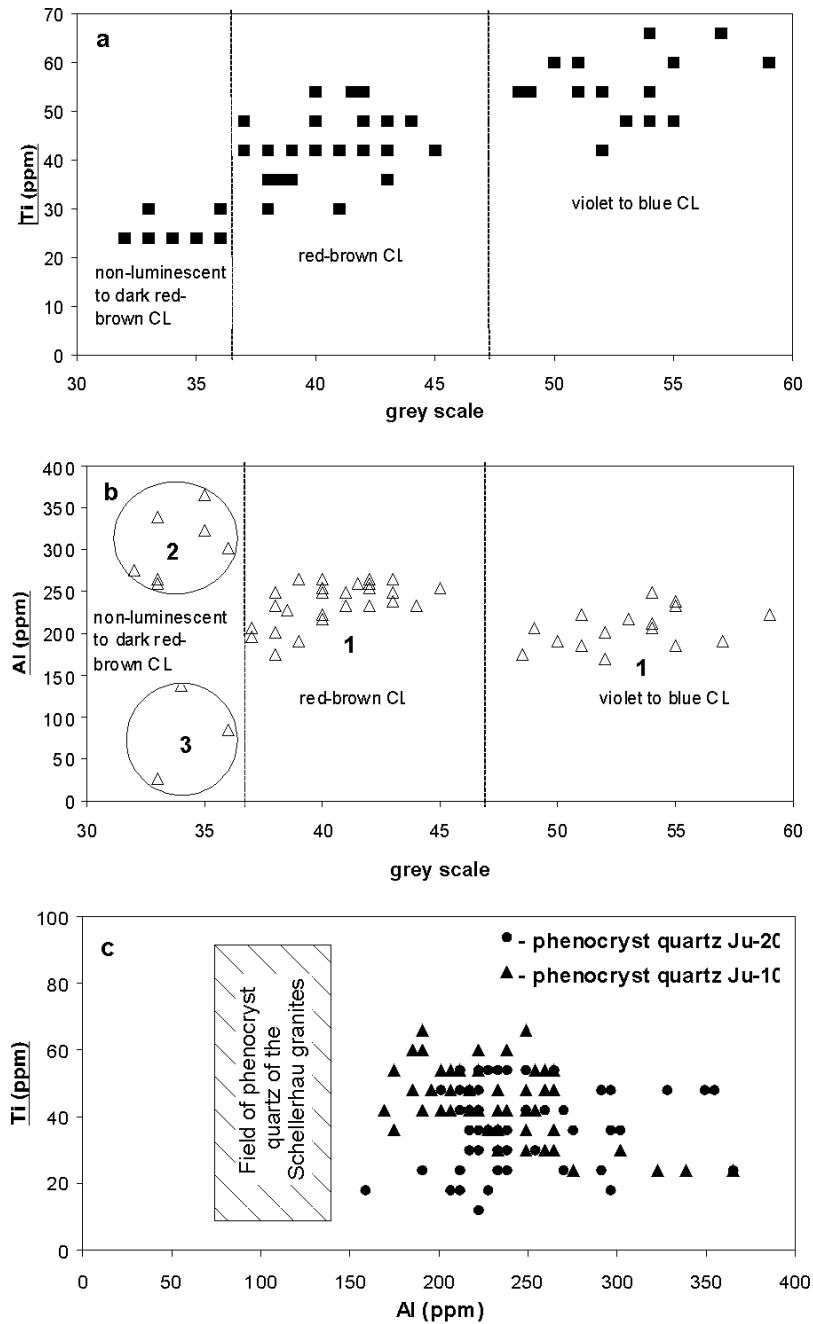


Fig. 9.5 (a) Correlation of Ti and CL signal plotted as grey scale within a zoned quartz phenocryst (qu1, Ju-10). The grey scale reflects the intensity ratio of red (1.7 – 2.2 eV) versus blue emission (2.4 – 3.1 eV). The higher the blue emission intensity the greater the amount of the grey scale. Quartz with high Ti shows violet to blue CL. (b) Al concentration of phenocryst quartz (1), matrix quartz (2), and secondary (post-magmatic) quartz (3). The matrix quartz (2) has high Al in contrast to the secondary quartz (3). (c) Comparison of the Ti-Al ratio of quartz phenocrysts from the Hub stock topaz-bearing granites and of Schellerhau tin granites (Eastern Erzgebirge). The phenocrysts of the different topaz-bearing granite varieties of the Hub stock show a similar trace element signature indicating a common magma source, whereas the phenocryst quartz of the Schellerhau tin granites has a lower Al concentration.

To understand the Ti variation of growth zones in the phenocrysts (qz1 and qz2) it is necessary to distinguish between zoning caused by self-organised growth and zoning caused by physico-chemical changes of external factors such as temperature, pressure and magma composition (e.g. Allegre et al., 1981; Anderson, 1984; Fowler, 1990; Shore and Fowler, 1996). The fine-scale oscillatory zoning observed arises from self-organised growth without the intervention of externally imposed periodicities in the state (pressure, temperature, or composition) of the melt from which the crystal grew (e.g. Sibley et al., 1976; Allegre et al., 1981; Ortoleva, 1990; Shore and Fowler, 1996). Self-organisation of the growth is controlled by cyclic competition of the crystal growth rate and the diffusion rate of silica and elements such as Ti within the crystal-melt reaction zone and boundary layer. In contrast, stepped zoning and resorption surfaces are zoning patterns typically caused by external factors (e.g. Allegre et al., 1981; Müller et al., 2000). The stepped zones are often truncated by resorption surfaces, which results in rounding of the crystals (Fig. 9.2c). Resorption (melting) of crystal surfaces indicates local SiO₂-undersaturation of the melt, which may be caused by an increase in temperature, isothermal decompression, or magma mixing. The continuous fractionation trend of the granite varieties of the Hub Stock and Krásno area (e.g. Jarchovský and Pavlu, 1991) gives no indications for magma mixing which may cause the multiple resorption events. Furthermore, the crystal settling effects in a magma chamber are small for viscous silicate melts (e.g. Dowty, 1989) and do not result in large-scale resorption of crystals.

Therefore, we favour isothermal decompression during adiabatic melt ascent as the cause of large-scale resorption. Adiabatic conditions are only possible by rapid magma ascent in dykes. Resorption drastically lowers the amount of suspended solids in the melt. The flow rate is elevated by reduction of the effective viscosity. This process may be initiated by brittle deformation during extension or shear in the upper crust. The occurrence of resorption surfaces is in accordance with the rapid ascent of granitic melts by dyke formation as found by Clemens and Mawer (1992), Petford et al. (1993), Petford (1996) and Johannes and Holtz (1996). After a resorption event (melt ascent), the subsequent growth of a new stepped zone begins with high Ti (blue CL) indicating a change of the crystallisation conditions. The Ti content decreases tendentially across the stepped zones during further growth and is overlain by a sub-ordinate oscillatory Ti variation. If the oscillatory Ti variation is controlled by the rate of Ti diffusion in the melt (self-organised growth), then the tendentious decrease in Ti within the stepped zone should have other causes. After a resorption event, here explained by adiabatic melt ascent, Ti incorporation is likely to be high as a result of rapid growth rates since the melt moved into cooler surroundings. We draw this conclusion from textural

observations. There may be some additional effects such as pressure and melt composition, which favour incorporation of Ti into the quartz lattice.

The growth zoning and CL properties of the phenocrysts of the granites (qz1 and qz2) are similar to those observed in phenocrysts of Permian-Carboniferous rhyolites of the German Variscides (Schneider, 1993; Müller, 2000) and may indicate similar crystallisation conditions. Thomas (1992) calculated the depth of quartz phenocryst crystallisation of tin granites of the Krušné Hory/Erzgebirge of up to 21 km provided by microthermometric studies of silicate melt inclusions. This is in accordance with the crystallisation depth of quartz phenocrysts of the Permian-Carboniferous rhyolites of the Erzgebirge, which was estimated at about 25 km (Thomas, 1992). Our observations and the calculations of the crystallisation depth by Thomas (1992) show that zoned quartz phenocrysts in granites with dominant blue CL represent a water-poor (<2.5wt% H₂O) “rhyolitic” crystallisation environment in the lower and middle crust. Such phenocrysts contained in granites exhibit early stages of magma evolution and show features similar to rhyolite magmas, thus may represent the capability of erupting magmas. The matrix quartz (qz3) is interpreted as the product of the last magmatic crystallisation stage during and after the subvolcanic melt emplacement taking place at ca. 1.5 km (Thomas, 1994). Derivable from the high Al incorporated in [2SiO₃H₂OM⁺2AlO₄] defects (M⁺ = Li⁺, Na⁺, K⁺) and from the dominance of the unstable red 1.96 eV CL emission, which is associated with hydroxyl defects and adsorbed H₂O in the lattice the matrix quartz grew in a residual “granitic” melt with higher water content.

Quartz phenocrysts in both topaz-bearing granites of the Hub stock exhibit a similar Al/Ti ratio (Fig. 9.5c). However, this differs from quartz phenocrysts of other topaz-bearing granites of the Krušné Hory/Erzgebirge like the Schellerhau granite (Müller et al., 2000). Similar observations have been made by Stuttner and Leininger (1972) who showed that Ti content is different for quartz derived from different batholiths. Thus, quartz phenocrysts formed from different magma sources have various Al/Ti ratios. We conclude that the two quartz phenocryst generations of the topaz-bearing granite varieties of the Hub stock represent the same crystallisation history and are derived from one-magma chamber. However, the rock textures, quartz generations, and growth patterns observed in CL are very similar for a number of topaz-bearing granites of the Krušné Hory/Erzgebirge (Müller et al., 2000; Müller, 2000). These similarities suggest that the quartz textures in the granite and the phenocryst growth patterns found in the Krušné Hory/Erzgebirge province are typical for Li-F-enriched melts, which are related to Sn-W-mineralizations.

10 Crystallisation, emplacement and deformation of S- and I-type granites in the Eastern Lachlan Fold Belt (SE Australia) indicated by quartz texture, cathodoluminescence, and Al-in-hornblende barometry

(this chapter has been submitted to Mineralogy and Petrology, co-authors: P. Lennox and R. Trzebski)

10.1 Abstract

The I-type Carcoar and Barry Granodiorites and the S-type Sunset Hills Granite were intruded in the Late Ordovician-Early Silurian into Early Ordovician greywacke and volcanoclastic pile at different levels and subsequently repeatedly deformed in the Lachlan Fold Belt, SE Australia. Whereas the Carcoar Granodiorite has one generation of anhedral quartz, the Barry Granodiorite consists of unzoned subhedral quartz phenocrysts and anhedral matrix quartz, which crystallised at or near the emplacement level. Both granodiorites are considered to have been derived from the same magma source and have experienced a continuous and rapid ascent to depths of 4 to 6 km as determined by Al-in-hornblende barometry. The Sunset Hills Granite has three generations of quartz, and is geochemically related and spatially linked to the adjacent Wyangala Batholith. It was intruded at depths of 10-12 km. The magma of the Sunset Hills Granite ascended in a stepwise fashion, causing multiple quartz nucleation, episodes of slow crystal growth, and resorption events. The Carcoar and Barry granodiorites both show syn- and post-magmatic foliations, whereas the Sunset Hills Granite only has a post-magmatic foliation. The post-magmatic, solid-state foliations were produced during regional transpression and transtension during two subsequent deformation events. The earlier deformation is related to the Early Devonian Bowring event which caused east-west compression accompanied by regional transpression and transtension and vertical uplift and contraction in the Eastern Lachlan Fold Belt. During the Bowring event, the granodiorites were deformed under brittle conditions at temperatures of 250 to 400°C; whereas the Sunset Hills Granite experienced ductile deformation at temperatures of around 550°C. The second deformation recorded in the quartz is the late Middle Devonian Tabberabberan event, which is not apparent in the granodiorites, whereas the Sunset Hills Granite was further deformed, uplifted and experienced transpression during this event. The multiple deformation of quartz

result in redistribution of Ti, Al and structurally bound water in the quartz lattice and the formation of muscovite (<0.5 μm) along slip planes in quartz.

10.2 Introduction

Structural analysis of granites with a polyphase deformation history often faces the difficulty of discriminating between generations of magmatic and deformation fabrics. In this paper, we present an method that combines microstructural, petrological and geochemical data to reconstruct the conditions of magma crystallisation, emplacement and deformation.

In recent years, cathodoluminescence (CL) of quartz has been increasingly applied to describe the processes of magma genesis, transport and deformation (Behr, 1989; Watt et al., 1997; Müller et al., 2000). In this study, CL was applied to characterise the conditions of magma crystallisation, emplacement and deformation of the Carcoar and Barry granodiorites and the Sunset Hills Granite in the Eastern Lachlan Fold Belt (SE Australia). Special emphasis was placed on the macro- and microtexture, trace element distribution in quartz, Al-in-hornblende barometry, and whole-rock geochemistry. We show how the CL behaviour of quartz and its textures at the microscale reflect the conditions and sequences of magma crystallisation and deformation. This is a complimentary study to previous structural and gravity modelling, which revealed the pluton shape at depth and the tectonic setting during emplacement of these granites (Trzebski et al., 1999).

10.3 Geological Setting

The northern part of the eastern Lachlan Fold Belt evolved in an island-arc setting during the lower Palaeozoic (Powell, 1984; Coney, 1992; Collins and Vernon, 1992; Gray et al., 1997). The Molong-Wyangala-Jerangle-Kuark Zone (abbreviated as Molong-Wyangala Zone) within the northern Lachlan Fold Belt may represent a fragment of a former Ordovician island arc and lies adjacent to the Hill End-Barradine Zone (abbreviated as Hill End Zone) a Mid-Silurian turbidite-filled trough (Glen et al., 1998; Scheibner, 1998).

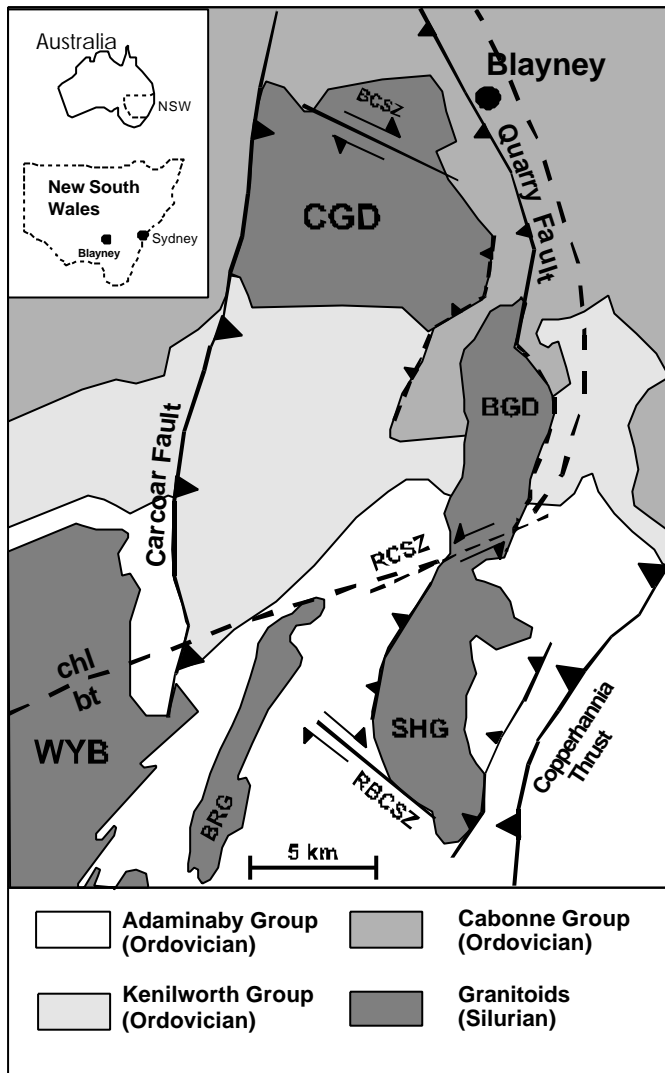


Fig. 10.1 Locality map and geological sketch map of the study area where CGD = Carcoar Granodiorite, BCSZ = Browns Creek Shear Zone, BGD = Barry Granodiorite, RCSZ = Reedy Creek Shear Zone, SHG = Sunset Hills Granite, RBCSZ = Rocky Bridge Creek Shear Zone, BRG = Bugs Ridge Granite, WYB = Wyangala Batholith and regional metamorphic zones in pelites from Smith (1969) are chl = chlorite and bt = biotite.

The Carcoar, Barry and Sunset Hills granites intruded the multiply deformed Molong-Wyangala Zone. This zone consists of Ordovician metasedimentary and volcanoclastic rocks, which were metamorphosed from prehnite-pumpellyite to greenschist conditions and deformed during the Late Ordovician/Early Silurian Benambran event (Smith, 1969). This event was followed by extensional and transcurrent deformation from the mid-Silurian to the mid-Devonian, which led to the formation of sedimentary basins (Hill End Zone) and emplacement of granitoids (Collins and Vernon, 1992; Glen, 1998).

The *Carcoar Granodiorite* is a roughly equant (10 x 10 km) pluton bound by the Carcoar Fault on the west and the Quarry Fault on the east. It is composed of fine- to medium-grained, enclave-bearing, hornblende-biotite granodiorite to tonalite, similar to other I-type granites in the area, and minor intrusions of diorite (Long Hill Diorite), monzonite, aplite and pegmatite. The *Barry Granodiorite* is a meridionally elongated body (5 x 12 km), consisting mainly of

hornblende and biotite granodiorite of tonalitic composition with minor microtonalite enclaves (Lennox et al., 1998). The *Sunset Hills Granite* crops out as a north-south elongated body (6 x 13 km) bound in part by a possible extension of the Quarry Fault in the west and the Copperhanna Thrust in the east (Fig. 10.1). It is mainly composed of a biotite granite intruded in places by aplite and muscovite-leucogranite dykes. Metasedimentary xenoliths of up to 5 m in length and 0.3-0.5 m in width represent stoped blocks of the host rocks (Adaminaby Group) and show a foliation oblique to the foliation in the granite, indicating deformation prior to granite emplacement (Lennox et al., 1998).

All three granites show poorly developed magmatic flow fabrics, and a poor to moderately pervasive tectonic fabric. The main solid-state fabric (Sg) in all granites consists of aligned biotite books, opaque grains, fractured feldspars, rarely aligned hornblende crystals and elongated muscovite aggregates. Cross-cutting mylonite zones, S-C microstructures and shear zones are better developed south of and adjacent to the Sunset Hills Granite. New zircon SHRIMP and published Ar-Ar, Rb-Sr and K-Ar dating studies (Lennox et al., 1998) indicate that the granites intruded about the same time, during the Early Silurian following the Benambran event. All three granites were multiply deformed during the Early Devonian Bowring, late Middle Devonian Tabberabberan and Early Carboniferous Kanimblan events (Lennox et al., 1998; Trzebski et al., 1999).

10.4 Methods

The CL emission of quartz was analysed using a hot-cathodoluminescence-microscope (Neuser et al., 1995) at an energy of 14 keV and a filament current of 0.18 mA. CL is generated by the emission of photons of ultra violet (UV) to infrared (IR) wavelength from activated electrons of the sample during electron bombardment. The spectral response of the CL was recorded with the grating (100 lines/mm and 1200 lines/mm) spectrograph TRIAX 320 and a LN₂-cooled CCD-detector, and corrected for the total instrument response. The high-resolution spectrograph was used to determine the energy of individual emission bands, which usually have a Gaussian shape if plotted in energy space. The position, width, and height of the Gaussian curves were calculated and adjusted in such a way that the sum of the individual components corresponds to the recorded CL spectra. The areas of the Gaussian curves were used to determine the percentage of the individual emission bands of the total

spectra between 1.4 and 3.1 eV. The peak area portions were correlated with the recorded trace elements.

The scanning electron microscope cathodoluminescence (SEM-CL) generates a high degree of spatial resolution of CL textures, and enables visualisation of magmatic growth zoning and deformation fabrics in quartz. A Geoscan 250-MK3, with a CL detector operating at an energy of 15 keV and a filament current of 8-12 nA was used for black-and-white images of the primary (growth) CL textures and secondary (post-magmatic) CL structures in quartz. Typical primary CL textures in magmatic quartz, as revealed by variations in CL, include (1) stepped zoning (50-1000 μm width) with subordinate oscillatory zoning (2-20 μm width), (2) resorption surfaces, (3) growth impediments, and (4) skeletal growth (Müller et al., 2000). Secondary CL structures, such as healed microcracks and recrystallised domains are also clearly detectable with CL (Behr, 1989).

Additional information about the nature and evolution of the magma can be obtained by analysing the grain size distribution of quartz and its framework. The application of the lacquer peel method (Behr 1966; see Fig. 10.3) enables detailed analyses of the quartz framework. Grain size analysis were carried out in thin sections and hand specimens. The length and width of quartz grains (≤ 1 mm) in thin sections. Quartz grains > 1 mm were measured by micrometer on polished hand specimen (15 x 15 cm). The grain size of each grain was calculated from the average of its length and width.

The high-resolution spectral analysis of CL was combined with Electron Probe Micro Analysis (EPMA) to establish a correlation between the CL emission bands and Al, Ti, K, and Fe, which may act as CL activators in quartz. The element concentrations in quartz and of Na, Si, Ti, Ca, Fe, Mg, Al, Cr, K, and Mn in hornblende were determined using the JEOL JXA 8900 electron probe micro analyser (EPMA) operating at 15 kV. To minimize the excitation volume during the measurements of the hornblende crystals the beam was set to 40 nA and to a diameter of 5 μm . For high precision and sensitivity of the trace element determination in quartz, the a beam current of 120 nA, a beam diameter of 7 μm , and a counting rate of 10 min per shot means 180 s per element were chosen. Detection limits were calculated for each trace element profile with a confidence level of 95% on the base of the standard deviation obtained from 12 background measurements (Plesch, 1982). Detection limits are 32 ppm for Al, 20 ppm for Ti, 13 ppm for K, and 15 ppm for Fe.

10.5 Geochemistry

The three granites show similarities in their geochemical composition and can be subdivided into two groups: the metaluminous I-type Carcoar and Barry granodiorites, with SiO_2 contents of 63-67wt.%, and the meta- to peraluminous Sunset Hills Granite and Wyangala Batholith with S-type affinity and with a SiO_2 content of 69-74wt.% (Fig. 10.2).

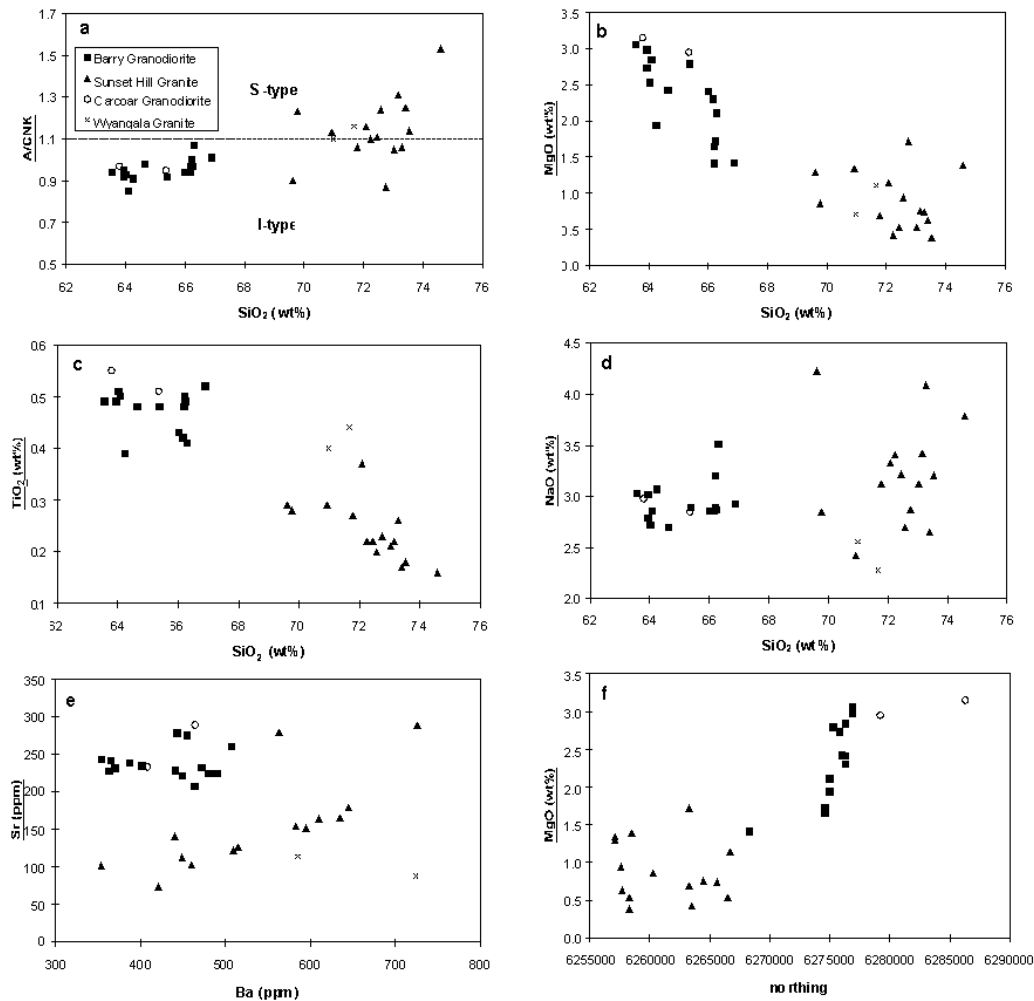


Fig. 10.2 Representative variation diagrams of whole rock samples of the Carcoar Granodiorite, Barry Granodiorite, Sunset Hills Granite and Wyangala Batholith. a - The Carcoar and Barry granodiorites are metaluminous I-type granites and the Sunset Hills Granite and Wyangala Batholith are meta- to peraluminous S-type granites. b - The decrease of MgO , FeO^{T} and CaO in the Barry Granodiorite with increasing SiO_2 indicates that melt differentiation occurred by fractionation (gravity settling) of hornblende. The Carcoar Granodiorite represents a primitive melt. c - The differentiation trend by decreasing TiO_2 is characterised by a gap which clearly separates the two granite groups. d - The variation of Sr indicates fractionation of plagioclase in the Barry Granodiorite, whereas the decrease of Ba concomitant with Sr shows that both K-feldspar and plagioclase were removed during differentiation of the Sunset Hills Granite.

The TiO_2 , Al_2O_3 , K_2O and Na_2O contents of the Barry Granodiorite are constant, whereas the MgO , FeO^{T} and CaO contents decrease with increasing SiO_2 . The distribution of the major elements, the constant Sr content and the minor variation of the Ba content indicate that differentiation occurred by fractionation (gravity settling) of hornblende. The Barry Granodiorite shows a progressive differentiation of major and trace elements from north to south, which is shown by the decrease of hornblende and the increase of quartz to the south. The geochemistry of the Carcoar Granodiorite shows similarities with the Barry Granodiorite, except that the Barry Granodiorite shows a higher degree of fractionation, as indicated by the depletion of hornblende.

In the Sunset Hills Granite, the MgO , FeO^{T} , TiO_2 , Al_2O_3 , and CaO contents decrease with increasing SiO_2 . The Na_2O and K_2O contents vary between 2.4-4.2wt.% and 0.6-4.7 wt.%, respectively. The decrease of Ba concomitant with Sr shows that both K-feldspar and plagioclase were removed during differentiation. In contrast to the Barry Granodiorite, the distribution of the major and trace elements shows an east-west trend in the Sunset Hills Granite. The highest fractionation was recorded at the western margin of the pluton.

10.6 Quartz texture and foliation development

Carcoar Granodiorite

The magmatic quartz of the Carcoar Granodiorite is represented by one anhedral generation, which forms irregular grain aggregates between the subhedral to euhedral feldspar and the hornblende grains (Fig. 10.3a). The grain size distribution of the weakly deformed samples shows one main peak around 650 μm , which indicates one nucleation event during magmatic crystallisation (Dowty, 1989) (Fig 10.4a).

The weak, post-magmatic deformation of the Carcoar Granodiorite is reflected in thin section by undulatory extinction of quartz, and by new grains at grain boundaries as a result of rotation recrystallisation (Fig. 10.3b). The degree of deformation in quartz generally increases with the proximity to shear zones. Measurements of the orientation of the subgrain boundaries of deformed quartz showed that the dominant feature are prismatic subgrain boundaries parallel to the c-axis. During the dynamic recrystallisation, bulges at grain boundaries formed where some new grains (~12 μm diameter) developed due to progressive rotation of subgrains (Fig. 10.3b, 10.4a). Biotite formed 'fish' and hornblende crystals were rigidly rotated into a post-magmatic foliation. Simple, open kink-bands associated with slip on the basal plane were

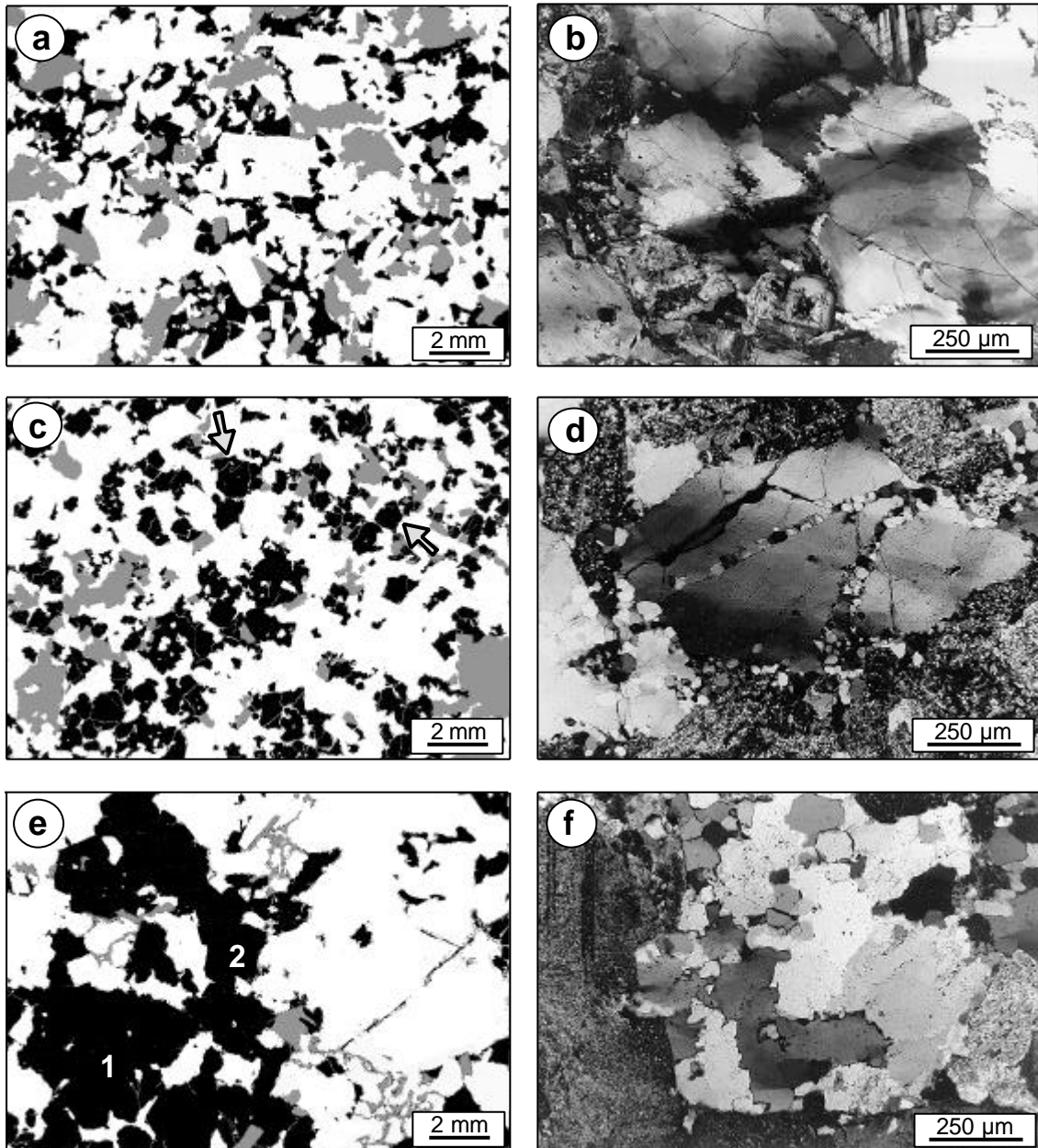


Fig. 10.3 The quartz framework of the Carcoar Granodiorite, Barry Granodiorite, and the Sunset Hills Granite. a - The anhedral quartz of the fine-grained Carcoar Granodiorite filled the irregular cavities between the subhedral to euhedral feldspar (white), biotite and hornblende crystals (grey) (contrasted lacquer peel). b - Deformed quartz of the Carcoar Granodiorite contains elongated subgrains and small recrystallized grains at the edges. c - The Barry Granodiorite contains subeuhedral quartz phenocrysts (arrows) overgrown by anhedral to aplitic matrix quartz. d - Elongated phenocryst of the Barry Granodiorite with subparallel contrasted subgrains cross-cut by trails of recrystallized quartz. e - The fine- to medium-grained, porphyritic magmatic texture of the Sunset Hills Granite with two euhedral zoned phenocryst generations (first and second) which are embedded in anhedral matrix quartz. f - Deformed phenocryst (first generation) of the Sunset Hills Granite entirely converted to new grains with high-angle boundary during recovery of subgrains.

developed in biotite, whereas hornblende reacted by intragranular, brittle displacement along the cleavage planes. The foliation within the shear zones is not parallel with the magmatic foliation marked by aligned hornblende and biotite. Muscovite occurs as fringes within strain shadows of feldspar.

Barry Granodiorite

The grain size distribution of quartz in the equigranular to weakly porphyritic Barry Granodiorite shows two maxima (Fig. 10.4). It contains sub-euhedral quartz phenocrysts with diameters between 800 and 900 μm (Fig. 10.3c, d), which are embedded in the anhedral matrix quartz with an average diameter of ~ 300 μm (Fig. 10.4b). In the southern part of the Barry Granodiorite, the isometric matrix quartz has an average diameter of about 100 μm , whereas the size of the phenocrysts remains constant at 800 to 900 μm .

The deformed quartz of the Barry Granodiorite shows elongate subgrains marked by ribbons and rims of polygonal, recrystallised quartz with high-angle grain boundaries formed by rotation recrystallisation (Fig. 10.3d). Prismatic subgrain boundaries parallel to the C-axis are dominant. The non-elongated recrystallised grains with an average grain size of 40 μm show straight boundaries and 120° triple junctions (Fig. 10.4b). The recrystallised quartz ribbons are similar to the Type 2 polycrystalline quartz ribbons after Boullier and Bouchez (1978). The feldspars within the post-magmatic shear zones are often entirely sericitised. Plagioclase is weakly recrystallised along microcracks. Likewise in the Carcoar Granodiorite, the magmatic foliation is marked by aligned hornblende and biotite. The post-magmatic deformation of biotite and hornblende caused slip along the cleavage planes, rigid body rotation, boudinage, and recrystallisation at the crystal edges.

Sunset Hills Granite

The porphyritic Sunset Hills Granite contains two generations of euhedral quartz phenocrysts embedded in anhedral matrix quartz (third generation) as shown in Fig. 10.4c. The quartz phenocrysts and aggregates were almost entirely converted to new grains with high-angle boundaries, due to rotation recrystallisation. The new grains with an average diameter of 100 μm are either microscopically strain-free or internally deformed (Fig. 10.4c). In deformed quartz, basal subgrain boundaries normal to the c-axis occur in addition to the prismatic subgrain boundaries, forming typically rectangular (“chessboard”) patterns. A number of the larger grains of the quartz aggregates shows strongly curved, sutured grain boundaries formed due to grain boundary migration recrystallisation. Recrystallised, polycrystalline quartz

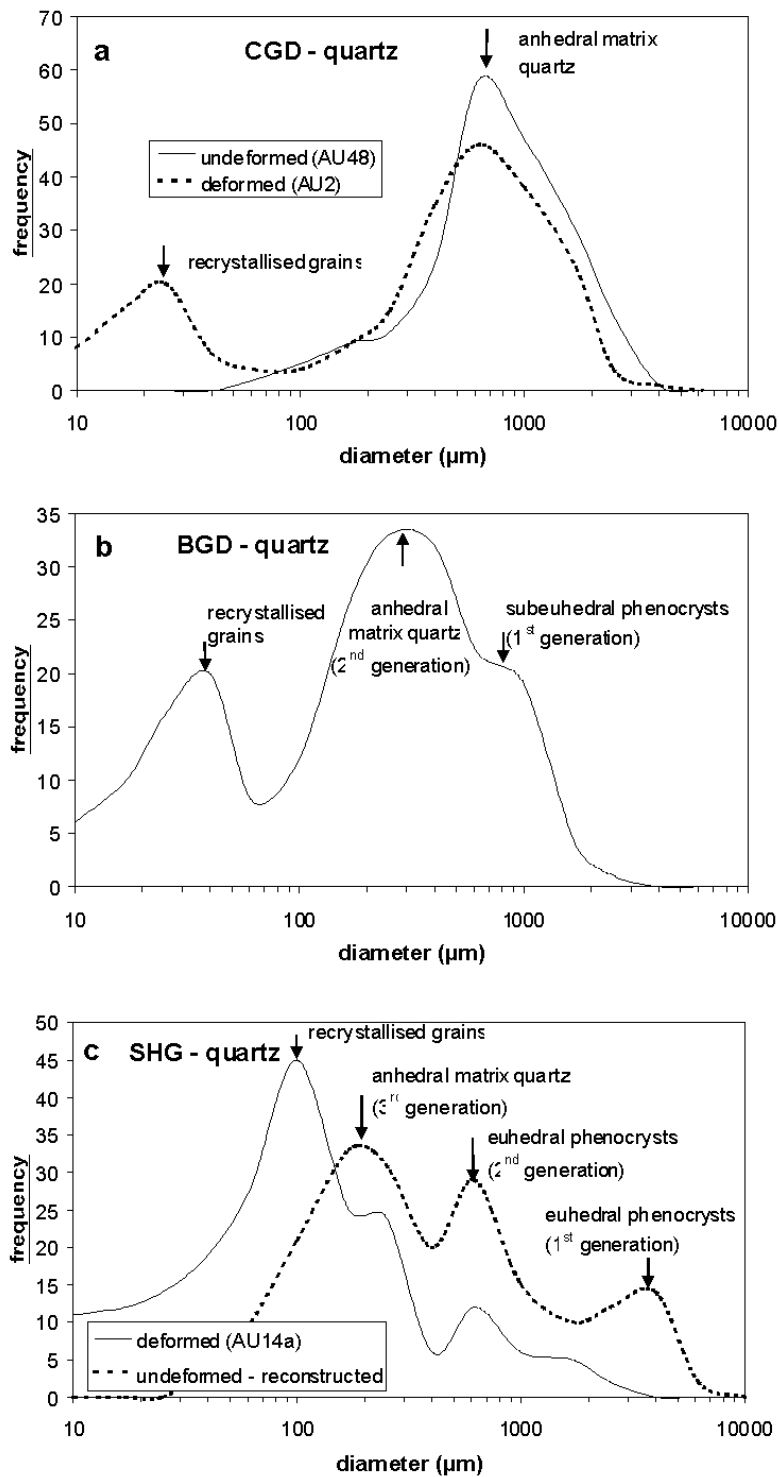


Fig. 10.4 Grain size distribution of quartz. a – of the Carcoar Granodiorite, b – of the Barry Granodiorite, c – of the Sunset Hills Granite. The original grain size maximum of 3.5 mm (reconstructed) of the large, first generation phenocrysts is reduced by deformation. This diagram shows that the maximum frequency of the matrix quartz is overlapped by the maximum frequency of grains modified by the post-magmatic rotation recrystallisation.

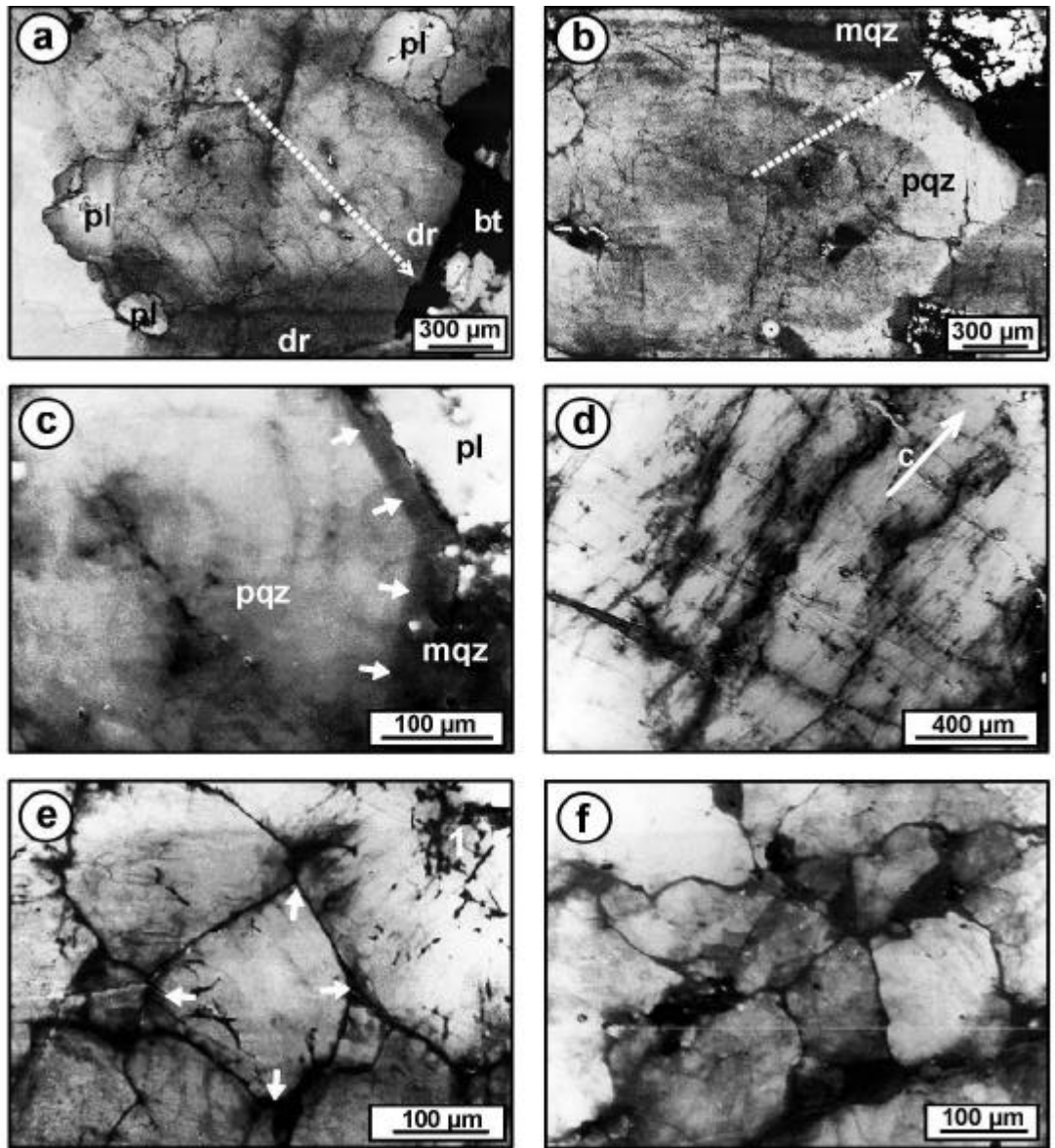


Fig. 10.5 SEM-CL images of quartz. a – Quartz grain of the Carcoar Granodiorite with a bright core and dark grey diffusion rim (dr) depleted in Ti and enriched in Fe. The high Fe concentration of the diffusion rim is derived from the neighbouring biotite (bt) (dashed line = position of the electron microprobe profile in Fig. 10.8a). b - Zoned quartz phenocryst (pqz) of the Sunset Hills Granite with magmatic growth zoning which is weakened and partly destroyed during deformation. It is overgrown by dark contrasted, unzoned matrix quartz (mqz). The brighter the CL of the zone the higher is the Ti concentration (dashed line = position of the electron microprobe profile in Fig. 10.8c). c - Euhedral quartz phenocryst (pqz) overgrown by dark red-brown luminescent, anhedral matrix quartz (mqz). The arrows mark the border between the two generations. d - The subgrains in the deformed quartz of the Barry Granodiorite are bordered by dark recrystallized quartz depleted in trace elements. The development of stress-induced Si-OH bonds along microsliding planes leads to this lamellate textures. Along the thin healed cracks at right angles to c are small star-like halos. e - Rotation recrystallization in the quartz of the Carcoar Granodiorite results in first stage star-like textures at the grain edges, as shown by the arrows. f - Advanced rotation crystallization in the quartz of the Sunset Hills Granite. The volume of newly crystallized (secondary), non-luminescent quartz (black) grows with the increase in the intensity of deformation.

ribbons (Type 2 and Type 4 ribbons after Boullier and Bouchez, 1978) cross-cut quartz aggregates and cataclastic feldspar. Biotite is entirely recrystallised with its (001) planes subparallel to the S-C fabrics. Feldspar is entirely sericitised in some samples and shows pressure-solution phenomena, particularly at contacts with muscovite layers or where cross-cut by muscovite layers. Indications of pre-existing magmatic foliation were not found.

10.7 Cathodoluminescence of quartz

Primary magmatic CL textures

Quartz phenocrysts of the Sunset Hills Granite (first and second generation) show weakly contrasted, relict growth zones typical of rhyolitic phenocrysts (Laemmlein 1930; Schneider 1993; Watt et al. 1997). Growth pattern, formed by oscillatory zoning (2-20 μm width), superordinate stepped zoning (50-1000 μm width) and resorption surfaces, is preserved in less deformed phenocrysts. However, these growth zones were largely erased due to high-temperature, post-magmatic deformation (Fig. 10.5b). On the other hand, experiments with zoned, rhyolitic quartz phenocrysts also show that the contrast of the CL growth zones weakens after several hours of heating at temperatures over 500°C. In contrast, the subhedral, quartz phenocrysts of the Barry Granodiorite are non-rhyolitic, do not show growth zoning. The red-brown luminescent quartz phenocrysts are overgrown in optical continuity by dark red-brown luminescent, anhedral matrix quartz (Fig. 10.5c). In all three granites, the anhedral matrix quartz shows no zoning.

Secondary CL structures

In all three granites, quartz shows fine, transgranular ruptures, which are healed by dark red-brown, nearly non-luminescent quartz. Star-like halos around fluid inclusions are arranged along these ruptures (Fig. 10.5d).

The deformed quartz of the Carcoar and Barry granodiorites exhibits lamellae, which are not detectable using polarisation microscopy (Fig. 10.5d, e). In contrast, quartz of the Sunset Hills Granite is free of lamellae as such lamellae (Fig. 10.5f). The subgrain boundaries are coated by dark red-brown luminescent, newly crystallised quartz (Fig. 10.5d). Rotation recrystallisation mainly produced star-like structures at grain edges (Fig. 10.5e). With progressive rotation recrystallisation, the new rotated grains become more rounded, and the volume of the newly crystallised quartz (secondary quartz; Fig. 10.5f) increases in the Barry

Granodiorite and Sunset Hills Granite. Transgranular, up to 200 μm wide diffusion rims along thin, open micro-cracks indicate circulation of fluids along these cracks. These structures are abundant in the Sunset Hills Granite and relatively rare in the Barry Granodiorite.

CL patterns and properties linked to trace elements in the quartz

The quartz of the Carcoar Granodiorite and Sunset Hills Granite luminescences blue to violet/red-brown; whereas the quartz of the Barry Granodiorite luminescences red-brown to dark red-brown. The emission spectra of quartz between 1.4 and 3.1 eV are composed of two broad emission ranges; blue (2.6-3.1 eV) and red (1.75-2.1 eV) resulting in blue, violet, and red-brown CL colours (Fig. 10.6). The blue range consists of five emission bands at 2.47, 2.58, 2.68, 2.79, 2.96 eV (Fig. 10.7), and the red range consists of four bands at 1.73, 1.84, 1.96, and 2.15 eV. The blue emission range is generally characterised by a decrease of the intensity during electron radiation, and is caused by the destruction of luminescent defects through electron radiation and partly through sample warming (Ramseyer et al. 1988; Ramseyer and Mullis 1990). Cathodoluminescence resulting from defect centres is partly due to the effect of interstitially or substitutionally incorporated trace elements. Electron microprobe profiling of quartz grains was used to determine the relationship between the CL properties and the distribution of trace elements. The profiles and the Ti, Al, K and Fe concentrations are shown in Fig. 10.8.

The Ti concentration of quartz correlates with the intensity of the blue 2.97 eV emission band. The quartz of the Carcoar Granodiorite with the highest average Ti content (~85 ppm) shows the highest intensity of the 2.96 eV emission. The intensity of this band and the Ti content decrease from the Sunset Hills Granite (~75 ppm), to the Barry Granodiorite (~45 ppm) to the new crystallised quartz (~15 ppm). Furthermore, the intensity of the 2.96 eV emission and the Ti vary within the zoned phenocrysts of the Sunset Hills Granite; blue luminescent zones show a higher intensity and Ti content than the violet and red zones. Similar observations have been made by Kerkhof et al. (1996) and Müller et al. (2000), who showed that blue to violet luminescent growth zones in high-temperature quartz have high Ti concentrations. With increasing degrees of deformation the primary magmatic Ti distribution is more and more overprinted, resulting in weakening of the growth zoning. The dark red-brown to non-luminescent, secondary CL patterns, such as star-like halos around fluid inclusions, diffusion rims along open micro-cracks, lamellae and domains of newly crystallised (secondary) quartz along healed micro-cracks (e.g. black areas of the quartz in Fig. 10.5d, e, f), are depleted in Ti (Fig. 10.9). Depletion of Ti occurs near grain boundary in all three granitoids.

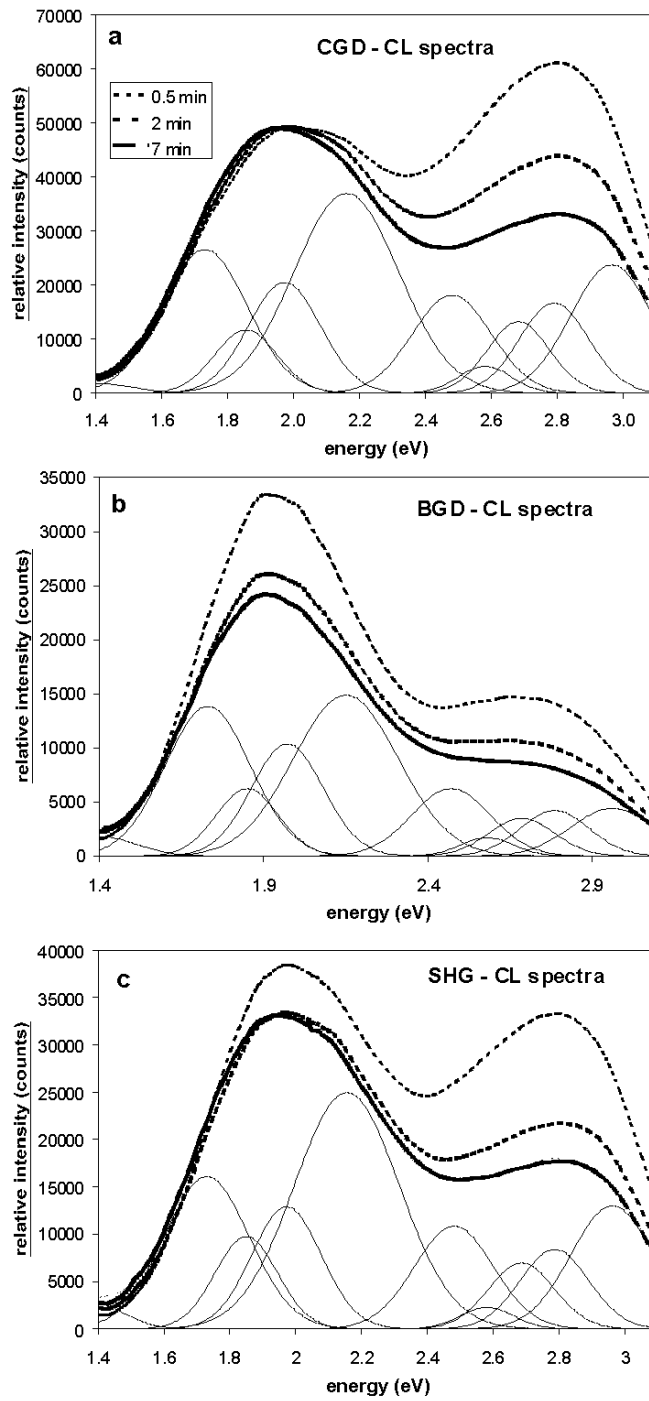


Fig. 10.6 CL spectra of quartz (1.4 - 3.1 eV) recorded with the 100 lines/mm grating after 30 s, 2 min, and 7 min of electron bombardment. The 7-min-spectra are fitted with Gaussian curves. Each Gaussian curve represents a single emission band. a - Carcoar Granodiorite (CGD). b - Barry Granodiorite (BGD). c - Sunset Hills Granite (SHG).

The Al distribution in all three granites is heterogeneous and the Al content is mostly below 32 ppm. At Al contents above the detection limit of 32 ppm, Al correlates with K (Fig. 10.10). The regression line corresponds to the Al/K weight ratio of an average muscovite composition. The muscovite flakes of up to 0.5 μm in diameter are finely dispersed in the quartz of all three granites, probably on slide planes and we assume they are the products of deformation.

The average Fe content of the three granites amounts approximately to the detection limit of 15 ppm. Despite the low Fe concentration, the spectra show the 1.73 eV emission band caused by Fe^{3+} defect structures (Pott and McNicol, 1971). The Fe content in quartz increases at the grain contacts with plagioclase, and particularly with biotite (Fig. 10.8), which indicates a high diffusion mobility of Fe in the quartz lattice.

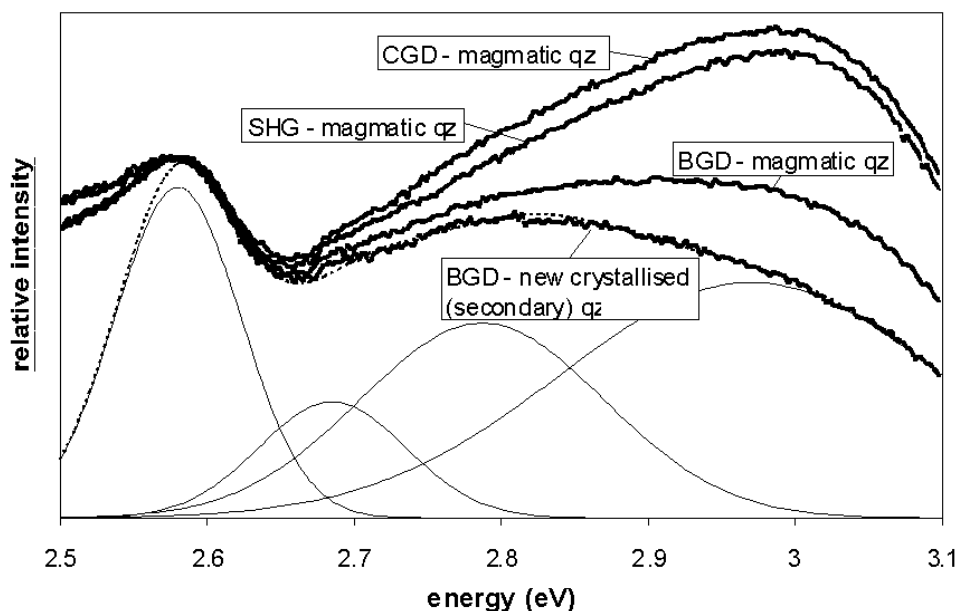


Fig. 10.7 Quartz CL spectra sections of the blue spectrum range (2.5 - 3.1 eV) recorded with the 1200 lines/mm grating after 7 min of electron bombardment where CGD = Carcoar Granodiorite, BGD = Barry Granodiorite and SHG = Sunset Hills Granite. The spectrum of BGD – new crystallised quartz is fitted with Gaussian curves.

The intensity of the 1.96 eV emission is constant during electron radiation in the quartz of the Carcoar Granodiorite, and decreases in the quartz of the Barry Granodiorite and Sunset Hills Granite. According to Siegel and Marrone (1981), Griscom (1985), and Stevens Kalceff and Phillips (1995), the red CL emission around 1.96 eV is related to OH and/or adsorbed H_2O . In undeformed quartz the 1.96 eV emission increases during electron radiation. This increase is explained by radiolysis of hydroxyl groups and/or adsorbed H_2O of quartz lattice, which

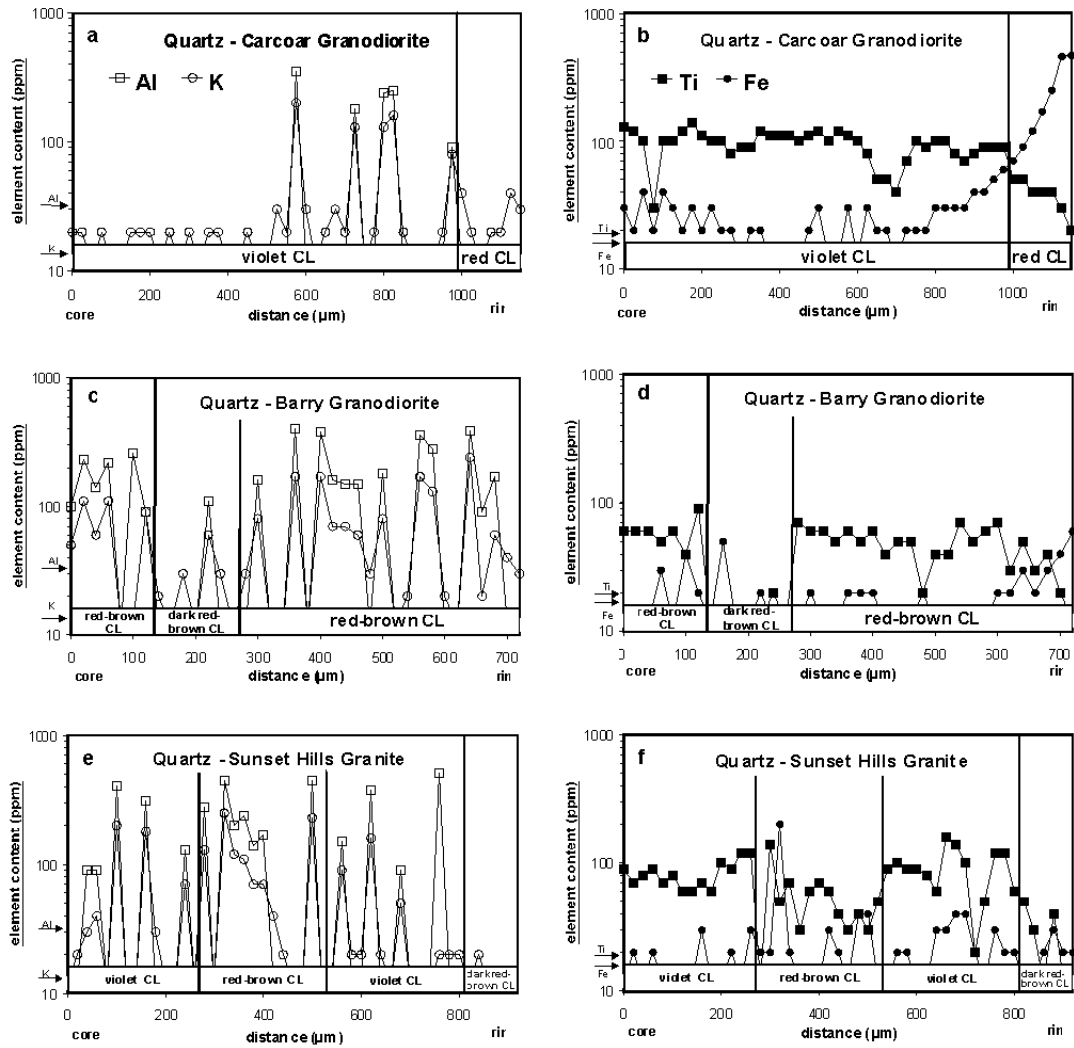


Fig. 10.8 Trace element profiles of quartz. a, b Carcoar Granodiorite. The position of the profile is shown in Figure 7a. c, d Barry Granodiorite. e, f Sunset Hills Granite. The position of the profile in the Sunset Hills Granite is shown in Figure 7b.

leads to the formation of non-bridging oxygen hole centres (NBOHC; Kalceff and Phillips, 1995). Hydroxyl groups and adsorbed H_2O act as charge compensators for $[2AlO_4/M^+]^-$ defects, where M^+ is a combination of Li, K, and Na ions (Bambauer et al., 1963; Maschmeyer and Lehmann, 1983; Kronenberg et al., 1986; Stenina 1995). As discussed above, the Al of the deformed quartz of the granites is removed from the quartz lattice and may be incorporated into the muscovite flakes. A similar process is assumed for the hydroxyl groups and adsorbed H_2O of the quartz lattice. Both bound water types may also be removed during deformation. This process explains the constant or slightly decreasing 1.96 eV emission, because no NBOHC is created during electron radiation, due to the absence of hydroxyl groups and adsorbed H_2O in the quartz lattice.

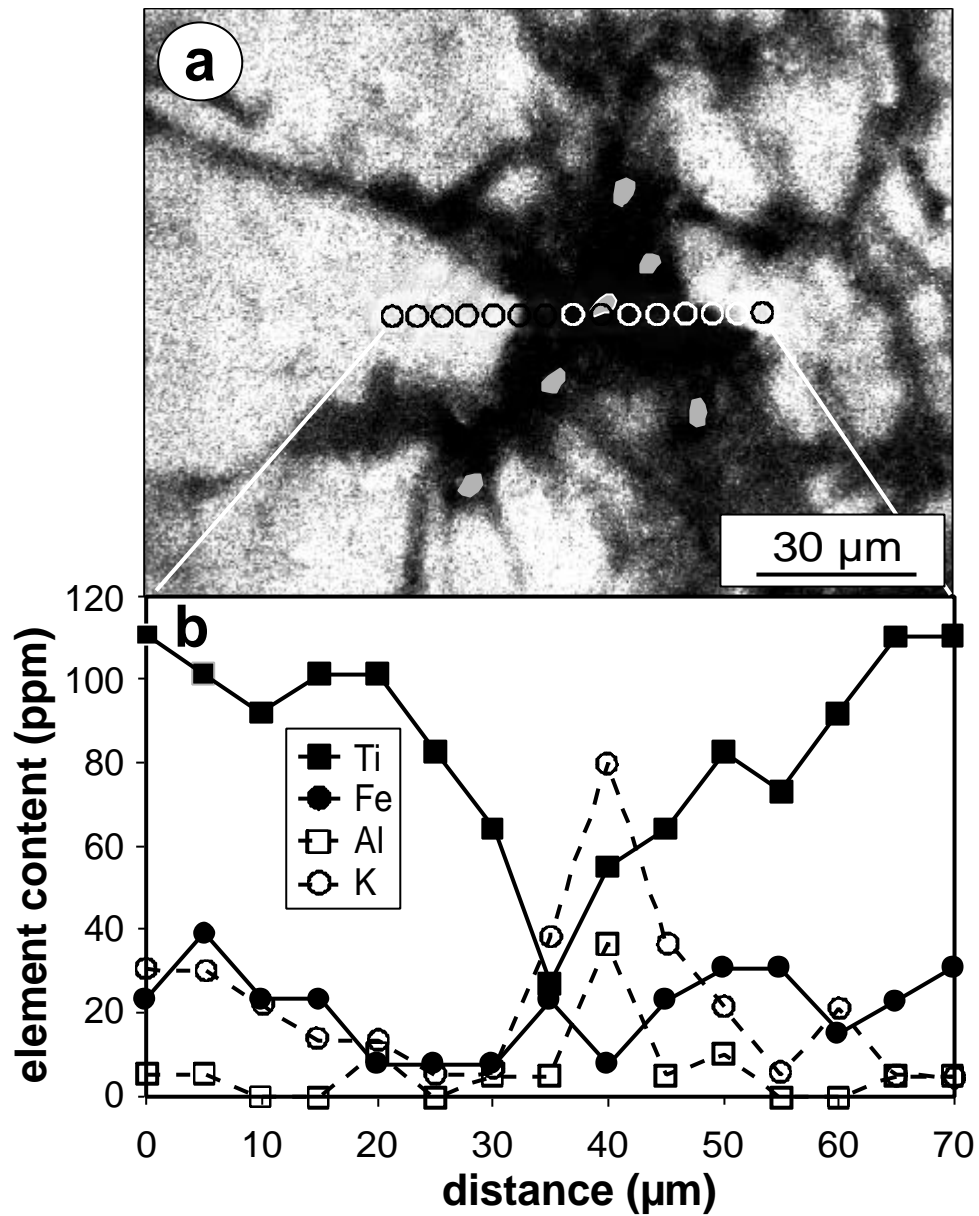


Fig. 10.9 a - SEM-CL image of quartz from the Carcoar Granodiorite. The black areas are dark red-brown to non-luminescent quartz around fluid inclusions. The residual porosity of the destroyed fluid inclusions at the sample surface are marked by grey dots. b - Trace element profile of the same quartz. The non-luminescent quartz is depleted in Ti. The high Al and K of the 40-μm point is caused by impurities in the fluid inclusion hole (grey).

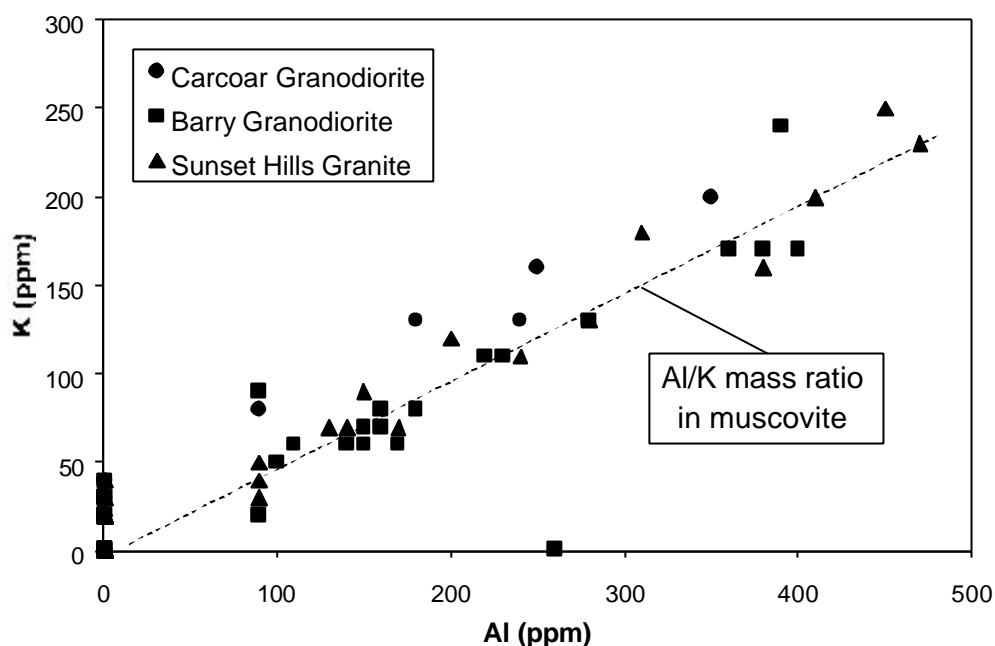


Fig. 10.10 Al versus K concentrations of the investigated quartz of the three granites. The regression line of the data above 50 ppm corresponds with the Al/K ratio of the average muscovite composition (dashed line). The deformation of magmatic quartz caused the development of submicroscopic muscovite flakes ($<0.5 \mu\text{m}$) along slip planes.

10.8 Al-in-hornblende geobarometry on the Carcoar and Barry granodiorites

The Al-in-hornblende barometer helps to estimate the crystallisation pressure of granites. The empirical correlation between the pressure of emplacement of calcalkaline granites, and the total Al content of hornblende equilibrated with quartz was proposed by Hammarstrom and Zen (1986) and Hollister et al. (1987). Experimental calibrations of the barometer were carried out by numerous workers (Johnson and Rutherford, 1989; Thomas and Ernst, 1990; Schmidt, 1992; Anderson and Smith, 1995). The barometer applies if the magmatic rocks (1) have the assemblage $\text{pl} + \text{ksp} + \text{qtz} + \text{hb} + \text{bt} + \text{tnt} + \text{Fe} - \text{Ti}$; and (2) plagioclase has a constant rim composition in the range of An^{25} and An^{35} ; (3) the analysis is limited only to the rim composition of hornblende; (4) the hornblende $\text{Fe}^{\text{T}}/(\text{Fe}^{\text{T}} + \text{Mg})$ ratios are in the range of 0.40-0.65, to exclude low $f\text{O}_2$, and (5) the pressure of crystallisation is above 1 kbar (Hammarstrom and Zen, 1986; Hollister et al., 1987; Anderson and Smith, 1995).

The Carcoar and Barry granodiorites have the appropriate mineral assemblage, with a plagioclase composition between An^{29} and An^{34} , and hornblende with $\text{Fe}^{\text{T}}/(\text{Fe}^{\text{T}} + \text{Mg})$ ratios

in the range of 0.42-0.53. The pressures during mineral growth were calculated using the calibration of Anderson and Smith (1995), including the effect of temperature, as the barometer is sensitive to variations in temperature. The temperatures were determined using the amphibole-plagioclase geothermometer after Blundy and Holland (1990) with the modified pressure term after Schmidt (1992).

Al-in-hornblende barometry on the Carcoar Granodiorite yields pressures of 1.7 ± 0.7 kbar (30 analyses) at 756 ± 12 C. Amphiboles of the Barry Granodiorite yield pressures of 1.8 ± 0.8 kbar (37 analyses) at 753 ± 22 C. No differences in the Al^{IV} -content were detected between the core and the rim of hornblende in the Carcoar and Barry granodiorites. Consequently, the crystallisation depth of the hornblende of the Carcoar and Barry granodiorites is 6.0 ± 2.6 km. These results are consistent with the estimated intrusion depths of 4-6 km for the Carcoar and Barry granodiorites based on the extent and nature of the contact aureole as calculated by Lennox and Fowler (pers. comm.)

10.9 Discussion and conclusions

Quartz cathodoluminescence

Three main conclusions can be made from CL analysis:

- (1) Magmatic quartz with high Ti content shows blue to violet CL, and with low Ti content red to red-brown CL. The variation of Ti in the quartz lattice relates with contrasts in the growth zoning of quartz phenocrysts referred to as the primary magmatic CL textures. With increasing deformation the homogeneity of Ti distribution decreases.
- (2) Dark red-brown to non-luminescent, secondary CL textures show low Al, Fe and Ti concentrations. The low trace element concentration of the star-like halos and the lamellae are due to systematic recovery of the defect centres of trace element, which was initiated by local stress around fluid inclusions and along slip planes (Kerkhof and Müller, 1999). The annealing of intragranular micro-shear zones led to formation of secondary quartz, depleted in trace elements.
- (3) In contrast to undeformed, natural quartz, interstitial water is absent from deformed quartz. We suggest that a large portion of the interstitial water, which was originally incorporated in the quartz lattice during magmatic crystallisation, was absorbed in the submicroscopical muscovite flakes during the post-magmatic deformation. The residual interstitial water reacted with silica due to pressure solution during deformation, and

formed Si-OH bonds along intragranular cracks caused by sliding (e.g. Michalske and Freiman, 1982).

Magmatic quartz textures

The analysis of the magmatic quartz texture, grain size distribution, and CL contrasted growth zoning of the phenocrysts leads to the following four conclusions:-

- (1) The Carcoar Granodiorite has one generation of anhedral quartz, which crystallised in cavities between feldspar and mafic minerals during and after emplacement.
- (2) The Barry Granodiorite formed one generation of unzoned, subeuhedral quartz phenocrysts overgrown by a second generation of anhedral matrix quartz. The homogeneous distribution of Al^I in hornblende indicates one main crystallisation stage. Therefore, both quartz generations must have crystallised at or near the emplacement level. First, quartz grew in a crystal mush, which facilitated a relatively unhindered growth and formation of planar crystal faces. Their growth may have been interrupted by magma degassing or magma pulsing. As a result, quartz with contrasting CL properties crystallised filling the residual space between the crystals. The grain size of the matrix quartz of the Barry Granodiorite is smaller in comparison to the Carcoar Granodiorite. In the south, the Barry Granodiorite shows aplitic textures and the grain size of the matrix quartz decreases to $\sim 100 \mu m$ indicating faster cooling rates of the melt. Both features indicate that a higher level of the Barry pluton is exposed in the south.
- (3) In contrast to the Carcoar and Barry granodiorites, the Sunset Hills Granite has three generations of quartz. The first two generations are phenocrysts of variable size, showing oscillatory and superordinate stepped zoning, and resorption surfaces. The stepped zoning and the resorption surfaces both indicate a change in melt composition, pressure and temperature during the early stage of magma ascent. The properties of these phenocrysts show similarities with rhyolitic phenocrysts. The third magmatic generation is represented by the homogeneous matrix quartz, which crystallised at the intrusion level, overgrowing the phenocrysts.
- (4) The melt of both granodiorites underwent a relatively continuous and rapid ascent; whereas the melt of the Sunset Hills Granite experienced a stepwise ascent that caused multiphase nucleation, episodes of slow crystal growth, and resorption events.

Geochemistry and Al-in-hornblende geobarometry

The similarities in chemical composition of the Carcoar and Barry granodiorites indicate derivation from one magma source. The geochemical difference between both granodiorites is documented by fractionation of hornblende within the Barry Granodiorite. The most fractionated, uppermost part of the Barry Granodiorite is exposed at the contact with the Sunset Hills Granite in the south. The intrusion depth is in the lower error range of the hornblende crystallisation depth between 3 and 6 km. This depth is consistent with estimations of 4-6 km for the emplacement depth of the Barry Granodiorite by Lennox and Fowler (pers. comm.), which are based on the extent and nature of the contact aureole. The intrusion depth of the Carcoar Granodiorite is in the upper error range of the hornblende crystallisation depth between 6 and 9 km, as also inferred by lower cooling rates and a wider contact aureole. Consequently, the northern part of the Carcoar Granodiorite represents a deeper part of the pluton compared with the southern part of the Barry Granodiorite, which is consistent with 3D gravity modelling of the pluton (Trzebski et al., 1999).

In contrast to the I-type Carcoar and Barry granodiorites, the Sunset Hills Granite shows S-type affinity. The magma of the Sunset Hills Granite we interpret as fractionation product derived from the magma of the Wyangala Batholith. Besides the compositional similarities of both granites, the Sunset Hills Granite occurs at the northeastern extremity of the negative gravity anomaly due to the Wyangala Batholith (Trzebski et al., 1999). Three-dimensional gravity modelling and re-interpretation of aeromagnetics suggest a subsurface connection and therefore a possible genetic link in magma genesis between both granites.

Deformation fabrics

The Carcoar and Barry granodiorites both show magmatic and post-magmatic foliation, whereas in the Sunset Hill Granite an intense post-magmatic foliation was developed, which may have possibly overprinted a pre-existing magmatic foliation. The magmatic foliation of the Carcoar and Barry granodiorites are marked by aligned biotite and hornblende and are cross-cut by the post-magmatic, solid-state foliation. This later foliation in all granitoids is post-magmatic, because it is (1) marked by secondary minerals, such as muscovite and chlorite, (2) is locally at high angles to pluton-host rock contacts, (3) is continuous with the regionally developed cleavage, and (4) cross-cuts aligned igneous minerals. In addition, the contact aureole of these granitoids overprints the earlier metamorphic fabrics (Lennox et al., 1991; Lennox and Fowler, 1994; McKinlay, 1993; Lennox et al., 1998). The post-magmatic deformation fabrics are probably related to regional shear zones.

The dominance of prismatic subgrain boundaries of quartz in the Carcoar and Barry granodiorites indicates slip along the basal plane, which is limited to the stability field of low-quartz (Blumenfeld et al., 1986; Kruhl, 1996). The beginning of quartz recrystallisation in the Carcoar Granodiorite indicates deformation temperatures of $\approx 290^{\circ}\text{C}$ (Voll 1976, 1980). The increase in size of the dynamically recrystallised quartz grains in the Barry Granodiorite, in comparison with that of the quartz in the Carcoar Granodiorite, is due to both increasing temperature and differential stress. Secondly, the new crystallised quartz grains with high-angle boundaries developed during the recovery of subgrains at moderate to high temperatures in the Barry Granodiorite (Hull and Bacon, 1984; Hirth and Tullis, 1992). The Barry Granodiorite was deformed at higher temperature than the Carcoar Granodiorite. The absence of widespread boundary migration recrystallisation indicates a maximum deformation temperature of 400°C (Guillopé and Poirier, 1979; Urai and Humphreys, 1981; Urai, 1983; Paschier and Trouw, 1998). Using the closure temperature of the Ar-Ar system in biotite, the likely temperatures during the post-magmatic Bowring deformation (405-410 Ma) are estimated to $\sim 350^{\circ}\text{C}$ for the Carcoar Granodiorite and to $350\text{-}400^{\circ}\text{C}$ for the Barry Granodiorite.

The boundary migration recrystallisation during dynamic recrystallisation in the quartz of the Sunset Hills Granite is a typical process at high temperatures of $400\text{-}700^{\circ}\text{C}$ (Guillopé and Poirier, 1979; Urai and Humphreys, 1981; Urai, 1983; Paschier and Trouw, 1998). The development of basal and prismatic subgrain boundaries in deformed quartz indicates prism slip of quartz, which is restricted to the stability field of high-quartz at temperatures around 550°C (Blacic and Christie, 1984; Blumenfeld et al., 1986; Kruhl, 1996). The increase of dynamically recrystallised grain size from the Barry Granodiorite to the Sunset Hills Granite is interpreted to be a result of the dominance of annealing recrystallisation over dynamic recrystallisation at temperatures around 550°C . This is consistent with the estimated deformation temperatures of 550°C for the adjacent Wyangala Batholith (Morand, unpubl. data in Paterson et al., 1990).

10.10 Geological implications

This study has quantified the conditions of magma crystallisation, emplacement and deformation of the Carcoar, Barry and Sunset Hills granites. Our previous work revealed the structural framework of these granites and their host rocks, the three-dimensional shape of the

plutons, their spatial relationship with faults and their distribution at depth (Lennox et al., 1998; Trzebski et al., 1999). New and published radiometric dating differentiated three events that indicate the timing of emplacement of the granites and their subsequent deformation (Lennox et al., 1998). These events are coeval with regional orogenic events in the Lachlan Fold Belt (e.g., Gray and Forster, 1997). The first event (Benambran), dated at approximately 430 Ma (Lower Silurian) by the zircon SHRIMP U-Pb method and by U-Pb dating of zircon fractions, indicates the emplacement time of all three granites (Lennox, unpublished data). Both subsequent events, dated to ~410 Ma (Bowning) and ~375 Ma (Tabberabberan) using the Rb-Sr-, Ar-Ar- and K-Ar-methods on biotite and hornblende, document two deformation stages following granite emplacement (Lennox et al., 1998; Glen et al., in press).

All three granites intruded synchronously, but at different crustal levels. The Carcoar and Barry granodiorites were emplaced at a depth of 6 ± 2.6 km under brittle to locally weakly ductile conditions. The elongate shape of the Barry Granodiorite is subparallel to the regional structural strain. In contrast, the almost square geometry of the Carcoar Granodiorite suggests emplacement in a brittle fashion which was structurally controlled by extensional faults and fractures at shallow crustal depths. Although the intrusion depth of the Sunset Hills Granite could not be determined, we assume that the magma accumulated at deeper levels on the basis of the upper greenschist facies and the ductile structures of the surrounding host rocks (Lennox and Fowler, 1994). The grain boundary migration recrystallisation and larger average size of recrystallised quartz grains (~100 μm) with high-angle boundaries further indicate that the Sunset Hills Granite remained in a hotter environment over a considerably longer period of time after emplacement. The concordance in structural development between the Sunset Hills Granite and the host-rocks, the geometry of foliation trends around the pluton and its elongated shape additionally indicate emplacement into host rocks at greater depth under ductile conditions. This is also supported by the fact that during the first post-magmatic Bowning event the Sunset Hills Granite was deformed at temperatures of ~550° C and at depths of 10-12 km when applying a likely geothermal gradient of 45-55°C/km (Packham, 1999). Similar intrusion depths were obtained by pressure data of 3-4 kbar for the adjacent and genetically related Wyangala Batholith (Morand quoted in Paterson et al., 1990). In contrast, during the same event both I-type granodiorites were deformed at temperatures of 350-400°C due to their higher emplacement level in the crust. The east-west contraction during the Upper Silurian/Lower Devonian causes uplift of both granodiorites and cooled through the closure temperature of biotite (~ 350° C) at around 412 Ma; whereas the deeper seated Sunset Hills Granite was synchronously cooled through the closure temperature of

hornblende (~550° C). The second post-magmatic deformation (Tabberabberan event), caused by regional east-west contraction, only weakly deformed the near-surface located more resistant granodiorites in a brittle fashion because the granodiorites were at upper crustal levels (Vernon and Flood, 1988). The Sunset Hills Granite experienced further vertical uplift due to east-vergent thrusting and cooling through the closure temperature of biotite (~350° C) at around 380 Ma (Paterson et al., 1990; Glen and Watkins, 1999). The youngest event around 340 Ma, which correlates with the Early Carboniferous Kanimblan deformation (Gray and Forster, 1997), was associated with north-south contraction and resulted in mega-kinking at a regional scale (Powell et al., 1985). North-south oriented thrusting may have further exposed all three granites along north-vergent ramps. This is supported by the fact that both granodiorites show deeper exposure levels in the north of the plutons.

References

- Agel A. (1992): Paramagnetische Defektzentren in polykristallinem Quarz granitischer und metamorpher Herkunft. *Thesis*, Univ. Marburg, 109 p.
- Agel A. and Petrov I. (1990): Im Quarzgitter substituiertes Aluminium als Indikator für dessen Bildungstemperatur. *Ber. Dtsch. Min. Ges., Beih. Eur. J. Mineral.*, **2/1**: 144.
- Allègre C.J., Provost A., Jaupart C. (1981): Oscillatory zoning: A pathological case of crystal growth. *Nature*, **294**: 223-228.
- Aines R.D. and Rossman G.R. (1984): Water in minerals? A peak in the infrared. *J. Geophys. Res.*, **89/B6**: 4059-4071.
- Alonso P.J., Halliburton L.E., Kohnke E.E. and Bossoli R.B. (1983): X-ray-induced luminescence in crystalline SiO₂. *J. Appl. Phys.*, **54/9**: 5369-5375.
- Anderson A.T. (1984): Probable relations between plagioclase zoning and magma dynamics, Fuego Volcano, Guatemala. *Amer. Mineral.*, **69**: 660-676.
- Anderson J.H. and Wickersheim K.A. (1964): Near infrared characterisation of water and hydroxyl groups on silica surfaces. *Surf. Sci.*, **2**: 252-260.
- Anderson J.L. and Smith D.R. (1995): The effects of temperature and *f*O₂ on the Al-in-hornblende barometer. *American Mineralogist*, **80**: 549-559.
- Arikas K. (1964): Geochemie und Petrologie der permischen Rhyolite in SW-Deutschland. *Fortschritte d. Mineral.*, Bh. 1, **64**: 9-10.
- Armstrong J.T. (1991): Quantitative elemental analysis of individual microparticles with electron beam instruments. In: Heinrich K.F.J. and Newbury D.E. (eds.): *Electron probe quantification*. Plenum Press, New York, London, 261-315.
- Audétat A. and Günther D. (1999): Mobility and H₂O loss from fluid inclusions in natural quartz crystals. *Contrib. Mineral. Petrol.*, **137**: 1-14.
- Baker B.G. and Sexton B.A. (1975): Electron beam effects in Auger analysis of physisorbed xenon. *Surf. Sc.*, **52**: 353-364.
- Bambauer H.U. (1961): Spurenelementgehalt und –Farbzentren in Quarzen aus Zerrklüften der Schweizer Alpen. *Schweiz. Mineral. Petrogr. Mitt.*, **41**: 335-369.
- Bambauer H.U., Brunner G.O., Laves F. (1963): Merkmale des OH-Spektrums alpiner Quarze (3 μ -Gebiet). *Schweiz. Mineral. Petrogr. Mitt.*, **43**: 259-268.
- Bard J.P. (1986): *Microtextures of igneous and metamorphic rocks*. - D. Reidel Publishing Company Dordrecht, Boston, Lancaster, 264 pp.
- Behr H.J. (1966): Die Verwendung von Lackfilmen (Ätzbildern) zur Strukturuntersuchung von metamorphen und magmatischen Gesteinen. *Monatsber. Dt. Akad. Wiss.*, **8/12**: 897-904.
- Behr H.J. (1989): Die geologische Aktivität von Krustenfluiden. In: *Gesteinsfluide - Ihre Herkunft und Bedeutung für geologische Prozesse*. Nds. Akad. Geowiss. Veröfftl. 1, Hannover, pp. 7-42.
- Behr H.-J. and Frenzel-Beyme K. (1989): Permeability and paleoporosity in crystalline bedrocks of the Central European basement-studies of cathodoluminescence. In: Boden A. and Eriksson K.G. (eds.): *Exploration of the deep continental crust*. Deep drilling in crystalline bedrock, volume 2. Springer, pp. 477-497.
- Behr H.-J. and Horn E.E. (1982): Fluid inclusion systems in metaplaya deposits and their relationship to mineralization and tectonics. *Chem. Geol.*, **37**: 173-189.
- Behr H.-J., Horn E.E., Porada H. (1983): Fluid inclusions and genetic aspects of the Damara Orogen. In: Martin H. and Eder F.W.: *Intracontinental Fold Belts*. Springer, pp. 611-654.
- Behr H.-J. and Schmidt-Mumm A. (1987): The role of sedimentary and tectonic brines in the Damara Orogen, Namibia. *Appl. Geochemistry*, **2**: 535-542.
- Bershov L.V., Krylova M.D. and Speranskij A.V. (1978): The electron holes centres O—Al and Ti³⁺ as indicator for temperature conditions during regional metamorphosis (in Russ.). *Izv. Akad. Nauk SSSR, Ser. geol.*, 113-117.
- Beskin S.M., Larin V.N., Marin Yu.B. (1994): Physiographic types of granitic rocks of Kazakhstan and their metallogenic significance. In: Shatov V., Seltmann R., Kremenetsky A., Lehmann B., Popov V., Ermolov P. (eds.): *Granite-related ore deposits of Central Kazakhstan and adjacent areas*. Glagol St. Petersburg 1996, pp 259-268.
- Beus A.A., Severov E.A., Sitnin A.A., Subbotin K.D. (1962): *Albitized and greisenized granites (apogranites)*. Izdat. Akad. Nauk SSSR, Moscow, 196 p. (in Russian).
- Blacic J.D. and Christie J.M. (1984): Plasticity and hydrolytic weakening of quartz single crystals. *J. Geophys. Res.*, **89**: 4223-4239.

- Blankenburg H.-J., Götze J. and Schulz J. (1994): *Quarzrohstoffe*. Deutscher Verlag für Grundstoffindustrie, Leipzig-Stuttgart, 296 pp.
- Blumenfeld P., Mainprice D. and Bouchez J.L. (1986): C-slip in quartz from subsolidus deformed granite. *Tectonophysics*, **127**: 97-115.
- Blundy J.D. and Holland J.B. (1990): Calcic amphibole equilibria and a new amphibole-plagioclase geothermometer. *Contrib. Mineral. Petrol.*, **104**: 208-24.
- Blundy J.D. and Holland J.B. (1994): Non-ideal interactions in calcic amphiboles and their bearing on amphibole-plagioclase thermometry. *Contrib. Mineral. Petrol.*, **116**: 433-47.
- Boiron M.C., Essarraj S., Sellier E., Cathelineau M., Lespinasse M. and Poty B (1992): Identification of fluid inclusions in relation to their host microstructural domains in quartz by cathodoluminescence. *Geochim. Cosmochim. Acta*, **56**: 175-185.
- Bottinga Y., Kudo A., Weill D. (1966): Some observations on oscillatory zoning and crystallisation of magmatic plagioclase. *Amer. Mineral.*, **51**: 792-806.
- Boullier A.M. and Bouchez J.L. (1978): Le quartz en rubans dans les mylonites. *Bull. Soc. geol. France*, **713**: 253-262.
- Breiter K., Sokolova M., Sokol A. (1991): Geochemical specialisation of the tin bearing granitoid massif of NW Bohemia. *Mineral. Deposita* **26**: 298-306.
- Breiter K., Förster H.J., Seltmann R. (1999): Variscan silicic magmatism and related tin-tungsten mineralization in the Erzgebirge-Slavkovsky les metallogenic province. *Mineralium Deposita*, **34**: 505-521.
- Breiter K., Fryda J., Seltmann R., Thomas R. (1997): Mineralogical evidence for two magmatic stages in the evolution of an extremely fractionated P-rich rare-metal granite: the Podlesi stock, Krušné Hory, Czech Republic. *J. Petrol.*, **38/12**: 1723-1739.
- Brown C. and Thomas L. (1960): The effect of impurities on the growth of synthetic quartz. *J. Phys. Chem. Solids*, **13**: 337.
- Bruckschen P., Neuser R.D., Richter D.K. (1992): Cement stratigraphy in Triassic and Jurassic limestones of the Weserbergland (northwest Germany). *Sedimentary Geology*, **81**: 195-214.
- Bruhn F., Bruckschen P., Meijer J., Stephan A., Richter D.K., Veizer J. (1996): Cathodoluminescence investigations and trace-element analysis of quartz by micro-PIXE: implications for diagenetic and provenance studies in sandstone. *Canadian Mineralogist* **34**: 1223-1232
- Brunner G.O., Wondratschek H. and Laves F. (1961): Ultrarotuntersuchung über den Einbau von H in natürlichen Quarz. *Z. Elektrochem.* **56**: 735-750.
- Candela P.A., Blevin P.L. (1995): Do some miarolitic granites preserve evidence of magmatic volatile phase permeability? *Economic Geology*, **90**: 2310-2316.
- Castaing R. (1951): Application des sondes électroniques à une méthode d'analyse ponctuelle chimique et cristallographique. (Electron beam based techniques for spatially resolved chemical and crystallographical analyses.) – Thèse, Université de Paris, France.
- Cobbing E.J., Pitfield P.E.J., Darbyshire D.P.F., Mallick D.I.J. (1992): *The granites of the South-East Asian tin belt*. British Geological Survey Overseas Memoir 10, London, 369 p.
- Cohen A.J. (1960): Substitutional and interstitial aluminium impurity in quartz, structure, and color centre interrelationships. *J. Phys. Chem. Solids*, **13**: 321-325.
- Collins P.J. and Vernon R.H. (1992): Paleozoic arc growth, deformation and migration across the Lachlan Fold Belt, southeastern Australia. *Tectonophysics*, **214**: 381-400.
- Coney P.J. (1992): The Lachlan Fold Belt of eastern Australia and Circum Pacific tectonic evolution. *Tectonophysics*, **214**: 381-400.
- Crookes W. (1879): Contributions to molecular physics in high vacuo. *Phil. Trans.*, **170**: 641-662.
- Demars C., Pagel M., Deloule E., Blanc P. (1996): Cathodoluminescence of quartz from sandstones: Interpretation of the UV range by determination of trace element distributions and fluid-inclusion P-T-X properties in authigenic quartz. *Amer. Mineral.*, **81**: 891-901.
- Dennen W.H. (1965): Stoichiometric substitution in natural quartz. *Geochimica et Cosmochimica Acta*, **30**: 1235-1241.
- Dennen W.H., Blackburn W.H., Quesada A. (1970): Aluminium in quartz as a geothermometer. *Contr. Mineral. and Petrol.*, **27**: 332-342.
- D'Lemos R.S., Kearsley A.T., Pembroke J.W., Watt G.R., Wright P. (1997): Complex quartz growth histories in granite revealed by scanning cathodoluminescence techniques. *Geol. Mag.*, **134/4**: 549-552.
- Donaldson C.H., Henderson C.M.B. (1988): A new interpretation of round embayments in quartz crystals. *Mineral. Mag.*, **52**: 27-33.
- Dowty E. (1989): Crystal growth and nucleation theory and the numerical simulation of igneous crystallization. In: Hargraves R.B. (ed.): *Physics of magmatic processes*. New Jersey, pp 419-485.
- Dudek H.J. (1970): Zeitlicher und räumlicher Temperaturverlauf im Material bei fokussierter Elektronenstrahlung. *Optik* **30/5**: 453-460.
- Dudley R.J. (1976): The use of cathodoluminescence in the identification of soil materials. *J. Soil Sci.*, **27**: 487-491.

- Evans J., Hogg A.J., Hopkins M.S., Howarth R.J. (1994): Quantification of quartz cements using combined SEM CL and image analysis. *J. Sed. Res.*, **64A**: 334-338.
- Fiala F. (1968): Granitoids of the Slavkovský (Čisavský) Les Mountains. *Sbor. geol. Vid, G*, **14**: 93-160.
- Flick H. (1984): Kristallisation des Quarzes in kieselsäurereichen Schmelzen – Möglichkeiten seiner Verwendung als geologisches Thermometer und Barometer. *Habilitation*, University Heidelberg, 133 pp.
- Flick H. (1987): Geotektonische Verknüpfung von Plutonismus und Vulkanismus im südwestdeutschen Variscicum. *Geol. Rdsch.* **76/3**: 699-707.
- Flicstein J. and Schieber M. (1974): Microsegregation of impurities in hydrothermally-grown quartz crystals. *J. Cryst. Growth* **24/25**: 603-609.
- Förster H.J., Tischendorf G. (1994): The western Erzgebirge-Vogtland granites: Implications to the Hercynian magmatism in the Erzgebirge-Fichtelgebirge anticlinorium. In: Seltmann R., Möller P., Kämpf H. (eds.): *Metallogeny of Collisional Orogens*. Czech Geological Survey Prague, pp 35-48.
- Förster H.J., Seltmann R., Tischendorf G. (1995): High-fluorine, low phosphorus A-type (post-collision) silicic magmatism in the Erzgebirge. In: 2nd Symp. Permocarboiferous Igneous Rocks. *Terra Nostra*, **7**: pp 32-35.
- Förster H.J., Seltmann R., Tischendorf G. (1996): Post-collisional A-type silicic magmatism in the Variscan Erzgebirge. *Journ. Confer. Abstracts*, **1**: p. 174.
- Fowler A.D. (1990): Self-organized mineral textures of igneous rocks: the fractal approach. *Earth-Science Reviews* **29**: 47-55
- Frentzel-Beyme K. (1989): *REM-Kathodolumineszenz-Strukturen im Quarzteilgefüge von Metamorphiten: Bestandsaufnahme und geologische Interpretation*. Dissertation University Göttingen, Photodruck Göttingen, 78 p.
- Friebele E.J., Griscom D.L. and Marrone M.J. (1985): The optical absorption and luminescence bands near 2 eV in irradiated and drawn synthetic silica. *J. Non-Cryst. Solids*, **71**: 133-144.
- Friskney C.A. and Haworth C.W. (1967): Heat-flow problems in electron-probe microanalysis. *J. Appl. Phys.* **38**: 3796-3798.
- Fuchs, H. and Götze, J. (1996): Origin of volcanic agate – evidence from cathodoluminescence, EPR and geochemical studies. *Intern. Conf. CL Rel. Techn. Geosci. Geomat.*, Nancy, Abstracts, pp. 49-50.
- Gallei E. and Parks G.A. (1972): Evidence for surface hydroxyl groups in attenuated total reflectance spectra of crystalline quartz. *J. Colloid Interface Sci.*, **38**: 650-651.
- Gerler J. (1990): Geochemische Untersuchungen an hydrothermalen, metamorphen, granitischen und pegmatitischen Quarzen und deren Flüssigkeitseinschlüssen. *Thesis*, Georg-August-Universität Göttingen, Germany, 169 pp.
- Glen R.A. (1998): The Eastern Belt of the Lachlan Orogen. In: Finlayson, D.M. and Jones, L.E.A. (eds.): *Mineral Systems and the crust-upper mantle of southeast Australia*. Australian Geological Survey Organisation Record, **2**: 80-82.
- Glen R.A., Walshe J.L., Barron L.M., Watkins J.J. (1998): Ordovician convergent-margin volcanism and tectonism in the Lachlan sector of east Gondwana. *Geology*, **26**: 751-754.
- Glen, R.A. and Walshe J.L. (1999): Cross-structures in the Lachlan Orogen: the Lachlan Transverse Zone example. *Australian Journal of Earth Science*, **46**: 641-658.
- Glen, R.A., Lennox, P.G. and Forster, D.A. (in press): 40Ar-39Ar dating of deformation west of the Hill End Through, Lachlan Orogen, New South Wales. *Quarterly Note, Geological Survey of New South Wales*.
- Goldstein E. (1907): *Über das Auftreten roten Phosphoreszenzlichtes an Geissler'schen Röhren: Bericht der Deutschen Physikalischen Gesellschaft*, 598-605.
- Gorobets B.S., Graft M.L., Podolskiy A.M. (1989): *Luminescence of minerals and ores*. Ministry of Geology USSR, Moscow, 53 pp., (in Russian).
- Gorton N.T., Walker G., Burley, S.D. (1996): Experimental analysis of the composite blue CL emission in quartz - is this related to aluminium content? In: *Abstracts SLMS International Conference on Cathodoluminescence*, Nancy, Sept 1996, p 59.
- Gottstein G. and Mecking H. (1985): Recrystallization. In: Wenk H.R. (ed.): *Preferred orientation in deformed metals and rocks - an introduction to modern texture analysis*. Academic Press, New York, pp. 183-218.
- Götze J. (2000): Cathodoluminescence microscopy and spectroscopy in applied mineralogy. *Habilitation*, TU Bergakademie Freiberg, 128pp.
- Götze J. and Plötze M. (1997): Investigation of trace element distribution in detrital quartz by electron paramagnetic resonance (EPR). *Eur. J. Mineral.* **9**: 529-537.
- Götze J., Plötze M., Fuchs H. and Habermann D. (1999): Defect structure and luminescence behaviour of agate – results of electron paramagnetic resonance (EPR) and cathodoluminescence (CL) studies. *Min. Mag.* **63/2**: 149-163.
- Grant P. (1978): The role of scanning electron microscope in cathodoluminescence petrology. In: Whalley B. (ed): *Scanning Electron Microscopy in the Study of Sediments*. Geo Abstracts, pp. 1-11.
- Grant P.R. and White S.H. (1978): Cathodoluminescence and microstructure of quartz overgrowths on quartz. *Scan. Electr. Micr.*, **1978/I**: 789-794.

- Gray D.R., Forster D.A., Bucher M. (1997): Recognition and definition of orogenic events in the Lachlan Fold Belt. *Australian Journal of Earth Sciences*, **44**: 489-501.
- Gray D.R. and Forster D.M. (1997): Orogenic concepts – applications and definition: Lachlan fold belt, eastern Australia. *American Journal of Science*, **297**: 859-891.
- Greenwood H.J., McTaggart K.C. (1957): Correlation of zones in plagioclase. *Amer J Sci* **255**: 656-666.
- Griggs D.T. (1967): Hydrolytic weakening of quartz and other silicates. *Geophys. J. R. Astron. Soc.* **14**: 19-32.
- Griggs D.T. and Blacic J.D. (1965): Quartz: Anomalous weakness of synthetic crystals. *Science*, **147**: 292-295.
- Griscom D.L. (1985): Defect structure of glass. - J. Non-Cryst. Solids **73**, 51-77.
- Griscom D.L. (1991): Optical properties and structure of defects in silica glass. *J. Cer. Soc. Japan*, **99**: 923.
- Gritsenko B.P. and Lisitsyn V.M. (1985): Intrinsic short-lived defects in quartz. *Sov. Phys. Solid State*, **27/7**: 1330-1331.
- Grün R., Tani A., Gurbanov A., Koshchug D., Williams I., Braun J. (2000): A new method for the estimation of cooling and denudation rates using paramagnetic centres in quartz: A case study on the Eldzhurtinsky Granite, Caucasus. *J. Geophys. Research* (in review).
- Guillopè M. and Poirier J.P. (1979): Dynamic recrystallization during creep of single crystalline halite: an experimental study. *J. Geophys. Res.*, **4**: 5557-5567.
- Guzzi M., Martini M., Mattaini M., Pio F., Spenolo G. (1987): Luminescence of fused silica: observation of the O₂⁻ emission band. *Phys. Rev. B*, **35**: 9407-9409.
- Haapala I. (1997): Magmatic and postmagmatic processes in tin-mineralized granites: Topaz-bearing leucogranite in the Eurajoki Rapakivi granite stock, Finland. *J. Petrol.*, **38/12**: 1645-1659.
- Haase C.S., Chandam J., Feinn D., Ortoleva P. (1980): Oscillatory zoning in plagioclase feldspar. *Science*, **209**: 272-274.
- Habermann D., Neuser R.D., Richter D.K. (2000): Quantitative high-resolution spectral analysis of Mn²⁺ activated CL in sedimentary calcite. In: Pagel M., Barbin V., Blanc P., Ohnenstetter D. (eds.): *Cathodoluminescence in Geosciences*. Springer, Berlin Heidelberg New York, pp. 331-358.
- Hagni R.D. (1984): Cathodoluminescence microscopy applied to mineral exploration and beneficiation. In: Park W.C., Hausen D.M., Hagni R.D. (eds.): *Applied mineralogy*. Proceedings of the Second International Congress on Applied Mineralogy, AIME, New York, p. 41-66.
- Hagni R.D. (1987): Industrial applications of cathodoluminescence microscopy. In: Hagni R.D. (ed.): *Process Mineralogy IV: Applications to precious metal deposits, industrial minerals, coal, liberation, mineral processing, agglomeration, metallurgical products, and refractories, with special emphasis on cathodoluminescence microscopy*. TMS, Warrendale, Pennsylvania, p. 37-52.
- Hammarstrom J.M. and Zen E-An (1986): Aluminium in hornblende: An empirical igneous geobarometer. *Am. Mineral.*, **71**: 1297-1313.
- Hanusiak W.M. (1975): *Low temperature cathodoluminescence of crystalline silica for use in the characterisation of respirable dusts*. MSc Thesis, State College, Penn State University.
- Hanusiak W.M. and White E.M. (1975): SEM cathodoluminescence for characterisation of damaged and undamaged alpha-quartz in respirable dusts. In: Johari O., Corvin I. (eds.): *Proceedings of the 8th annual Scanning Electron Microscope Symposium*, pp. 125-132.
- Harris D.W., Anderson A.T. (1984): Volatiles H₂O, CO₂ and Cl in a subduction related basalt. *Contrib. Mineral. Petrol.*, **87**: 120-128.
- Hartmann P. (1978): Sur la morphologie des cristaux. *Bull. Mineral.*, **101**: 195.
- Hashimoto T., Sakaue S., Aoki H., Ichino M. (1994): Dependence of TL-property changes of natural quartzes on aluminium contents accompanied by thermal annealing treatment. *Radiat. Meas.*, **23**: 293-299.
- Hay R.S. and Evans B. (1987a): Chemically induced grain boundary migration in calcite: temperature dependence, phenomenology, and possible applications to geologic systems. *Contrib. Mineral. Petrol.*, **97**: 127-141.
- Hay R.S. and Evans B. (1987b): Chemically induced grain boundary migration in low and high angle calcite grain boundaries. *Acta Metal.*, **135**: 2049-2062.
- Hayes W., Kane M.J., Salminen O., Wood R.L. and Doherty S.P. (1984): ODMR of recombination centers in crystalline quartz. *J. Phys. C*, **17**: 2943-2951.
- Heggie M.I. (1992): A molecular water pump in quartz dislocations. *Nature*, **355/23**: 337-339.
- Helbig C., Beyer F. (1970): Zur relativen Alterstellung und petrotektonischen Analyse des Schellerhauer Granits. *Jb. Geol.*, 3/1967, Berlin, pp. 217-242.
- Hess P.C. (1989): *Origin of igneous rocks*. Harvard University Press, 336 pp.
- Hirth G. and Tullis J. (1992): Dislocation creep regimes in quartz aggregates. *J. Struct. Geol.*, **14**: 145-160.
- Hollister L.S., Grissom G.C., Peters E.K., Stowell H.H., and Sisson V.B. (1987): Confirmation of the empirical correlation of Al in hornblende with pressure of solidification of calc-alkaline plutons. *Am. Mineral.*, **72**: 231-239.
- Holt D.B. (1992): New directions in scanning electron microscopy cathodoluminescence microcharacterisation. *Scanning Microscopy*, **6**: 1-21.

- Holt D.B. and Saba F.M. (1985): The cathodoluminescence mode of the scanning electron microscope: a powerful microcharacterisation technique. *Scanning Electron Microscopy*, **1985/III**: 1023-1045.
- Holtén T., Jamtveit B., Meakin P., Cortini M., Blundy J., Austrheim H. (1997): Statistical characteristics and origin of oscillatory zoning in crystals. *Amer. Min.*, **82**: 596-606.
- Holtz F., Johannes W. (1994): Maximum and minimum water contents of granitic melts: implications for chemical and physical properties of ascending magmas. *Lithos*, **32**: 149-159.
- Hull D. and Bacon D.S. (1984): *Introduction to dislocation*. Pergamon Press, New York, 251p.
- Isoya J., Bowman M.K., Norris J.R., Weil J.A. (1983): An electron spin echo envelope modulation study of lithium hyperfine and quadrupole coupling in the Al (Ti-Li) center of α -quartz. *J.Chem.Phys.*, **78**: 1735-1746.
- Itoh C., Suzuki T., Itoh N. (1990): Luminescence and defect formation in undensified and densified amorphous SiO₂. *Phys. Rev. B*, **41/6**: 3794-3799.
- Jackson K. (1979): *Theory of crystal growth*. Treatise on solid Chemistry Vol. 5, Hannay N. (ed.), Plenum Press, New York.
- Jani M., Halliburton L.E., Kohnke E.E. (1983): Point defects in crystalline SiO₂: thermally stimulated luminescence above room temperature. *J. Appl. Phys.*, **54**: 6321.
- Jarchovský T. and Pavlů D. (1991): Albite-topaz microgranite from Horní Slavkov (Slavkovský Les Mts.) North Bohemia. *Věst. Ústř. úst. geol.*, **66**: 13-22.
- Jarchovský T., Pavlů D., Morysek J., Najman K., Kozubek P. (1994): Li-F granite cupolas and Sn-W mineralization in the Slavkovský les Mts., Czech Republic. *Monograph Series on Mineral Deposits*, **31**: 131-148.
- Johannes W., Holtz F. (1996): *Petrogenesis and experimental petrology of granitic rocks*. Springer, Berlin Heidelberg New York, 335 p.
- Johnson, M.C. and Rutherford, M.J. (1989): Experimental calibration of the aluminium-in-hornblende geobarometer with application to Long valley caldera (California) volcanic rocks. *Geology*, **17**: 837-841.
- Jones C.E. and Embree D. (1976): Correlations of the 4.77-4.28-eV luminescence band in silicon dioxide with the oxygen vacancy. *J. Appl. Phys.*, **47/12**: 5365-5371.
- Just G., Schilka W., Seltmann R. (1987): INAA investigations in tin-bearing granites of the Altenberg and Sadisdorf ore deposits. In: *Proc. 4th Meeting on Nuclear Analytical Methods*, Vol. 1, pp. 242-251.
- Kalceff S.M.A. and Phillips M.R. (1995): Cathodoluminescence microcharacterization of the defect structure of quartz. *Phys. Review B*, **52/5**: 3122-3134.
- Kalceff S.M.A., Phillips M.R., Moon A.R. (1997): Cathodoluminescence microcharacterisation of the irradiation sensitive defect structure of amorphous silicon dioxide. *Microscopy and Microanalysis*, **3**: 751.
- Kalceff S.M.A., Phillips M.R., Moon A.R., Kalceff W. (2000): Cathodoluminescence microcharacterisation of silicon dioxide polymorphs. In: Pagel M., Barbin V., Blanc P., Ohnenstetter D.: *Cathodoluminescence in Geosciences*. Springer, Berlin Heidelberg New York, pp. 193-224.
- Kats A. (1962): Hydrogen in alpha-quartz. *Philips Res. Repts*, **17**: 133-279.
- Kempe U., Götze J., Dandar, S., Habermann, D. (1999): Magmatic and metasomatic processes during formation of the Nb-Zr-REE deposits from Khaldzan Buregte (Mongolian Altai): Indications from a combined CL-SEM study. *Miner. Mag.*, **63**: 165-177.
- Kennedy S.K. and Arikani F. (1990): Spalled quartz overgrowths as a potential source of silt. *J. Sed. Petrol.*, **60**: 438-444.
- Kerkhof A.M. van den, Scherer T., Riganti A. (1996): Cathodoluminescence and EPR analysis of Archean quartzites from the Nondweni Greenstone Belt, South Africa. In: *Abstracts SLMS International Conference on Cathodoluminescence*, Nancy, Sept 1996, p. 75.
- Kerkhof A.M. van den, Behr H.-J., and Müller A. (1999): *Charakterisierung von Defektstrukturen in Quarz mit Kathodolumineszenz*. SFB 468 Wechselwirkungen an geologischen Grenzflächen, Arbeits- und Ergebnisbericht, Universität Göttingen.
- Kerkhof A.M. van den and Müller A. (1999): Fluid inclusion re-equilibration and trace element redistribution in quartz: observations by cathodoluminescence microscopy. ECROFI XV 1999 Abstracts and Program, Potsdam, *Terra Nostra*, **99/6**: 161-162.
- Khanlary M.R., Townsend P.D., Townsend J.E. (1993): Luminescence spectra of germanosilicate optical fibres. I: radioluminescence and cathodoluminescence. *J. Phys. D*, **26**: 371.
- Kirkham R.V., Sinclair W.D. (1988): Comb quartz layers in felsic intrusions and their relationship to porphyry deposits. In: Taylor R.P., Strong D.F. (eds.): *Canadian Institute of Mining and Metallurgy*. Special Volume **39**: pp 50-71.
- Kirkpatrick R.J. (1975): Crystal growth from the melt: A review. *Amer. Mineral.*, **60**: 798-814.
- Kirkpatrick R.J. (1981): Kinetics of crystallization of igneous rocks. *Mineral. Soc. Amer., Rev. Mineral.*, **8**: 321-398.
- Kostov R.I. and Bershov L.V. (1987): Systematics of paramagnetic electron-hole centres in natural quartz (in Russian). *Izvest. AN SSSR, ser. geol.*, **7**: 80-87.

- Kovalenko V.I. (1977): *Petrology and geochemistry of rare-metal granitoids*. Novosibirsk: Nauka, 225 p. (in Russian).
- Kozłowski A. (1981): Melt inclusions in pyroclastic quartz from the Carboniferous deposits of the Holy Cross Mts, and the problem of magmatic corrosion. *Acta Geologica Polonica*, **31/3-4**: 273-283.
- Koyama H. (1980): Cathodoluminescence study of SiO₂. *J. Appl. Phys.*, **51**: 2228-2235.
- Krbetschek M.R., Götze J., Dietrich A., Trautmann T. (1997): Spectral information from minerals relevant for luminescence dating. *Radiat. Meas.* **27/5,6**: 695-748.
- Kronenberg A.K., Kirby S.H., Aines R.D., Rossmann G.R. (1986): Solubility and diffusional uptake of hydrogen in quartz at high water pressures: implications for hydrolytic weakening in the laboratory and within the earth. *Tectonophysics* **172**: 255-271.
- Kruhl J.H. (1996): Prism- and basal-plane parallel subgrain boundaries in quartz: a microstructural geothermobarometer. *J. metam. Geol.*, **14**: 581-589.
- Kuznetov V. and Lobachev A. (1973): Hydrothermal method for the growth of crystals. *Sov. Phys. Crystallography*, **17**: 775.
- Laemmlein G. (1930): Korrosion und Regeneration der Porphyr-Quarze. *Z Kristallogr.* **75**: 109-127.
- Lange H., Tischendorf G., Pälchen W., Klemm I., Osenkopf W. (1972): Fortschritte der Metallogenie im Erzgebirge. B. Zur Petrographie und Geochemie der Granite des Erzgebirges. *Geologie*, **21/4-5**: 457-493.
- Laubach S.E. (1997): Method to detect natural fracture strike in sandstones. *AAPG Bulletin*, **81/4**: 640-623.
- Lehmann G. and Bambauer H.V. (1973): Quarzkristalle und ihre Farben. *Angew. Chem.* **7**: 281-289.
- Lehmann G. (1975): On the colour centres of iron in amethyst and synthetic quartz: a discussion. *Amer. Mineral.* **60**: 335-337.
- Lennox P.G., Hawley S., Fowler T.J. (1991): Intraorogenic Barry Granite – two granites in one! Lachlan Fold Belt Conference, *Abstracts*, **29**: 17.
- Lennox P.G. and Fowler T.J. (1994): Tectonism, deformation gradients and intrusion styles. *7th Specialist Group in Tectonics and Structural Geology*, Field Conference, Jindabyne. Geological Society of Australia, *Abstracts*, **36**: 93-94.
- Lennox P.G., Fowler T. and Foster D. (1998): Barry Granodiorite and Sunset Hill Granite: Wyangala-style intrusion at the margin of a regional ductile shear zone, northern Lachlan Fold Belt, New South Wales. *Australian Journal of Earth Sciences*, **45**: 849-863.
- Lennox P.G., Trzebski R.C., Siebel W., Armstrong R. (*in prep.*): Crustal architecture in the eastern Lachlan Fold Belt, Australia.
- Lobin M. (1983): Pflanzenfunde aus den Tuffiten des Teplicer Quarzporphyrs. *Exk. Führ. U. Kurzref. "Fortschr. Paläont. Stratigr. Rotl."*, Ges. Geol. Wiss. DDR, Berlin, p. 31.
- Long J.V.P. and Agrell S.O. (1965): The cathodoluminescence of minerals in thin section. *Miner. Mag.*, **34**: 318-326.
- Loomis T.P. (1982): Numerical simulations of crystallization processes of plagioclase in complex melts: the origin of major and oscillatory zoning of plagioclase. *Contr. Miner. Petr.*, **81**: 219-229.
- Lowenstern J.B. (1995): Applications of silicate-melt inclusions to the of magmatic volatiles. In: Thompson J.F.H. (ed.): *Magmas, fluids and ore deposits*. Mineralogical Association of Canada Short Course, **23**: 71-99.
- Luff B.J. and Townsend P.D. (1990): Cathodoluminescence of synthetic quartz. *J. Phys. Condens. Matter*, **2**: 8089-8097.
- Lysakov V.S. (1978): Luminescence of quartz activated with manganese ions. *Sov. Phys. J.*, **21**: 946-947.
- MacLellan H.E., Trembath T.T. (1991): The role of quartz crystallization in the development and preservation of igneous texture in granitic rocks: Experimental evidence at 1 kbar. *Amer. Mineral.*, **76**: 1291-1305.
- Magnus M. and Götze (1998): Mineral composition of Lower Turonian sandstones of the Elbe Zone (Germany): evidence from combined CL and image analysis. *Zbl. Geol. Paläont. Teil 1*, **11/12**: 1255-1262.
- Marfunin A.S. (1979a): *Physics of Minerals and Inorganic materials*. Springer, Berlin.
- Marfunin A.S. (1979b): *Spectroscopy, luminescence and radiation centres in minerals*. Translated from Russian by V.V. Schiffer, Springer, Berlin, 352 pp.
- Marfunin A.S. (1995): *Advanced Mineralogy*. Vol.2 – Methods and instrumentations: Results and recent developments. Springer, Berlin Heidelberg New York.
- Martin J. and Armington A. (1983): Effect of growth rate on quartz defects. *J. Cryst. Growth*, **62**: 203.
- Maschmeyer D. and Lehmann G. (1983a): New hole centres in natural quartz. *Phys. Chem. Minerals*, **10**: 84-88.
- Maschmeyer D. and Lehmann G. (1983b): A trapped-hole centre causing rose coloration of natural quartz. *Z. Kristallogr.* **163**: 181-196.
- Marshall D.J. (1988): *Cathodoluminescence of geological materials*. Allen & Unwin Inc., Winchester/Mass., 146 pp.
- Matter A. and Ramseyer K. (1985): Cathodoluminescence microscopy as a tool for provenance studies of sandstones. In: Zuffa G.G. (ed.): *Provenance of arenites*. Dordrecht Reidel, pp. 191-212.
- McKinlay S. (1993): *Geology of the Carcoar Granite, Blayney*. BSc(Hons) thesis, The University of New South Wales, Sydney (unpubl.).

- McLaren A.C., Phakey P.P. (1966): Transmission electron microscope study of bubbles and dislocations in amethyst and citrine quartz. *Aust. J. Phys.*, **19**: 19-24.
- McLaren A.C., Cook R.F., Hyde S.T., Tobin R.C. (1983): The mechanisms of the formation and growth of water bubbles and associated dislocation loops in synthetic quartz. *Phys. Chem. Minerals*, **9**: 79-94.
- Medlin W.L. (1964): Trapping centers in thermoluminescent calcite. *Phys. Rev.* **135**: 1770-1779.
- Merino E., Harvey C., and Murray H.H. (1989): Aqueous-chemical control of the tetrahedral-Aluminium content of quartz, halloysite, and other low-temperature silicates. *Clays and Clay Minerals* **37/2**: 135-142.
- Merlet C. and Bodinier J.-L. (1990): Electron microprobe determination of minor and trace transition elements in silicate minerals: A method and its application to mineral zoning in the peridotite nodule PHN 1611. *Chemical Geol.* **83**: 55-69.
- Michalske A. and Freiman W. (1982): A molecular interpretation of stress corrosion in silica. *Nature* **295**: 511-512.
- Miller J.C. and Miller J.N. (1988): Basic statistical methods for analytical chemistry: Part I: Statistics of repeated measurements. A review. *Analyst*, **113**: 1351-1356.
- Miller J.N. (1991): Basic statistical methods for analytical chemistry: Part 2: Calibration and regression methods. *Analyst*, **116**: 3-14.
- Milliken K.L. (1994): Cathodoluminescent textures and the origin of quartz silt in Oligocene mudrocks South Texas. *J. Sed. Res.*, **64A**: 567-571.
- Müller A. (1995): Untersuchung magmatischer, metamorpher und hydrothermalmer Quarze aus der Oberpfalz mit thermischer Schallemissionsanalyse. *Diploma*, Universität Göttingen, 61 pp.
- Müller A. and Behr H.J. (1997): The lacquer peels method and cathodoluminescence applied to quartz in granites and rhyolites. *IAVCEI Abstracts, Puerto Vallarta, Mexico*, p 101.
- Müller A. and Seltmann R. (1999): The genetic significance of snowball quartz in high fractionated tin granites of the Krušné Hory/Erzgebirge. In: Stanley et al.: *Mineral deposits: processes to processing*. Volume 1, Balkema, Rotterdam, pp. 409-412.
- Müller A., Seltmann R. and Behr H.-J. (2000a): Application of cathodoluminescence to magmatic quartz in a tin granite – case study from the Schellerhau Granite Complex, Eastern Erzgebirge, Germany. *Mineralium Deposita*, **35/2-3**: 169-189.
- Müller A., Trzebski, R. and Lennox P. (2000b): Magma crystallisation, emplacement and deformation of S- and I-type granitoids in the Eastern Lachlan Fold (SE Australia) as constrained by quartz cathodoluminescence and Al-in-hornblende barometry. (in prep.).
- Müller A. and René M. (2000): Cathodoluminescence microcharacterization of magmatic quartz of the topaz-bearing granites from the tin ore deposit Krásno (Slavkovský Les Mts., Czech Republic). *Terra Nova* (in review).
- Nassau K. and Prescott B.E. (1975): A reinterpretation of smoky quartz. *Phys. Stat. Sol. (A)* **29**: 659-663.
- Neuser R. D. (1988): Zementstratigraphie und Kathodolumineszenz des Korallenoolith (Malm) im Südniedersächsischen Bergland. *Bochumer geol. u. geotechn. Arb.* **32**: 172.
- Neuser R. D., Bruhn F., Götze J., Habermann D. and Richter D. K. (1995): Kathodolumineszenz: Methodik und Anwendung. *Zbl. Geol. Paläont. Teil 1*, **1/2**: 287-306.
- Neuser R.D., Richter D.K., Vollbrecht A. (1988): Natural quartz with brown/violet cathodoluminescence - Genetic aspects evident from spectral analysis. *Zbl. Geol. Paläont. Teil 1*, **7/8**: 919-930.
- Nicolas A. and Poirier J.P. (1976): *Crystalline plasticity and solid state flow in metamorphic rocks*. Wiley London, 444 pp.
- Nishikawa H., Shiroyama Y., Nakamura R., Ohki Y., Nagasawa K., Hama Y. (1992): Photoluminescence from defect centers in high-purity silica glasses observed under 7.9-eV excitation. *Phys. Rev. B* **45/2**: 586-591.
- Nuttall R.H.D. and Weil J.A. (1980): Two hydrogenic trapped-hole species in α -quartz. *Solid State Commun.* **33**: 99-102.
- Nuttall R.H.D., Weil J.A. (1981): The magnetic properties of the oxygen-hole aluminium centers in crystalline SiO₂. I. [Al₄O]⁰. *Canad. J. Phys.* **59**: 1696-1708.
- O'Keefe M. and Hyde B.G. (1978): On Si-O-Si configurations in silicates. *Acta Crystallogr.* **B34**: 27-32.
- O'Reilly E.P. and Robertson J. (1983): Theory of defects in vitreous silicon dioxide. *Phys. Rev. B* **27**: 3780-3795.
- Owen M.R. (1984): Southern source of the Jackford sandstone determined by petrography, cathodoluminescence of quartz, and hafnium content of zircons. *Abstracts with Programs 16, Boulder, Co: Geol. Soc. Amer.*, p. 616.
- Owen M.R. (1988): Radiation-damage halos in quartz. *Geology*, **16**: 529-532.
- Owen M.R. (1991): Application of cathodoluminescence to sandstone provenance. In: Barker E., Kopp O.C. (eds.): *Luminescence microscopy and spectroscopy. Quantitative and qualitative applications*. Soc. Sed. Geol., Tulsa Oklahoma, p. 67-75.
- Packham G.H. (1999): Radiometric evidence for Middle Devonian inversion of the Hill End Trough, northeast Lachlan Fold Belt. *Australian Journal of Earth Sciences*, **46**: 23-33.

- Pagel M., Barbin V., Blanc P., Ohnenstetter D. (2000): *Cathodoluminescence in Geosciences*. Springer, Berlin Heidelberg New York, 514 pp.
- Pälchen W. (1968): Zur Geochemie und Petrologie der postorogenen variszischen Magmatite des sächsischen Osterzgebirges. *Thesis*, TU Bergakademie Freiberg, 142 pp.
- Pälchen W., Ossenkopf P. (1967): Über das relative Alter des Schellerhauer Granitmassivs und seiner Varietäten. *Ber deutsch Ges geol Wiss B, Miner. Lagerstättenf.*, **12/4**: 359-371.
- Pankrath R. (1988): Spurenelementeinbau in Tief-Quarz als Funktion der Wachstumsbedingungen und Umprägungen unter trockenen und hydrothermalen Bedingungen. *Thesis*, Ruhr-Universität Bochum, Germany.
- Parks G.A. (1984): Surface and interfacial free energies of quartz *J. Geophys. Res.*, **89/B6**: 3997-4008.
- Passchier C.W. and Trouw R.A.J. (1998): *Microtectonics*. Springer Verlag, Berlin Heidelberg New York.
- Paterson S.R., Tobisch O.T., Morand V.J. (1990): The influence of large ductile shear zones on the emplacement and deformation of the Wyangala Batholith, SE Australia. *J. Struct. Geol.*, **12**: 639-650.
- Paterson S.R., Vernon R.H., Tobisch O.T. (1989): A review of criteria for determining magmatic and solid-state foliations in granitoids. *J. Struct. Geol.*, **11**: 349-363.
- Pearce T.H. (1993): A simple deterministic model of oscillatory zoning in magmatic plagioclase. *Geol. Assoc. Can. – Mineral. Assoc. Can.*, Program Abstr. 18, p. A-81.
- Pearce T.H. and Kolisnik A.M. (1990): Observations of plagioclase zoning using interference imaging. *Earth-Science Reviews*, **29**: 9-26.
- Perny B., Eberhardt P., Ramseyer K., Mullis J., Pankrath R. (1992): Microdistribution of aluminium, lithium and sodium in a quartz: possible causes and correlation with short lived cathodoluminescence. *Amer. Mineral.*, **77**: 534-544.
- Pfenninger H. (1961): Diffusion von Kationen und Abscheidung von Metallen in Quarz unter elektrischer Feldeinwirkung. *Thesis*, Universität Zürich, Switzerland.
- Picouet P.A. (1999): Cathodoluminescence spectroscopy and the orientation of a hydrothermal quartz crystal. *Schweiz. Mineral. Petrol. Mitt.*, **79**: 455-460.
- Pitfield P.E.J., Teoh L.H., Cobbing E.J. (1990): Textural variation and tin mineralization in granites from the Main Range Province of the Southeastern Asian Tin Belt. *Geol. J.*, **25**: 419-429.
- Plesch R. (1982): *Auswerten und Prüfen in der Röntgenspektrometrie*. G-I-T Verlag Ernst Giebel, Darmstadt, 147 pp.
- Plimer I.R. (1987): Fundamental parameters for the formation of granite-related tin deposits. *Geol. Rundschau*, **76/1**: 23-40.
- Plötze M. (1995): Investigation of quartz, scheelite and fluorite from hydrothermal rare-metal deposits by EPR (in German). *Thesis*, TU Bergakademie Freiberg, 141 pp.
- Poirier J.P. and Guillope M. (1979): Deformation-induced recrystallisation of minerals. *Bull. Mineral.*, **102**: 67-74.
- Pott G.T. and McNicol B.D. (1971): Spectroscopy study of the coordination and valence of Fe and Mn ions in and on the surface of aluminas and silicas. *Disc. Faraday Soc.* **52**: 121-131.
- Potts P.J., Bowles J.F.W., Reed S.J.B., and Cave M.R. (1995): Microprobe techniques in the earth sciences. *The Mineralogy Society Series*, vol. 6, Chapman and Hall, London, 419 pp.
- Poty B. (1969): La croissance des cristaux de quartz dans les filons sur l'exemple du filon de la Gardette (Bourg d'Oisans) et des filons du massif du Mont-Blanc. *Thesis*, University of Nancy, France, 162 pp.
- Poutiainen M., Scherbakova T.F. (1998): Fluid and melt inclusion evidence for the origin of idiomorphic quartz crystals in topaz-bearing granite from the Salmi batholith, Karelia, Russia. *Lithos*, **44**: 141-151.
- Powell C.McA. (1984): Ordovician to earliest Silurian: marginal sea and island arc. In: Veevers J.J. (ed.): *Phanerozoic Earth History of Australia*. Oxford University Press, Oxford, 29-309.
- Powell C.McA., Cole J.P., Cudahy T.J. (1985): Megakinking in the Lachlan Fold Belt, Australia. In: Hancock P.L. and Powell C.McA. (eds.): *Multiple Deformation in Ductile and Brittle Rocks*. *J. Struct. Geology*, **7**: 281-300.
- Rakov L.T., Kuvshinova K.A., Moiseev B.M., Pleskova M.A., Kandinov M.N. (1991): Typomorphic properties of Ti centres in quartz (in Russian). *Dokl. Akad. Nauk SSSR*, **317**: 181-185.
- Ramseyer K., Baumann J., Matter A., and Mullis J. (1988): Cathodoluminescence colours of a-quartz. *Miner. Magazine*, **52**: 669-677.
- Ramseyer K. and Mullis J. (1990): Factors influencing short-lived blue cathodoluminescence of a-quartz. *Amer. Miner.*, **75**: 791-800.
- Reed S.J.B. (1996): *Electron microprobe analysis and scanning electron microscopy in geology*. Cambridge University Press, Cambridge, 201 pp.
- Reimer L. (1985): "SEM" – *Physics of image formation of microanalysis*. Springer Verlag, Berlin-Heidelberg-New York-Tokyo.
- Remond G. (1977): Applications of cathodoluminescence in mineralogy. *J. Luminescence*, **15/2**: 121-155.

- Remond G., Le Gressus C., Okuzumi H. (1979): Electron beam effects observed in cathodoluminescence and Auger electron spectroscopy in natural minerals: Evidence for ionic diffusion. *Scanning Electron Microsc.*, **1**: 237-244.
- Remond G., Cesbron F., Chapoulie R., Ohnenstetter D., Rouques-Carmes C. and Schvoerer M. (1992): Cathodoluminescence applied to the microcharacterization of mineral materials: a present status in experimentation and interpretation. *Scanning Microsc.*, **6/1**: 23-69.
- René M. (1998): Development of topaz-bearing granites of the Krudum massif (Karlovy Vary pluton). *Acta Univ. Carolinae, Geol.*, **42/1**: 103-109.
- Renno A. (1997): *Zur Petrogenese der Albitgranite von Abu Dabbab und Nuweibi*. Thesis. Berlin: Techn. Univ., Logos-Verl. D 83.
- Richter D.K. and Zinkernagel U. (1975): Petrographie des „Permoskyth“ der Jaggl-Plawen-Einheit (Südtirol) und Diskussion der Detritusherkunft mit Hilfe von Kathoden-Lumineszenz-Untersuchungen. *Geol. Rdsch.*, **64**: 783-807.
- Rink W.J., Rendell H., Marseglia E.A., Luff B.J., and Townsend P.D. (1993): Thermoluminescence Spectra of igneous quartz and hydrothermal quartz. *Phys. Chem. Minerals*, **20**: 353-361.
- Rinneberg H., Weil J.A. (1972): EPR studies of $Ti^{3+}-H^+$ centers in X-irradiated -quartz. *J. Chem. Phys.*, **56**: 2019-2028.
- Rovetta M.R., Blacic J.D., Hervig R.L. and Holloway J.R. (1989): An experimental study of hydroxyl in quartz using infrared spectroscopy and ion microprobe techniques. *J. Geophys. Res.*, **94**: 5840-5850.
- Rub M.G., Stempok M., Rub M.G. (1997): On the tantalum mineralization in the rare metal granites of the Cinovec massif (Czechia). *Dokl. Akad. Nauk.*, **352**: 795-798 (in Russian).
- Rumyantsev V. and Novozhilov A. (1980): Dependence on concentration of aluminium centres and anomalous pleochroism on certain crystallisation parameters in synthetic quartz. *Sov. Phys. Crystallography*, **25**: 75.
- Ruppert L.F. (1987): Applications of cathodoluminescence of quartz and feldspar to sedimentary petrology. *Scanning Microscopy*, **1**: 63.
- Scala C.M. and Hutton D.R. (1976): Site assignment of Fe^{3+} in α -quartz. *Physica Status Solidi*, **B73**: K115-K117.
- Scheibner E. (1998): In: Basden H. (ed.): *Geology of New South Wales – Synthesis*. Volume 2. - Geological Survey of New South Wales, Memoirs in Geology 13.
- Schilka W., Baumann L. (1996): Metasomatische Prozesse im Schellerhauer Granitmassiv (Osterzgebirge). *Freib. Forsch.-H.*, **C467**: 151-175.
- Schmidt W. (1992): Amphibole composition in tonalite as a function of pressure: an experimental calibration of the Al-in-hornblende barometer. *Contrib. Mineral. Petrol.*, **110**: 304-310.
- Schmidt-Mumm A. (1991): Low frequency acoustic emission from quartz upon heating from 90-610°C. *Phys. Chem. Minerals*, **17**: 545-553.
- Schmidt-Mumm A. and Behr H.-J. (1987): Fluid systems in metaplaya sequences in the Damara Orogen (Namibia): Evidence for sulphur-rich brines – general evolution and first results. *Chem. Geol.*, **61**: 135-145.
- Schneider N. (1993): Das lumineszenzaktive Strukturinventar von Quarzphänokristen in Rhyolithen. *Göttinger Arb. Geol. Paläont.*, **60**: 81 pp.
- Schrön W., Schmädicke E., Thomas R., Schmidt W. (1988): Geochemische Untersuchungen an Pegmatitquarzen. *Z. geol. Wiss.*, **16**: 229-244.
- Schust F. (1980): Zum Zusammenhang zwischen der paläogeographischen Entwicklung und der Intrusionstiefe der Granite im Osterzgebirge. *Z. angew. Geol.* **26/8**: 405-411.
- Schust F., Thomas U., Schwandke E. (1991): Erkenntnisfortschritte zur Geologie des Harzes. *Z. geol. Wiss.* **19/6**: 625-635.
- Schwartz M.O. (1992): Geochemical criteria for distinguishing magmatic and metasomatic albite-enrichment in granitoids – examples from the Ta-Li granite Yichun (China) and the Sn-W deposit Tikus (Indonesia). *Mineralium Deposita*, **27**: 101-108.
- Seim R., Eidam J., Korich D. (1982): Zur Elementverteilung in einem Zinngranit (Schellerhauer Massiv/Osterzgebirge). *Chem Erde*, **41**: 219-235.
- Seltmann R. (1994): Sub-volcanic minor intrusions in the Altenberg caldera and their metallogeny. In: Seltmann R., Möller P., Kämpf H. (eds.): *Metallogeny of Collisional Orogens*. Czech Geological Survey Prague, pp 198-206.
- Seltmann R., Bankwitz P., Frischbutter A., Thomas R. (1992): Metallogenic position of breccia-related granite bodies and tin ore deposits at the north-western border of the Bohemian Massif (Krusne Hory - Krasny Les area). In: Kukul Z. (ed.): *Proceed 1st Internat Conf Bohemian Massif in Prague 1988*. Czech Geol Survey Prague: pp 257-268.
- Seltmann R., Stempok M. (1994): Textural evidence for the existence of two-phase granites in the younger intrusive complex granites of the Krusne Hory/Erzgebirge Province. *J. of the Czech Geol. Soc.*, **39/1**: 103-104.
- Seltmann R., Stempok M., Müller A. (2000): Textures of rare-metal granites as exploration tool. Extended Abstract. *Proceed. 31st IGC*, Rio de Janeiro (in print).

- Serebrennikov A.I., Valter A.A., Mashkovtsev R.I., Shcherbakova M.Ya. (1982): The investigation of defects in shock-metamorphosed quartz. *Phys. Chem. Minerals*, **8**: 153-157.
- Shore M., Fowler A.D. (1996): Oscillatory zoning in minerals: a common phenomenon. *Canadian Mineral.* **34**: 1111-1126.
- Sibley D.F., Vogel T.A., Walker B.M., Byerly G. (1976): The origin of oscillatory zoning in plagioclase: A diffusion and growth controlled model. *Amer. J. Sci.* **276**: 275-284.
- Siebel W., Trzebski R., Stettner G., Hecht L., Casten U., Höhdorf A., Müller P. (1997): Granitoid magmatism of the NW Bohemian massif revealed: gravity data, composition, age relations and phase concept. *Geol. Rdsch., Suppl.*, **86**:45-63.
- Siebers F.B., Giese U., Flörke O.W. (1984): Growth of doped quartz and the anisotropy of impurity distribution. *Zeitschrift für Kristallographie*, **167**: 189-190.
- Siebers F.B. and Klapper H. (1984): Zelluläres Wachstum und Verunreinigungsverteilung im Zuchtquarz, aufgezeigt mit Röntgentopographie. *Zeitschrift für Kristallographie*, **167**: 177-178.
- Siebers F.B. (1986): Inhomogene Verteilung von Verunreinigungen in gezüchteten und natürlichen Quarzen als Funktion der Wachstumsbedingungen und ihr Einfluß auf kristallphysikalische Eigenschaften. *Thesis*, Ruhr-Universität Bochum, Germany, 133 pp.
- Siegel G.H. and Marrone M.J. (1981): Photoluminescence in as-drawn and irradiated silica optical fibers: An assessment of the role of nonbridging oxygen defect centres. *J. Non-Cryst. Solids* **45**: 235-247.
- Simakin A.G. (1984): A simple quantitative model of rhythmic zoning in crystals. *Geochem. Int.*, **21**: 13-26.
- Simpson C. (1985): Deformation of granitic rocks across the brittle-ductile transition. *J. Struct. Geol.*, **7**: 503-511.
- Singer B.S., Dunger M.A., Layne G.D. (1995): Textures and Sr, Ba, Mg, Fe, K, and Ti compositional profiles in volcanic plagioclase: Clues to the dynamics of calc-alkaline magma chambers. *American Mineralogist*, **80**: 776-798.
- Sippel R.F. (1965): Simple device for luminescence petrography. *Rev. Sci. Instrum.*, **36**: 1556-1558.
- Sippel R.F. (1968): Sandstone petrology. Evidence from luminescence petrography. *J. Sed. Petrol.*, **38**: 530-554.
- Skuja L. and Trukhin A. (1989): Comment on the "Luminescence of fused silica: Observation of the O₂-emission band". *Phys. Rev. B*, **39**: 3909.
- Smith J.V. and Stenstrom R.C. (1965): Electron-excited luminescence as a petrologic tool. *J. Geol.*, **73**: 627-635.
- Smith R.E. (1969): Zones of progressive regional burial metamorphism in part of the Tasman Geosyncline, Eastern Australia. *J. Petrol.*, **10**: 144-163.
- Sonyushkin V.E., Sukhorukov Y.T., Scherbakova T.F. (1991): P-T environment of crystallization of quartz in granites of the Salmi batholith, Russian Karelia. In: Haapala I. and Rämö O.T. (eds.): *Symposium on Rapakivi Granites and Related Rocks*, p. 47. Geol. Surv. Finland Guide, vol. 34.
- Spengler E. (1949): *Über die Abtragung des variszischen Gebirges in Sachsen*. Abh. Geol. Landesanst., Berlin, 212 p.
- Sprunt E. (1979): Microcracking and healing in granites: New evidence from cathodoluminescence. *Science*, **205**: 495-497.
- Sprunt E. (1981): Causes of quartz cathodoluminescence colors. *Scan. Electron Micr.*, **1981**: 525-535.
- Spry A. (1969): *Metamorphic textures*. Pergamon Press, Oxford, 352 pp.
- Stemprok M. (1986): Petrology and geochemistry of the Czechoslovak part of the Krusne hory Mts. granite pluton. *Sbor. geol. ved. LGM*, **27**: 111-156.
- Stemprok M. (1993): Magmatic evolution of the Krusne Hory–Erzgebirge batholith. *Z. geol. Wiss.*, **21/1-2**: 237-245.
- Stemprok M., Novak J.K., David J. (1994): The association between granites and tin-tungsten mineralization in the eastern Krusne hory (Erzgebirge), Czech Republic. In: von Gehlen K., Klemm D.D. (eds.): *Monograph Series on Mineral Deposits 31*. Gebr. Boertraeger, Berlin Stuttgart, pp. 97-129.
- Stemprok M., Sulcek Z. (1969): Geochemical profile through an ore-bearing lithium granite. *Econ. Geol.*, **64**: 392-404.
- Stenina N.G., Bazarov L.S., Shcherbakova M.Y., Mashkovtsev R.I. (1984): Structural state and diffusion of impurities in natural quartz of different genesis. *Phys. Chem. Minerals*, **10**: 180-186.
- Stenina N.G., Sotnikov V.I., Korolyuk V.N., Kovaleva L.T. (1988): Microstructural features of hydrothermal vein quartz as an indicator of mineralization. *Geokhimiya*, **5**: 641-653, (English translation).
- Stenina N.G. (1995): Energy aspect in the formation of granitic magma and ore deposits. In: Pašava J., Kribek B. and Zák K. (eds): *Mineral deposits: from their origin to their environmental impacts*. Balkema, Rotterdam, pp. 539-542.
- Sterner S.M. and Bodnar R.J. (1989): Synthetic fluid inclusions – VII. Re-equilibration of fluid inclusions in quartz during laboratory-simulated metamorphic burial and uplift. *J. Metamorphic Geol.*, **7**: 243-260.
- Stoecklein W. and Gobel R. (1992): Application of cathodoluminescence in paint analysis. *Scanning Microscopy*, **6**: 669-678.
- Stünitz H. (1998): Syndeformational recrystallisation – dynamic or compositionally induced? *Contrib. Mineral. Petrol.*, **131**: 219-236.

- Suttner L.J. and Leininger R.K. (1972): Comparison of the trace element content of plutonic, volcanic, and metamorphic quartz from southwestern Montana. *Geol. Soc. Am. Bull.*, **83**: 1855-1862.
- Swanson S.E. (1977): Relation of nucleation and crystal-growth rate to the development of granitic textures. *Amer. Mineral.*, **62**: 966-978.
- Swanson S.E. and Fenn P.M. (1986): Quartz crystallization in igneous rocks. *Amer. Mineral.*, **71**: 331-342.
- Thomas R. (1992): Results of investigations on melt inclusions in various magmatic rocks from the northern border of the Bohemian Massif. In: Kukul Z. (ed.) *Proceed 1st Internat Conf Bohemian Massif in Prague 1988*, Czech Geol Surv Prague, pp 298-306.
- Thomas R. (1994a): Fluid evolution to the emplacement of the Variscan granites in the Erzgebirge region: a review of the melt and fluid inclusion evidence. In: Seltmann R, Möller P, Kämpf H (eds.): *Metallogeny of Collisional Orogens*. Czech Geological Survey Prague, pp 70-82.
- Thomas R (1994b) Estimation of water content of granitic melts from inclusion data. In: Seltmann R, Möller P, Kämpf H (eds.): *Metallogeny of Collisional Orogens*. Czech Geological Survey Prague, pp 224-229.
- Thomas W.M. and Ernst W.G. (1990): The aluminium content of hornblende in calc-alkaline granitic rocks: A mineralogic barometer calibrated experimentally to 12 kbars. - In: Spencer R.J. and I-Ming Chou (eds.): *Fluid-mineral interactions: A tribute to H.P. Eugster*. The Geochemical Society, Special Publication 2, 59-63.
- Tischendorf G (1964) Stand der Kenntnisse bei der Suche nach Zinnlagerstätten im Osterzgebirge. *Zeitschrift für Angewandte Geologie* **10/5**: 225-238
- Tischendorf G., Förster H.J. (1990): Acid magmatism and related metallogenesis in the Erzgebirge. *Geol. J.*, **25**: 443-454.
- Tobisch O.T. and Paterson S.R. (1990): The Yarra granite: An intradeformational pluton associated with ductile thrusting, Lachlan Fold Belt, southeastern Australia. *Geol. Soc. Am. Bull.*, **102**: 693-703.
- Toramaru A. (1991): Model of nucleation and growth of crystals in cooling magmas. *Contrib. Mineral. Petrol.*, **108**: 106-117.
- Tovey N.K. and Krinsley D.H. (1980): A cathodoluminescent study of quartz sand grains. *J. Microscopy*, **120**: 279-289.
- Townsend P.D. and Rowlands A.P. (2000): Information encoded in cathodoluminescence emission spectra. In: Pagel M., Barbin V., Blanc P., Ohnenstetter D. (eds.): *Cathodoluminescence in Geosciences*. Springer, Berlin Heidelberg New York, pp. 41-57.
- Trukhin A.N. and Plaudis A.E. (1979): Investigation of intrinsic luminescence of SiO₂. *Sov. Phys. Solid State*, **21/4**: 644-646.
- Trzebski R., Lennox P., Palmer D. (1999): Contrasts in morphogenesis and tectonic setting during contemporaneous emplacement of S- and I-type granitoids in the Eastern Lachlan Fold Belt, southeastern Australia. In: Castro A., Fernandez C., Vigneresse J.L. (eds.): *Understanding Granites: Integrating New and Classical Techniques*. Geol. Soc., London, Sp. Publ., **158**: 123-140.
- Tsinober L. and Kamentsev I. (1964): Effect of growth rate on the concentration of centers of smoky color and on the unit cell parameters of synthetic quartz crystals. *Sov. Phys. Crystallography*, **9**: 374.
- Urai J.L. (1983): Water assisted dynamic recrystallization and weakening in polycrystalline bischofite. *Tectonophysics*, **96**: 125-127.
- Urai J.L. and Humphreys F.J. (1981): The development of shear zones in polycrystalline camphor. *Tectonophysics*, **78**: 677-685.
- Valley J.W. and Graham C.M. (1996): Ion microprobe analysis of oxygen isotope ratios in quartz from Skye granite: healed micro-cracks, fluid flow, and hydrothermal exchange. *Contrib. Mineral. Petrol.*, **124**: 225-234.
- Vernon R.H. and Flood R.H. (1988): Contrasting deformation of S- and I-type granitoids in the Lachlan Fold Belt, eastern Australia. *Tectonophysics*, **147**: 127-144.
- Voll G. (1976): Recrystallization of quartz, biotite and feldspars from Erstfeld to the Leventina Nappe, Swiss Alps, and its geological significance. *Schweiz. mineral. Petrogr. Mitt.*, **56**: 641-47.
- Voll G. (1980): Ein Querprofil durch die Schweizer Alpen vom Vierwaldstätter See zur Wurzelzone – Strukturen und ihre Entwicklung durch Deformationsmechanismen wichtiger Minerale. *N. Jb. Geol. Pal. Abh.*, **160**: 321-335.
- Walker G. (1985): Mineralogical applications of luminescence technique. In: Berry F.J., Vaughan D.J. (eds.): *Chemical bonding and spectroscopy in mineral chemistry*. Chapman and Hall, London, 103-140.
- Watt G.R., Wright P., Galloway S., McLean C. (1997): Cathodoluminescence and trace element zoning in quartz phenocrysts and xenocrysts. *Geochim Cosmochim Acta*, **61**: 4337-4348.
- Waychunas G.A. (1988): Luminescence, X-ray emission and new spectroscopies. In: Hawthorne F.C. (ed.) *Spectroscopic methods in mineralogy and geology*. *Rev. Miner.* **18**: 639-698.
- Weeks R.A. (1994): The many varieties of E' centres: a review. *J. Non-Cryst. Solids*, **179**: 1-9.
- Weil J.A. (1984): A review of electron spin spectroscopy and its application to the study of paramagnetic defects in crystalline quartz. *Phys. Chem. Minerals*, **10**: 149-165.

- Wiebe R.A. (1968): Plagioclase stratigraphy: A record of magmatic conditions and events in a granite stock. *Am. J. Sci.*, **266**: 690-703.
- Wilkins C. and Smart G. (1997): Browns Creek gold-copper deposit. In: Berkmann D.A. and Mackenzie D.H. (eds.): *Geology of Australian and Papua New Guinean Mineral Deposits*. The Australian Institute of Mining and Metallurgy, Melbourne, 575-580.
- Williamson B.J., Stanley C.J., Wilkinson J.J. (1997): Implications from inclusions in topaz for greisenisation and mineralisation in the Hensbarrow topaz granite, Cornwall, England. *Contrib. Mineral. Petrol.*, **127**: 119-128.
- Winslow D.M., Bodnar R.J., and Tracy R.J. (1994): Fluid inclusion evidence for an anticlockwise metamorphic P-T path in central Massachusetts. *J. Metamorphic Geology*, **12**: 361-371.
- Wyborn D. and Henderson G.A.M. (1996): Notes to accompany geological map Blayney 1 : 100000 sheet area. *Australian Geol. Surv. Organisation Report*, **56**.
- Yang X.H. and McKeever S.W.S. (1990): The pre-dose effect in crystalline quartz. *J. Phys. D: Appl. Physics*, **23**: 237-244.
- Yang X.H., Townsend P.D., Holgate S.A. (1994): Cathodoluminescence and depth profiles of tin in float glass. *J. Phys. D*, **27**: 1757.
- Yin L., Pollard P.J., Hu Shouxi, Taylor R.G. (1995): Geologic and geochemical characteristics of the Yichun Ta-Nb-Li deposit, Jiangxi Province, South China. *Economic Geology*, **90/3**: 577-585.
- Yoder H.S. (1950): High-low quartz inversion up to 10,000 bars. *Transactions Amer Geophys Union*, **31**: 827.
- Ziebold T.O. (1967): Precision and sensitivity in electron microprobe analysis. *Anal. Chem.*, **39**: 858-861.
- Zinkernagel U. (1978): Cathodoluminescence of quartz and its application to sandstone petrology. *Contrib. Sedimentology*, **8**: 1-69.

Appendix A

List of CL emission band parameters of quartz

Sample	1.73 eV - Band					1.84 eV - Band				
	Position (eV)	Sigma (eV)	Half-width (eV)	If	If (%)	Position (eV)	Sigma (eV)	Half-width (eV)	If	If (%)
1 Megaquartz	1.74	0.13	0.3	5000	4.3	1.84	0.095	0.22	3500	3.0
	1.74	0.13	0.3	8600	13.0	1.84	0.095	0.22	5000	7.6
	1.73	0.13	0.3	10500	17.5	1.84	0.095	0.22	8000	13.4
2 Fissile Quartz	1.74	0.14	0.32	5500	9.0	1.84	0.095	0.22	3000	4.9
	1.74	0.14	0.32	7700	12.3	1.84	0.095	0.22	3700	5.9
	1.74	0.13	0.3	11500	16.5	1.84	0.095	0.22	5000	7.2
3 Oil-bearing Quartz	1.735	0.13	0.31	6500	7.5	1.84	0.095	0.22	3500	4.1
	1.735	0.13	0.31	13000	15.7	1.84	0.095	0.22	6000	7.3
	1.735	0.13	0.31	17000	22.7	1.84	0.095	0.22	8000	10.7
4 Schoenfeld Rhyolite	1.73	0.13	0.3	5000	4.6	1.845	0.095	0.23	8000	7.3
	1.73	0.13	0.3	7500	7.4	1.845	0.095	0.23	9000	8.8
	1.73	0.13	0.3	11000	10.8	1.845	0.095	0.23	9600	9.5
5 Teplice Rhyolite blue CL/ phenocryst	1.73	0.13	0.3	3714	7.2	1.84	0.095	0.22	1864	3.6
	1.73	0.13	0.3	5200	10.6	1.84	0.095	0.22	2200	4.5
	1.73	0.13	0.3	7000	13.5	1.84	0.095	0.22	3000	5.8
5 Teplice Rhyolite red CL/ phenocryst	1.73	0.125	0.3	39600	36.1	1.835	0.095	0.23	8500	7.7
	1.735	0.125	0.29	38000	34.9	1.835	0.095	0.23	9600	8.8
	1.73	0.13	0.3	36000	31.1	1.835	0.095	0.23	14000	12.1
6 Schellerhau Granite blue CL/ phenocryst	1.735	0.125	0.29	9000	7.0	1.837	0.095	0.23	5000	3.9
	1.735	0.125	0.29	12000	10.1	1.837	0.095	0.23	6000	5.0
	1.735	0.13	0.31	15500	14.3	1.84	0.095	0.22	7700	7.1
6 Schellerhau Granite red CL/ phenocryst	1.734	0.125	0.28	12000	14.3	1.84	0.095	0.22	5300	6.3
	1.734	0.125	0.28	17000	19.1	1.84	0.095	0.22	7000	7.9
	1.735	0.13	0.31	20000	22.2	1.84	0.095	0.22	8800	9.8
6 Schellerhau Granite red CL/ matrix quartz	1.735	0.13	0.31	5500	7.9	1.836	0.095	0.23	6400	9.2
	1.735	0.13	0.31	10300	13.4	1.836	0.095	0.23	7500	9.7
	1.735	0.13	0.31	13500	17.2	1.84	0.095	0.22	8000	10.2
7 Eibenstock Granite	1.725	0.135	0.31	4500	17.2	1.85	0.095	0.22	1350	5.2
	1.73	0.14	0.32	6000	21.0	1.835	0.09	0.21	1600	5.6
	1.725	0.135	0.31	7000	22.8	1.85	0.095	0.22	2500	8.1
8 Aue Granite	1.73	0.12	0.28	8620	5.9	1.85	0.095	0.22	3080	2.1
	1.73	0.12	0.28	12500	9.1	1.85	0.095	0.22	4000	2.9
	1.73	0.13	0.31	13000	10.9	1.85	0.095	0.22	5000	4.2
9 Vein Quartz	1.7	0.15	0.36	2200	2.8	1.84	0.095	0.22	1	0.0
	1.71	0.15	0.36	2400	5.8	1.84	0.095	0.22	1	0.0
	1.7	0.15	0.36	2420	13.9	1.84	0.095	0.22	1	0.0
10 Wachtelberg Rhyolite blue CL	1.73	0.13	0.3	4190	6.1	1.84	0.095	0.22	4325	6.3
	1.73	0.13	0.3	4630	7.4	1.84	0.095	0.22	4780	7.7
	1.73	0.13	0.3	4960	8.3	1.84	0.095	0.22	5120	8.5
10 Wachtelberg Rhyolite red CL	1.723	0.125	0.29	5000	9.4	1.84	0.095	0.22	5500	10.3
	1.723	0.125	0.29	6000	12.0	1.84	0.095	0.22	5500	11.0
	1.73	0.13	0.3	6200	12.7	1.84	0.095	0.22	6400	13.1
11 Beucha Rhyolite blue CL	1.73	0.13	0.3	6384	7.6	1.85	0.095	0.22	4910	5.8
	1.73	0.13	0.3	8300	10.8	1.85	0.095	0.22	5400	7.0
	1.73	0.13	0.3	10000	13.2	1.85	0.095	0.22	5300	7.0
11 Beucha Rhyolite red CL	1.73	0.13	0.3	6375	10.6	1.84	0.095	0.22	3312	5.5
	1.73	0.13	0.3	8287	13.9	1.84	0.095	0.22	3810	6.4
	1.73	0.13	0.3	10200	15.9	1.84	0.095	0.22	5300	8.3

List of CL emission band parameters of quartz (continued)

Sample	1.73 eV - Band					1.84 eV - Band				
	Position (eV)	Sigma (eV)	Half-width (eV)	If	If (%)	Position (eV)	Sigma (eV)	Half-width (eV)	If	If (%)
12 Flossenbuerg Granite	1.73	0.135	0.31	12000	8.0	1.84	0.095	0.22	3500	2.3
	1.73	0.135	0.31	8500	6.1	1.832	0.095	0.22	7000	5.0
	1.735	0.13	0.3	15000	10.4	1.84	0.095	0.22	10000	7.0
13 Leucosome Quartz	1.74	0.13	0.3	5000	6.7	1.84	0.095	0.22	4000	5.4
	1.74	0.13	0.3	7000	8.3	1.84	0.095	0.22	5700	6.8
	1.74	0.13	0.3	11500	11.4	1.84	0.095	0.22	8800	8.7
14 Ramberg Granite	1.735	0.13	0.31	7000	6.6	1.84	0.09	0.22	5500	5.2
	1.735	0.13	0.31	11000	11.3	1.84	0.09	0.22	7500	7.7
	1.735	0.13	0.31	15000	10.4	1.84	0.095	0.22	10000	7.0
15 Weinheim Rhyolite blue CL	1.735	0.125	0.29	9800	5.1	1.845	0.095	0.22	13000	6.8
	1.735	0.125	0.29	12000	6.6	1.845	0.095	0.22	15000	8.3
	1.73	0.13	0.31	14300	8.5	1.845	0.095	0.22	15000	8.9
15 Weinheim Rhyolite red CL	1.73	0.13	0.31	12575	14.9	1.84	0.095	0.22	9494	11.3
	1.73	0.13	0.31	19400	18.4	1.84	0.095	0.22	14160	13.4
	1.73	0.13	0.31	21000	20.1	1.84	0.095	0.22	15000	14.4

Sample	1.96 eV - Band					2.15 eV - Band				
	Position (eV)	Sigma (eV)	Half-width (eV)	If	If (%)	Position (eV)	Sigma (eV)	Half-width (eV)	If	If (%)
1 Megaquartz	1.96	0.1	0.24	4100	3.5	2.16	0.16	0.38	30000	25.6
	1.96	0.1	0.24	9000	13.6	2.16	0.16	0.38	19500	29.5
	1.96	0.1	0.24	9800	16.4	2.15	0.16	0.38	20300	33.9
2 Fissile Quartz	1.955	0.1	0.23	5000	8.2	2.155	0.16	0.37	12600	20.6
	1.955	0.1	0.23	7000	11.1	2.15	0.16	0.38	14000	22.3
	1.955	0.1	0.23	11000	15.8	2.145	0.16	0.37	16000	22.9
3 Oil-bearing Quartz	1.96	0.1	0.24	5300	6.1	2.155	0.175	0.41	22000	25.5
	1.956	0.1	0.24	12400	15.0	2.15	0.155	0.36	21000	25.4
	1.96	0.1	0.24	14500	19.4	2.14	0.16	0.38	20300	27.1
4 Schoenfeld Rhyolite	1.972	0.087	0.2	13700	12.5	2.15	0.16	0.38	17000	15.5
	1.972	0.095	0.22	16000	15.7	2.15	0.16	0.38	17000	16.7
	1.967	0.1	0.24	19000	18.7	2.15	0.16	0.38	19000	18.7
5 Teplice Rhyolite blue CL/ phenocryst	1.956	0.09	0.22	3076	5.9	2.15	0.16	0.38	6863	13.2
	1.956	0.09	0.22	4000	8.2	2.15	0.16	0.38	7000	14.3
	1.956	0.1	0.24	7000	13.5	2.16	0.16	0.38	8300	16.0
5 Teplice Rhyolite red CL/ phenocryst	1.976	0.085	0.21	18000	16.4	2.14	0.16	0.38	20000	18.2
	1.97	0.085	0.2	20800	19.1	2.14	0.16	0.38	19800	18.2
	1.972	0.1	0.24	25500	22.0	2.13	0.16	0.38	25000	21.6
6 Schellerhau Granite blue CL/ phenocryst	1.957	0.093	0.22	8500	6.6	2.155	0.16	0.37	21000	16.3
	1.957	0.1	0.24	13000	10.9	2.15	0.16	0.38	22000	18.5
	1.957	0.105	0.26	17300	16.0	2.15	0.16	0.38	23300	21.5
6 Schellerhau Granite red CL/ phenocryst	1.955	0.095	0.23	9400	11.2	2.15	0.16	0.38	19500	23.3
	1.954	0.105	0.24	17500	19.7	2.145	0.155	0.37	22000	24.7
	1.957	0.11	0.26	20500	22.7	2.14	0.16	0.38	23800	26.4
6 Schellerhau Granite red CL/ matrix quartz	1.968	0.095	0.22	8500	12.2	2.143	0.16	0.37	13800	19.8
	1.96	0.105	0.24	15300	19.9	2.143	0.16	0.37	17400	22.6
	1.962	0.11	0.26	18300	23.3	2.14	0.16	0.38	19000	24.2
7 Eibenstock Granite	1.942	0.09	0.2	1500	5.7	2.136	0.17	0.4	8200	31.4
	1.942	0.09	0.2	2400	8.4	2.136	0.17	0.4	9300	32.6
	1.942	0.09	0.2	2700	8.8	2.122	0.17	0.4	10500	34.1
8 Aue Granite	1.935	0.09	0.21	5140	3.5	2.19	0.152	0.36	53000	36.2
	1.935	0.09	0.21	7200	5.2	2.19	0.152	0.36	48000	35.0
	1.935	0.09	0.21	7700	6.4	2.185	0.155	0.36	46500	38.8

List of CL emission band parameters of quartz (continued)

Sample	1.96 eV - Band					2.15 eV - Band				
	Position (eV)	Sigma (eV)	Half-width (eV)	If	If (%)	Position (eV)	Sigma (eV)	Half-width (eV)	If	If (%)
9 Vein Quartz	1.95	0.11	0.26	600	0.8	2.17	0.175	0.44	7000	9.0
	1.95	0.11	0.26	600	1.4	2.17	0.175	0.44	5000	12.1
	1.95	0.11	0.26	600	3.4	2.167	0.18	0.41	3150	18.1
10 Wachtelberg Rhyolite blue CL	1.962	0.095	0.22	9200	13.4	2.173	0.16	0.38	10500	15.3
	1.962	0.095	0.22	10800	17.4	2.173	0.16	0.38	9500	15.3
	1.962	0.1	0.24	12144	20.2	2.17	0.16	0.38	9000	15.0
10 Wachtelberg Rhyolite red CL	1.967	0.089	0.22	13200	24.7	2.163	0.16	0.37	6350	11.9
	1.963	0.089	0.22	14200	28.5	2.163	0.155	0.36	5900	11.8
	1.962	0.1	0.23	15180	31.1	2.16	0.16	0.38	5700	11.7
11 Beucha Rhyolite blue CL	1.95	0.1	0.24	10760	12.8	2.165	0.16	0.38	14020	16.7
	1.95	0.1	0.24	11300	14.7	2.165	0.16	0.38	13600	17.7
	1.95	0.1	0.24	14100	18.6	2.16	0.16	0.38	14000	18.5
11 Beucha Rhyolite red CL	1.956	0.1	0.24	8542	14.2	2.16	0.16	0.38	7777	12.9
	1.956	0.1	0.24	10250	17.2	2.16	0.16	0.38	8555	14.3
	1.956	0.1	0.24	14950	23.4	2.16	0.16	0.38	10500	16.4
12 Flossenbuerg Granite	1.95	0.09	0.22	8000	5.3	2.155	0.16	0.37	29700	19.8
	1.95	0.09	0.22	9000	6.5	2.145	0.16	0.37	28700	20.7
	1.956	0.1	0.24	15000	10.4	2.14	0.16	0.38	33000	23.0
13 Leucosome Quartz	1.96	0.1	0.24	7000	9.4	2.155	0.16	0.37	13200	17.8
	1.96	0.1	0.24	10700	12.7	2.155	0.16	0.37	15300	18.1
	1.96	0.1	0.24	15500	15.3	2.14	0.16	0.38	20600	20.4
14 Ramberg Granite	1.958	0.085	0.2	12600	12.0	2.16	0.16	0.38	17400	16.5
	1.962	0.09	0.22	16000	16.4	2.15	0.16	0.38	18500	18.9
	1.956	0.1	0.24	15000	10.4	2.14	0.16	0.38	33000	23.0
15 Weinheim Rhyolite blue CL	1.96	0.085	0.2	25500	13.3	2.16	0.16	0.38	19000	9.9
	1.96	0.085	0.2	27000	14.9	2.16	0.16	0.38	19000	10.5
	1.955	0.09	0.22	28000	16.6	2.16	0.16	0.38	19000	11.2
15 Weinheim Rhyolite red CL	1.958	0.1	0.24	24333	28.8	2.165	0.16	0.38	9383	11.1
	1.958	0.1	0.24	40200	38.2	2.165	0.16	0.38	12000	11.4
	1.958	0.1	0.24	43800	42.0	2.165	0.16	0.38	12200	11.7

Sample	2.47 eV - Band					2.58 eV - Band				
	Position (eV)	Sigma (eV)	Half-width (eV)	If	If (%)	Position (eV)	Sigma (eV)	Half-width (eV)	If	If (%)
1 Megaquartz	2.44	0.15	0.36	48300	41.2	2.58	0.08	0.18	3400	2.9
	2.445	0.14	0.32	16400	24.8	2.58	0.08	0.18	2300	3.5
	2.465	0.125	0.29	11000	18.4	2.58	0.08	0.18	750	1.3
2 Fissile Quartz	2.46	0.137	0.32	14600	23.9	2.58	0.08	0.18	2500	4.1
	2.46	0.13	0.3	12300	19.6	2.58	0.08	0.18	2500	4.0
	2.465	0.125	0.29	11000	15.8	2.58	0.08	0.18	2100	3.0
3 Oil-bearing Quartz	2.455	0.15	0.35	25000	29.0	2.58	0.08	0.18	2900	3.4
	2.455	0.13	0.31	15100	18.3	2.58	0.08	0.18	2400	2.9
	2.465	0.125	0.29	9400	12.6	2.58	0.08	0.18	1200	1.6
4 Schoenfeld Rhyolite	2.46	0.122	0.28	18800	17.1	2.58	0.08	0.18	5000	4.6
	2.46	0.122	0.28	15000	14.7	2.58	0.08	0.18	4700	4.6
	2.47	0.12	0.28	13800	13.6	2.58	0.08	0.18	3100	3.1
5 Teplice Rhyolite blue CL/ phenocryst	2.465	0.13	0.31	10715	20.6	2.58	0.08	0.18	1790	3.4
	2.465	0.13	0.31	9000	18.4	2.58	0.08	0.18	1700	3.5
	2.47	0.125	0.3	7900	15.2	2.58	0.08	0.18	1500	2.9
5 Teplice Rhyolite red CL/ phenocryst	2.465	0.125	0.29	11000	10.0	2.58	0.08	0.18	1900	1.7
	2.465	0.125	0.29	10000	9.2	2.58	0.08	0.18	1900	1.7
	2.47	0.125	0.3	9500	8.2	2.58	0.08	0.18	1600	1.4

List of CL emission band parameters of quartz (continued)

Sample	2.47 eV - Band					2.58 eV Band				
	Position (eV)	Sigma (eV)	Half-width (eV)	If	If (%)	Position (eV)	Sigma (eV)	Half-width (eV)	If	If (%)
6 Schellerhau Granite blue CL/ phenocryst	2.463	0.135	0.32	25000	19.4	2.58	0.08	0.18	4500	3.5
	2.463	0.135	0.32	20000	16.8	2.58	0.08	0.18	3800	3.2
	2.47	0.125	0.3	14000	12.9	2.58	0.08	0.18	3000	2.8
6 Schellerhau Granite red CL/ phenocryst	2.462	0.13	0.3	14300	17.1	2.58	0.08	0.18	2500	3.0
	2.462	0.13	0.3	11000	12.4	2.58	0.08	0.18	2200	2.5
	2.47	0.125	0.3	8700	9.6	2.58	0.08	0.18	1500	1.7
6 Schellerhau Granite red CL/ matrix quartz	2.465	0.13	0.31	11300	16.2	2.58	0.08	0.18	2700	3.9
	2.465	0.13	0.31	9300	12.1	2.58	0.08	0.18	2050	2.7
	2.47	0.125	0.3	7700	9.8	2.58	0.08	0.18	1500	1.9
7 Eibenstock Granite	2.48	0.11	0.26	2700	10.3	2.58	0.08	0.18	850	3.3
	2.48	0.11	0.26	2400	8.4	2.58	0.08	0.18	820	2.9
	2.48	0.11	0.26	2600	8.5	2.58	0.08	0.18	600	2.0
8 Aue Granite	2.48	0.11	0.26	18000	12.3	2.58	0.08	0.18	6525	4.5
	2.48	0.11	0.26	15300	11.2	2.58	0.08	0.18	6200	4.5
	2.48	0.11	0.26	10500	8.8	2.58	0.08	0.18	5500	4.6
9 Vein Quartz	2.47	0.145	0.34	17000	21.9	2.58	0.08	0.18	4000	5.1
	2.47	0.145	0.34	8500	20.5	2.58	0.08	0.18	2000	4.8
	2.47	0.125	0.3	2700	15.5	2.58	0.08	0.18	700	4.0
10 Wachtelberg Rhyolite blue CL	2.465	0.13	0.31	11770	17.1	2.58	0.08	0.18	2500	3.6
	2.465	0.13	0.31	9800	15.8	2.58	0.08	0.18	1900	3.1
	2.465	0.13	0.31	9000	15.0	2.58	0.08	0.18	1580	2.6
10 Wachtelberg Rhyolite red CL	2.457	0.137	0.33	7900	14.8	2.58	0.08	0.18	1750	3.3
	2.457	0.137	0.33	6500	13.0	2.58	0.08	0.18	1500	3.0
	2.465	0.125	0.28	5800	11.9	2.58	0.08	0.18	1000	2.1
11 Beucha Rhyolite blue CL	2.485	0.12	0.29	11585	13.8	2.58	0.08	0.18	3043	3.6
	2.485	0.12	0.29	9500	12.3	2.58	0.08	0.18	2800	3.6
	2.48	0.12	0.28	9500	12.5	2.58	0.08	0.18	1800	2.4
11 Beucha Rhyolite red CL	2.48	0.125	0.3	10416	17.3	2.58	0.08	0.18	1733	2.9
	2.48	0.125	0.3	9166	15.4	2.58	0.08	0.18	1698	2.8
	2.48	0.125	0.3	7500	11.7	2.58	0.08	0.18	1300	2.0
12 Flossenbuerg Granite	2.47	0.13	0.3	29700	19.8	2.58	0.08	0.18	5000	3.3
	2.47	0.13	0.3	25000	18.0	2.58	0.08	0.18	5000	3.6
	2.48	0.125	0.3	22500	15.7	2.58	0.08	0.18	3000	2.1
13 Leucosome Quartz	2.47	0.127	0.29	14600	19.7	2.58	0.08	0.18	2500	3.4
	2.47	0.13	0.3	14600	17.3	2.58	0.08	0.18	2700	3.2
	2.47	0.125	0.28	15200	15.0	2.58	0.08	0.18	3100	3.1
14 Ramberg Granite	2.465	0.13	0.31	19000	18.0	2.58	0.08	0.18	4000	3.8
	2.465	0.125	0.28	14700	15.0	2.58	0.08	0.18	3200	3.3
	2.48	0.125	0.3	22500	15.7	2.58	0.08	0.18	3000	2.1
15 Weinheim Rhyolite blue CL	2.45	0.138	0.32	36000	18.8	2.571	0.08	0.18	1080	5.6
	2.45	0.138	0.32	31400	17.4	2.571	0.08	0.18	1040	5.8
	2.46	0.135	0.32	28000	16.6	2.58	0.08	0.18	7600	4.5
15 Weinheim Rhyolite red CL	2.46	0.125	0.3	11875	14.1	2.58	0.08	0.18	2717	3.2
	2.46	0.125	0.3	10000	9.5	2.58	0.08	0.18	2420	2.3
	2.46	0.125	0.3	8200	7.9	2.58	0.08	0.18	1900	1.8

List of CL emission band parameters of quartz (continued)

Sample	2.68 eV - Band					2.79 eV - Band				
	Position (eV)	Sigma (eV)	Half-width (eV)	If	If (%)	Position (eV)	Sigma (eV)	Half-width (eV)	If	If (%)
1 Megaquartz	2.685	0.1	0.23	11000	9.4	2.79	0.11	0.26	10200	8.7
	2.685	0.1	0.23	4000	6.1	2.79	0.11	0.26	4100	6.2
	2.685	0.1	0.23	3500	5.8	2.79	0.11	0.26	2500	4.2
2 Fissile Quartz	2.685	0.1	0.23	6700	10.9	2.792	0.11	0.26	7300	11.9
	2.685	0.1	0.23	6500	10.4	2.792	0.11	0.26	6800	10.8
	2.685	0.1	0.23	6150	8.8	2.795	0.11	0.26	6200	8.9
3 Oil-bearing Quartz	2.685	0.1	0.23	7200	8.3	2.79	0.11	0.26	8700	10.1
	2.685	0.1	0.23	6000	7.3	2.79	0.11	0.26	6000	7.3
	2.685	0.1	0.23	4500	6.0	2.79	0.11	0.26	3500	4.7
4 Schoenfeld Rhyolite	2.685	0.1	0.23	13100	11.9	2.79	0.11	0.26	15200	13.8
	2.685	0.1	0.23	11200	11.0	2.79	0.11	0.26	12700	12.5
	2.685	0.1	0.23	9800	9.7	2.79	0.11	0.26	10800	10.6
5 Teplice Rhyolite blue CL/ phenocryst	2.68	0.1	0.24	7060	13.6	2.8	0.11	0.26	8700	16.8
	2.68	0.1	0.24	6000	12.2	2.8	0.11	0.26	7100	14.5
	2.68	0.1	0.24	5700	11.0	2.8	0.11	0.26	6300	12.1
5 Teplice Rhyolite red CL/ phenocryst	2.685	0.1	0.23	6000	5.5	2.8	0.11	0.26	5800	5.3
	2.685	0.1	0.23	6000	5.5	2.8	0.11	0.26	5000	4.6
	2.685	0.1	0.23	5300	4.6	2.8	0.11	0.26	5500	4.8
6 Schellerhau Granite blue CL/ phenocryst	2.68	0.1	0.24	15000	11.6	2.8	0.11	0.26	18500	14.3
	2.68	0.1	0.24	12100	10.2	2.8	0.11	0.26	14200	11.9
	2.68	0.1	0.24	9000	8.3	2.8	0.11	0.26	10800	10.0
6 Schellerhau Granite red CL/ phenocryst	2.68	0.1	0.24	8000	9.6	2.8	0.11	0.26	8000	9.6
	2.68	0.1	0.24	5500	6.2	2.8	0.11	0.26	6300	7.1
	2.68	0.1	0.24	5000	5.5	2.8	0.11	0.26	5000	5.5
6 Schellerhau Granite red CL/ matrix quartz	2.68	0.1	0.24	6700	9.6	2.8	0.11	0.26	8600	12.4
	2.68	0.1	0.24	6000	7.8	2.8	0.11	0.26	6700	8.7
	2.68	0.1	0.24	4900	6.2	2.8	0.11	0.26	5600	7.1
7 Eibenstock Granite	2.685	0.1	0.23	2200	8.4	2.79	0.105	0.24	2300	8.8
	2.685	0.1	0.23	1980	6.9	2.79	0.105	0.24	2050	7.2
	2.685	0.1	0.23	2000	6.5	2.79	0.105	0.24	1850	6.0
8 Aue Granite	2.685	0.1	0.23	15568	10.6	2.785	0.105	0.24	16436	11.2
	2.685	0.1	0.23	13700	10.0	2.785	0.105	0.24	14300	10.4
	2.685	0.1	0.23	9650	8.1	2.785	0.105	0.24	11200	9.4
9 Vein Quartz	2.685	0.1	0.23	10500	13.5	2.8	0.11	0.26	18000	23.1
	2.685	0.1	0.23	5500	13.3	2.8	0.11	0.26	8500	20.5
	2.685	0.1	0.23	2250	12.9	2.8	0.11	0.26	2600	14.9
10 Wachtelberg Rhyolite blue CL	2.685	0.1	0.23	8100	11.8	2.8	0.11	0.26	8100	11.8
	2.685	0.1	0.23	6735	10.8	2.8	0.11	0.26	6745	10.9
	2.685	0.1	0.23	6150	10.3	2.8	0.11	0.26	6160	10.3
10 Wachtelberg Rhyolite red CL	2.685	0.1	0.23	4700	8.8	2.8	0.11	0.26	5400	10.1
	2.685	0.1	0.23	3800	7.6	2.8	0.11	0.26	4400	8.8
	2.685	0.1	0.23	4000	8.2	2.8	0.11	0.26	3900	8.0
11 Beucha Rhyolite blue CL	2.685	0.1	0.23	9195	10.9	2.79	0.11	0.26	11850	14.1
	2.685	0.1	0.23	8000	10.4	2.79	0.11	0.26	9000	11.7
	2.685	0.1	0.23	6500	8.6	2.79	0.11	0.26	7600	10.0
11 Beucha Rhyolite red CL	2.685	0.1	0.23	6050	10.1	2.79	0.11	0.26	7073	11.8
	2.685	0.1	0.23	5444	9.1	2.79	0.11	0.26	6295	10.5
	2.685	0.1	0.23	4900	7.7	2.79	0.11	0.26	5600	8.8
12 Flossenbuerg Granite	2.68	0.1	0.24	17000	11.4	2.79	0.11	0.26	19300	12.9
	2.68	0.1	0.24	15900	11.4	2.795	0.11	0.26	18800	13.5
	2.68	0.1	0.24	14500	10.1	2.79	0.11	0.26	16100	11.2
13 Leucosome Quartz	2.685	0.1	0.23	9000	12.1	2.79	0.11	0.26	9000	12.1
	2.685	0.1	0.23	9800	11.6	2.79	0.11	0.26	9200	10.9
	2.685	0.1	0.23	10200	10.1	2.79	0.11	0.26	10000	9.9

List of CL emission band parameters of quartz (continued)

Sample	2.68 eV - Band					2.79 eV - Band				
	Position (eV)	Sigma (eV)	Half-width (eV)	If	If (%)	Position (eV)	Sigma (eV)	Half-width (eV)	If	If (%)
14 Ramberg Granite	2.68	0.1	0.24	11800	11.2	2.8	0.11	0.26	13500	12.8
	2.68	0.1	0.24	9300	9.5	2.8	0.11	0.26	10500	10.7
	2.68	0.1	0.24	14500	10.1	2.79	0.11	0.26	16100	11.2
15 Weinheim Rhyolite blue CL	2.685	0.095	0.22	22300	11.6	2.79	0.11	0.26	26500	13.8
	2.685	0.095	0.22	19000	10.5	2.79	0.11	0.26	25000	13.8
	2.685	0.1	0.23	17400	10.3	2.79	0.11	0.26	23600	14.0
15 Weinheim Rhyolite red CL	2.685	0.1	0.23	6704	7.9	2.8	0.11	0.26	7800	9.2
	2.685	0.1	0.23	6750	6.4	2.8	0.11	0.26	7000	6.6
	2.685	0.1	0.23	5300	5.1	2.8	0.11	0.26	5500	5.3

Sample	2.96 eV - Band				
	Position (eV)	Sigma (eV)	Half-width (eV)	If	If (%)
1 Megaquartz	2.955	0.125	0.28	5200	4.4
	2.96	0.125	0.3	2200	3.3
	2.96	0.125	0.3	1500	2.5
2 Fissile Quartz	2.96	0.12	0.28	7000	11.4
	2.96	0.12	0.28	6000	9.6
	2.96	0.12	0.28	5800	8.3
3 Oil-bearing Quartz	2.96	0.127	0.3	8700	10.1
	2.965	0.125	0.29	6700	8.1
	2.96	0.125	0.3	4500	6.0
4 Schoenfeld Rhyolite	2.96	0.13	0.3	22000	20.0
	2.96	0.13	0.3	17800	17.5
	2.96	0.13	0.3	15000	14.8
5 Teplice Rhyolite blue CL/phenocryst	2.96	0.128	0.3	10000	19.3
	2.96	0.128	0.3	9000	18.4
	2.96	0.128	0.3	8200	15.8
5 Teplice Rhyolite red CL/phenocryst	2.97	0.13	0.3	7500	6.8
	2.97	0.13	0.3	7500	6.9
	2.97	0.13	0.3	7300	6.3
6 Schellerhau Granite blue CL/phenocryst	2.965	0.135	0.31	27500	21.3
	2.965	0.135	0.31	22000	18.5
	2.965	0.135	0.31	15500	14.3
6 Schellerhau Granite red CL/phenocryst	2.965	0.135	0.31	10000	11.9
	2.965	0.135	0.31	7500	8.4
	2.965	0.135	0.31	5700	6.3
6 Schellerhau Granite red CL/matrix quartz	2.97	0.135	0.32	12500	18.0
	2.97	0.135	0.32	10000	13.0
	2.97	0.135	0.32	8000	10.2
7 Eibenstock Granite	2.965	0.13	0.31	3900	14.9
	2.965	0.13	0.31	3600	12.6
	2.96	0.13	0.3	3500	11.4
8 Aue Granite	2.96	0.125	0.3	23000	15.7
	2.96	0.125	0.3	20000	14.6
	2.96	0.125	0.3	15700	13.1
9 Vein Quartz	2.96	0.125	0.3	18500	23.8
	2.96	0.125	0.3	8900	21.5
	2.96	0.125	0.3	3000	17.2
10 Wachtelberg Rhyolite blue CL	2.965	0.135	0.31	14470	21.0
	2.965	0.135	0.31	12045	19.4
	2.965	0.135	0.31	11000	18.3

List of CL emission band parameters of quartz (continued)

Sample	2.96 eV - Band				
	Position (eV)	Sigma (eV)	Half-width (eV)	If	If (%)
10 Wachtelberg Rhyolite red CL	2.965	0.135	0.31	9100	17.0
	2.965	0.135	0.31	7600	15.2
	2.965	0.135	0.31	7000	14.4
11 Beucha Rhyolite blue CL	2.962	0.135	0.32	17300	20.6
	2.962	0.135	0.32	14500	18.8
	2.962	0.135	0.32	12300	16.2
11 Beucha Rhyolite red CL	2.965	0.135	0.31	12100	20.1
	2.965	0.135	0.31	10000	16.8
	2.965	0.135	0.31	9000	14.1
12 Flossenbuerg Granite	2.957	0.13	0.3	29000	19.4
	2.957	0.13	0.3	28000	20.2
	2.957	0.13	0.3	24500	17.1
13 Leucosome Quartz	2.965	0.135	0.31	14000	18.8
	2.96	0.135	0.31	15000	17.8
	2.965	0.135	0.31	15000	14.8
14 Ramberg Granite	2.965	0.135	0.31	20000	19.0
	2.965	0.135	0.31	14500	14.8
	2.957	0.13	0.3	24500	17.1
15 Weinheim Rhyolite blue CL	2.955	0.135	0.31	42000	21.9
	2.955	0.135	0.31	37000	20.5
	2.96	0.125	0.3	31000	18.4
15 Weinheim Rhyolite red CL	2.96	0.125	0.3	9000	10.7
	2.96	0.125	0.3	7600	7.2
	2.96	0.125	0.3	6500	6.2

Appendix B

List of kinetic law parameters of CL intensity change for the 1.96 and 2.79 eV emission

Function of the 1.96 eV emission increase (and ^b): $I_r = I_{rs} - I_{r1} * \exp(-t/k_{r1}) - I_{r2} * \exp(-t/k_{r2})$ where I_r = intensity of red CL at the radiation time t ; I_{rs} = intensity of red CL for $t \rightarrow \infty$; I_{r1} = intensity of the slow increasing CL component for $t \rightarrow \infty$; k_{r1} = velocity constant of the slow increasing CL component; I_{r2} = intensity of the fast increasing CL component for $t \rightarrow \infty$; k_{r2} = velocity constant of the fast increasing CL component; t = radiation time.

Function of the 2.79 eV emission decay (and ^a): $I_b = I_{bs} + I_{b1} * \exp(-t/k_{b1}) + I_{b2} * \exp(-t/k_{b2})$ where I_b = intensity of blue CL at the radiation time t ; I_{bs} = intensity of stable blue CL; I_{b1} = intensity of the slow decreasing CL component at $t = 0$; k_{b1} = velocity constant of the slow decreasing CL component; I_{b2} = intensity of the fast decreasing CL component at $t = 0$; k_{b2} = velocity constant of the fast decreasing CL component; t = radiation time. Intensities are normalised for the highest measured intensity (I_{rs} of sample 15). The reproducibility of the parameters lies in the error range of 10 – 20 %.

No.	Sample name	1.96 eV emission					2.79 eV emission				
		I_{rs} (%)	I_{r1} (%)	k_{r1}	I_{r2} (%)	k_{r2}	I_{bs} (%)	I_{b1} (%)	k_{b1}	I_{b2} (%)	k_{b2}
1	Megaquartz	46.2	16.1	512	3.0	7	4.5	4.5	254	72.2	14
2	Fissile Quartz	49.8	30.2	498	7.2	10	12.1	3.5	234	25.7	7
3	Oil quartz	55.0	15.6	470	29.2	36	6.9	10.2	248	37.8	10
4	Schoenfeld Rhyolite	61.6	18.1	502	4.4	36	23.0	9.9	259	17.9	16
5	Teplice rhyolite – blue CL	23.1	6.6	513	4.9	18	13.0	4.5	250	16.8	8
5	Teplice Rhyolite- red CL	95.6	37.2	522	3.8	11	12.0	0.9	245	4.7	8
6	Schellerhau Granite – blue CL/phenocryst	64.2	26.0	489	11.0	42	21.0	19.3	261	33.0	15
6	Schellerhau Granite – red CL/Phenocryst	72.7	26.9	495	23.8	45	9.3	6.4	256	9.8	22
6	Schellerhau Granite – red CL/matrix quartz	59.2	17.2	504	36.9	33	11.2	6.8	252	14.7	15
7	Eibenstock Granite	21.1	9.3	521	5.6	23	4.8	6.8	243	6.2	10
8	Aue Granite	47.0	8.1	506	9.9	16	22.0	0.6	245	22.5	10
9	Vein Quartz	30.1 ^a	3.5 ^a	244 ^a	1.3 ^a	8 ^a	2.2	22.8	257	74.6	16
10	Wachtelberg Rhyolite – blue CL	31.8	5.6	491	3.2	26	15.1	24.7	271	11.3	20
10	Wachtelberg Rhyolite – red CL	35.8	3.3	509	2.4	26	9.4	3.7	240	11.4	20
11	Beucha Rhyolite– blue CL	44.2	13.6	531	0.5	18	16.7	6.6	255	11.4	20
11	Beucha Rhyolite – red CL	40.1	6.2	485	2.7	24	12.7	8.2	247	9.0	20
12	Flossenbuerg Granite	80.1	47.3	492	25.4	12	35.2	2.7	254	51.1	8
13	Leucosome Quartz	68.4	44.6	479	6.0	27	24.4 ^b	11.9 ^b	495 ^b	3.9 ^b	24 ^b
14	Ramberg Granite	60.4	16.0	488	22.6	24	21.6	1.4	263	45.3	17
15	Weinheim Rhyolite – blue CL	78.0	8.0	504	7.1	20	47.5	2.3	254	23.5	10
15	Weinheim Rhyolite – red CL	100.0	15.6	521	6.8	26	10.4	16.5	247	11.1	8

Appendix C

List of trace element analysis of quartz (LA ICP-MS)

1 Megaquartz

Sample	Li	Na	Al	Ca	Ti	Cr	Mn	Fe	Ge
hakos01 1	36.5	108.8	229.5	1506.6	14.3	39.8	2.2	44.9	15.7
hakos02 1	29.5	348.1	168.8	1286.5	16.2	42.4	4.4	72.1	11.7
hakos03 1	33.4	378.9	238	1787.9	14.8	35.7	3.0	57.7	12.8
hakos04 1	27.2	225.3	156.4	991	20	30.3	1.8	29.8	14.4
hakos05 1	38.7	309.5	204.8	1371.7	22.2	37.6	2.3	38.3	20.2
hakos06 1	45.8	357.4	217.6	1273.3	12.1	34.2	2.4	43.6	12.4
hakos07 1	34.8	246.2	237.1	893.4	14.2	43.2	1.2	50.0	11.2
hakos08 1	25.8	217.6	178.7	1391.2	18.1	34.2	2.2	44.4	9.8
hakos09 1	36.9	253.9	216.1	1123.1	14.2	37.5	2.4	53.2	12.2
hakos10 1	29.7	264.3	181.1	1023.3	15.3	30.2	1.8	40.3	13.8

2 Fissile quartz

Sample	Li	Na	Al	Ca	Ti	Cr	Mn	Fe	Ge
spalt01 1	2.8	241.4	125.6	464.5	14.4	0.1	4.1	90.3	2.6
spalt02 1	2.7	250.3	144.4	378.2	26.3	2.0	2.1	51.9	0.1
spalt03 1	2.5	241.7	168.3	280.4	20.0	0.9	1.8	63.9	1.1
spalt04 1	2.1	251.4	170.4	7.1	12.2	0.1	1.9	74.7	0.4
spalt05 1	2.2	154.7	103.3	0.1	9.4	0.1	1.5	77.5	0.9
spalt06 1	2.7	247.5	157.9	345.3	11.1	0.8	1.8	72.0	1.2
spalt07 1	2.4	249.2	162.4	0.1	13.6	0.1	1.5	51.6	0.4
spalt08 1	2.3	258.3	167.0	293.2	9.0	0.1	2.0	61.3	1.2
spalt09 1	2.2	138.2	126.8	397.4	12.9	1.7	3.0	77.6	2.1
spalt10 1	2.7	263.9	149.2	0.1	11.2	0.1	3.2	86.5	0.1

3 Oil-bearing quartz

Sample	Li	Na	Al	Ca	Ti	Cr	Mn	Fe	Ge
oel01 1	134.3	1788.2	410.4	200.8	16.8	0.1	0.4	76.4	7.2
oel02 1	118.8	2416.2	472.4	256.5	14.9	0.1	0.2	36.7	6.7
oel03 1	131.2	3458.0	630.3	215.4	15.0	0.1	0.6	60.5	5.5
oel04 1	118.6	3375.5	487.7	125.7	14.6	2.7	0.8	63.6	2.9
oel05 1	119.1	1288.4	597.9	152.1	9.3	0.1	1.7	92.0	7.0
oel06 1	112.8	3921.5	493.7	234.8	10.1	0.1	0.2	44.1	5.4
oel07 1	123.8	3545.2	417.1	176.4	8.2	0.1	0.6	58.6	6.3
oel08 1	109.6	3455.0	518.2	349.2	12.5	0.1	0.8	63.3	3.2
oel09 1	116.3	2392.2	483.7	281.8	13.2	0.1	0.2	36.3	7.3
oel010 1	121.0	1823.3	417.1	175.8	14.5	0.1	1.4	75.5	2.9

5 Teplice Rhyolite

Sample	Li	Na	Al	Ca	Ti	Cr	Mn	Fe	Ge
lug102 1	32.4	89.9	157.4	452.9	99.2	1.8	0.8	61.9	2.2
lug103 1	29.5	79.6	152.7	0.1	124.1	0.1	0.9	81.0	1.3
lug104 1	34.8	75.4	149.3	116.1	167.4	0.1	1.3	57.1	1.9
lug105 1	34.0	0.1	157.6	154.0	93.1	0.1	0.5	0.1	0.4
lug106 1	28.0	0.1	159.2	0.1	107.8	0.1	0.1	0.1	1.5
lug107 1	28.6	6.4	149.9	149.0	124.3	0.1	0.9	0.1	2.4
lug108 1	27.1	88.3	140.6	761.0	85.1	0.1	0.1	8.4	1.6
lug109 1	25.7	424.1	171.2	0.1	60.1	0.1	12.6	17.4	1.2
lug110 1	18.3	393.1	175.1	141.3	35.3	0.1	5.4	0.1	1.3
lug111 1	17.5	70.7	170.4	0.1	50.7	0.1	2.0	0.1	1.4
lug113 1	29.3	0.1	160.2	0.1	54.2	0.1	1.2	0.1	1.0

List of trace element analysis of quartz (LA ICP-MS) (continued)

5 Teplice Rhyolite

Sample	Li	Na	Al	Ca	Ti	Cr	Mn	Fe	Ge
lug114 1	29.5	0.1	155.1	0.1	74.5	0.1	0.3	0.1	1.2
lug115 1	23.5	26.5	178.1	0.1	69.2	0.1	0.2	6.5	1.3
lug116 1	32.4	0.1	170.0	2180.3	136.2	0.1	0.5	0.1	0.9
lug119 1	27.0	121.6	161.6	133.5	98.6	1.3	3.6	9.0	0.8
lug120 1	30.1	113.8	163.2	363.7	89.1	0.1	1.0	21.8	0.5
lug201 1	31.9	354.8	123.2	453.1	149.4	0.9	3.8	14.4	2.5
lug202 1	34.2	0.1	134.4	260.3	124.9	0.1	0.6	2.2	2.8
lug203 1	35.9	0.1	159.6	0.1	176.6	0.1	1.4	13.1	1.2
lug204 1	37.8	144.9	134.9	0.1	80.6	0.1	11.1	8.8	0.8
lug205 1	26.8	104.1	129.0	0.1	60.7	2.7	16.0	5.1	0.7
lug206 1	33.6	194.4	122.1	491.2	70.1	2.2	1.0	4.0	0.4
lug207 1	33.4	0.1	129.0	0.1	55.0	0.1	0.2	2.1	1.8
lug208 1	31.1	0.1	125.1	70.7	60.4	0.1	0.9	1.7	3.2
lug209 1	39.9	0.1	177.4	0.1	107.9	0.1	2.2	7.3	0.8
lug210 1	30.8	0.1	161.1	290.2	144.3	0.1	1.4	6.3	1.6
lug211 1	34.1	0.1	147.1	0.1	165.1	0.1	0.4	10.8	1.5
lug212 1	38.2	0.1	142.6	0.1	169.9	0.1	0.4	7.0	0.2
lug213 1	28.9	0.1	155.6	0.1	199.8	4.5	0.1	22.9	0.1
lug301 1	30.4	0.1	133.9	0.1	87.0	0.1	1.5	31.0	0.1
lug302 1	32.6	0.1	144.2	179.7	86.2	0.1	4.3	26.9	0.1
lug304 1	35.7	94.9	144.3	475.8	103.2	3.6	1.5	29.8	1.4
lug305 1	33.0	0.1	140.5	162.4	120.2	0.1	0.1	25.1	1.1
lug306 1	30.1	0.1	146.5	240.8	146.7	2.5	0.3	19.3	1.4
lug307 1	32.7	0.1	144.4	0.1	102.5	0.1	0.5	10.8	0.8
lug308 1	26.9	0.1	134.5	0.1	51.6	0.1	0.2	17.1	1.1
lug309 1	22.6	0.1	117.8	224.4	63.0	0.8	0.1	20.1	1.0
lug310 1	24.9	0.1	115.4	105.0	57.3	0.1	0.1	16.6	0.1
lug311 1	22.8	0.1	119.0	185.5	47.2	0.1	0.1	5.0	0.4
lug312 1	25.2	0.1	112.5	196.9	58.3	0.1	0.1	3.1	0.1
lug501 1	26.3	1368.4	183.6	45.6	58.4	14.9	5.0	49.2	1.0
lug502 1	20.1	1110.3	174.5	0.1	64.1	5.3	1.0	41.4	0.2
lug503 1	20.8	1128.7	170.2	0.1	57.3	6.3	2.7	53.8	1.7
lug504 1	22.8	899.5	163.0	135.5	51.4	5.1	0.4	68.5	2.4
lug505 1	20.9	903.4	145.8	0.1	41.7	1.1	0.1	38.8	1.5
lug506 1	19.8	911.1	151.8	224.9	26.6	3.3	0.5	58.7	1.1
lug507 1	20.9	795.1	155.8	29.3	15.4	3.0	0.2	24.8	1.5
lug508 1	20.7	835.5	149.3	26.3	36.2	5.8	0.1	21.1	2.1
lug509 1	19.2	918.8	141.2	41.4	44.6	3.4	0.2	24.2	2.4
lug510 1	16.8	1059.0	141.4	0.1	42.4	7.1	1.8	34.0	0.7
lug511 1	18.7	999.0	150.1	0.1	59.2	4.3	0.1	13.7	1.5
lug512 1	17.3	878.0	151.7	0.1	40.3	6.2	0.1	18.4	2.0
lug513 1	17.8	1034.4	160.2	0.1	20.3	8.0	0.1	12.1	0.9
lug514 1	16.0	1031.9	157.1	0.1	46.8	10.8	0.1	22.9	1.9
lug515 1	14.7	1223.0	158.8	271.4	39.6	5.8	0.2	55.8	1.5
lug516 1	16.4	1202.4	156.4	0.1	46.7	3.8	0.1	48.5	2.1

6 Schellerhau Granite

Sample	Li	Na	Al	Ca	Ti	Cr	Mn	Fe	Ge
sh69101	29.2	136.3	300.7	3156.9	26.1	17.5		23.0	5.8
sh69102	27.3	19.0	119.0	3043.8	100.7	9.8		7.1	0.1
sh69103	24.5	32.2	87.0	3434.3	83.1	1.7		2.3	7.5
sh69105	20.2	13.3	114.6	2823.5	24.9	5.7		0.1	2.1
sh69106	30.6	282.0	124.2	3345.0	25.6	11.3		0.1	4.1
sh69107	20.4	64.9	96.4	2864.5	10.5	21.9		0.1	1.2
sh69108	29.0	71.9	140.5	2709.6	86.9	13.3		2.2	0.1
sh69109	27.0	1.6	88.5	2706.3	102.0	4.9		0.1	7.8
sh69110	44.8	44.1	444.0	2157.2	123.7	0.1		12.5	0.1
sh69111	43.6	110.0	454.1	2174.7	100.1	4.7		0.1	0.7
sh69112	38.7	14.9	124.5	3641.5	76.0	0.1		0.1	0.1
sh69113	15.2	55.8	183.0	3353.2	30.8	11.9		16.0	0.6

List of trace element analysis of quartz (LA ICP-MS) (continued)

6 Schellerhau Granite

Sample	Li	Na	Al	Ca	Ti	Cr	Mn	Fe	Ge
sh69201	35.1	1.8	108.8	3047.9	73.0	0.1		8.8	1.5
sh69202	33.2	2.3	116.8	2786.4	83.6	0.1		63.1	0.1
sh69204	27.7	0.1	138.5	2940.4	57.8	0.8		0.1	2.9
sh69205	35.3	0.1	110.7	3273.3	73.8	0.1		0.1	8.6
sh69206	40.8	0.1	99.4	3757.0	150.3	0.1		32.2	3.3
sh69207	24.5	0.1	108.4	3706.7	9.9	0.1		0.1	0.1
sh69209	37.6	98.7	117.7	3254.6	22.5	0.1		26.4	1.2
sh69210	27.1	0.1	101.4	3442.2	45.2	0.3		0.1	0.1
sh69211	21.9	110.6	124.9	2523.5	62.9	0.1		0.1	0.1
sh69212	20.2	0.1	175.3	2696.9	34.3	0.1		68.3	0.1
sh69401	25.0		423.7	0.1	20.9	24.7		130.9	0.9
sh69402	25.3		216.2	1958.7	15.4	12.9		110.6	2.4
sh69403	26.5		92.2	0.1	13.8	14.3		136.2	0.1
sh69404	29.9		104.8	0.1	21.1	11.9		20.5	0.1
sh69405	33.6		149.4	0.1	20.1	14.3		11.1	0.1
sh69406	34.5		124.0	0.1	20.9	15.4		34.4	28.3
sh69407	24.6		106.1	2230.8	16.1	16.3		73.8	1.4
sh69408	32.2		85.2	1550.0	18.1	10.8		188.7	7.7
sh69409	17.5		106.2	455.6	16.7	19.0		130.9	0.1
sh69410	23.0		79.0	415.1	20.3	14.6		130.5	0.1
sh69411	26.0		263.7	6309.7	18.2	15.5		104.8	0.1
sh70101	21.6		261.3	0.1	16.6	15.8		81.7	51.7
sh70102	31.1		257.0	494.1	16.3	12.8		19.9	28.3
sh70103	40.2		258.8	1761.7	15.9	13.7		0.1	15.3
sh70104	35.7		269.4	2293.9	17.1	15.0		18.9	0.1
sh70105	36.3		283.9	0.1	18.0	13.4		12.9	9.3
sh70106	32.5		229.0	1094.8	15.6	16.5		19.4	19.4
sh70107	27.8		271.5	0.1	18.1	14.4		15.9	0.1
sh70108	39.3		262.5	0.1	18.9	14.2		55.4	0.1
sh70109	23.2		248.0	0.1	12.9	11.8		83.8	0.8
sh70110	22.0		166.1	698.1	23.1	14.2		60.7	20.6
sh70201	32.0		116.1	1418.6	18.7	11.3		102.0	22.6
sh70202	30.2		94.6	0.1	15.0	11.8		99.6	37.5
sh70203	26.5		111.0	1205.4	13.1	16.4		139.8	6.0
sh70204	23.7		104.3	516.9	17.4	17.8		151.6	30.6
sh70205	16.1		96.4	0.1	14.2	14.0		208.4	2.8
sh70206	19.3		126.6	1450.1	19.4	17.8		86.0	0.1
sh70207	29.2		135.6	526.8	12.4	14.3		138.1	49.0
sh70209	29.3		162.6	1005.9	22.3	15.2		56.3	29.5
sh70210	33.7		138.3	293.0	21.8	14.7		30.4	0.1
sh70211	22.8		122.3	541.2	19.3	18.8		4.5	48.5
sh70212	19.8		113.7	1589.9	14.3	11.9		218.2	28.5
sh70213	17.5		91.9	647.8	13.9	13.5		294.0	0.1
sh70214	13.8		110.7	468.4	18.4	18.2		113.0	18.6
sh70215	18.1		108.5	167.3	19.1	12.6		225.6	28.1
sh70303	27.6		261.5	0.1	11.9	13.8		266.7	0.1
sh70304	38.8		189.4	1795.5	12.4	10.5		11.1	0.1
sh70305	39.3		242.9	510.5	21.7	17.9		26.1	0.1
sh70306	28.2		176.6	737.0	18.1	12.8		58.0	48.7
sh70307	33.2		206.3	732.8	16.9	12.1		36.9	0.1
sh70308	28.8		267.7	1266.7	14.4	16.9		41.1	7.3
sh70309	27.7		298.9	0.1	14.7	15.2		42.3	31.2
sh70310	24.9		158.8	456.5	14.6	13.1		31.2	0.1
sh70311	33.8		114.3	2930.2	19.9	18.3		33.8	0.1
sh70312	11.9		125.1	0.1	17.2	16.1		185.7	0.1
sh70313	21.6		235.8	527.7	21.0	15.7		68.8	10.7
sh70314	25.3		192.4	675.2	12.9	19.7		203.8	49.0
sh70315	28.0		176.4	1028.7	19.2	14.4		67.3	0.1
sh70316	22.3		239.6	33.0	13.6	13.4		75.1	17.8
sh72101	23.7		119.6	0.1	13.7	15.6		40.6	0.1
sh72102	20.3		108.0	43.8	13.5	10.0		323.0	0.1
sh72103	25.8		118.4	0.1	15.0	13.9		112.5	0.1

List of trace element analysis of quartz (LA ICP-MS) (continued)

6 Schellerhau Granite

Sample	Li	Na	Al	Ca	Ti	Cr	Mn	Fe	Ge
sh72104	29.8		118.8	527.3	17.9	13.0		11.9	0.1
sh72105	24.3		141.6	943.7	18.8	15.1		61.1	0.1
sh72106	26.0		116.0	2011.4	17.3	11.4		58.9	0.1
sh72107	29.9		101.7	204.1	15.3	17.4		81.9	0.1
sh72108	25.7		179.2	0.1	16.6	20.1		168.1	0.1
sh72109	32.5		123.2	636.8	16.9	13.8		90.5	6.8
sh72110	16.2		110.2	1175.5	18.8	13.2		120.2	0.1
sh72111	16.7		109.4	800.6	18.5	12.6		139.7	0.1
sh72112	25.8		98.1	238.1	15.8	15.1		78.3	0.1
sh72113	29.5		103.1	0.1	11.8	13.3		120.7	0.1
sh72114	25.4		98.3	456.9	16.4	13.1		140.5	0.1
sh72115	27.8		91.0	218.0	16.3	12.6		146.1	0.1
sh72116	28.9		133.5	782.9	16.9	13.5		146.5	0.1
sh72117	24.0		114.6	769.8	17.0	15.7		153.9	3.5
sh72201	25.7		185.1	1096.1	15.4	16.6		10.3	3.4
sh72202	30.9		136.1	3925.0	19.7	9.9		41.7	10.2
sh72203	28.3		99.0	115.8	14.8	13.1		148.6	17.0
sh72204	30.2		125.5	1238.7	13.8	13.5		136.1	5.2
sh72205	27.9		83.5	344.5	12.6	15.3		47.9	0.1
sh72206	16.6		66.3	736.8	15.0	13.2		55.4	7.9
sh72208	20.4		141.2	0.1	17.6	16.0		11.4	0.1
sh72209	22.4		120.6	1278.3	16.9	12.6		5.6	44.6
sh72210	23.7		192.7	5354.0	15.1	14.5		9.7	39.1
sh72211	24.5		200.3	407.2	14.2	14.6		7.9	12.2
sh72212	23.3		100.3	138.7	13.9	13.5		34.5	0.1
sh72213	16.2		98.6	1441.2	15.1	6.5		219.4	61.3
sh72214	17.7		109.5	1537.8	16.1	10.8		215.9	12.6
sh72302	28.1		114.3	2848.6	14.1	14.4		24.2	0.1
sh72303	27.9		85.5	4205.8	17.8	11.6		115.1	0.1
sh72304	48.7		259.7	5011.6	7.0	13.2		27.8	92.6
sh72305	29.7		144.1	0.1	18.8	16.9		23.0	0.1
sh72306	33.7		112.8	6278.7	13.2	11.5		26.1	0.1
sh72307	27.2		65.3	2568.9	12.2	12.4		0.1	0.1
sh72308	27.1		93.1	1448.1	18.3	11.0		0.1	0.1
sh72309	25.4		42.5	0.1	13.8	13.3		29.9	1.9
sh72310	21.4		68.8	3507.5	11.6	7.5		65.4	0.1
sh72311	24.4		103.8	1566.7	11.8	6.4		0.1	0.1
sh72312	29.8		103.7	1693.1	15.9	12.9		20.7	0.1
sh72315	31.1		51.4	5600.9	21.9	11.9		97.0	2.5
sh72316	25.7		86.3	4696.6	17.0	14.2		90.0	0.9

7 Eibenstock Granite

Sample	Li	Na	Al	Ca	Ti	Cr	Mn	Fe	Ge
eiben01 1	25.98	4654.1	696.6	66.3	54.0	1.7	5.2	59.9	2.1
eiben02 1	33.66	3454.4	625.3	83.1	48.3	0.1	5.5	30.2	2.3
eiben03 1	30.36	3815.6	701.7	0.1	52.6	0.9	5.1	50.1	1.9
eiben04 1	32.82	1974.8	726.0	89.0	67.4	2.1	3.8	32.4	1.2
eiben05 1	35.76	1128.3	627.0	0.1	66.2	3.7	0.1	24.6	2.2
eiben06 1	30.3	3954.3	714.2	0.1	55.5	0.7	5.6	43.7	1.8
eiben07 1	26.76	2596.3	635.2	0.1	70.2	2.3	6.3	58.5	2.7
eiben08 1	34.02	4294.4	734.2	112.1	65.4	3.1	5.3	23.7	1.3
eiben09 1	35.04	3867.4	678.5	67.4	68.4	2.3	5.7	51.7	2.1
eiben10 1	33	3444.3	658.4	0.1	53.2	2.1	3.9	32.1	1.9

List of trace element analysis of quartz (LA ICP-MS) (continued)

8 Aue Granite

Sample	Li	Na	Al	Ca	Ti	Cr	Mn	Fe	Ge
auer101 1	49.2	491.4	231.0	0.0	46.9	0.0	3.5	33.5	0.0
auer102 1	48.8	403.4	222.7	0.0	75.1	0.5	1.7	24.2	0.1
auer103 1	33.4	386.4	281.4	0.0	62.2	0.0	4.2	52.2	0.1
auer104 1	31.6	578.9	152.4	0.0	71.6	0.0	4.5	49.3	2.0
auer105 1	28.7	427.1	207.4	0.0	80.2	0.4	2.4	27.3	0.4
auer106 1	40.8	552.6	247.7	0.0	53.0	0.0	5.1	54.8	1.4
auer107 1	50.2	545.5	276.5	0.0	78.1	3.5	2.7	38.4	0.6
auer108 1	38.4	511.8	180.8	0.0	59.7	0.0	2.5	24.9	1.4
auer109 1	27.2	308.9	153.9	0.0	44.7	3.5	1.1	17.8	1.1
auer110 1	33.1	643.9	162.8	0.0	67.6	3.8	3.1	26.5	0.5
auer111 1	43.2	466.8	169.8	0.0	80.2	0.0	3.1	34.6	0.2
auer112 1	52.0	379.3	211.8	0.0	63.2	2.4	4.5	48.5	0.7

10 Wachtelberg Rhyolite

Sample	Li	Na	Al	Ca	Ti	Cr	Mn	Fe	Ge
wacht101 1	25.9	922.8	164.6	0.1	90.7	0.1	4.9	40.2	0.2
wacht102 1	25.0	520.6	177.5	0.1	69.4	0.1	0.1	21.8	1.4
wacht103 1	20.4	387.6	154.5	0.1	50.1	0.1	0.1	23.1	0.5
wacht104 1	21.2	622.5	150.4	89.9	55.2	0.1	5.0	42.4	1.8
wacht105 1	21.3	458.8	157.0	161.2	41.1	0.1	1.4	28.5	0.1
wacht108 1	22.6	607.5	158.8	31.3	38.2	0.1	0.5	23.2	0.3
wacht109 1	21.0	796.1	152.2	6.4	28.4	3.2	0.1	37.6	1.5
wacht110 1	20.5	373.3	163.2	53.9	72.0	1.2	3.7	45.8	1.5
wacht111 1	20.9	374.3	175.8	27.9	58.6	0.1	0.1	71.5	1.4
wacht112 1	19.6	293.1	160.1	0.1	74.5	0.1	0.1	39.2	1.7
wacht402 1	24.5	75.1	147.9	41.3	40.8	0.1	0.4	23.3	1.5
wacht403 1	24.4	78.6	127.6	332.9	24.1	5.3	0.1	28.1	1.4
wacht404 1	25.9	111.6	132.6	159.3	12.7	9.2	0.5	21.3	1.5
wacht405 1	29.3	28.3	148.1	173.6	9.1	1.1	0.1	11.6	0.7
wacht406 1	24.7	162.0	135.9	545.8	5.9	4.9	0.1	13.2	1.3
wacht407 1	22.1	10.2	134.4	107.4	11.4	1.9	0.1	24.9	0.8
wacht408 1	21.2	305.8	133.2	0.1	25.5	3.0	7.2	15.3	1.2
wacht409 1	22.5	114.6	134.3	0.1	40.7	0.1	1.3	18.8	2.5
wacht410 1	24.8	163.9	140.3	0.1	98.4	0.1	0.1	21.0	1.6
wacht411 1	22.0	117.3	144.7	0.1	98.4	8.4	0.1	25.1	0.7
wacht501 1	26.4	231.0	186.1	38.0	90.7	0.1	7.3	63.4	2.3
wacht502 1	28.6	526.8	141.7	210.4	108.0	3.2	0.5	58.5	0.7
wacht503 1	22.7	554.3	119.9	271.5	14.2	8.9	0.8	26.0	0.1
wacht504 1	22.2	464.3	124.0	0.1	23.5	0.1	0.1	22.8	2.3
wacht505 1	21.6	290.6	119.2	116.8	22.3	5.7	0.3	26.1	0.8
wacht506 1	22.1	397.7	129.8	0.1	25.2	0.1	0.2	46.9	2.7
wacht507 1	21.5	418.8	141.6	0.1	9.2	7.6	0.1	34.9	0.8
wacht508 1	22.4	365.4	140.1	0.1	80.4	3.9	0.1	32.9	1.3
wacht201 1	23.4	658.5	145.4	0.1	99.0	9.5	4.2	71.8	0.5
wacht202 1	32.0	82.8	149.7	427.3	132.1	1.8	4.0	49.0	0.9
wacht203 1	27.4	0.1	137.8	0.1	108.0	6.7	1.5	40.6	1.9
wacht204 1	23.8	0.1	116.4	0.1	58.0	7.8	0.3	20.7	1.3
wacht205 1	26.0	0.1	114.8	90.1	16.6	3.2	0.3	0.1	0.1
wacht206 1	23.0	0.1	109.5	0.1	30.7	2.8	0.2	4.4	2.9
wacht207 1	27.8	0.1	123.2	0.1	83.5	5.3	0.5	8.2	0.1
wacht208 1	24.6	0.1	118.0	0.1	32.3	0.1	0.1	16.8	1.9
wacht209 1	27.5	0.1	114.5	0.1	21.9	4.4	5.3	21.8	1.6
wacht211 1	22.3	121.3	109.2	0.1	20.2	0.1	2.3	1.0	0.6
wacht212 1	37.1	388.8	112.8	0.1	32.1	0.1	4.5	0.1	0.8
wacht213 1	22.6	328.2	120.6	891.5	23.1	1.6	4.1	25.6	2.0
wacht214 1	36.0	219.4	135.1	0.1	108.4	0.7	3.9	40.9	1.1
wacht215 1	46.8	235.4	153.8	0.1	93.9	0.1	1.5	84.8	0.1
wacht302 1	27.3	0.1	141.3	0.1	113.5	0.1	17.0	68.5	2.0
wacht303 1	26.7	116.9	155.1	0.1	78.0	0.1	14.2	76.9	1.1

List of trace element analysis of quartz (LA ICP-MS) (continued)

10 Wachtelberg Rhyolite

Sample	Li	Na	Al	Ca	Ti	Cr	Mn	Fe	Ge
wacht304 1	22.2	197.2	161.5	582.7	57.9	3.9	28.0	71.1	0.7
wacht305 1	22.5	0.1	123.2	0.1	39.4	0.1	5.8	54.1	0.8
wacht306 1	28.4	0.1	146.5	591.5	110.7	2.6	1.0	51.6	1.4
wacht307 1	24.5	0.1	126.4	416.9	78.1	2.5	0.1	12.8	1.0
wacht308 1	27.3	0.1	131.8	0.1	93.4	2.4	0.5	10.1	0.2
wacht309 1	23.8	30.7	172.2	0.1	73.1	0.1	0.1	13.0	2.9
wacht310 1	23.8	29.7	154.5	0.1	27.2	0.1	0.1	15.1	0.7
wacht311 1	24.0	0.1	121.6	0.1	44.8	0.1	0.6	21.8	0.4
wacht312 1	29.3	0.1	137.9	0.1	122.3	0.1	0.1	30.1	0.8

11 Beucha Rhyolite

Sample	Li	Na	Al	Ca	Ti	Cr	Mn	Fe	Ge
beuch101	21.78	1486.3	197.5	0.1	79.0	15.7	4.2	32.1	1.5
beuch102	18.54	1178.9	195.0	258.4	71.1	10.9	0.1	45.1	2.0
beuch103	18.18	759.2	190.0	63.2	77.4	7.7	5.1	31.8	2.0
beuch104	18.66	1017.8	186.2	0.1	73.2	10.3	0.1	29.2	1.3
beuch105	19.08	1081.5	211.8	0.1	112.5	4.8	0.1	54.8	1.2
beuch201	22.38	948.9	186.2	164.1	95.7	5.8	0.8	39.9	2.2
beuch202	16.44	958.5	179.7	121.0	80.2	2.2	0.9	42.5	1.9
beuch203	19.74	800.1	178.1	260.8	85.6	7.9	0.3	25.6	0.5
beuch204	18.84	803.9	182.7	151.1	82.0	8.0	0.1	17.6	1.3
beuch205	19.2	971.4	178.0	0.1	83.4	8.4	0.1	29.1	1.5
beuch206	19.44	727.3	188.4	0.1	91.4	1.7	0.1	58.0	1.0

12 Flossenbürg Granite

Sample	Li	Na	Al	Ca	Ti	Cr	Mn	Fe	Ge
floss01 1	11.3	833.3	49.4	0.1	13.5	0.1	0.1	13.1	1.9
floss02 1	12.5	279.7	71.3	147.2	36.4	0.2	0.1	4.9	2.6
floss03 1	12.7	357.1	84.1	257.2	34.8	0.1	0.1	7.5	2.2
floss04 1	23.1	512.9	145.9	0.1	37.5	0.4	0.1	0.1	0.3
floss05 1	16.9	498.5	116.9	110.4	33.1	0.1	0.1	20.9	1.9
floss06 1	17.9	372.2	138.1	211.2	37.0	0.1	0.1	0.1	2.0
floss07 1	12.0	467.2	68.1	16.6	28.5	1.1	0.1	16.7	1.5
floss08 1	12.3	456.3	85.3	201.4	34.2	0.5	0.1	8.3	1.9
floss09 1	16.4	546.4	72.1	0.1	32.1	0.1	0.1	0.1	2.2
floss10 1	12.5	438.4	110.2	174.2	35.4	0.1	0.1	12.1	1.9

13 Leucosome quartz

Sample	Li	Na	Al	Ca	Ti	Cr	Mn	Fe	Ge
exsud01 1	9.3	273.2	229.6	234.9	27.3	7.9	1.8	140.1	1.1
exsud02 1	12.0	409.5	210.8	306.1	15.4	9.1	1.6	82.0	1.0
exsud03 1	8.5	359.3	234.6	287.6	22.3	7.8	1.9	127.2	1.2
exsud04 1	6.2	346.1	246.5	264.8	23.3	8.0	4.4	100.7	1.6
exsud05 1	5.7	276.0	232.2	192.1	21.8	3.4	3.1	45.5	2.1
exsud06 1	10.3	439.2	243.8	304.7	18.8	7.6	2.1	60.5	1.2
exsud07 1	9.4	297.3	227.5	293.5	25.3	8.1	1.8	58.7	2.1
exsud08 1	6.4	321.2	212.0	253.9	22.6	5.6	3.0	114.2	1.3
exsud09 1	9.2	482.1	250.6	304.5	21.3	9.0	3.3	128.2	3.5
exsud10 2	8.3	403.2	237.9	295.4	22.6	8.9	2.7	94.0	2.0

List of trace element analysis of quartz (LA ICP-MS) (continued)

14 Ramberg Granite

Sample	Li	Na	Al	Ca	Ti	Cr	Mn	Fe	Ge
ram01 1	13.7	650.5	389.4	880.8	42.8	19.4	2.4	85.6	3.0
ram02 1	13.8	494.0	421.9	483.8	28.3	6.6	1.3	56.6	2.0
ram03 1	19.5	505.4	428.9	282.5	23.1	8.1	0.6	46.2	1.2
ram04 1	14.2	870.5	378.9	1056.0	36.5	5.3	1.3	73.1	2.3
ram05 1	14.7	764.4	471.9	545.3	35.7	14.3	1.0	71.5	2.1
ram06 1	15.6	647.5	479.7	657.4	34.4	6.5	1.4	68.9	2.1
ram07 1	18.5	530.3	398.7	943.2	25.2	8.3	0.8	50.3	3.2
ram08 1	15.3	732.2	456.9	456.3	35.9	11.2	1.6	71.9	2.4
ram09 1	16.5	842.5	498.0	645.3	36.8	9.4	1.3	73.6	2.0
ram10 1	14.3	653.9	423.8	899.7	37.8	6.4	1.7	75.5	1.9

15 Weinheim Rhyolite

Sample	Li	Na	Al	Ca	Ti	Cr	Mn	Fe	Ge
wein101 1	29.2	746.2	185.7	0.1	24.9	1.0	1.7	0.1	1.6
wein102 1	46.5	55.5	179.8	0.1	44.1	0.1	1.3	0.1	2.5
wein103 1	56.2	123.7	171.0	331.4	75.4	6.8	1.2	4.6	5.6
wein104 1	43.7	0.1	169.1	0.1	99.5	6.4	0.4	0.1	3.7
wein105 1	34.8	0.1	169.2	0.1	98.0	0.1	0.3	0.1	1.6
wein106 1	25.9	309.6	170.6	97.2	79.0	0.1	0.4	0.1	1.0
wein107 1	30.8	5474.6	170.3	0.1	87.6	5.8	5.5	0.1	1.3
wein108 1	33.0	1307.6	172.7	0.1	51.7	0.1	9.7	0.1	0.8
wein109 1	24.8	445.5	184.9	268.6	44.3	0.5	1.3	0.1	0.9
wein110 1	22.6	350.8	173.9	283.8	33.7	0.1	0.1	0.1	2.0
wein201 1	31.1	449.4	155.3	547.6	62.3	0.1	0.5	30.7	2.3
wein202 1	37.1	0.1	184.0	247.6	60.1	1.8	1.3	11.3	0.9
wein203 1	34.7	6474.0	214.7	208.3	178.8	10.4	1.7	45.2	3.3
wein204 1	31.0	563.6	192.6	0.1	84.3	0.4	1.5	0.1	2.0
wein206 1	39.4	245.1	196.3	249.2	162.6	10.5	2.2	49.2	0.7
wein207 1	39.7	181.3	189.3	40.5	123.8	0.1	1.4	0.1	1.8
wein208 1	37.9	211.1	170.5	270.9	52.7	0.1	1.2	54.6	1.3
wein209 1	24.8	80.9	162.2	239.4	40.5	4.3	0.1	22.9	2.0
wein301 1	35.9	540.4	152.6	307.9	35.7	1.7	4.8	0.1	1.2
wein302 1	42.8	0.1	154.3	454.1	13.7	0.1	0.5	0.1	0.1
wein303 1	50.6	0.1	162.5	637.3	58.7	0.1	1.5	0.1	3.2
wein304 1	44.8	0.1	165.3	326.3	105.3	2.7	0.7	36.8	2.8
wein305 1	34.7	0.1	172.4	0.1	132.9	0.1	0.7	24.5	0.8
wein308 1	32.1	3122.5	170.2	787.0	186.6	0.1	2.5	28.2	7.6
wein309 1	33.3	1289.3	174.7	0.1	122.0	7.6	6.1	26.4	1.6
wein310 1	32.5	502.6	165.5	344.7	165.6	1.0	8.5	38.2	0.8
wein401 1	28.3	185.2	171.2	246.5	38.5	0.1	0.5	0.1	0.6
wein402 1	27.3	191.7	194.4	77.0	45.5	0.4	0.4	0.1	1.5
wein403 1	31.4	152.8	195.7	281.6	75.8	1.7	0.1	0.1	2.2
wein404 1	34.0	241.9	202.6	314.0	69.4	0.1	0.5	0.1	0.5
wein405 1	32.6	109.1	199.2	4.0	71.1	1.1	0.1	0.1	0.7
wein406 1	27.4	145.4	189.9	239.6	62.8	0.1	0.5	0.1	1.3
wein407 1	26.3	1104.7	189.2	364.0	36.1	0.1	0.8	0.1	1.0
wein408 1	28.1	1611.2	176.9	402.9	26.0	5.2	1.4	0.1	1.5
wein501 1	28.5	544.5	173.7	0.1	66.0	0.6	3.8	19.6	2.5
wein502 1	41.6	556.1	179.2	0.1	113.9	2.5	0.2	32.2	0.1
wein503 1	46.3	776.2	195.7	0.1	241.7	14.4	7.6	30.0	2.1
wein504 1	54.1	899.0	196.2	0.1	305.7	1.5	0.1	55.1	2.5
wein505 1	48.1	1065.4	204.8	0.1	267.0	44.7	0.1	44.0	2.8
wein506 1	42.7	1026.0	223.0	0.1	221.8	1.3	2.2	24.0	0.7
wein507 1	46.7	1289.3	225.7	0.1	259.9	1.3	0.4	38.4	1.7
wein508 1	51.4	909.6	215.5	0.1	203.6	7.2	0.4	23.7	2.2
wein509 1	35.4	944.0	167.8	0.1	50.7	7.9	0.1	19.2	2.8

Appendix D

List of trace element analysis of quartz (EPMA)

1 Megaquartz

Sample	Al	Ti	K	Fe
Megaquartz	158.8	0.0	33.2	15.5
Megaquartz	142.9	0.0	24.9	7.8
Megaquartz	153.5	0.0	8.3	15.5
Megaquartz	127.1	12.0	16.6	15.5
Megaquartz	5.3	6.0	8.3	7.8
Megaquartz	5.3	12.0	16.6	15.5
Megaquartz	5.3	6.0	16.6	0.0
Megaquartz	5.3	0.0	0.0	0.0
Megaquartz	5.3	0.0	24.9	0.0
Megaquartz	5.3	0.0	24.9	7.8

2 Fissile quartz

Sample	Al	Ti	K	Fe
Fissile	21.2	18.0	33.2	7.8
Fissile	15.9	0.0	58.1	23.3
Fissile	21.2	18.0	41.5	0.0
Fissile	15.9	0.0	49.8	7.8
Fissile	21.2	6.0	66.4	15.5
Fissile	26.5	18.0	99.6	15.5
Fissile	10.6	12.0	66.4	7.8
Fissile	21.2	6.0	49.8	7.8
Fissile	21.2	0.0	83.0	0.0
Fissile	21.2	30.0	58.1	0.0

3 Oil-bearing quartz

Sample	Al	Ti	K	Fe
Oil	455.3	0.0	41.5	0.0
Oil	465.9	0.0	33.2	7.8
Oil	460.6	0.0	33.2	31.1
Oil	471.2	18.0	24.9	0.0
Oil	434.1	18.0	41.5	15.5
Oil	434.1	18.0	49.8	0.0
Oil	476.5	0.0	58.1	0.0
Oil	476.5	6.0	41.5	15.5

6 Schellerhau Granite

Sample	Al	Ti	K	Fe
Schel matrix	199.0	0.0		7.8
Schel matrix	273.2	0.0		15.5
Schel matrix	214.9	21.0		15.5
Schel matrix	199.0	17.0		0.0
Schel matrix	214.9	19.0		0.0
Schel matrix	199.0	25.0		15.5
Schel matrix	225.5	24.0		15.5
Schel matrix	183.1	27.0		15.5
Schel matrix	156.6	30.0		23.3
Schel matrix	209.6	30.0		15.5
Schel matrix	193.7	30.0		15.5
Schel matrix	206.2	36.0		23.3
Schell red CL	98.3	11.0		0.0
Schell red CL	124.8	12.0		23.3
Schell red CL	98.3	14.0		0.0

6 Schellerhau Granite

Sample	Al	Ti	K	Fe
Schell red CL	108.9	16.0		0.0
Schell red CL	103.6	18.0		0.0
Schell red CL	114.2	18.0		23.3
Schell red CL	93.0	18.0		31.1
Schell red CL	124.8	18.0		15.5
Schell red CL	135.4	16.0		0.0
Schell red CL	135.4	18.0		7.8
Schell red CL	188.4	29.0		0.0
Schell red CL	119.5	24.0		7.8
Schell red CL	130.1	21.0		0.0
Schell red CL	93.0	24.0		0.0
Schell red CL	93.0	25.0		0.0
Schell red CL	114.2	24.0		15.5
Schell red CL	103.6	26.0		23.3
Schell red CL	108.9	27.0		0.0
Schell red CL	82.4	31.0		23.3
Schell red CL	119.5	29.0		15.5
Schell red CL	98.3	33.0		0.0
Schell red CL	103.6	35.0		7.8
Schell red CL	135.4	32.0		0.0
Schell red CL	114.2	28.0		0.0
Schell red CL	103.6	30.0		15.5
Schell red CL	93.0	36.0		23.3
Schell red CL	98.3	36.0		15.5
Schell red CL	130.1	36.0		15.5
Schell red CL	103.6	38.0		15.5
Schell red CL	87.7	48.0		7.8
Schell blue CL	87.7	36.0		7.8
Schell blue CL	124.8	42.0		7.8
Schell blue CL	108.9	42.0		7.8
Schell blue CL	93.0	42.0		0.0
Schell blue CL	93.0	42.0		15.5
Schell blue CL	93.0	48.0		7.8
Schell blue CL	93.0	50.0		0.0
Schell blue CL	77.1	46.0		0.0
Schell blue CL	124.8	51.0		0.0
Schell blue CL	103.6	54.0		15.5
Schell blue CL	82.4	54.0		7.8
Schell blue CL	98.3	55.0		7.8
Schell blue CL	87.7	57.0		15.5
Schell blue CL	98.3	58.0		15.5
Schell blue CL	98.3	62.0		0.0

8 Aue Granite

Sample	Al	Ti	K	Fe
aue	58.2	60.0	41.5	23.3
aue	42.4	60.0	49.8	31.1
aue	63.5	60.0	41.5	15.5
aue	68.8	65.9	49.8	38.9
aue	79.4	65.9	33.2	23.3
aue	58.2	65.9	33.2	7.8
aue	74.1	71.9	83.0	23.3

List of trace element analysis of quartz (EPMA) (continued)

9 Vein quartz

Sample	Al	Ti	K	Fe
Vein	3377.6	30.0	33.2	31.1
Vein	3488.7	36.0	41.5	31.1
Vein	4155.8	24.0	58.1	15.5
Vein	4214.0	30.0	66.4	31.1
Vein	3769.3	24.0	41.5	15.5
Vein	2779.4	30.0	24.9	23.3
Vein	3044.1	18.0	24.9	31.1
Vein	2567.6	18.0	33.2	38.9
Vein	2721.1	30.0	33.2	23.3
Vein	2832.3	24.0	24.9	31.1
Vein	2212.9	18.0	24.9	15.5
Vein	2408.8	24.0	16.6	15.5
Vein	4351.7	18.0	356.9	31.1
Vein	3282.3	18.0	33.2	15.5
Vein	3165.8	24.0	16.6	23.3
Vein	3102.3	36.0	41.5	23.3
Vein	3049.3	18.0	33.2	23.3
Vein	2954.1	24.0	33.2	31.1
Vein	3991.7	18.0	16.6	15.5
Vein	4383.4	18.0	16.6	23.3
Vein	4277.6	36.0	24.9	31.1
Vein	4886.4	36.0	24.9	23.3
Vein	4886.4	24.0	16.6	31.1
Vein	3022.9	24.0	24.9	15.5
Vein	3245.2	30.0	41.5	31.1
Vein	3123.5	36.0	33.2	23.3
Vein	3277.0	30.0	33.2	23.3
Vein	3377.6	18.0	33.2	23.3

10 Wachtelberg Rhyolite

Sample	Al	Ti	K	Fe
wachtell	26.5	42.0	16.6	38.9
wachtell	21.2	42.0	24.9	38.9
wachtell	21.2	42.0	16.6	15.5
wachtell	26.5	42.0	16.6	31.1
wachtell	26.5	48.0	16.6	15.5
wachtell	15.9	48.0	16.6	23.3
wachtell	21.2	54.0	16.6	15.5
wachtell	31.8	54.0	8.3	31.1
wachtell	26.5	54.0	8.3	31.1
wachtell	26.5	60.0	8.3	31.1
wachtell	26.5	60.0	16.6	31.1
wachtell	31.8	60.0	8.3	31.1
wachtell	15.9	65.9	16.6	23.3
wachtell	26.5	65.9	16.6	31.1
wachtell	21.2	65.9	16.6	23.3
wachtell	15.9	65.9	16.6	31.1
wachtell	37.1	65.9	8.3	31.1
wachtell	21.2	71.9	16.6	23.3
wachtell	31.8	71.9	8.3	31.1
wachtell	26.5	71.9	16.6	31.1
wachtell	26.5	71.9	16.6	38.9
wachtell	26.5	77.9	16.6	31.1

11 Beucha Rhyolite

Sample	Al	Ti	K	Fe
beuch red CL	142.9	18.0	16.6	15.5
beuch red CL	153.5	18.0	8.3	31.1
beuch red CL	148.2	18.0	33.2	15.5
beuch red CL	37.1	24.0	16.6	15.5
beuch red CL	52.9	30.0	8.3	7.8
beuch red CL	201.2	30.0	24.9	31.1
beuch red CL	153.5	30.0	8.3	38.9
beuch red CL	15.9	36.0	24.9	31.1
beuch red CL	137.6	36.0	8.3	31.1
beuch red CL	132.4	42.0	8.3	15.5
beuch blue CL	37.1	48.0	8.3	38.9
beuch blue CL	37.1	48.0	16.6	23.3
beuch blue CL	58.2	54.0	8.3	23.3
beuch blue CL	148.2	54.0	8.3	46.6
beuch blue CL	42.4	65.9	24.9	31.1
beuch blue CL	37.1	65.9	16.6	38.9
beuch blue CL	158.8	65.9	8.3	46.6
beuch blue CL	31.8	65.9	24.9	46.6
beuch blue CL	42.4	71.9	8.3	38.9
beuch blue CL	58.2	71.9	8.3	46.6
beuch blue CL	31.8	77.9	24.9	101.0
beuch blue CL	153.5	83.9	0.0	62.2
beuch blue CL	164.1	95.9	8.3	70.0
beuch blue CL	164.1	95.9	8.3	46.6
beuch blue CL	174.7	95.9	0.0	62.2
beuch blue CL	42.4	95.9	16.6	38.9
beuch blue CL	153.5	95.9	8.3	62.2
beuch blue CL	58.2	101.9	33.2	70.0
beuch blue CL	164.1	101.9	8.3	70.0
beuch blue CL	164.1	101.9	8.3	70.0
beuch blue CL	158.8	101.9	16.6	93.3
beuch blue CL	116.5	113.9	16.6	108.8
beuch blue CL	42.4	113.9	24.9	101.0
beuch blue CL	42.4	119.9	8.3	147.7
beuch blue CL	52.9	119.9	16.6	155.5
beuch blue CL	42.4	125.9	16.6	241.0
beuch blue CL	74.1	125.9	24.9	349.8

12 Flossenbürg Granite

Sample	Al	Ti	K	Fe
Floss_1	5.3	24.0	8.3	15.5
Floss_1	5.3	24.0	8.3	15.5
Floss_2	5.3	24.0	8.3	7.8
Floss_2	5.3	30.0	8.3	23.3
Floss_2	5.3	30.0	8.3	15.5
Floss_2	5.3	30.0	8.3	15.5
Floss_2	5.3	30.0	8.3	23.3
Floss_2	5.3	36.0	8.3	15.5
Floss_2	15.9	42.0	8.3	15.5
Floss_2	5.3	42.0	0.0	23.3
Floss_2	5.3	42.0	8.3	7.8

List of trace element analysis of quartz (EPMA) (continued)

13 Leucosome quartz

Sample	Al	Ti	K	Fe
Leucosome	84.7	24.0	49.8	7.8
Leucosome	100.6	30.0	83.0	15.5
Leucosome	84.7	30.0	74.7	7.8
Leucosome	95.3	18.0	107.9	7.8
Leucosome	95.3	0.0	74.7	0.0
Leucosome	100.6	12.0	132.8	0.0
Leucosome	90.0	18.0	74.7	0.0
Leucosome	116.5	12.0	33.2	23.3
Leucosome	84.7	12.0	33.2	7.8
Leucosome	84.7	24.0	24.9	15.5

14 Ramberg Granite

Sample	Al	Ti	K	Fe
ramb	5.3	36.0	16.6	15.5
ramb	5.3	42.0	33.2	23.3
ramb	47.6	42.0	16.6	15.5
ramb	127.1	48.0	33.2	23.3
ramb	111.2	60.0	16.6	38.9
ramb	47.6	60.0	24.9	31.1
ramb	95.3	60.0	8.3	7.8
ramb	153.5	77.9	49.8	23.3
ramb	5.3	42.0	8.3	15.5

15 Weinheim Rhyolite

Sample	Al	Ti	K	Fe
wein red CL	180.0	24.0	8.3	23.3
wein red CL	169.4	24.0	24.9	31.1
wein red CL	142.9	24.0	16.6	23.3
wein red CL	142.9	24.0	16.6	31.1
wein red CL	142.9	36.0	8.3	15.5
wein red CL	142.9	36.0	16.6	23.3
wein red CL	148.2	42.0	8.3	15.5
wein red CL	180.0	42.0	8.3	7.8
wein red CL	180.0	42.0	8.3	7.8
wein red CL	180.0	42.0	8.3	15.5
wein red CL	158.8	42.0	8.3	23.3
wein blue CL	185.3	42.0	8.3	7.8
wein blue CL	52.9	42.0	16.6	23.3
wein blue CL	68.8	42.0	33.2	46.6
wein blue CL	153.5	48.0	16.6	15.5
wein blue CL	185.3	48.0	16.6	7.8
wein blue CL	148.2	48.0	16.6	15.5
wein blue CL	169.4	48.0	16.6	23.3
wein blue CL	158.8	54.0	16.6	7.8
wein blue CL	158.8	54.0	8.3	15.5
wein blue CL	74.1	54.0	16.6	31.1
wein blue CL	153.5	54.0	16.6	7.8
wein blue CL	148.2	54.0	8.3	15.5
wein blue CL	169.4	54.0	8.3	15.5
wein blue CL	158.8	54.0	8.3	7.8
wein blue CL	164.1	60.0	16.6	7.8
wein blue CL	169.4	60.0	8.3	31.1
wein blue CL	68.8	60.0	16.6	31.1
wein blue CL	164.1	60.0	24.9	23.3
wein blue CL	137.6	65.9	16.6	7.8
wein blue CL	158.8	65.9	16.6	23.3
wein blue CL	153.5	65.9	16.6	15.5
wein blue CL	185.3	65.9	16.6	7.8
wein blue CL	169.4	65.9	16.6	7.8

15 Weinheim Rhyolite

Sample	Al	Ti	K	Fe
wein blue CL	169.4	71.9	16.6	15.5
wein blue CL	52.9	71.9	24.9	31.1
wein blue CL	58.2	89.9	24.9	23.3
wein red CL	158.8	18.0	8.3	15.5
wein red CL	127.1	18.0	16.6	15.5
wein red CL	142.9	18.0	8.3	31.1
wein red CL	132.4	18.0	16.6	46.6
wein red CL	142.9	18.0	58.1	70.0

Carcoar Granodiorite

Sample	Al	Ti	K	Fe
carcor	350	110	200	30
carcor	0	100	30	0
carcor	0	80	0	30
carcor	0	50	20	20
carcor	0	50	30	20
carcor	0	40	20	0
carcor	180	70	130	20
carcor	0	100	0	20
carcor	0	90	20	20
carcor	240	100	130	30
carcor	250	100	160	30
carcor	0	80	20	30
carcor	0	70	0	30
carcor	0	80	0	40
carcor	0	90	0	40
carcor	0	90	20	50
carcor	90	90	80	60
carcor	0	50	40	70
carcor	0	50	20	90
carcor	0	40	0	120
carcor	0	40	20	170
carcor	0	40	20	250
carcor	0	30	40	460
carcor	0	20	30	470
carcor	0	130	20	30
carcor	0	120	20	20
carcor	0	100	0	40
carcor	0	30	20	20
carcor	0	100	0	40
carcor	0	100	0	30
carcor	0	120	20	20
carcor	0	140	20	30
carcor	0	110	20	20
carcor	0	100	0	30
carcor	0	100	20	20
carcor	0	80	0	20
carcor	0	90	20	0
carcor	0	90	0	20
carcor	0	120	20	20
carcor	0	110	20	0
carcor	0	110	0	0
carcor	0	110	0	0
carcor	0	100	20	0
carcor	0	110	0	20
carcor	0	120	0	30
carcor	0	100	30	0
carcor	0	120	20	0

List of trace element analysis of quartz (EPMA) (continued)

Barry Granodiorite

Sample	Al	Ti	K	Fe
bary	100	60	50	0
bary	230	60	110	0
bary	140	60	60	0
bary	220	50	110	30
bary	0	60	0	0
bary	260	40	0	40
bary	90	90	90	20
bary	0	0	20	12
bary	0	0	0	50
bary	0	0	30	0
bary	0	0	0	0
bary	110	0	60	20
bary	12	20	30	0
bary	12	12	12	0
bary	12	70	30	0
bary	160	60	80	20
bary	0	60	0	0
bary	0	50	0	0
bary	400	60	170	20
bary	0	50	0	20
bary	380	60	170	20
bary	160	40	70	0
bary	150	50	70	0
bary	150	50	60	0
bary	0	20	30	20
bary	180	40	80	0
bary	0	40	0	0
bary	0	70	20	0
bary	360	50	170	0
bary	280	60	130	0
bary	0	70	20	20
bary	0	30	0	20
bary	390	50	240	30
bary	90	30	20	20
bary	170	40	60	30
bary	0	20	40	40
bary	0	0	30	60

Sunset Hills Granite

Sample	Al	Ti	K	Fe
sunset	0	90	0	0
sunset	0	70	20	20
sunset	90	80	30	0
sunset	90	90	40	20
sunset	0	70	0	0
sunset	410	80	200	0
sunset	0	60	0	0
sunset	0	60	0	0
sunset	310	70	180	30
sunset	0	60	30	0
sunset	0	100	0	0
sunset	0	90	0	20
sunset	130	120	70	0
sunset	0	120	0	30
sunset	280	0	130	20
sunset	0	140	0	20
sunset	450	50	250	200
sunset	200	70	120	20
sunset	240	30	110	0
sunset	140	60	70	0
sunset	170	70	70	0

Sunset Hills Granite

Sample	Al	Ti	K	Fe
sunset	0	60	40	30
sunset	0	40	20	20
sunset	0	30	0	0
sunset	0	40	0	40
sunset	470	30	230	40
sunset	0	50	0	0
sunset	0	90	0	0
sunset	150	100	90	20
sunset	12	90	20	20
sunset	12	90	20	0
sunset	380	80	160	0
sunset	12	60	20	30
sunset	12	160	0	30
sunset	90	140	50	40
sunset	0	100	0	40
sunset	0	20	0	20
sunset	0	50	0	0
sunset	510	120	20	30
sunset	0	120	20	20
sunset	0	60	20	20
sunset	0	50	0	0
sunset	0	30	20	0
sunset	0	0	0	20
sunset	0	40	0	30
sunset	0	0	0	20
sunset	0	0	0	20

Porphyritic topaz-albite granite (Ju 10)

Sample	Al	Ti	K	Fe
Ju_10_1	222.3	60.0	8.3	31.1
Ju_10_1	232.9	48.0	24.9	38.9
Ju_10_1	185.3	48.0	16.6	23.3
Ju_10_1	238.2	60.0	16.6	31.1
Ju_10_1	84.7	24.0	16.6	23.3
Ju_10_1	238.2	42.0	16.6	31.1
Ju_10_1	232.9	42.0	8.3	38.9
Ju_10_1	232.9	30.0	16.6	38.9
Ju_10_1	217.1	42.0	8.3	38.9
Ju_10_1	227.6	36.0	16.6	15.5
Ju_10_1	248.8	30.0	8.3	31.1
Ju_10_1	254.1	42.0	24.9	31.1
Ju_10_1	254.1	54.0	24.9	38.9
Ju_10_1	259.4	48.0	16.6	15.5
Ju_10_1	264.7	48.0	8.3	15.5
Ju_10_1	259.4	54.0	16.6	23.3
Ju_10_1	248.8	36.0	24.9	23.3
Ju_10_1	259.4	48.0	16.6	38.9
Ju_10_1	254.1	54.0	24.9	31.1
Ju_10_1	264.7	54.0	16.6	54.4
Ju_10_1	248.8	48.0	24.9	15.5
Ju_10_1	222.3	42.0	16.6	38.9
Ju_10_1	190.6	42.0	24.9	38.9
Ju_10_1	232.9	48.0	16.6	23.3
Ju_10_1	222.3	54.0	16.6	15.5
Ju_10_1	201.2	54.0	16.6	23.3
Ju_10_1	190.6	60.0	16.6	31.1
Ju_10_1	174.7	54.0	24.9	31.1
Ju_10_1	206.5	48.0	24.9	23.3
Ju_10_1	248.8	65.9	33.2	15.5
Ju_10_1	211.8	54.0	16.6	23.3
Ju_10_1	217.1	48.0	16.6	15.5

List of trace element analysis of quartz (EPMA) (continued)

Porphyritic topaz-albite granite (Ju 10)

Sample	Al	Ti	K	Fe
Ju_10_1	169.4	42.0	16.6	23.3
Ju_10_1	185.3	60.0	16.6	23.3
Ju_10_1	206.5	54.0	16.6	31.1
Ju_10_1	174.7	36.0	16.6	23.3
Ju_10_1	195.9	48.0	8.3	31.1
Ju_10_1	206.5	42.0	16.6	38.9
Ju_10_1	190.6	65.9	16.6	31.1
Ju_10_1	232.9	36.0	16.6	23.3
Ju_10_1	201.2	42.0	24.9	31.1
Ju_10_1	264.7	36.0	8.3	23.3
Ju_10_1	248.8	42.0	16.6	23.3
Ju_10_1	264.7	48.0	16.6	23.3
Ju_10_1	264.7	36.0	41.5	23.3
Ju_10_1	26.5	24.0	33.2	31.1
Ju_10_1	264.7	30.0	24.9	15.5
Ju_10_1	301.8	30.0	33.2	23.3
Ju_10_1	259.4	30.0	16.6	15.5
Ju_10_1	137.6	24.0	16.6	23.3
Ju_10_1	365.3	24.0	49.8	31.1
Ju_10_1	322.9	24.0	8.3	23.3
Ju_10_1	275.3	24.0	8.3	15.5
Ju_10_1	338.8	24.0	24.9	38.9

Topaz-albite microgranite (Ju 20)

Sample	Al	Ti	K	Fe
Ju_20_1	222.3	48.0	24.9	31.1
Ju_20_1	222.3	36.0	10.0	15.5
Ju_20_1	545.3	48.0	74.7	38.9
Ju_20_1	211.8	48.0	16.6	15.5
Ju_20_1	561.2	48.0	265.6	77.7
Ju_20_1	291.2	48.0	33.2	31.1
Ju_20_1	222.3	30.0	16.6	15.5
Ju_20_1	9.0	12.0	8.3	23.3
Ju_20_1	9.0	12.0	16.6	7.8
Ju_20_1	201.2	48.0	16.6	15.5
Ju_20_1	217.1	42.0	16.6	38.9
Ju_20_1	248.8	54.0	24.9	31.1
Ju_20_1	217.1	48.0	8.3	15.5
Ju_20_1	534.7	60.0	149.4	38.9
Ju_20_1	227.6	54.0	24.9	23.3
Ju_20_1	354.7	48.0	74.7	38.9
Ju_20_1	217.1	48.0	8.3	23.3
Ju_20_1	238.2	30.0	24.9	23.3
Ju_20_1	238.2	54.0	16.6	15.5
Ju_20_1	259.4	42.0	16.6	15.5
Ju_20_1	222.3	42.0	16.6	7.8
Ju_20_1	270.0	42.0	33.2	31.1
Ju_20_1	211.8	54.0	24.9	7.8
Ju_20_1	232.9	54.0	16.6	23.3
Ju_20_1	248.8	42.0	24.9	23.3
Ju_20_1	254.1	30.0	24.9	23.3
Ju_20_1	264.7	54.0	16.6	7.8
Ju_20_1	349.4	48.0	74.7	31.1
Ju_20_1	328.2	48.0	33.2	15.5
Ju_20_1	222.3	48.0	24.9	23.3
Ju_20_1	217.1	42.0	16.6	31.1
Ju_20_1	238.2	36.0	33.2	15.5
Ju_20_1	222.3	54.0	16.6	15.5

Topaz-albite microgranite (Ju 20)

Sample	Al	Ti	K	Fe
Ju_20_1	217.1	42.0	16.6	31.1
Ju_20_1	232.9	36.0	16.6	31.1
Ju_20_1	296.5	36.0	49.8	23.3
Ju_20_1	296.5	48.0	8.3	7.8
Ju_20_1	217.1	36.0	8.3	23.3
Ju_20_1	238.2	24.0	24.9	31.1
Ju_20_1	211.8	42.0	8.3	31.1
Ju_20_1	211.8	18.0	16.6	15.5
Ju_20_1	275.3	36.0	41.5	31.1
Ju_20_1	502.9	36.0	149.4	54.4
Ju_20_1	190.6	24.0	16.6	23.3
Ju_20_1	217.1	36.0	16.6	15.5
Ju_20_1	232.9	24.0	24.9	23.3
Ju_20_1	291.2	24.0	16.6	31.1
Ju_20_1	296.5	18.0	24.9	15.5
Ju_20_1	211.8	24.0	8.3	31.1
Ju_20_1	227.6	36.0	24.9	38.9
Ju_20_1	301.8	36.0	24.9	38.9
Ju_20_1	217.1	30.0	16.6	46.6
Ju_20_1	836.5	48.0	298.8	124.4
Ju_20_1	222.3	12.0	16.6	38.9
Ju_20_1	270.0	24.0	24.9	38.9
Ju_20_1	206.5	18.0	16.6	54.4
Ju_20_1	365.3	24.0	49.8	77.7
Ju_20_1	227.6	18.0	16.6	77.7
Ju_20_1	206.5	18.0	16.6	116.6
Ju_20_1	158.8	18.0	24.9	163.2
Ju_20_1	232.9	30.0	66.4	272.1
Ju_20_2	301.8	30.0	49.8	38.9
Ju_20_2	206.5	48.0	16.6	31.1
Ju_20_2	248.8	42.0	24.9	31.1
Ju_20_2	481.8	36.0	141.1	54.4
Ju_20_2	741.2	36.0	215.8	93.3
Ju_20_2	232.9	30.0	8.3	23.3
Ju_20_2	206.5	48.0	16.6	15.5
Ju_20_2	291.2	42.0	8.3	23.3
Ju_20_2	217.1	42.0	8.3	15.5
Ju_20_2	211.8	30.0	16.6	23.3

Podlesi dyke granite

Sample	Al	Ti	K	Fe
Podlesi	160	40	20	0
Podlesi	150	30	20	10
Podlesi	180	30	10	10
Podlesi	160	40	20	10
Podlesi	160	10	20	0
Podlesi	230	30	20	0
Podlesi	270	20	30	20
Podlesi	250	40	10	10
Podlesi	350	30	30	0
Podlesi	170	20	20	20
Podlesi	480	30	30	0
Podlesi	490	20	30	0
Podlesi	570	20	30	20
Podlesi	620	20	20	20
Podlesi	480	20	40	20
Podlesi	410	30	20	0

List of trace element analysis of quartz (EPMA) (continued)

Podlesi dyke granite

Sample	Al	Ti	K	Fe
Podlesi	410	20	0	0
Podlesi	570	20	30	10
Podlesi	400	10	20	10
Podlesi	2000	20	30	10
Podlesi	280	40	20	10
Podlesi	390	20	20	10
Podlesi	2000	30	1140	90
Podlesi	130	20	20	20
Podlesi	220	20	10	10
Podlesi	120	10	20	20
Podlesi	160	20	60	0
Podlesi	490	30	170	0
Podlesi	570	30	150	0
Podlesi	120	10	30	10
Podlesi	130	10	10	20
Podlesi	2000	50	20	90
Podlesi	880	30	30	40
Podlesi	260	20	20	40
Podlesi	280	20	10	50
Podlesi	180	10	20	60
Podlesi	280	20	40	90
Podlesi	510	30	80	110

Schellerhau SG3

Sample	Al	Ti	K	Fe
Schell G3	720	60	10	20
Schell G4	120	50	10	10
Schell G5	50	20	0	10
Schell G6	490	20	10	0
Schell G7	10	10	10	0
Schell G8	30	30	10	0
Schell G9	30	30	10	20
Schell G10	280	10	20	10
Schell G11	370	30	10	10
Schell G12	280	50	10	10
Schell G13	280	40	10	0
Schell G14	270	40	10	10
Schell G15	1810	30	0	10
Schell G16	410	40	20	20
Schell G17	580	20	10	0
Schell G18	240	60	20	30
Schell G19	690	20	20	10
Schell G20	500	20	0	0
Schell G21	1150	40	0	0
Schell G22	1740	40	50	10
Schell G23	260	30	20	10
Schell G24	380	20	20	0
Schell G25	350	10	10	0
Schell G26	30	20	20	0

Schellerhau SG3

Sample	Al	Ti	K	Fe
Schell G27	330	20	0	10
Schell G28	10	20	20	0
Schell G29	370	20	0	10
Schell G30	270	40	10	10
Schell G31	100	30	10	0
Schell G32	10	0	10	0
Schell G33	80	20	20	10
Schell G34	70	30	10	0
Schell G35	130	40	0	10
Schell G36	520	30	20	10
Schell G37	130	40	10	0
Schell G38	130	30	10	20
Schell G39	0	40	10	10
Schell G40	160	30	20	0
Schell G41	230	20	20	0
Schell G42	130	20	10	0
Schell G43	230	10	0	10
Schell G44	100	20	0	0
Schell G45	70	20	10	0
Schell G46	30	0	10	0
Schell G47	30	10	0	0
Schell G48	40	10	10	10
Schell G49	0	30	10	20
Schell G50	30	10	0	10
Schell G51	80	10	50	10
Schell G52	40	20	10	10
Schell G53	30	0	0	0
Schell G54	20	30	0	0
Schell G55	10	10	10	0
Schell G56	30	20	10	0
Schell G57	30	20	0	0
Schell G58	10	20	0	10
Schell G59	0	20	0	0
Schell G60	0	10	0	0
Schell G61	0	10	10	10
Schell G62	0	0	0	0
Schell G63	0	20	20	10
Schell G64	0	20	10	0
Schell G65	0	10	10	10
Schell G66	0	10	0	10
Schell G67	0	20	10	10
Schell G68	0	0	10	0
Schell G69	0	0	0	10
Schell G70	0	10	0	0
Schell G71	0	0	10	10
Schell G72	0	20	0	10
Schell G73	0	30	20	0
Schell G74	0	20	10	0
Schell G75	0	30	20	10
Schell G76	0	10	0	0

Appendix E

List of trace element analysis of quartz (SIMS) given in relative concentrations ($X/^{30}\text{Si}$)

1 Megaquartz

Sample	6Li/30Si	23Na/30Si	27Al/30Si	39K/30Si	48Ti/30Si	54Fe/30Si
Hak01	2.16E-04	3.78E-05	1.54E-02	2.12E-05	2.52E-06	2.88E-06
Hak02	1.06E-05	1.51E-05	3.10E-03	1.72E-05	1.14E-06	2.67E-07
Hak03	2.84E-04	2.39E-05	1.50E-02	9.12E-06	2.07E-06	2.75E-06
Hak04	2.21E-04	1.69E-05	1.03E-02	5.36E-06	1.82E-06	2.15E-06
Hak05	3.02E-04	1.92E-05	1.53E-02	6.55E-06	1.66E-06	3.48E-06
Hak06	7.17E-06	1.93E-05	7.87E-04	1.09E-05	8.76E-12	1.47E-07

8 Aue Granite

Sample	6Li/30Si	23Na/30Si	27Al/30Si	39K/30Si	48Ti/30Si	54Fe/30Si
AUE01	5.20E-04	3.86E-04	2.80E-02	6.64E-04	1.82E-04	1.40E-05
AUE02	5.25E-04	1.43E-04	2.56E-02	1.27E-04	1.77E-04	1.13E-05
AUE03	4.90E-04	1.79E-04	2.53E-02	1.30E-04	1.90E-04	1.28E-05
AUE04	3.90E-04	1.70E-04	2.10E-02	1.23E-04	2.04E-04	1.20E-05
AUE05	4.16E-04	1.06E-04	2.05E-02	6.77E-05	1.92E-04	9.15E-06
AUE06	3.04E-04	1.06E-04	1.56E-02	7.66E-05	2.22E-04	7.41E-06
AUE07	2.89E-04	1.51E-04	1.60E-02	9.13E-05	2.24E-04	8.69E-06
AUE08	1.29E-04	1.92E-04	1.16E-02	1.49E-04	2.70E-05	6.15E-06
AUE10	3.25E-04	2.81E-04	2.14E-02	2.36E-04	2.02E-04	1.26E-05
AUE11	1.23E-04	9.85E-04	1.47E-02	4.32E-04	1.33E-04	9.44E-06
AUE12	1.79E-04	4.69E-04	1.77E-02	1.97E-04	2.07E-04	1.08E-05
AUE14	1.87E-04	3.08E-04	1.53E-02	1.54E-04	2.10E-04	9.91E-06
AUE15	1.89E-04	3.70E-04	1.62E-02	1.96E-04	2.06E-04	1.15E-05
AUE17	1.73E-04	2.24E-04	1.50E-02	1.46E-04	1.89E-04	1.10E-05
AUE18	2.23E-04	1.80E-04	1.60E-02	1.28E-04	1.92E-04	1.07E-05
AUE19	2.33E-04	1.77E-04	1.67E-02	1.29E-04	2.01E-04	1.11E-05
AUE20	3.23E-04	1.87E-04	2.31E-02	1.47E-04	2.31E-04	1.83E-05
AUE21	3.26E-04	1.48E-04	1.67E-02	9.06E-05	2.26E-04	8.31E-06
AUE24	2.26E-04	1.49E-04	1.67E-02	1.10E-04	2.23E-04	1.60E-05
AUE25	2.79E-04	2.32E-04	2.14E-02	1.49E-04	1.39E-04	2.94E-05
AUE27	1.17E-04	3.38E-04	1.38E-02	1.85E-04	8.42E-06	5.52E-05
AUE28	1.90E-04	1.44E-03	2.93E-02	3.74E-04	1.28E-04	3.01E-05
AUE29	1.89E-04	6.53E-04	1.98E-02	4.89E-04	0.000129	2.78E-05
AUE30	2.26E-04	2.94E-04	2.08E-02	2.15E-04	1.27E-04	2.23E-05
AUE31	2.89E-04	3.28E-04	2.37E-02	2.71E-04	1.27E-04	2.35E-05
AUE32	2.46E-04	5.01E-04	2.21E-02	3.28E-04	1.37E-04	2.02E-05
AUE33	2.22E-04	4.98E-04	2.15E-02	3.52E-04	1.59E-04	2.20E-05
AUE35	1.49E-04	4.71E-04	1.74E-02	3.85E-04	2.06E-04	1.82E-05
AUE36	1.63E-04	3.99E-04	1.78E-02	2.12E-04	2.03E-04	1.61E-05
AUE38	2.90E-04	4.33E-04	2.78E-02	3.14E-04	9.90E-05	2.98E-05
AUE39	1.31E-04	8.14E-04	1.64E-02	5.72E-04	1.64E-04	1.85E-05
AUE40	2.54E-04	2.80E-04	1.87E-02	2.00E-04	2.00E-04	1.91E-05

15 Weinheim Rhyolite

Sample	6Li/30Si	23Na/30Si	27Al/30Si	39K/30Si	48Ti/30Si	54Fe/30Si
Rhy01	2.32E-04	2.05E-04	1.83E-02	1.87E-04	1.76E-04	2.26E-05
Rhy02	2.18E-04	2.16E-04	1.61E-02	1.94E-04	2.26E-04	1.90E-05
Rhy04	9.44E-05	2.43E-04	1.66E-02	2.11E-04	2.44E-04	1.91E-05
Rhy05	1.10E-04	2.39E-04	1.63E-02	2.15E-04	2.37E-04	2.02E-05
Rhy06	9.01E-05	2.19E-04	1.61E-02	1.98E-04	2.38E-04	1.89E-05
Rhy07	9.22E-05	2.52E-04	1.53E-02	2.18E-04	2.28E-04	1.87E-05
Rhy08	1.34E-04	2.66E-04	1.75E-02	2.53E-04	1.86E-04	2.09E-05
Rhy09	2.46E-04	1.35E-03	3.20E-02	3.04E-03	2.97E-04	4.04E-05
Rhy10	2.91E-04	2.60E-03	3.38E-02	3.34E-03	3.07E-04	4.31E-05
Rhy11	3.66E-04	6.38E-04	2.29E-02	7.56E-04	2.41E-04	3.06E-05
Rhy13	2.79E-04	2.70E-04	1.64E-02	2.31E-04	7.65E-05	1.93E-05
Rhy14	2.18E-04	2.47E-04	1.40E-02	1.98E-04	4.64E-05	1.80E-05
Rhy15	1.55E-04	1.53E-03	1.94E-02	1.03E-03	1.29E-04	5.97E-05

Curriculum vitae

Date & place of birth:

2 June 1970, Dresden, Germany

Education:

1977-1983 Polytechnische Oberschule, Dresden

1983-1987 Polytechnische Oberschule, Leipzig

1987-1989 Abitur, Halle

1989-1990 Civil Service

1990-1993; Mining Academy Freiberg

1993-1996; University Göttingen

Diploma in Geology/Paleontology

Advisor: H.-J. Behr

Co-advisor: D. Helmcke

Thesis: Part I - Investigation of magmatic, metamorphic and hydrothermal quartz from the Oberpfalz/Germany with thermal acoustic emission analysis [in German];

Part II – Geological mapping SE of the Flossenbürg Granite Massif, Oberpfalz, Germany [in German]

1996-1997; University Göttingen

Work on DEKORP-Project: Development and application of gravimetric methods for the evidence of steep dipping structures in seismic profiles

1997-2000; University Göttingen

Ph.D. Studies in Earth Sciences

Advisor: H.-J. Behr

Co-advisor: K. Weber

Thesis: Cathodoluminescence and characterisation of defect structures in quartz with applications to the study of granitic rocks